University of Alberta

THE DECISION OF STATIONARITY

by

Jason A. McLennan

A thesis submitted to the Faculty of Graduate Studies and Research in partial fulfillment of the requirements for the degree of **Doctor of Philosophy**

in

Mining Engineering

Department of Civil and Environmental Engineering

Edmonton, Alberta
Spring 2007

Library and
Archives Canada

Published Heritage
Branch

395 Wellington Street
Ottawa ON K1A 0N4
Canada

Bibliothèque et
Archives Canada

Direction du
Patrimoine de l'édition

395, rue Wellington
Ottawa ON K1A 0N4
Canada

Your file Votre référence
ISBN: 978-0-494-29713-1
Our file Notre référence
ISBN: 978-0-494-29713-1

NOTICE:
The author has granted a non-exclusive license allowing Library and Archives Canada to reproduce, publish, archive, preserve, conserve, communicate to the public by telecommunication or on the Internet, loan, distribute and sell theses worldwide, for commercial or non-commercial purposes, in microform, paper, electronic and/or any other formats.

The author retains copyright ownership and moral rights in this thesis. Neither the thesis nor substantial extracts from it may be printed or otherwise reproduced without the author's permission.

AVIS:
L'auteur a accordé une licence non exclusive permettant à la Bibliothèque et Archives Canada de reproduire, publier, archiver, sauvegarder, conserver, transmettre au public par télécommunication ou par l'Internet, prêter, distribuer et vendre des thèses partout dans le monde, à des fins commerciales ou autres, sur support microforme, papier, électronique et/ou autres formats.

L'auteur conserve la propriété du droit d'auteur et des droits moraux qui protège cette thèse. Ni la thèse ni des extraits substantiels de celle-ci ne doivent être imprimés ou autrement reproduits sans son autorisation.

In compliance with the Canadian Privacy Act some supporting forms may have been removed from this thesis.

While these forms may be included in the document page count, their removal does not represent any loss of content from the thesis.

Conformément à la loi canadienne sur la protection de la vie privée, quelques formulaires secondaires ont été enlevés de cette thèse.

Bien que ces formulaires aient inclus dans la pagination, il n'y aura aucun contenu manquant.

Canada

… there are known knowns… things we know we know…
… there are known unknowns… things we know we do not know…
… and there are unknown unknowns… things we do not know we do not know…

Dedication

To my wife Trudy: your love and support mean the world to me

To my son Nicholas: you are a constant source of joy and happiness in my life

And, yes, to you too Willy, Billy, and Joe

Also to my parents, Marianne and Doug, for giving me the courage to set and reach goals

ABSTRACT

Geostatistical prediction is applied with a stationary random function (SRF). Stationarity is defined in this thesis as a decision involving five key phases of intervention from the practitioner: (1) choosing domain types, (2) boundary modeling, (3) determining the nature of transitions across boundaries, (4) trend modeling, and (5) predicting with a trend. The framework is a support system for making reasonable decisions of stationarity.

Four new modeling techniques are prototyped within each of the last four phases: (1) boundary modeling with volume functions, (2) near boundary model mixing with a linear mixing model, (3) probability combination schemes for building 3D trend models from lower dimensional trends, and (4) sequential Gaussian simulation with a locally varying transformation to account for the trend.

Making a reasonable decision of stationarity is essential for building numerical models with realistic geological heterogeneity. These improved models then lead to improved geological and production uncertainty characterization.

ACKNOWLEDGEMENTS

I would like to thank my supervisor, Dr. Clayton V. Deutsch, for unwavering help and support throughout this research and throughout my entire academic career. Clayton has an incredible ability to invent exciting research prospects, communicate and motivate them, inspire students to explore and conquer them, and then direct them into useful research contributions in collaboration with the student. This dissertation is no different.

I would also like to thank NSERC and Teck Cominco Limited for continued financial support throughout my graduate career.

TABLE OF CONTENTS

1 INTRODUCTION 1

1.1 Problem Setting 1
1.2 Terminology 3
1.3 An Introductory Example 4
1.4 Dissertation Outline 8

2 FUNDAMENTAL GEOSTATISTICAL CONCEPTS 10

2.1 From Statistics to Geostatistics 10
2.2 The Random Function Model 10
2.3 Univariate Description 14
2.4 Bivariate Description 17
2.5 Statistical Inference 21
2.6 Multivariate Gaussian Distribution 25
2.7 Estimation 25
2.8 Simulation 30
2.9 Reasonability Criteria 32

3 THE DECISION OF STATIONARITY 34

3.1 Framework of a Decision of Stationarity 34
3.2 Choosing Domain Types 38
3.3 Boundary Modeling 42
3.4 Nature of Boundaries 46
3.5 Trend Modeling 50
3.6 Prediction with the Trend Model 54
3.7 Remarks 57

4 BOUNDARY MODELING 58

4.1 Boundary Modeling Principles 58
4.2 Boundary Modeling Approaches 59
4.3 Choosing a Boundary Modeling Technique 64
4.4 Volume Function Boundary Modeling with Global Uncertainty 66
4.5 Application Example 85

4.6 Remarks 90

5 NEAR BOUNDARY MODEL MIXING 94

5.1 Principles for Near Boundary Model Mixing 94
5.2 Contact Analysis 94
5.3 The Linear Model of Coregionalization (LMC) Approach 99
5.4 The Linear Mixing Model (LMM) Approach 99
5.5 Reasonableness 102
5.6 Remarks 103

6 TREND MODELING 105

6.1 Trend Modeling Principles 105
6.2 Key Trend (Modeling) Concepts 106
6.3 Trend Modeling Approaches 109
6.4 Combining Lower Order Trend Models 117
6.5 Remarks 121

7 PREDICTION WITH A TREND 122

7.1 Principles for Predicting with the Trend 122
7.2 Explicit Approaches to Estimation with the Trend 123
7.3 Explicit Approaches to Simulation with the Trend 125
7.4 Inference of the Underlying Spatial Law 128
7.5 Simulation with the Trend via Locally Varying Transformations 138
7.6 Application Example 148
7.7 Remarks 154

8 CONCLUDING REMARKS 155

8.1 A Reasonable Decision of Stationarity 155
8.2 Practical Application 157
8.3 Future Research 160
8.4 Final Remark 162

LIST OF TABLES

3.1 Empty report card for evaluating different boundary modeling 46
3.2 Empty report card for evaluating different trend models 56
3.3 Empty report card for evaluating different approaches to 56
4.1 Report card for evaluating the continuum of boundary 63
7.1 Report card for evaluating different approaches to account 128
8.1 Report card for evaluating boundary modeling 156
8.2 Report card for evaluating different approaches to account 156
8.3 Report card for evaluating different approaches to 156

LIST OF TABLES

3.1 Empty report card for evaluating different boundary modeling 3-13
3.2 Empty report card for evaluating different trend models....................................3-21
3.3 Empty report card for evaluating different approaches to 3-23
4.1 Report card for evaluating the continuum of boundary 4-6
7.1 Report card for evaluating different approaches to account 7-7
8.1 Report card for evaluating boundary modeling 8-2
8.2 Report card for evaluating different approaches to account 8-2
8.3 Report card for evaluating different approaches to....................................8-2

LIST OF FIGURES

1.1 The histogram (left) and location (right) of 67 gold grade 6
1.2 The experimental (points) and model (line) variogram in 7
1.3 Three possible trend models ranging from high 7
1.4 The first three realization maps (left) and etype map (right) 7
1.5 The first three realization maps (left) and etype map (right) 8
2.1 The 2D example geostatistical setting for this chapter 12
2.2 The distribution of reservoir quality 15
2.3 Location map and non-overlapping moving window 18
2.4 The h-scatterplot for the h = h ~ 200m lag (left) 20
2.5 The scatterplot approximations of the bivariate 20
2.6 The original (left), polygonal declustered 21
2.7 The original (left) and normal score 25
2.8 A smooth simple kriging map of the reservoir quality variable 28
2.9 A sequential Gaussian simulation 32
3.1 The framework for the decision of stationarity 35
3.2 A photograph of a gold-quartz vein (left) 39
3.3 A photograph of a layered sand-shale 40
3.4 An illustration of the hierarchical approach 41
3.5 A schematic 2D example showing unavoidable 43
3.6 The setting for modeling boundaries of a vein-type 43
3.7 The setting for modeling boundaries of a clastic 43
3.8 An illustration of the continuum of boundary 43
3.9 DD (left), VF (middle), and SPB (right) boundary 44
3.10 DD (left), VF (middle), and SPB (right) boundary 45
3.11 Representative copper grade profiles (%Cu by weight) 48
3.12 Soft boundary copper grade profile (left) 49
3.13 Hard boundary grade profile (left) 49
3.14 A corehole photograph from the 51
3.15 A manual (left) and automatic (right) trend model 52
3.16 An illustration of the implicit approach 55
3.17 An illustration of the explicit approach 55
4.1 Schematic drawings of vein-type (top left), ... 65
4.2 The rocktype model and corresponding volume function 68

4.3 The true geological model, sample data locations, ... 69
4.4 A small example showing the VF distance codes 69
4.5 The VF for the circle geometry in Figure 4-2 shown 71
4.6 A schematic 2D example showing six risk based 72
4.7 The 25 sample locations drawn on a 74
4.8 The 25 sample locations drawn on a randomized 75
4.9 The p10 and (left) and p90 (right) simple kriging 76
4.10 The transformed p10 (left) and p90 (right) 77
4.11 The transformed p10 (left) and p90 (right) 78
4.12 A linear parameterization of the fDC data 80
4.13 A quadratic parameterization of the fDC data 80
4.14 The data conditioned inverse distance p10 (left) and p90 81
4.15 The data conditioned inverse distance p10 (left) and p90 82
4.16 A 2D illustration of the locally varying grid refinement 82
4.17 The refined p10 (left) and p90 (right) VF rendered 83
4.18 The extracted optimistic p10 (left) and pessimistic 83
4.19 A schematic fluvial channel domain 85
4.20 A regional map showing the overall CBM 85
4.21 The application with 111 wells (open bullets) 87
4.22 The histogram (left) and map (right) of top 87
4.23 The distribution of layer coal thickness 88
4.24 The distribution of 47,541 VF distance codes (left) 88
4.25 Two elevation sections (XZ at Y = 6239300 on left 91
4.26 Two elevation sections (XZ at Y = 6239300 on left 92
4.27 The experimental and model horizontal (left) and vertical 93
4.28 Two elevation sections (XZ at Y = 6239300 on left 93
5.1 A schematic illustration of soft boundaries 95
5.2 The 2D rocktype model (left) and 310 mineral 96
5.3 The histogram of all 310 samples (left), ... 96
5.4 The results of a first order contact analysis 97
5.5 The calculated (points) and model (line) variogram 98
5.6 The ak(u;d) weighting functions used in Figure 3-12 100
5.7 The Z1(u) and Z2(u) simulation results assuming 101
5.8 The ak(u;d) weighting functions used 102
5.9 The near boundary LMM mixing model merge 102

6.1 A corehole photograph from the Athabasca Oil Sands, ... 108
6.2 Township domain and 159 corehole locations used 110
6.3 The by-facies vertical moving window averages 112
6.4 The McMurray Formation by-facies vertical 112
6.5 The McMurray Formation by-facies horizontal 114
6.6 The McMurray Formation by-facies horizontal 115
6.7 Pre-posterior A|B and A|C and posterior A|B,C 118
6.8 The full independence (left) and permanence 123
7.1 A schematic illustration of relation (7-7) 131
7.2 An illustration of the 1D porosity profile example 134
7.3 The true R(u), Z(u), and m(u) spatial laws 135
7.4 The 50 randomly chosen z(u) sample data 136
7.5 The r(u) residual data at the 50 randomly 137
7.6 The true gammaR(h) variogram and spatial law using 138
7.7 The true gammaR(h) variogram and spatial law 138
7.8 An illustration of the stationary cdf used for 144
7.9 An illustration of the effect of increasing the 145
7.10 An illustration of the procedure implemented 145
7.11 The distribution of original z sample data shown spatially 149
7.12 The location map (left) and cdf (right) of 150
7.13 The location map (left) and cdf (right) of 150
7.14 The local $F_Z(u; z)$ cdf and spatial distribution 151
7.15 The trend m(u) map (left) and cdf calculated 151
7.16 The y values normal score gammaY(h) experimental 152
7.17 The first four LVT SGS simulated realization maps (left) 153
7.18 The comparison between the input m(u) 154

CHAPTER 1

INTRODUCTION

A key aspect of resource management is a clear understanding of the size, orientation, and quality of the resource. Numerical modeling is becoming an increasingly important tool for quantifying these aspects in natural resource evaluations. This research is aimed at improving numerical modeling for natural resource characterization.

Geostatistics has evolved to the method of choice for numerical models of environmental, mineral, and petroleum developments [1]. Geostatistical tools are used to create mulitple realizations of geological heterogeneity honoring all available information. The variation between geological realizations is a measure of geological uncertainty. The geolgoical realizations are processed to calculate production realizations. The variation between production realizations is a measure of production uncertainty. Production uncertainty provides a basis for risk qualified decision making.

Mineral and hydrocarbon accumulations are created by a series of depositional events visible through deterministic spatial trends in petrophysical properties. Geology, however, is not just deterministic; it is also probabilistic due to chaotic non-linear processes. Uncertainty is the consequence. The central aim of geostatistics for numerical modeling is uncertainty characterization; however, large-scale geological features should also be reproduced. Conventional geostatistical prediction techniques do not adequately handle the deterministic nature of trends and the probabilistic nature of uncertainty simultaneously [2, 3].

The theory and practice of geostatistics is extended in this thesis to generate a reasonable balance between determinism and probability for more geologically realistic numerical models of uncertainty. This is achieved through a novel five-step framework for making a reasonable decision of stationarity. The five steps are (1) choosing the number and types of domains for numerical petrophysical property modeling, (2) modeling these domain boundaries, (3) near boundary type detection and model mixing, (4) trend modeling, and (5) predicting with a trend model.

1.1 Problem Setting

An important goal of numerical modeling is the accurate depiction of deterministic large-scale variability. This dissertation will address the challenges associated with integrating determinism into geostatistical models of uncertainty. This is achieved by making a reasonable decision of stationarity.

1.1.1 The Decision of Stationarity

Geostatistical inference requires a decision of stationarity entailing geological homogeneity within the chosen domains. For this decision to be deemed reasonable, a total of five modeling steps or phases are undertaken: the first is choosing the number and type of domains to model petrophysical properties within; the second is modeling the boundaries of these domains; the third is quantifying the nature of transitions across the boundaries; the fourth is quantifying trends within the boundaries; and the fifth is ensuring the trend is reproduced in prediction. The collective approach to these five geostatistical modeling phases is presented in this work as the decision of stationarity. Each of these modeling phases has a context, modeling alternatives, and reasonability criteria in its effect on improving a decision of stationarity. A reasonable decision of stationarity is achieved by addressing these five aspects.

A stationary random function (SRF) is a probabilistic representation of a petrophysical property with constant expected value and covariance moments independent of location. The entire resource accumulation is seldom an appropriate domain to apply a SRF model. There is a need to identify separate domains with separate SRF models that are deemed more consistent with the mathematical assumptions of a SRF.

The boundaries separating different stationary random functions (SRFs) are frequently modeled deterministically. Manually digitizing is time consuming, subjective, inflexible, and unable to capture inherent structural uncertainty. There is a need for automatic boundary modeling techniques capable of accessing uncertainty.

The boundary models that separate different SRF models may result in abrupt and geologically unrealistic transitions in the final numerical model. Alternative models for transitions will be reviewed and developed for this purpose.

A trend is a gradually varying expectation in a geological variable within some boundary. One is always present regardless of how small the domain size and SRF influence. A trend should always be constructed and reproduced in any viable numerical model. There are several algorithms and associated options to consider for trend modeling. Finding the right balance between deterministic variability captured within the trend and probabilistic variability captured by subsequent geostatistical uncertainty modeling is a continuing challenge. There is a need to find this balance and implement trend modeling techniques designed around this balance.

It may not be necessary to integrate the trend into geostatistical prediction when the amount of available data is sufficient to implicitly reproduce it. If there are insufficient data, however, an explicit method to account for the trend is required. Techniques for geostatistical prediction with a trend are reviewed and developed for this purpose.

1.1.2 Dissertation Contribution

The decision of stationarity and its consequences for numerical modeling are introduced first. Multiple domain types may need to be identified; boundary models would then be needed to separate SRFs throughout the numerical model; the transitional nature of these boundaries may need to be incorporated; a trend may need to be built; and prediction must honor the trend.

Decisions of stationarity are routinely debated by practitioners on the basis of subjective geological conditions. The five phase framework for decisions of stationarity presented in this dissertation acknowledges this criterion by including realistic geological consistency as a minimum standard for reasonable approaches within each phase, but also offers additional more objective criteria.

Current approaches are reviewed and new approaches are developed within the proposed phases of a decision of stationarity. New approaches should not yet be considered fully developed and mainstream. They are prototypes of good ideas that need to be followed up with additional research and development.

The results of this research are the generation of more realistic models of heterogeneity in the presence of deterministic and probabilistic variability. These models can be used for improved prediction of geological and production uncertainty.

1.2 Terminology

Stationarity and this dissertation are of an intrinsically subjective nature. As such, there is some contentious terminology used throughout. For clarity, some key terms are defined as they are applied in this thesis here in order to avoid any misinterpretation later.

1.2.1 Decision of Stationarity

The *decision* of stationarity is arguably an *assumption*. Defining an assumption as a fact taken to be true, stationarity is indeed a mathematical first and second order assumption required of a random function (RF) to perform geostatistical prediction. However, since the assumption of stationarity can be determined differently given an identical setting by different individuals and interpretations, stationarity is also referred to as a subjective decision. The latter classification of stationarity as a decision is the most popular in practice and literature and is adopted for the remainder of this dissertation. This thesis presents five major considerations the practitioner should address in order to make a reasonable decision of stationarity.

1.2.2 Methodology

Some important methodological terminology will be used to classify currently available and new modeling techniques.

Implicit and Explicit Approaches

An implicit approach in this dissertation is defined as one that intrinsically or inherently honors realistic geological heterogeneity although this heterogeneity is not directly incorporated into the formulation or implementation of the methodology. An explicit approach is then a methodology that has been tailored to directly incorporate the desired geological heterogeneity.

Stochastic, Deterministic, and Probabilistic

The SRF models used in geostatistics are stochastic meaning that they contain elements of random and deterministic variability. The random component represents uncertainty and is modeled with probabilistic algorithms such as ones available within the discipline of geostatistics. The deterministic component represents causal determinations based on preceding events or natural geological laws. These terms are used throughout the entire thesis to describe various techniques.

Subjective and Objective

Subjectivity can be defined as making observations and conclusions that are dependent on the interpreter. A subjective technique would then be one that is in general non-repeatable. Objectivity and objective techniques are then independent of individual interpretation. These two terms are used primarily to evaluate the reasonableness of various techniques.

1.2.3 Mining and Petroleum

This dissertation does not focus solely on mining or petroleum natural resource settings. Although the basic concepts are the same, the terminology is different. Some widespread parallelisms used throughout the dissertation are:

1. *Rocktype (Mining) and Facies (Petroleum)* are both terms used to describe different rock material with significantly different geological properties;
2. *Mineral (Mining) and Hydrocarbon (Petroleum)* are terms referring to the material of economic interest within the entire natural resource accumulation;
3. *Net and Non-Net* are classifications of either rocktypes (mining) that do and do not host economic mineral concentrations or facies (petroleum) that do and do not host economic hydrocarbon concentrations;
4. *Petrophysical Property* is a common term to both mining and petroleum referring to geological variables regionalized within the natural resource accumulation;
5. *Grade (Mining) and Value (Petroleum)* are general terms used to describe concentrations of petrophysical properties.

Throughout the thesis, the distinction between mining and petroleum examples and discussions is made clear with these terms.

1.3 An Introductory Example

A small example is presented to illustrate (1) the choice of how many SRFs to use, (2) establishing the significance of a trend, (3) constructing a trend model, (4) choosing the amount of variability to capture with a trend, and (5) geostatistical simulation with and without the trend model.

The grades in this example are from a vein-type gold deposit. There are 67 samples located on a 2D easting-elevation (*X-Z*) cross section. The grades are in g/t and distances are meters. Figure 1-1 shows the histogram (left) and location map (right) of the samples.

The gold grade distribution is positively skewed with a mean and variance of 1.36 and 1.72, respectively.

Variography is performed on the normal score transforms of the gold grade data. The best correlation and principle variogram direction is in the direction 45° from the elevation coordinate; the perpendicular minor variogram direction is then 135°. Figure 1-2 shows the final variogram points and models for both the 45° principle (dark) and 135° minor (shaded) direction. The variogram shows that there is effectively no spatial correlation for distances greater than roughly 50m in the 135° direction and 150m in the 45° direction.

Choosing to represent gold grade with a single SRF implies the expected gold grade of 1.36, variance of 1.72, and covariance/variogram function in Figure 1-2 are constant and independent of location within the full 600 x 300m domain. The corresponding boundary model for this decision is the 600 x 300m rectangular accumulation limits. However, Figures 1-1 and 1-2 suggest that there are two distinct populations of gold grades: lower gold grades at higher depths and further along in the easting direction and higher gold grades at lower depths and not as far along in the easting direction. Two SRFs could be used: one for higher grades at higher elevations and the other for lower grades at lower elevations. The assumptions of mathematical homogeneity for each separate SRF are improved over those for a single SRF. For two SRFs, a boundary model would be needed between the high and low grade areas to separate the influence of the corresponding SRFs; boundary transitions would also need to be considered. The decision to separate the full accumulation limits into multiple domain types with multiple SRF representations must consider a balance between the degree of homogeneity and the number of available data for inference. In this introductory example, a single SRF is used to ensure there are sufficient data to infer the SRF parameters and to increase the influence of any trend.

Figures 1-1 and 1-2 show some indications of a significant trend within the accumulation limits. With the exception of two high grade samples at a depth of approximately 460m, the location map suggests low gold grades are more commonly encountered at higher depths and further along in the easting direction. Deterministic geological interpretation should be used to confirm this observation in practice. Variography can also be used for confirmation. Figure 1-2 shows that the significance of a trend is not isotropic; the trend is particularly important in this example for the minor variogram direction shown by a steady increase in experimental points past the sill or overall variance. Moreover, comparing the variogram range to the average spacing between potential prediction and sample locations, there is a significant portion of lower elevation locations where the variogram will exert very little control during prediction. In these sparsely sampled locations, the numerical model runs the risk of departing from realistic geological heterogeneity due to an overruling influence of SRF assumptions. The trend is more important in these locations; the SRF assumptions should be relaxed and a trend model should receive more influence over prediction. A trend model will be needed in this example to represent important large-scale variability.

Three different trend models are created at a 2 x 2m resolution and shown in Figure 1-3. They represent high (left), medium (middle), and low (right) amounts of variability in the trend. These models are built using global ordinary kriging with a long range variogram with zero, 5%, and 50% nugget effects, respectively. The decision to choose one trend model over another is a subjective balance between the amount of deterministic variability modeled by the trend and probabilistic variability left to more conventional geostatistical modeling algorithms.

A traditional sequential Gaussian simulation (SGS) is implemented using the distribution of 67 sample data in Figure 1-1 and variogram in Figure 1-2 to condition 30 realizations. Figure 1-4 shows the first 3 realizations and expected value maps and confirms the need to explicitly model and incorporate the trend into the simulation algorithm. In the regions of widely spaced data in the deeper-eastern parts of the cross section, the weight given to the stationary mean of 1.36 increases and the etype result converges to this mean. This contradicts all of the deterministic trend models shown in Figure 1-3 and would not be appropriate for geological and production uncertainty quantification. This discrepancy between predictions and the trend becomes less significant as the prediction locations approach the sample data locations.

There is a need to explicitly account for the trend model within a simulation framework. There are several options available to incorporate the trend model in simulation. Figure 1-5 shows the results of perhaps the most popular and definitely the most straightforward option. In this approach, the medium variability trend model in Figure 1-2 is used to calculate residual values at the 67 sample locations. A traditional SGS is then applied to the residuals and added back to the trend model. The first 3 realizations and expected value maps are shown in Figure 1-5. The results appear more consistent with the medium variability trend model in Figure 1-3 and would be more appropriate for geological and production uncertainty quantification.

This small example shows a short preview of some issues addressed in this dissertation. In particular, the choice of the number of SRFs to adopt, establishing when the trend is significant enough to incorporate explicitly into prediction, constructing the trend model, choosing the amount of deterministic variability to model in the trend, and the results of simulation with and without incorporating the trend.

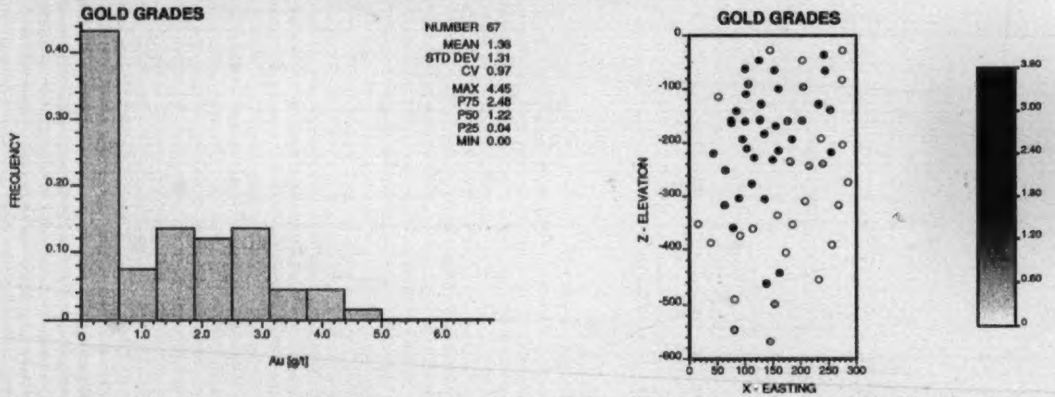

Figure 1-1: The histogram (left) and location (right) of 67 gold grade samples used in this introductory example.

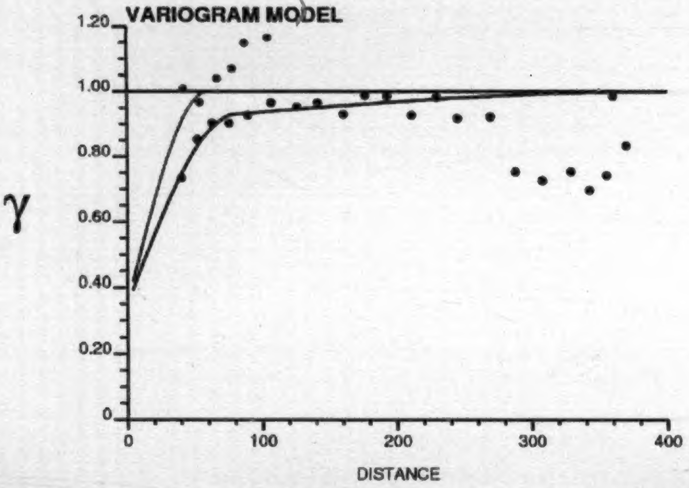

Figure 1-2: The experimental (points) and model (line) variogram in the 45° principle (dark) and 135° minor (shaded) directions.

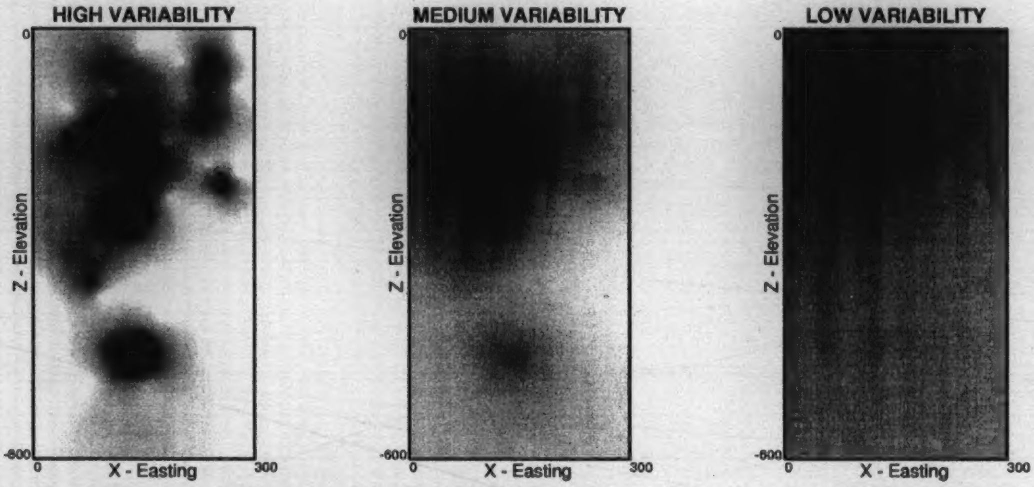

Figure 1-3: Three possible trend models ranging from high (left), medium (middle), and low (right) spatial variability. The gray scale used is shown in Figure 1-1.

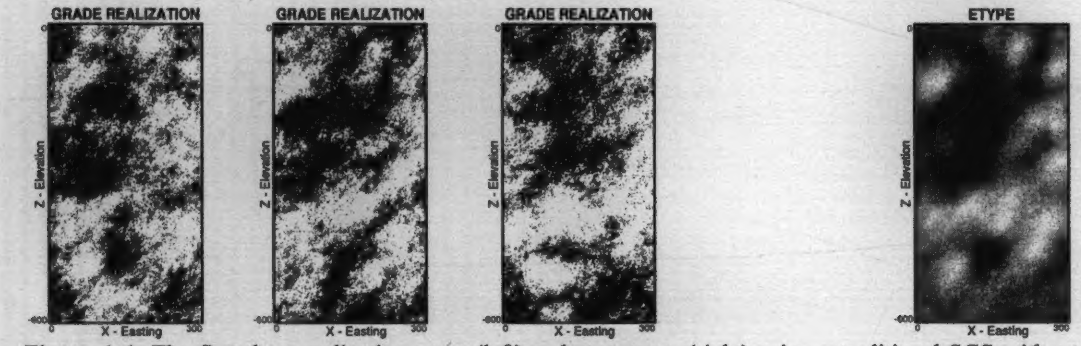

Figure 1-4: The first three realization maps (left) and etype map (right) using a traditional SGS without explicitly accounting for the trend. The gray scale used is shown in Figure 1-1.

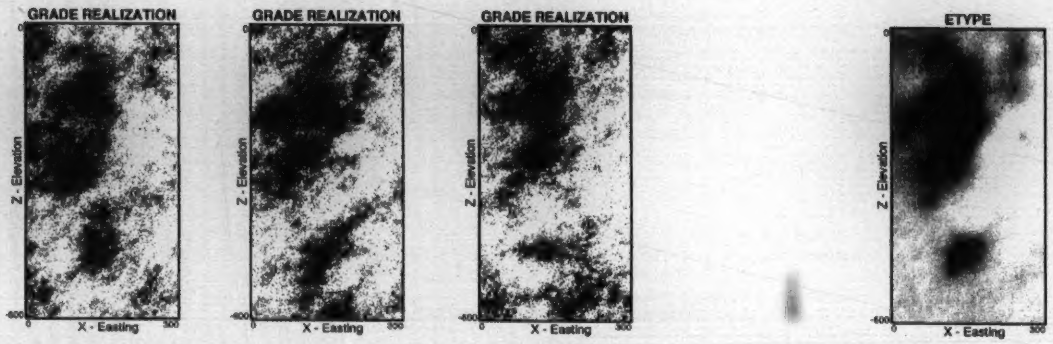

Figure 1-5: The first three realization maps (left) and etype map (right) using SGS on the residuals calculated from the medium variability trend model in Figure 1-3. The gray scale used is shown in Figure 1-1.

1.4 Dissertation Outline

The central theme of this dissertation is the presentation of the five phase framework to a decision of stationarity. This idea is fully developed. Within each phase, techniques to handle non-stationarity are proposed. These new techniques are not fully developed.

Chapter 2 outlines the theoretical basis needed to develop and understand the concepts and techniques illustrated in the remainder of the dissertation.

The third chapter is the most significant. It presents the framework for making a decision of stationarity including the context, alternative modeling approaches, and reasonability criteria for each of the five steps required for making a decision of stationarity.

Chapter 4 reviews deterministic and probabilistic boundary modeling methodologies. A new boundary modeling idea with what are referred to as smooth volume functions is then proposed. An application to coal-bed-methane (CBM) is presented for illustration.

Chapter 5 addresses the detection of different transitional natures of petrophysical properties across geological boundaries as well as techniques to model these transitions. A new linear mixing model idea is proposed as a simple model for representing the influence of surrounding SRF predictions across soft boundaries. An application example is presented for illustration.

Chapter 6 addresses trend modeling including the various methods available for modeling the trend. The application of different probability combination schemes to combine lower dimensional trends into full 3D trends is proposed. An application example is presented for illustration.

Chapter 7 addresses the integration of trend models into geostatistical prediction. A new geostatistical simulation algorithm using locally varying transformation tables is proposed. Application to the same data used in this chapter is presented for illustration.

Chapter 8 concludes the dissertation with final comments. An appraisal of what this dissertation offers, some practical guidelines for implementation, and the numerous opportunities for future work on the techniques proposed within each phase of making a reasonable decision of stationarity are discussed.

CHAPTER 2

FUNDAMENTAL GEOSTATISTICAL CONCEPTS

This chapter presents an overview of the concepts, theory, and notation underlying the practice of geostatistics for numerical modeling. This chapter also provides a foundation for subsequent techniques and developments in this dissertation. A 2D reservoir quality example is used for illustration. The geostatistical material presented in this chapter is derived from a comprehensive foundation of statistical and mathematical theory [1, 2, 3, 4, 5, 6, 7, 8]. These references are cited throughout this chapter.

2.1 From Statistics to Geostatistics

Statistics relates to the collection, organization, analysis, interpretation, and presentation of data. Statistics are applicable to a wide variety of disciplines. The field of geostatistics is one such discipline where statistics are applied to earth sciences phenomenon. There are three fundamental differences between geostatistics applications and classic statistics:

1. Emphasis on the geological context of the sample data;
2. Quantification of the spatial correlation between data; and
3. Integration of a variety of data from different volume scales, precision, and quality.

The first difference relates to the decision of stationarity where the geological context of both boundary modeling and trend modeling are integrated into geostatistical modeling.

2.2 The Random Function Model

Statistics and geostatistics alike are concerned with population inference from a sample of a population. The *population* is an unattainable set of exhaustive sample measurements over the entire study area, the *sample* is the limited set of measurements available for study, and *inference* refers to prediction at unknown locations.

An essential prerequisite for applying any prediction algorithm is a choice of model type dictating how unsampled locations are represented and described. Two types of models are available: deterministic and stochastic. Deterministic models are possible when the geological context of the sample data is well understood and there is essentially zero uncertainty attached to predicting at unknown locations. Unfortunately, however, very few earth science phenomenons are understood in sufficient detail to permit a fully deterministic prediction approach [2]. There is always uncertainty due to incomplete geological information. The geostatistical approach to prediction is based on a stochastic model that is capable of capturing this inherent uncertainty with probabilistic algorithms. This stochastic model is referred to as the RF model.

2.2.1 Setting

Petrophysical properties of natural resource phenomenon are referred to as regionalized variables (ReV) distributed through 3D space. The paradigm of geostatistics is predicting ReV values at unsampled locations via location dependent random variables (RVs). A random variable (RV) is typically denoted with a capital letter such as Z while its actual values are denoted with the corresponding lower case letter z. The notation $Z(\mathbf{u})$ indicates that each RV is attached to a certain location given by the vector of 3D coordinates $\mathbf{u}$, making it also a ReV.

Where the $\mathbf{u}$ location is a sample location, a RV is unnecessary since the sample value is recognized with zero uncertainty (assuming no sampling error). At unsampled locations, a RV $Z(\mathbf{u})$ is used to model the uncertainty about the true unknown z value through a cumulative distribution function (cdf) denoted $F(\mathbf{u}; z)$. Often the cdf is updated by n relevant sample data; the cdf in this case is referred to as a conditional cdf (ccdf) and is denoted $F(\mathbf{u}; z|(n))$. The uncertainty about z is a function of the location $\mathbf{u}$ as well as the amount, configuration, and values of the n neighboring sample data.

Figure 2-1 shows the setting for the 2D example used throughout this chapter. There are a total of 310 scattered z samples of reservoir quality within a domain measuring 3 x 5km in the easting and northing directions, respectively. Typically, a full grid of RV locations is considered and the $\mathbf{u}$ location is taken at the centre of these grid blocks. A 100 x 100m RV location is outlined and highlighted in Figure 2-1. There are a total of $n = 26$ sample data within a predetermined search neighborhood that can be used to condition the corresponding local ccdf. The goal of geostatistical modeling is to build the ccdf for each of the uninformed locations. The inference of the $F(\mathbf{u}; z|(n))$ ccdfs using n relevant sample data can be achieved with the RF model formalism presented in this section.

2.2.2 Random Variable Formalism

A continuous RV is one that takes on an infinite number of possibilities. In the example, $Z(\mathbf{u})$ is a continuous RV representing reservoir quality in units of percent. Any particular $z(\mathbf{u})$ sample then takes on any value within the interval [0, 100%].

A continuous RV is fully characterized by its ccdf, which provides the probability that the attribute Z is no greater than any threshold value z conditional to n surrounding data:

$$F\left(\mathbf{u};z|(n)\right)=\text{Prob}\left\{Z(\mathbf{u})\le z|(n)\right\} \quad \forall z \qquad (2\text{-}1)$$

The ccdf in relation (2-1) must be a non-decreasing function within the interval [0, 1]:

$$\begin{aligned} &F\left(\mathbf{u};z|(n)\right)\in[0,1] \quad \forall z \\ &F\left(\mathbf{u};z|(n)\right)\le F\left(\mathbf{u};z'|(n)\right) \quad \forall z'>z \end{aligned} \qquad (2\text{-}2)$$

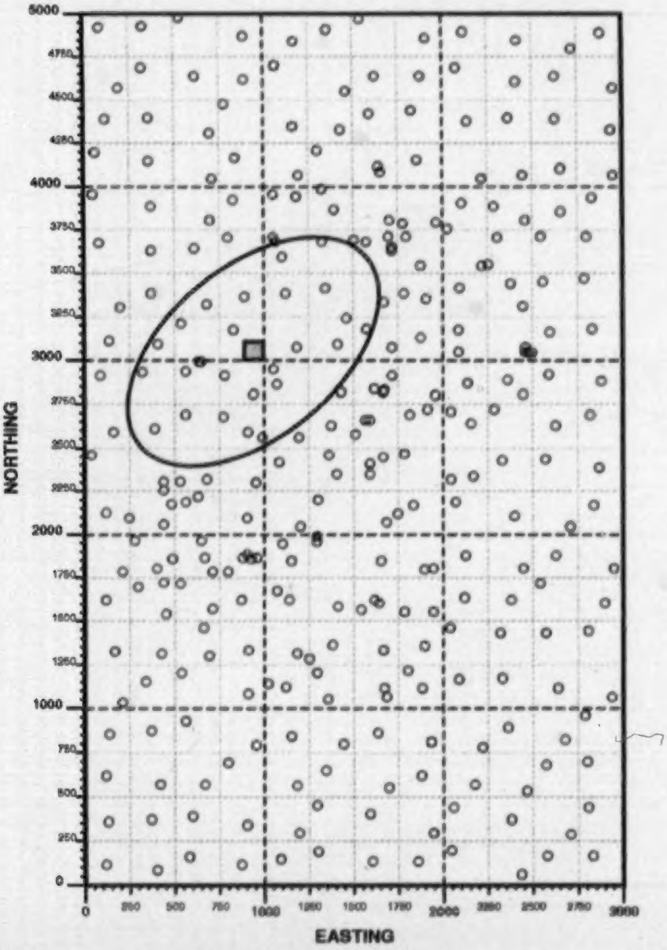

Figure 2-1: The 2D example geostatistical setting for this chapter. There are a total of 310 z sample data within a 3 x 5km domain. A 100 x 100m grid block is shown; the search window centered on this location retains $n = 26$ samples for conditioning the corresponding local ccdf.

2.2.3 Random Function Formalism

A RF is defined as a collection of RVs within a preset domain. The RF for a continuous RV Z is the set of RVs: $\{Z(\mathbf{u})$ for all $\mathbf{u}$ in domain $\mathbf{D}\}$. For a total number of RV locations L, the entire RF is fully characterized by the set of ccdfs:

$$F\left(\mathbf{u}_1,\ldots,\mathbf{u}_L;z_1\middle|(n),\ldots,z_L\middle|(n)\right)=\mathrm{Prob}\left\{Z(\mathbf{u}_1)\le z_1\middle|(n),\ldots,Z(\mathbf{u}_L)\le z_L\middle|(n)\right\} \tag{2-3}$$

for all possible numbers of RV locations $l = 1,\ldots, L$ and all possible combinations of the locations of these L RVs, $\mathbf{u}_1,\ldots, \mathbf{u}_L$. This multivariate ccdf describes the joint uncertainty about the L unknown $z_1,\ldots, z_L$ values and is referred to as the spatial law of the RF. In general, there are ${}_L C_l$ possible combinations of RV locations for each value of l and ${}_L C_1$ +..., + ${}_L C_L$ ccdfs to infer in total. For example, a grid of just 15 x 25 RV locations (500m x 500m blocks) in Figure 2-1 would require 10^{112} unique ccdfs. Practical geostatistical applications, therefore, usually limit the spatial law to the set of univariate distributions at each L location **u** and the set of bivariate distributions at each $_LC_2$ pair of two different locations, $\mathbf{u}_l = \mathbf{u}$ ($z_l = z$) and $\mathbf{u}_{l'} = \mathbf{u}'$ ($z_{l'} = z'$):

$$\begin{aligned} F\left(\mathbf{u};z|(n)\right) &= \text{Prob}\left\{Z(\mathbf{u}) \le z|(n)\right\} \\ F\left(\mathbf{u},\mathbf{u}';z|(n),z'|(n)\right) &= \text{Prob}\left\{Z(\mathbf{u}) \le z|(n), Z(\mathbf{u}') \le z'|(n)\right\} \end{aligned} \qquad (2\text{-}4)$$

If this now $L = 2$-variate spatial law is then assumed multivariate Gaussian, its evaluation reduces to inferring the first order mean of all L univariate ccdfs and the second order covariance of all $_LC_2$ bivariate ccdfs. These moments are denoted:

$$\begin{aligned} m(\mathbf{u}) &= \mathrm{E}\left\{Z(\mathbf{u})\right\} \\ C_z(\mathbf{u},\mathbf{u}') &= \mathrm{E}\left\{Z(\mathbf{u})\cdot Z(\mathbf{u}')\right\} - \mathrm{E}\left\{Z(\mathbf{u})\right\}\cdot \mathrm{E}\left\{Z(\mathbf{u}')\right\} \end{aligned} \qquad (2\text{-}5)$$

The first order mean appears as the result of the expected value of a set of z samples at location **u**. The second order covariance is also a function of the expected value operator and requires a set of paired samples at locations **u** and **u'**. These sample sets do not exist.

2.2.4 Decision of Stationarity

It is impossible to infer the mean or covariance function in (2-5) with the sample data since there is at most one sample per **u** location and one pair of samples per two locations **u** and **u'**. The decision of stationarity is made in order to substitute the need for repetitive realizations at all locations for scattered sampling at sample locations [3]. This decision allows the spatial law to be inferred from sample data alone.

The assumption of stationarity entails invariance of the spatial law under any translation vector **h** from location **u** to location **u'** (**u'** = **u** + **h**):

$$F\left(\mathbf{u}_1,\dots,\mathbf{u}_L;z_1|(n),\dots,z_L|(n)\right) = F\left(\mathbf{u}_1+\mathbf{h},\dots,\mathbf{u}_L+\mathbf{h};z_1|(n),\dots,z_L|(n)\right) \quad \forall\mathbf{h} \qquad (2\text{-}6)$$

However, since classical geostatistical analysis does not exceed the bivariate distribution, a much less stringent assumption of second order stationarity is required. This entails L = 2 in (2-6). This assumption of stationarity allows inference of the spatial law in (2-6). The stationary univariate distribution $F(z)$ and associated first order mean m can be inferred from the cdf of z sample data available within the domain **D**:

$$\begin{aligned} F(\mathbf{u};z) &= F(z) \quad \forall\mathbf{u}\in\mathbf{D} \\ m(\mathbf{u}) &= m \quad \forall\mathbf{u}\in\mathbf{D} \end{aligned} \qquad (2\text{-}7)$$

And the stationary bivariate distribution $F(\mathbf{h};z,z')$ and associated second order covariance $C_Z(\mathbf{h})$ can be inferred from the bivariate cdf of all z and z' sample data collected from all **u** to **u'** pairs of locations, respectively, approximately separated by the lag vector **h**:

$$\begin{aligned} F(\mathbf{u},\mathbf{u}';z,z') &= F(\mathbf{h};z,z') \quad \forall(\mathbf{u},\mathbf{u}')\in\mathbf{D} \\ C_z(\mathbf{u},\mathbf{u}') &= C_z(\mathbf{h}) = \mathrm{E}\left\{Z(\mathbf{u})\cdot Z(\mathbf{u}+\mathbf{h})\right\} - m^2 \quad \forall(\mathbf{u},\mathbf{u}')\in\mathbf{D} \end{aligned} \qquad (2\text{-}8)$$

The spatial law in (2-6) can be calculated with the assumption of stationarity. The stationary first order mean m is inferred from the global stationary univariate cdf $F(z)$; the stationary second order covariance $C_Z(\mathbf{h})$ is inferred from the stationary **h**-bivariate cdf $F(\mathbf{h}; z, z')$. This type of function is referred to as a stationary random function (SRF). Once the spatial law is quantified, it is exploited in geostatistical prediction to update the global stationary univariate cdf $F(z)$ to local $F(\mathbf{u}; z|(n))$ ccdfs using n sample data surrounding each unknown **u** location.

Relations (2-6), (2-7), and (2-8) represent the assumption of stationarity required to perform geostatistical prediction mathematically. For practical modeling purposes, the decision of stationarity involves consideration of a number of separate phases. Five steps are listed and investigated in this dissertation: (1) choosing the number and types of domains for numerical petrophysical property modeling, (2) modeling these domain boundaries, (3) near boundary type detection and model mixing, (4) trend modeling, and (5) predicting with a trend model. The aim of this dissertation is the development and clear presentation of a support system for integrating these components of a decision of stationarity into a reasonable numerical model of geological heterogeneity.

It is important to note that stationarity is not a geological property – stationarity refers to the mathematical properties of a SRF in (2-7) and (2-8) needed to perform inference. A mineral deposit or hydrocarbon reservoir is, therefore, not *stationary*; however, a SRF can be applied within the limits of the deposit or reservoir.

2.2.5 Trend Modeling

The spatial distribution of a geological variable is of dual character: partly structured and partly random. The structured component manifests from a particular sequence of interpretable depositional events that acted to originally concentrate the ReV; the random component is due to chance fluctuations in these geological formation processes. This notion of dual character can be represented analytically. The typical decomposition technique calls for dissociation of the $Z(\mathbf{u})$ RF into an additive structured and random component:

$$Z(\mathbf{u}) = m(\mathbf{u}) + R(\mathbf{u}) \qquad (2\text{-}9)$$

where $m(\mathbf{u})$ is the structured trend part and $R(\mathbf{u})$ is the random residual part. The first order assumption of stationarity assumes the trend model is a constant m value with no spatial variability; however, this assumption may not contain sufficient variability to reproduce large-scale deterministic geological variability in the final numerical model. In these cases, a locally varying mean or trend may need to be integrated into geostatistical prediction explicitly.

2.3 Univariate Description

Geostatistical modeling starts from petrophysical property samples at a limited number of locations. The ultimate goal is to characterize unsampled areas; however, a combined spatial and statistical description of the available sample data exerts significant control on prediction at unsampled locations. The results of this data analysis inform the practitioner about the intricacies of the data and may reveal problem, outlier, or erroneous data. These descriptions can also be used to determine or help determine important geostatistical parameters of the global univariate distribution as well as detect and even calculate large-scale trend models.

One particularly important summary of any continuous RV Z is its cdf. In geostatistics, this is the unique stationary cdf $F(z)$ computed from all available z samples:

$$F(z) = {}^{1}\!/_{S} \sum_{s=1}^{S} x\left(z(\mathbf{u}_s);z\right) \quad \forall z \tag{2-10}$$

where $z(\mathbf{u}_s)$ is the z measurement at the $\mathbf{u}_s$ sample location and its indicator transform is:

$$x\left(z(\mathbf{u}_s);z\right) = \begin{cases} 1 & \text{if } z(\mathbf{u}_s) \le z \\ 0 & \text{otherwise} \end{cases} \quad \forall z \tag{2-11}$$

The plot of the proportion of data equal to and below each z data versus the z data is the $F(z)$ cdf. A similar depiction of the distribution of a RV Z is a histogram which is essentially a bar chart of frequencies within z bin widths.

2.3.1 Summary Statistics

Figure 2-2 shows a histogram and cdf of the reservoir quality variable available at the 310 sample data locations in Figure 2-1. The information contained in these distributions is important for subsequent application of geostatistics. Several informative summaries of these RVs are reported and written next to the distributions. These are now described.

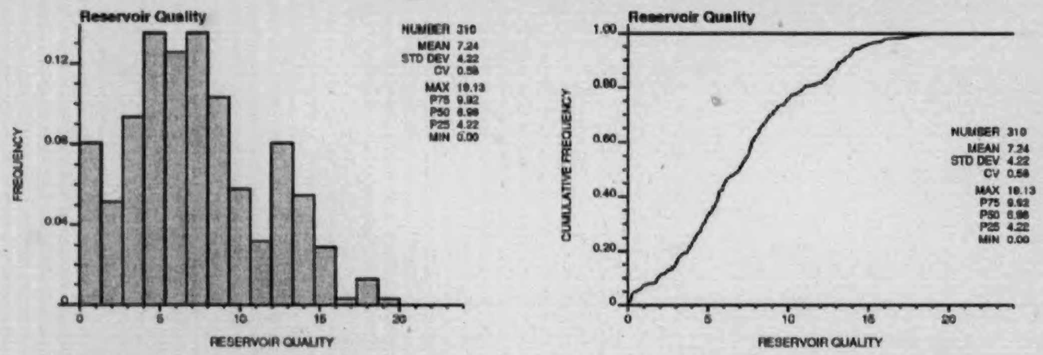

Figure 2-2: The distribution of reservoir quality in the example shown as a histogram (left) and cdf (right). The summary statistics of both are reported.

Measures of Central Tendency

The central value of a continuous distribution is usually taken as the arithmetic mean, m:

$$m = {}^{1}\!/_{S} \sum_{s=1}^{S} z(\mathbf{u}_s) \tag{2-12}$$

The mean of the reservoir quality variable is reported in Figure 2-2 as 7.24.

The median quantile denoted $z_{0.50}$ or M is another measure of central tendency. This value is $M = 6.96$ for the reservoir quality data in Figure 2-2. The median is a more appropriate measure than the mean m when the distribution is highly skewed.

Quantiles

In general, the q quantile or z_q value is equal to $F^{-1}(q)$ which is the value where approximately $100 \cdot q$% of the data is less than z_q. Typically used quantiles are the three quartiles $z_{0.25}$, $z_{0.50}$, …, $z_{0.75}$ (4.22, 6.96, and 9.92, respectively, in Figure 2-2), nine deciles $z_{0.10}$, $z_{0.20}$, …, $z_{0.90}$, and ninety-nine percentiles $z_{0.01}$, $z_{0.02}$, …, $z_{0.99}$.

Measures of Spread

The most popular and robust measure of spread is the variance σ^2 calculated as:

$$\sigma^2 = \frac{1}{S}\sum_{s=1}^{S}\left(z(\mathbf{u}_s) - m\right)^2 \qquad (2\text{-}13)$$

The standard deviation σ is the square root of the variance. The σ and σ^2 values are 4.22 and 17.81, respectively.

Another measure of spread is the ratio of the standard deviation to the mean σ/m referred to as the coefficient of variation *CV*. The *CV* measure can only be calculated for strictly positive or strictly negative variables. The *CV* measure can be useful when comparing variation of variables with significantly different units.

The data range, that is, the difference between the minimum *MIN* (0.00) and maximum *MAX* (19.13) is another measure of spread; however, this can be misleading due to the irregular nature of extreme values. The range is 19.13 in Figure 2-4. Similar but more robust measures of spread are inter-quantile ranges *IQR*. The range ($z_{0.75} - z_{0.25}$) is one possible *IQR* often referred to as the inter-quartile range. The $z_{0.25}$, $z_{0.75}$, and ($z_{0.75} - z_{0.25}$) *IQR* are 4.22, 9.92, and 5.70, respectively.

2.3.2 Spatial Description

The statistical summaries presented in the previous section do not take into account the locations **u** attached to each of the sample data $z(\mathbf{u}_s)$. The spatial arrangement of data is important for extending classical statistics to geostatistical applications.

Location Map

A basic spatial description of a ReV consists of posting the $z(\mathbf{u}_s)$ sample values within the domain. Location maps are simple to construct and useful for visualizing the data, determining if the data are representative, detecting trends, and helping decide on parameters for subsequent geostatistical operations. Figure 2-3 shows the location and value of the 310 reservoir quality samples.

Moving Window Statistics

Moving window statistics are an effective tool for summarizing the spatial distribution of a variable. Summary statistics such as the mean m and variance σ^2 are easily calculated within local windows. Figure 2-3 reports the m and σ^2 within the fifteen 1km^2 non-overlapping windows indicated with dark broken lines and shows a cross plot of these (m, σ^2) pairs. This plot reveals a specific type of heteroscedasticity referred to as the proportional effect where the standard deviation or variance increases with the mean.

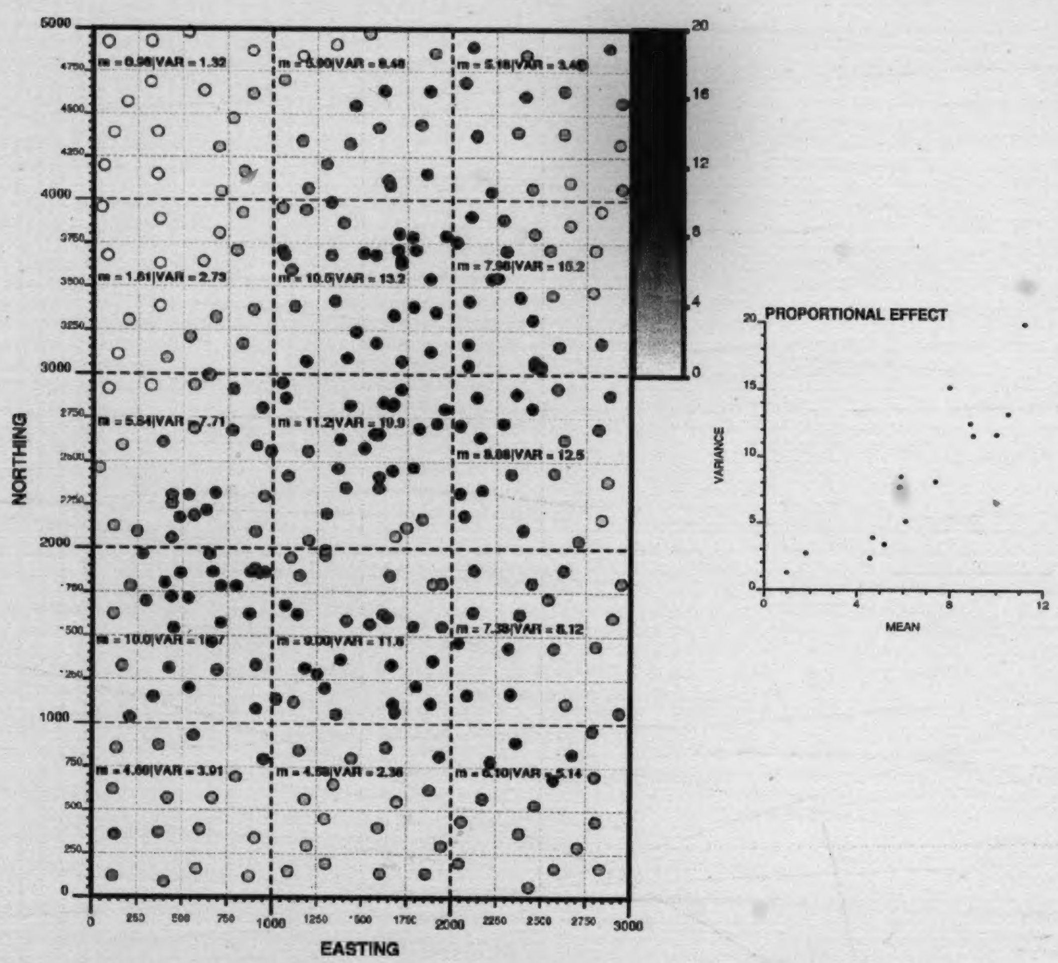

Figure 2-3: Location map and non-overlapping moving window statistics using 310 reservoir quality data (left) showing a proportional effect by increasing variance for increasing means (right).

2.4 Bivariate Description

In order to undertake geostatistical prediction, the spatial law of the SRF is needed. The stationary mean m was presented in the previous section along with other summaries. This section describes calculating the stationary covariance $C_Z(\mathbf{h})$, a summary of the stationary bivariate $F(\mathbf{h};z,z')$ distribution. Other summary statistics are also considered. Similar to the univariate description, this bivariate analysis gives the practitioner a more thorough understanding about the intricacies of the data.

2.4.1 Single Variable Type h Distributions

The implications of the assumption of stationarity allow replacing an investigation of all possible combinations of two RV locations, $Z(\mathbf{u})$ and $Z(\mathbf{u}')$, with an investigation of just those $\mathbf{u}$ and $\mathbf{u}'$ locations approximately separated by $\mathbf{h}$; thus, $Z(\mathbf{u})$ and $Z(\mathbf{u}+\mathbf{h})$. The start of the vector $\mathbf{h}$ at $z(\mathbf{u}_s)$ is usually referred to as the head value and the end of the vector $\mathbf{h}$

at $z(\mathbf{u}_s+\mathbf{h})$ is usually referred to as the tail value. Using this notation, these distributions are made up of all $(z(\mathbf{u}_s), z(\mathbf{u}_s+\mathbf{h}))$ pairs of sample data. In practice, only a few **h** values are possible due to limited sampling. The covariance, correlogram, and variogram are summary statistics of this stationary bivariate $F(\mathbf{h};z,z')$ distribution.

h Scatterplot

The bivariate distribution of samples from the same ReV at all locations approximately separated by lag **h** can be viewed as a scatterplot of data pairs $(z(\mathbf{u}_s), z(\mathbf{u}_s+\mathbf{h}))$. These plots are useful for geological understanding and identifying problem or outlier data. Both the distance and direction of the **h** vector have prescribed tolerances to ensure there are enough data within the resulting **h**-scatterplot to visualize interactions and calculate reliable statistical summaries.

Figure 2-4 (left) shows the **h**-scatterplot for **h** ~ 200m using the reservoir quality variable posted on the location map in Figure 2-3. The direction tolerance is set so that **h** is independent of direction and the distance tolerance is 100m below and above h = 200m; therefore, **h** in this plot are distances within the interval [100m, 300m]. There are a total of 1,520 $(z(\mathbf{u}_s), z(\mathbf{u}_s+\mathbf{h}))$ pairs in this bivariate scatter. These pairs are symmetric about the 45° line since **h** does not depend on direction. In general, however, the plotted points are not symmetric when direction-dependent lag vectors are used.

Notice the relatively strong relationship of the reservoir quality variable between any two locations **u** and **u** + 200m. This means a low or high value at any particular location **u** generally implies a correspondingly low or high value at locations roughly 200m away. The degree of similarity is an important characteristic of the **h**-scatterplot. There are many quantitative summaries of this measure of similarity. The covariance, correlogram, and variogram are summaries described here.

Semivariogram

The semivariogram, often referred to as the variogram, denoted $\gamma_Z(\mathbf{h})$ is a measure of dissimilarity between the $z(\mathbf{u}_s)$ head and $z(\mathbf{u}_s+\mathbf{h})$ tail value pairs on the **h**-scatterplot. The variogram is one half the variance of the $(z(\mathbf{u}_s) - z(\mathbf{u}_s+\mathbf{h}))$ **h**-increments:

$$2\gamma_Z(\mathbf{h}) = \mathrm{E}\left\{\left(Z(\mathbf{u}) - Z(\mathbf{u}+\mathbf{h})\right)^2\right\} \qquad (2\text{-}14)$$

A simplification in (2-14) is made under the first order assumption of stationarity where the expected value of $Z(\mathbf{u})$ and $Z(\mathbf{u}+\mathbf{h})$ are the same stationary mean m. The variogram is not sensitive to the mean. The variogram is experimentally calculated as:

$$\gamma_Z(\mathbf{h}) = \frac{1}{2P(\mathbf{h})}\sum_{s=1}^{P(\mathbf{h})}\left(z(\mathbf{u}_s) - z(\mathbf{u}_s+\mathbf{h})\right)^2 \qquad (2\text{-}15)$$

where $P(\mathbf{h})$ is the number of pairs. $P(\mathbf{h})$ = 1,520 in Figure 2-4. Figure 2-4 also shows the $\gamma_Z(\mathbf{h})$ function for the Z RV at **h** = h ~ 200m, 400m, …, 2400m lag vectors each with the 100m tolerance below and above. The **h** ~ 200m case is represented by the large dark bullet. The γ_Z(200m) value is low since the 200m-scatterplot shows good correlation. In general, as the **h** value increases, the **h**-scatterplot shows less correlation and $\gamma_Z(\mathbf{h})$

increases. There are, however, exceptions to this generalization for different geological settings.

Covariance

The covariance provides a measure of similarity of the pairs in an **h**-scatterplot. In expected value notation, and assuming second order stationarity, the covariance is:

$$C_Z(\mathbf{h}) = \mathrm{E}\{Z(\mathbf{u}) \cdot Z(\mathbf{u}+\mathbf{h})\} - m^2 \qquad (2\text{-}16)$$

And can be calculated:

$$C_Z(\mathbf{h}) = \frac{1}{P(\mathbf{h})} \sum_{s=1}^{P(\mathbf{h})} \left(z(\mathbf{u}_s) \cdot z(\mathbf{u}_s + \mathbf{h}) \right) - m^2 \qquad (2\text{-}17)$$

The covariance is sensitive to the mean. This is why the variogram is often used instead. Figure 2-4 shows the $C_Z(\mathbf{h})$ function for the same lags as $\gamma_Z(\mathbf{h})$. The **h** ~ 200m case is shown by the larger shaded bullet. The C_Z(200m) value is high since the 200m-scatterplot shows good correlation.

Correlogram

The correlogram $\rho_Z(\mathbf{h})$ is the standardized covariance. The stationary correlogram is obtained by dividing each $C_Z(\mathbf{h})$ covariance by the stationary variance:

$$\rho_Z(\mathbf{h}) = \frac{C_Z(\mathbf{h})}{C_Z(0)} \qquad (2\text{-}18)$$

Where the covariance at $\mathbf{h} = 0$ $C_Z(0)$ is the stationary variance σ^2.

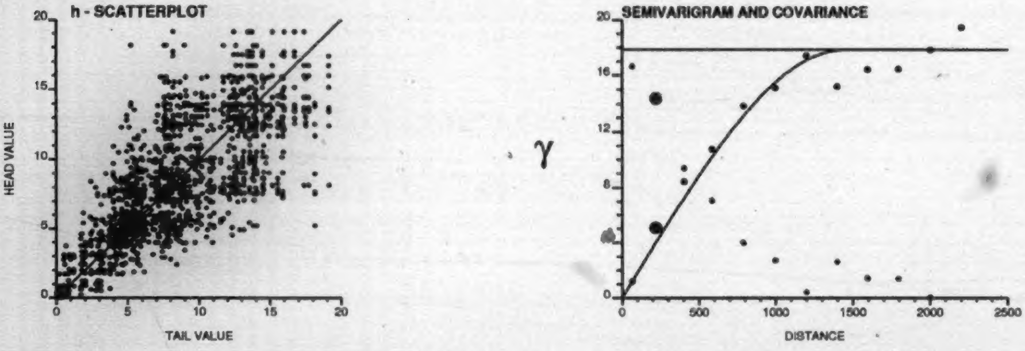

Figure 2-4: The **h**-scatterplot for the **h** = h ~ 200m lag (left) and the semivariogram (dark) and covariance functions (shaded) summarizing the distribution of all **h** = h ~ 200m, 400m, …, 2400m scatterplots (right); the h = 200m summaries are shown with larger circles.

The variogram is a more robust bivariate summary statistic than covariance since it is less sensitive to the stationary mean *m*. For this reason, it is the variogram that is primarily used to quantify spatial correlation. The covariance $C_Z(\mathbf{h})$ needed to identify the spatial law is then obtained through the following relation allowed by stationarity:

$$\gamma_Z(\mathbf{h}) = C_Z(\mathbf{0}) - C_Z(\mathbf{h}) = C_Z(\mathbf{0})(1 - \rho_Z(\mathbf{h})) \tag{2-19}$$

Therefore, under the assumption of second order stationarity, the variogram, covariance, and correlation contain equivalent information about the SRF.

2.4.2 Two Variable Type Distributions

Consider two different ReV types Z and Y available at the same locations. The variables are referred to as collocated. Dropping the $\mathbf{u}_s$ notation, these distributions are made up of all collocated (z, y) pairs of sample data and provide insight into the relationship between the Z and Y ReVs.

Scatterplot

The distribution between two different variables at the same location could be visualized in a scatterplot. This plot shows an approximation of the full Z vs. Y bivariate distribution by the density of (z, y) sample pairs. Figure 2-5 shows scatterplots of the reservoir quality variable Z versus a net continuous bitumen *NCB* variable in meters (left) and Z versus a volume of shale V_{SHALE} variable (right). The reservoir quality samples are strongly related to both *NCB* and V_{SHALE} samples; however, the nature of the relationship is different. That is, an increase in reservoir quality corresponds to an increase in *NCB*, but a decrease in V_{SHALE}.

Correlation Coefficient

The summary statistic used most often for a scatterplot is the correlation coefficient ρ_{ZY}:

$$\rho_{ZY} = \frac{\sigma_{ZY}}{\sigma_Z \sigma_Y} \tag{2-20}$$

where σ_Z and σ_Y are the standard deviations of z and y samples and σ_{ZY} is a covariance:

$$\sigma_{ZY} = \frac{1}{P}\sum_{s=1}^{P}(z \cdot y) - m_Z m_Y \tag{2-21}$$

The interpretation for the correlation coefficient is both the strength and type (positive or negative) of linear relationship between two variables. The correlation coefficient exists in the interval [-1, +1]. When $\rho = -1$, an increase in one variable corresponds to a decrease in the other; when $\rho = +1$, an increase in one variable corresponds to an increase in the other. And as ρ approaches zero, the two variables show less similarity. The correlation coefficients between reservoir quality and the *NCB* and V_{SHALE} variables are 0.79 and -0.85, respectively, indicating relatively strong increasing and decreasing linear relationships with increasing reservoir quality.

It is important to note that the correlation coefficient measures only the degree of linear similarity. This means that two variables may be strongly related and still have a low correlation coefficient.

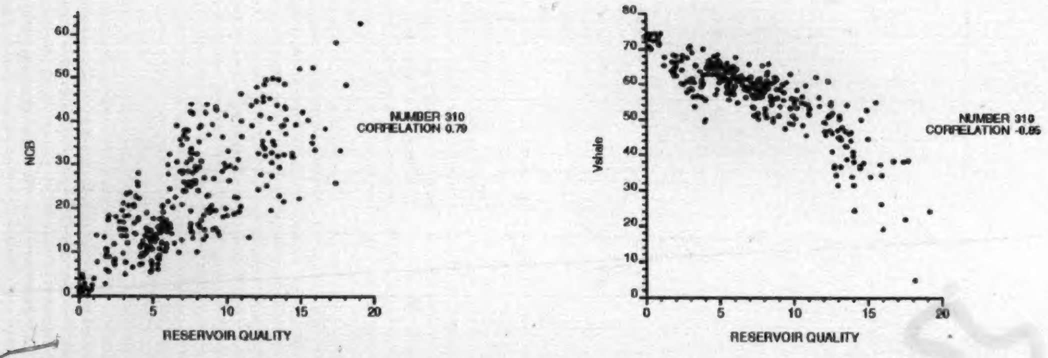

Figure 2-5: The scatterplot approximations of the bivariate distributions for reservoir quality versus *NCB* (left) and reservoir quality versus V_{SHALE} ReVs. The correlations are 0.79 and -0.85, respectively, indicating strong positive and negative linear relationships.

2.5 Statistical Inference

The previous two sections presented several descriptions of continuous RVs. Seldom, however, is the final goal of a geostatistical study a description of the available sample data. Ultimately, the goal is to model the SRF spatial law in order to predict beyond the available sample data. Univariate inference of the first order mean and bivariate inference of the second order variogram and covariance are addressed in the following sections.

2.5.1 Univariate Inference

The goal here is to attain a stationary univariate distribution representative of the entire domain. Often this distribution is different than the raw histogram. Two reasons for this are preferential sampling and incomplete sampling. Both sampling practices commonly occur in practice. Declustering and debiasing procedures correct the biased distributions that represent such settings.

Declustering

Preferential sampling of high potential reservoir is a common and encouraged practice. Notice the clustering of high reservoir qualities in Figure 2-3. However, the univariate distribution or histogram of $z(\mathbf{u}_s)$ samples is often biased due to clustering. The mean in particular is high and not representative of the entire area to be modeled. For example, the mean reservoir quality of 7.24 in Figure 2-3 must be lowered in order to account for the fact that this value is calculated using preferentially sampled high reservoir qualities.

All forms of declustering assign declustering weights $w(\mathbf{u}_s)$ to the $z(\mathbf{u}_s)$ data in order to decrease the influence of clustered values in the univariate distribution. Since data are often clustered in higher sampled areas, the influence of lower quality samples is usually increased. The new representative stationary univariate distribution $F(z)$ is calculated:

$$F(z)=\frac{1}{\sum_{s=1}^{S} w(\mathbf{u}_s)}\sum_{s=1}^{S} w(\mathbf{u}_s)\cdot x\big(z(\mathbf{u}_s);z\big) \quad \forall z \qquad (2\text{-}22)$$

with the indicator $x(z(\mathbf{u}_s);z)$ the same as in (2-11). The declustered mean m is then:

$$m=\frac{1}{\sum_{s=1}^{S}w(\mathbf{u}_s)}\sum_{s=1}^{S}w(\mathbf{u}_s)z(\mathbf{u}_s) \qquad (2\text{-}23)$$

And the declustered variance σ^2 is:

$$\sigma^2=\frac{1}{\sum_{s=1}^{S}w(\mathbf{u}_s)}\sum_{s=1}^{S}w(\mathbf{u}_s)\left(z(\mathbf{u}_s)-m\right)^2 \qquad (2\text{-}24)$$

Different types of declustering assign declustering weights $w(\mathbf{u}_s)$ differently. Polygonal and cell declustering techniques are two common techniques. Polygonal declustering assigns weights inversely proportional to the data polygonal areas of influence $A(\mathbf{u}_s)$:

$$w^{\mathrm{PD}}(\mathbf{u}_s)=\frac{S\cdot A(\mathbf{u}_s)}{\sum_{s=1}^{S}A(\mathbf{u}_s)} \qquad (2\text{-}25)$$

Polygonal declustering is typically used in 2D settings when the domain boundaries are well known. Cell declustering is often used in 3D settings and assigns weights inversely proportional to the number of data within cells:

$$w^{\mathrm{CD}}(\mathbf{u}_s)=\frac{S}{\sum_{s=1}^{S}w^{\mathrm{CD}}(\mathbf{u}_s)}\cdot\frac{1}{K\cdot s_K(\mathbf{u}_s)} \qquad (2\text{-}26)$$

where K is the number of cells that contain at least one datum and $s_K(\mathbf{u}_s)$ is the number of data in the cell within which the sample location $\mathbf{u}_s$ exists. The sum of cell and polygonal weights is S; therefore, $z(\mathbf{u}_s)$ samples that receive more influence have $w(\mathbf{u}_s) > 1.0$ while $z(\mathbf{u}_s)$ samples that receive less influence have $w(\mathbf{u}_s) < 1.0$.

Polygonal and cell declustering are both applied to the reservoir quality example in this chapter. Figure 2-6 shows the original reservoir quality distribution (left) with more representative or declustered distributions calculated with polygonal declustering weights $w^{\mathrm{PD}}(\mathbf{u}_s)$ (middle) and cell declustering weights $w^{\mathrm{CD}}(\mathbf{u}_s)$ (right). Both declustering methods reduce the mean m from 7.24 to roughly 6.4 by accounting for the clustering of high reservoir quality samples. Notice also the drop in standard deviation σ which is consistent with the previously observed proportional effect.

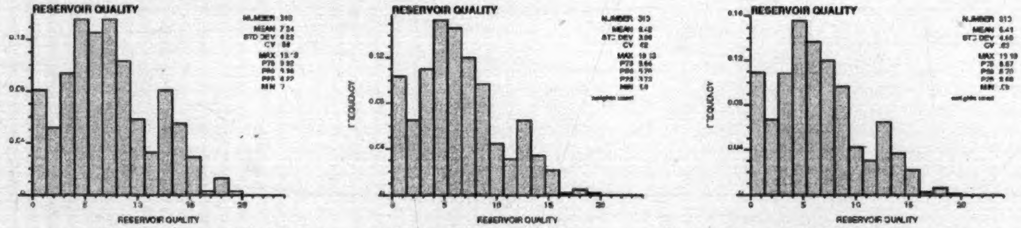

Figure 2-6: The original (left), polygonal declustered (middle), and cell declustered (right) distributions.

Debiasing

Declustering corrects the global cdf for clustered samples extracted from higher potential deposit or reservoir areas and requires ample data in both high and low potential areas. It is important to note, however, that declustering is in fact not effective in correcting the cdf in the presence of incomplete information. For instance, in the absence of lower reservoir quality, there are simply no low quality data to assign higher weights to. In these situations, a different approach must be taken.

2.5.2 Bivariate Inference

The variogram and covariance calculations in (2-15) and (2-17) are available for only a few discrete **h** lags. The variogram and covariance values for intermediate **h**'s are needed to define the full spatial law. This section deals with inference of the complete model of spatial correlation for all possible **h** that may be encountered during prediction.

The spatial law for a SRF is usually inferred from the previously calculated experimental variogram and is, therefore, referred to as a variogram model. The solid black line in Figure 2-4 is actually a variogram model. It provides the degree of dissimilarity between $Z(\mathbf{u})$ and $Z(\mathbf{u}+\mathbf{h})$ RVs for all **h** in between the discrete **h** points where the variogram is not calculated directly. In general, there are three main reasons for variogram modeling:

1. The covariance $C_Z(\mathbf{h})$ for all lag distances and directions **h** is required to perform geostatistical prediction;
2. A positive definite covariance $C_Z(\mathbf{h})$ must be ensured; and
3. The covariance $C_Z(\mathbf{h})$ model must incorporate any available analog or deterministic geological knowledge.

Variogram modeling is not a curve-fitting exercise. There are several factors to consider while modeling a variogram from the few available experimental points. Some factors are addressed here.

Anisotropy

Geological phenomenon is rarely isotropic – there are always preferential directions of greater and less spatial continuity. There are generally two types of anisotropy. The first is known as geometric anisotropy meaning the variogram model reaches the same maximum variability of the overall variability or sill, but the distance or range where this occurs is different depending on the orientation of **h**. The second type is referred to as zonal anisotropy meaning the variogram model reaches a different sill for different **h** orientations. Different directions can also have different ranges for a zonal anisotropy.

The procedure used to account for both geometric and zonal anisotropy is specifying different range parameters in different **h** directions. In calculating the separation distance between any two RV locations, these ranges are then used to scale the component distances within the **h** vector to an anisotropic distance. For example, to specify a geometric anisotropy such that the horizontal variogram is more correlated for longer distances than the vertical, horizontal distances are divided by larger ranges making them geologically closer while vertical distances are divided by smaller ranges making them geologically further. A horizontal zonal anisotropy is defined by setting the horizontal range to infinity. This simple variography procedure offers a considerable amount of flexibility for modeling various types of complex anisotropic geology in three dimensions [4].

Positive Definite Models

In application to variogram modeling, the condition of positive definiteness is interpreted to mean that the variogram $\gamma_Z(\mathbf{h})$ be non-negative. A negative variogram value implies a negative distance that is not physically possible. Only non-negative variogram values can be used for subsequent estimation and simulation.

In order to ensure a variogram is positive definite, a group of previously determined positive definite variogram models have been collected to ensure the final variogram model is positive definite [5]. The four most commonly used positive definite models are the (1) nugget effect, (2) spherical, (3) exponential, and (4) Gaussian models. The definition of these models is a function of the anisotropic geological distance and direction vector **h**. The nugget effect model is used to account for variability at short scale distances approximately equal to zero; the rest of the models are used to describe larger distances.

Nested Variogram Structures

Typically, the variance on the ordinate axis of the experimental variogram plot is divided into significantly different variance contributions, each of which is modeled by a separate anisotropic variogram model. The models are then combined linearly; since each separate variogram model is positive definite, the full variogram model is also positive definite. The variogram model shown in Figure 2-4 has a spherical structure with zero nugget and isotropic range of 1.35km.

Limited Data

Often there are limited samples for building numerical models. Some **h**-scatterplots have too little data for inferring reliable bivariate summary statistics. For example, although vertical coreholes often yield reliable or stable vertical variograms, the aerial sample spacing may be too high to infer reliable horizontal variograms. In these situations, some analog geological background information is required in addition to the sample data in order to produce a credible variogram model [6].

Outlier Data

Like univariate statistical summaries, bivariate variogram and covariance summaries are sensitive to outlier data. Any discussion on how to handle outlier data is subjective, that is, different geological and personnel situations call for different techniques. Nonetheless, these data can be detected from visualizing histograms and **h**-scatterplots of the different petrophysical properties and simply flagging data that do not seem to belong to the population. Once identified, these outlier data and their locations must be investigated for possible explanations and a decision must be made as to weather to include this data in further analyses.

Proportional Effect

When the proportional effect is combined with clustered data, the **h**-scatterplot for small **h** includes mostly pairs of higher potential sample data and the calculated variogram summary of such bivariate distributions is high since the variance is inherently higher for higher potential data. This leads to the appearance of a more random spatial structure and in particular overestimation of the nugget effect. In these cases, the variogram model must somehow take into account this bias.

2.6 Multivariate Gaussian Distribution

A common implicit assumption involved with predicting at unsampled locations is that the SRF follows a multivariate Gaussian or normal spatial law. This assumption is made for convenience. Recall, for example, the necessary assumption of multivariate Gaussianity made before presenting the first order mean and second order covariance in (2-5) as the only necessary moments required to infer the spatial law of a SRF.

Continuous RVs never exactly obey the distinctive symmetric bell shape normal density nor the perfectly elliptical bivariate normal **h**-scatterplot contours. There is no bivariate transformation to ensure all the **h**-scatterplots are normal; however, there exists a well known, proven, and straightforward univariate normal transformation technique to ensure the univariate distribution of a ReV is Gaussian regardless of its original shape. The Gaussian transform $y(\mathbf{u}_s)$ of each sample data $z(\mathbf{u}_s)$ is obtained by matching its cdf value to the cdf value on a standardized Gaussian distribution G with zero mean and unit standard deviation:

$$y(\mathbf{u}_s) = G^{-1}\left(F\left(z(\mathbf{u}_s)\right)\right) \qquad \text{(2-27)}$$

The resulting distribution of $y(\mathbf{u}_s)$ data is normal with a mean of zero and variance of one. This transformation is easily reversed to real units. Figure 2-7 shows the original (left) and normal score distribution (right) of the reservoir quality variable before and after a univariate Gaussian transformation. Both the histograms (top) and cdfs (bottom) are shown. The transformation of $z(\mathbf{u}_s) = 9.92$ to $y(\mathbf{u}_s) = 0.67$ for the 0.75 quantile is shown explicitly with arrows. Any distribution can be transformed into a Gaussian distribution.

2.7 Estimation

The early development of geostatistics is rooted to the mining industry and estimation of various ReVs from drillhole/blasthole samples in the 1940s. These early methods include hand contouring, polygonal estimation, triangulation, inverse distance, moving window averages, and so on. These maps were used calculating recoverable reserves and mine planning. Estimation algorithms have evolved from these subjective hand and machine contouring procedures to more sophisticated objective statistically optimum schemes.

One particular problem with the earliest subjective mapping techniques was the sacrifice of local or conditional bias for global unbiasedness. Conditional bias is the systematic overestimation of high grades and underestimation of low grades. Correcting this bias was of particular concern to mining engineers involved in South African underground gold mining deposits. The existence of truly lower grade areas where higher grades were predicted was obviously undesirable. The pioneering work of Daniel Krige during the 1950s to correct conditional bias was the seed for the currently most popular group of estimation techniques collectively referred to as kriging [7].

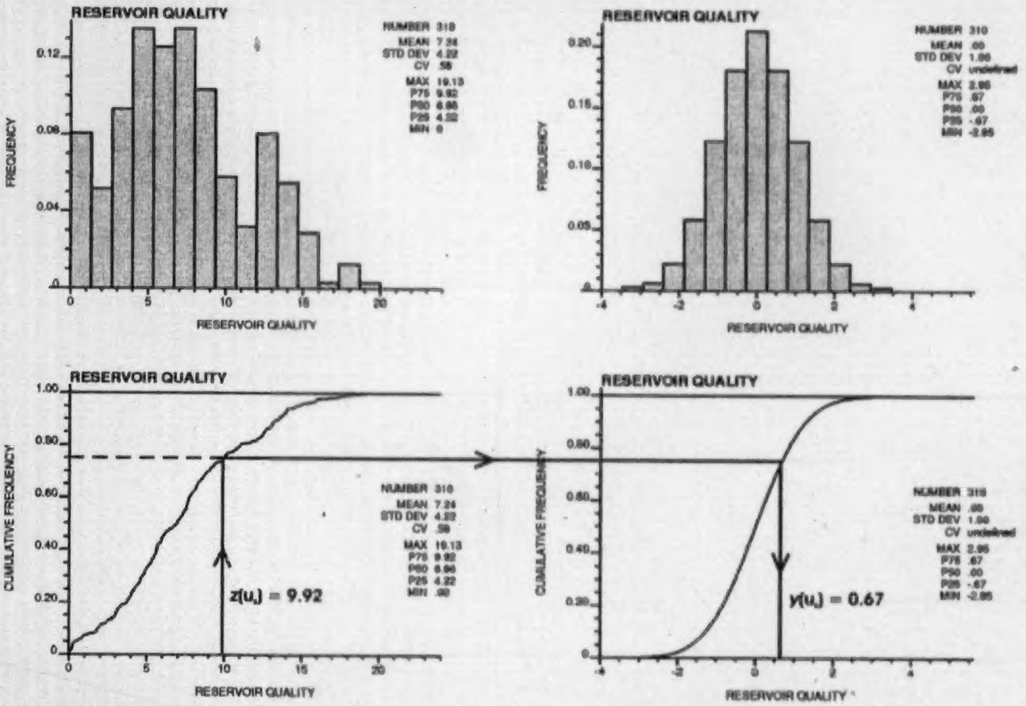

Figure 2-7: The original (left) and normal score Gaussian (right) histograms (top) and cdfs (bottom) for the reservoir quality data.

The kriging estimator is often replaced with the acronym **BLUE**:

- **B**est since the estimate is optimum in that the error variance is a minimum;
- **L**inear since the estimate is a weighted linear combination of surrounding data;
- **U**nbiased since the expected value of the estimate and true value are the same;
- **E**stimate.

This objective criteria for optimum estimation is the reason for the popularity of kriging.

From the 1960s, kriging was used to calculate recoverable reserves for mine planning and economic forecasting [8]. From the early 1980s until present, however, the use of kriging or any type of estimation for production planning is no longer recommended due to the inherent smoothing effect and persistence of conditional bias in these methods. Although kriging is not used exclusively, its simplest form, simple kriging, serves a central role in supplementing modern geostatistical simulation.

2.7.1 A General Kriging Estimator

The kriging estimator at the unsampled location $\mathbf{u}_0$ takes on the form:

$$z_K^*(\mathbf{u}_0) = A + \sum_{s=1}^{n} \lambda_K(\mathbf{u}_s) \cdot z(\mathbf{u}_s) \tag{2-28}$$

A is a constant shift parameter and the $\lambda_K(\mathbf{u}_s)$'s are the kriging weights assigned to the n surrounding $z(\mathbf{u}_s)$ sample data. Probabilistically, the kriging estimator is:

$$Z_K^*(\mathbf{u}_0) = A + \sum_{s=1}^{n} \lambda_K(\mathbf{u}_s) \cdot Z(\mathbf{u}_s) \tag{2-29}$$

The actual error of estimation $e(\mathbf{u}_0)$ is:

$$e(\mathbf{u}_0) = z(\mathbf{u}_0) - z_K^*(\mathbf{u}_0) \tag{2-30}$$

Little can be done about this error unless its probabilistic version $E(\mathbf{u}_0)$ is considered:

$$E(\mathbf{u}_0) = Z(\mathbf{u}_0) - Z_K^*(\mathbf{u}_0) \tag{2-31}$$

In this case, the expected value and variance of $E(\mathbf{u}_0)$ can be calculated and thus acted upon. In particular, we require the expected value of $E(\mathbf{u}_0)$ to be zero for unbiasedness and the variance of $E(\mathbf{u}_0)$ to be a minimum for optimality. The expected value of $E(\mathbf{u}_0)$ is:

$$\begin{aligned} \mathrm{E}\{E(\mathbf{u}_0)\} &= \mathrm{E}\{Z(\mathbf{u}_0)\} - \mathrm{E}\{A\} - \mathrm{E}\left\{\sum_{s=1}^{n} \lambda_K(\mathbf{u}_s) z_K(\mathbf{u}_s)\right\} \\ &= m(\mathbf{u}_0) - A - \sum_{s=1}^{n} \lambda_K(\mathbf{u}_s) m(\mathbf{u}_s) \end{aligned} \tag{2-32}$$

where E is the expected value operator. In order for the kriging estimator $Z^*_K(\mathbf{u}_0)$ to be unbiased, this expected error must be zero. For this, the shift parameter A is set to:

$$A = m(\mathbf{u}_0) - \sum_{s=1}^{n} \lambda_K(\mathbf{u}_s) m(\mathbf{u}_s) \tag{2-33}$$

Indeed, the $\mathrm{E}\{E(\mathbf{u}_0)\}$ is zero; and the kriging estimator is then:

$$\begin{aligned} Z_K^*(\mathbf{u}_0) &= m(\mathbf{u}_0) - \sum_{s=1}^{n} \lambda_K(\mathbf{u}_s) m(\mathbf{u}_s) + \sum_{s=1}^{n} \lambda_K(\mathbf{u}_s) Z(\mathbf{u}_s) \\ &= m(\mathbf{u}_0) + \left(\sum_{s=1}^{n} \lambda_K(\mathbf{u}_s) [Z(\mathbf{u}_s) - m(\mathbf{u}_s)] \right) \\ R^*(\mathbf{u}_0) &= \sum_{s=1}^{n} \lambda_K(\mathbf{u}_s) R(\mathbf{u}_s) \end{aligned} \tag{2-34}$$

The other moment of $E(\mathbf{u}_0)$ required to develop the kriging equations is the variance:

$$\begin{aligned} \mathrm{VAR}\{E(\mathbf{u}_0)\} &= \sum_{s=0}^{n} \sum_{s'=0}^{n} \lambda_K(\mathbf{u}_s) \lambda_K(\mathbf{u}_{s'}) C_Z(\mathbf{u}_s - \mathbf{u}_{s'}) \\ &= C_Z(\mathbf{0}) - 2\sum_{s=1}^{n} \lambda_K(\mathbf{u}_s) C_Z(\mathbf{u}_0 - \mathbf{u}_s) + \sum_{s=1}^{n} \sum_{s'=1}^{n} \lambda_K(\mathbf{u}_s) \lambda_K(\mathbf{u}_{s'}) C_Z(\mathbf{u}_s - \mathbf{u}_{s'}) \end{aligned} \tag{2-35}$$

where VAR is the variance operator, $\mathbf{u}_s - \mathbf{u}_{s'}$ is the **h** lag between two sample data $z(\mathbf{u}_s)$ and $z(\mathbf{u}_s+\mathbf{h})$, and $\mathbf{u}_0 - \mathbf{u}_s$ is the **h** lag between the estimation location and the sample datum $z(\mathbf{u}_s)$. The error variance in (2-35) is interpreted as the sum of the overall variance (first term), closeness (second term), and redundancy (last term). The error variance increases with increasing overall variance, decreased closeness, and increased redundancy of the *n* surrounding sample data.

2.7.2 Simple Kriging

The simple or unconstrained kriging algorithm assumes first order stationarity in (2-7) with constant mean $m(\mathbf{u}) = m$. The shift parameter A then becomes:

$$\mathrm{A} = m - \sum_{s=1}^{n} \lambda_{\mathrm{SK}}(\mathbf{u}_s) m \qquad (2\text{-}36)$$

And the simple kriging estimator $Z^*_{\mathrm{SK}}(\mathbf{u}_0)$ is:

$$\begin{aligned} Z^*_{\mathrm{SK}}(\mathbf{u}_0) &= m - \sum_{s=1}^{n} \lambda_{\mathrm{SK}}(\mathbf{u}_s) m + \sum_{s=1}^{n} \lambda_{\mathrm{SK}}(\mathbf{u}_s) Z(\mathbf{u}_s) \\ &= m + \left(\sum_{s=1}^{n} \lambda_{\mathrm{SK}}(\mathbf{u}_s) \left[Z(\mathbf{u}_s) - m \right] \right) \end{aligned} \qquad (2\text{-}37)$$

The simple kriging estimator is unbiased since the expected error is zero:

$$\begin{aligned} \mathrm{E}\{E(\mathbf{u}_0)\} &= \mathrm{E}\{Z(\mathbf{u}_0)\} - \mathrm{E}\{Z^*_{\mathrm{SK}}(\mathbf{u}_0)\} \\ &= m - m - \sum_{s=1}^{n} \lambda_{\mathrm{SK}}(\mathbf{u}_s) \mathrm{E}\{Z(\mathbf{u}_s)\} + \sum_{s=1}^{n} \lambda_{\mathrm{SK}}(\mathbf{u}_s) m \\ &= m - m - \sum_{s=1}^{n} \lambda_{\mathrm{SK}}(\mathbf{u}_s) m + \sum_{s=1}^{n} \lambda_{\mathrm{SK}}(\mathbf{u}_s) m \\ &= 0 \end{aligned} \qquad (2\text{-}38)$$

There remains to determine the simple kriging weights $\lambda_{\mathrm{SK}}(\mathbf{u}_s)$, s = 1,…, *n*. These weights are determined such that the error variance is a minimum. This is done by setting one half the partial derivatives of the error variance in (2-35) with respect to each of the *n* $\lambda_{\mathrm{SK}}(\mathbf{u}_s)$ simple kriging weights to zero:

$$\frac{\partial\left(\mathrm{VAR}\{E(\mathbf{u}_0)\}\right)}{2\partial\left(\lambda_{\mathrm{SK}}(\mathbf{u}_s)\right)} = C_Z(\mathbf{u}_0 - \mathbf{u}_s) - \sum_{s'=1}^{n} \lambda_{\mathrm{SK}}(\mathbf{u}_{s'}) C_Z(\mathbf{u}_{s'} - \mathbf{u}_s) = 0 \quad s = 1,\ldots,n \qquad (2\text{-}39)$$

This results in the following system of simple kriging equations:

$$\sum_{s'=1}^{n} \lambda_{\mathrm{SK}}(\mathbf{u}_{s'}) C_Z(\mathbf{u}_{s'} - \mathbf{u}_s) = C_Z(\mathbf{u}_0 - \mathbf{u}_s) \quad s = 1,\ldots,n \qquad (2\text{-}40)$$

There are *n* equations with as many simple kriging weights $\lambda_{\mathrm{SK}}(\mathbf{u}_s)$ to be determined. This vector of weights $\boldsymbol{\lambda}_{\mathrm{SK}}$ is solved by inverting the matrix of redundancy covariances $\mathbf{C} = C_Z(\mathbf{u}_{s'} - \mathbf{u}_s)$ and multiplying this by the vector of closeness covariances $\mathbf{c} = C_Z(\mathbf{u}_0 - \mathbf{u}_s)$, that is, $\boldsymbol{\lambda}_{\mathrm{SK}} = \mathbf{C}^{-1}\mathbf{c}$. The simple kriging estimate $z^*_{\mathrm{SK}}(\mathbf{u}_0)$ is then simply the sum of weights multiplied by the sample data vector $\mathbf{z} = z(\mathbf{u}_s)$, that is, $z^*_{SK}(\mathbf{u}_0) = \boldsymbol{\lambda}_{SK}\mathbf{z}^T$. From (2-39) and (2-40), the minimized simple kriging variance $\sigma^2_{SK}(\mathbf{u}_0)$ is then:

$$\sigma^2_{SK}(\mathbf{u}_0) = C_Z(\mathbf{0}) - \sum_{s=1}^{n} \lambda_K(\mathbf{u}_s) C_Z(\mathbf{u}_0 - \mathbf{u}_s) \qquad (2\text{-}41)$$

Simple kriging is referred to as unconstrained kriging since no constraints are imposed in order to achieve unbiasedness in (2-38) or the minimum error variance in (2-39).

Consider a grid of 150,000 (300 x 500) RV locations in the example setting. Figure 2-8 shows a map of simple kriging estimates using the reservoir quality data. A large search routine is used to condition each estimate. The result is a smooth reservoir quality map.

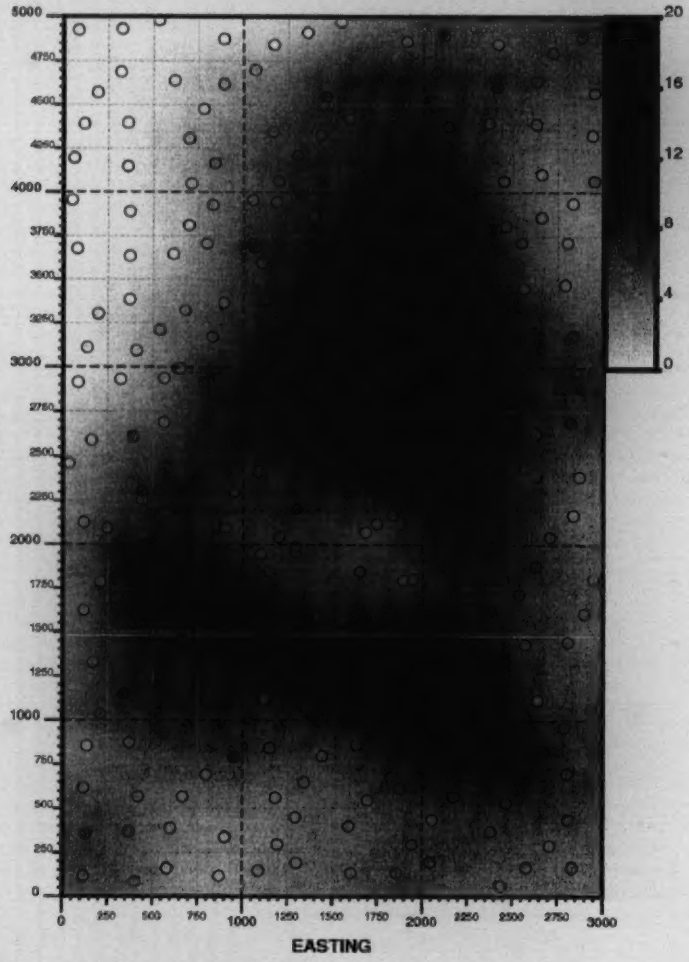

5000
4750
4500
4250
4000
3750
3500
3250
3000
2750
2500
2250
2000
1750
1500
1250
1000
750
500
250
0
NORTHING
0
250
500
750
1000
1250
1500
1750
2000
2250
2500
2750
3000
EASTING
20
16
12
8
4
0

Figure 2-8: A smooth simple kriging map of the reservoir quality variable.

2.7.3 Ordinary and Universal Kriging

These variations of kriging correspond to locally varying forms for the mean $m(\mathbf{u})$. These kriging algorithms are referred to as *kriging with a trend* (KT). The current approach is to assume $m(\mathbf{u})$ is a smoothly varying deterministic function of the coordinates vector $\mathbf{u}$ whose unknown V parameters are fit from the n data within local search windows [4]:

$$m(\mathbf{u})=\sum_{v=0}^{V} a_v(\mathbf{u}) f_v(\mathbf{u}) \tag{2-42}$$

The $f_v(\mathbf{u})$'s are known and constant functions of the coordinate vectors over the domain $\mathbf{D}$. The $a_v(\mathbf{u})$'s are estimated functional coefficients and constant within local search windows. The actual mean value $m(\mathbf{u})$ is unknown since the $a_v(\mathbf{u})$'s are also unknown. By convention $f_0(\mathbf{u}) = 1$ and $m(\mathbf{u}) = a_0(\mathbf{u})$ corresponding to what is referred to as *Ordinary Kriging* where the mean $m(\mathbf{u})$ is re-estimated to a constant $a_0(\mathbf{u})$ value within local often overlapping search windows.

To derive the KT kriging equations, the mean $m(\mathbf{u})$ is substituted into the expression for A in (2-32), which can then be substituted into (2-29) to obtain the KT kriging estimator. For unbiasedness, $V + 1$ constraints are needed:

$$\sum_{s=1}^{n} \lambda_{KT}(\mathbf{u}_s) f_v(\mathbf{u}_s) = f_v(\mathbf{u}) \quad v=0,\ldots,V \tag{2-43}$$

where the $f_v(\mathbf{u})$'s are the monomial trend functions evaluated at unsampled locations $\mathbf{u}$ and the $f_v(\mathbf{u}_s)$'s are the monomial trend functions evaluated at the sample locations $\mathbf{u}_s$. By considering these constraints, the estimator $Z^*_{UK}(\mathbf{u})$ is unbiased. In order to determine the n $\lambda_{KT}(\mathbf{u}_s)$ constrained kriging weights, the error variance in relation (2-35) is minimized under the $V + 1$ constraints in (2-43). These constraints call for the Lagrangian formalism.

2.8 Simulation

It is no longer acceptable to report a single deemed best estimate within a particular area or volume of interest without any attached uncertainty. Geological uncertainty can be quantified with geostatistical simulation. Many geostatistical simulation algorithms have been forwarded to generate multiple stochastic and equally probable realizations of the spatial distribution of ReVs. These include matrix approaches (LU decomposition) used for select areas due to computer resource demand, turning band methods where the variable is simulate on 1D lines and then combined into a 3D model, (3) spectral methods using FFTs, (4) fractals that are imbedded with a signature of self-similarity, (5) moving average methods, (6) object-based modeling for lithofacies and rock type uncertainty and (7) sequential methods such as sequential Gaussian and indicator simulation [6]. The details of sequential Gaussian simulation (SGS) are covered here.

2.8.1 Sequential Gaussian simulation (SGS)

The following are 3 minimum criteria for a map of a particular petrophysical property, estimated or simulated, used for recoverable reserves and making production decisions:

1. The data-to-data covariance $C_Z(\mathbf{u}_s - \mathbf{u}_{s'})$ involving the sample data is reproduced after prediction;
2. The estimate-to-data covariance $C_Z(\mathbf{u}_0 - \mathbf{u}_s)$ involving the predicted values and sample data is reproduced after prediction; and

3. The estimate-to-estimate covariance $C_Z(\mathbf{u}_0 - \mathbf{u}_0)$ which is the variance of predicted values reproduces the stationary variance σ^2.

The motivation for simulation techniques can be derived by evaluating these three criteria for simple kriging. The first of these three conditions is easily met. The sample data do not change after estimation; therefore, the data-to-data covariance $C(\mathbf{u}_s - \mathbf{u}_{s'})$ is the same after prediction. The second condition, however, involves the $z^*_{\mathrm{SK}}(\mathbf{u}_0)$ estimates and is checked:

$$\begin{aligned} C_Z(\mathbf{u}_0-\mathbf{u}_s) &= \mathrm{E}\{R^*_{\mathrm{SK}}(\mathbf{u}_0)R(\mathbf{u}_s)\} - \mathrm{E}\{R^*_{\mathrm{SK}}(\mathbf{u}_0)\}\mathrm{E}\{R(\mathbf{u}_s)\} \\ &= \mathrm{E}\left\{\sum_{s'=1}\lambda_{\mathrm{SK}}(\mathbf{u}_{s'})R(\mathbf{u}_{s'})R(\mathbf{u}_s)\right\} \\ &= \sum_{s'=1}^{n}\lambda_{\mathrm{SK}}(\mathbf{u}_{s'})C_Z(\mathbf{u}_{s'}-\mathbf{u}_s) \\ &= C_Z(\mathbf{u}_0-\mathbf{u}_s) \end{aligned} \qquad (2\text{-}44)$$

Therefore, in probabilistic terms, the second condition is also satisfied for SK. Note the use of the SK system of equations in (2-40) to make the last substitution. It is also important to note that this condition can not be met with the KT algorithm. The third condition involves the new set of $z^*_{\mathrm{SK}}(\mathbf{u}_0)$ estimates and is also be checked:

$$\begin{aligned} \mathrm{VAR}\{Z^*_{\mathrm{SK}}(\mathbf{u}_0)\} &= \mathrm{E}\{R^*(\mathbf{u}_0)R^*(\mathbf{u}_0)\} \\ &= \sum_{s=1}^{n}\sum_{s'=1}^{n}\lambda_{\mathrm{SK}}(\mathbf{u}_s)\lambda_{\mathrm{SK}}(\mathbf{u}_{s'})C_Z(\mathbf{u}_s-\mathbf{u}_{s'}) \\ &= \sigma^2_{\mathrm{SK}}(\mathbf{u}_0) - C_Z(0) + 2\sum_{s=1}^{n}\lambda_{\mathrm{SK}}(\mathbf{u}_0)C_Z(\mathbf{u}_0-\mathbf{u}_s) \\ &= \sigma^2_{\mathrm{SK}}(\mathbf{u}_0) - C_Z(0) + 2\left(C_Z(0)-\sigma^2_{\mathrm{SK}}(\mathbf{u}_0)\right) \\ &= C_Z(0) - \sigma^2_{\mathrm{SK}}(\mathbf{u}_0) \\ &= \sigma^2 - \sigma^2_{\mathrm{SK}}(\mathbf{u}_0) \end{aligned} \qquad (2\text{-}45)$$

The variance of the estimates $\mathrm{VAR}\{Z^*_{\mathrm{SK}}(\mathbf{u}_0)\}$ is underestimated by an amount equal to the SK estimation variance in (2-41). This is known as the smoothing effect of kriging. Ideally, the variance of the kriging estimator would be the global variance σ^2 in expected value. This deficiency of kriging is the motivation for simulation.

Simulation acts to correct the variance via the addition of a random residual $Q(\mathbf{u})$:

$$z_{\mathrm{SGS}}(\mathbf{u}_0) = R^*(\mathbf{u}_0) + Q(\mathbf{u}_0) \qquad (2\text{-}46)$$

The residual is drawn randomly from a Gaussian distribution with an expected value of zero and variance equal to the kriging variance $\sigma^2_{\mathrm{SK}}(\mathbf{u}_0)$. This does not change the optimal kriging estimate $z^*_{\mathrm{SK}}(\mathbf{u}_0)$, but does act to increase the variance by the amount missing in (2-45). Therefore, the variance of the newly simulated values $z_{\mathrm{SGS}}(\mathbf{u}_0)$ is the correct global variance σ^2. Therefore, the first and third minimum criteria previously identified are upheld for the $z_{\mathrm{SGS}}(\mathbf{u}_0)$ simulation values. The second condition is also satisfied since the addition of the random residual $Q(\mathbf{u})$ does not change the estimate-to-data covariance:

$$\begin{aligned} C_Z(\mathbf{u}_0-\mathbf{u}_s) &= \mathrm{E}\left\{R_{\mathrm{SGS}}(\mathbf{u}_0)R(\mathbf{u}_s)\right\} - \mathrm{E}\left\{R^{*}_{\mathrm{SK}}(\mathbf{u}_0)\right\}\mathrm{E}\left\{R(\mathbf{u}_s)\right\} \\ &= \mathrm{E}\left\{\left[\sum_{s'=1}^{n}\lambda_{\mathrm{SK}}(\mathbf{u}_{s'})R(\mathbf{u}_{s'})+Q(\mathbf{u}_0)\right]R(\mathbf{u}_s)\right\} \\ &= \sum_{s'=1}^{n}\lambda_{\mathrm{SK}}(\mathbf{u}_{s'})\mathrm{E}\left\{R(\mathbf{u}_{s'})R(\mathbf{u}_s)\right\}+\mathrm{E}\left\{Q(\mathbf{u}_0)R(\mathbf{u}_s)\right\} \\ &= C_Z(\mathbf{u}_0-\mathbf{u}_s) \end{aligned} \qquad (2\text{-}47)$$

Therefore, the simulated values $z_{\mathrm{SGS}}(\mathbf{u}_0)$ satisfy all three criteria.

As its name suggests there are two key concepts involved in deriving an SGS algorithm. The first is the process of proceeding sequentially by adding previously simulated nodes $z_{\mathrm{SGS}}(\mathbf{u}_0)$ to the pool of conditioning data for subsequent simulation locations. As shown in (2-47), this ensures the estimate-to-data covariance is correct. The other core concept in SGS is the multivariate Gaussian assumption for the $Q(\mathbf{u}_0)$ residual distribution. The SK variance in (2-41) and mean of zero is all that is needed to completely parameterize these distributions. The $q(\mathbf{u}_0)$ draws are then simply added to the SK estimate $z^{*}_{\mathrm{SK}}(\mathbf{u}_0)$ to obtain the simulated value $z_{\mathrm{SGS}}(\mathbf{u}_0)$.

The following is a basic seven step SGS algorithm:

1. Transform the $z(\mathbf{u}_s)$ sample data to follow a normal distribution;
2. Visit an unsampled location $\mathbf{u}_0$ and perform simple kriging to obtain $z^{*}_{\mathrm{SK}}(\mathbf{u}_0)$ and $\sigma^2_{\mathrm{SK}}(\mathbf{u}_0)$;
3. Draw a random residual $q(\mathbf{u}_0)$ from a normal distribution centered at 0 and spread with $\sigma^2_{\mathrm{SK}}(\mathbf{u}_0)$;
4. Add the simple kriging estimate $z^{*}_{\mathrm{SK}}(\mathbf{u}_0)$ and random residual $q(\mathbf{u}_0)$ to obtain the simulated value $z_{\mathrm{SGS}}(\mathbf{u}_0)$;
5. Add $z_{\mathrm{SGS}}(\mathbf{u}_0)$ to the set of conditioning data;
6. Repeat 2 through 5 visiting all unsampled $\mathbf{u}_0$ locations in random order; and
7. Back transform the $z_{\mathrm{SGS}}(\mathbf{u}_0)$ from Gaussian to real units.

A map of simulated values using the SGS algorithm is generated for the same 300 x 500 resolution used for the kriging estimates and is shown in Figure 2-9.

2.9 Reasonability Criteria

The reasonability of making a decision of stationarity is evaluated within each of the five phases proposed for making the decision of stationarity. That is, any technique reviewed is evaluated according to some criteria. The techniques prototyped are intentioned to satisfy all criteria. The two most basic and important criteria are simplicity and geological realism.

The technique formulation, description, and implementation within each phase of making a decision of stationarity should be relatively straightforward. Too complex algorithms will be difficult to implement, explain, and justify in practical settings. More popular mainstream algorithms are generally more straightforward.

After a technique is simple, it must capture realistic geology; but what exactly is realistic geology when the truth is never known before recovery begins. In this dissertation geological reality means plausible geological features that are known and considered to have a significant impact on production uncertainty.

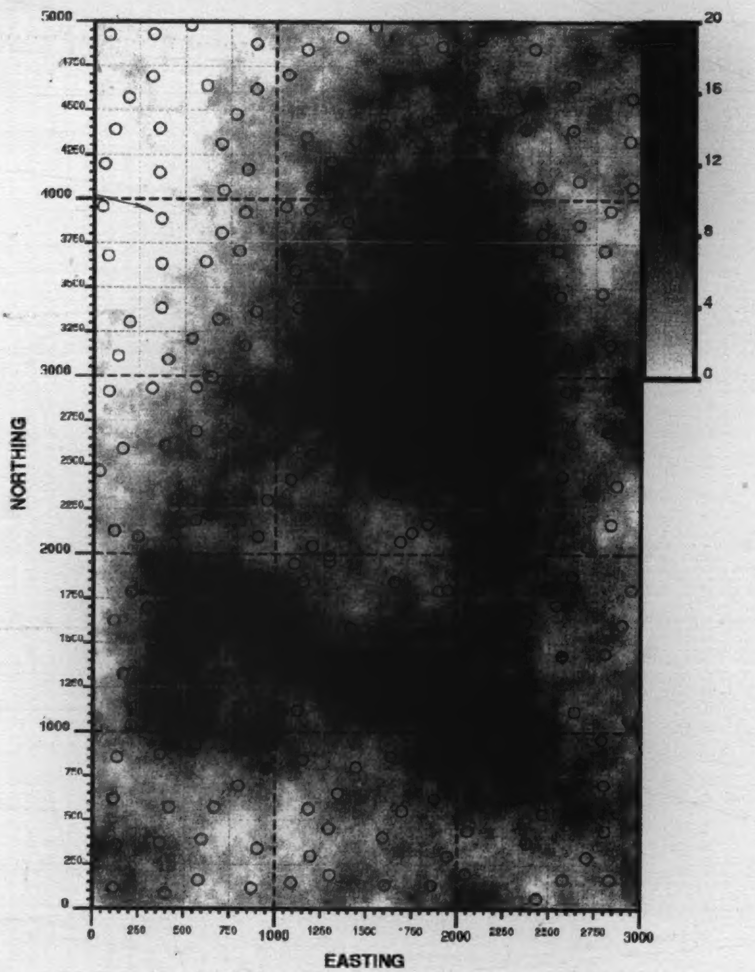

NORTHING
5000
4750
4500
4250
4000
3750
3500
3250
3000
2750
2500
2250
2000
1750
1500
1250
1000
750
500
250
0
EASTING
0
250
500
750
1000
1250
1500
1750
2000
2250
2500
2750
3000
20
16
12
8
4
0

Figure 2-9: A sequential Gaussian simulation map of the reservoir quality variable.

CHAPTER 3

THE DECISION OF STATIONARITY

The decision of stationarity is a five step process: (1) choosing the number and type of domains to apply separate SRFs within, (2) modeling domain boundaries, (3) quantifying and modeling the nature of transitions across domain boundaries, (4) quantifying large-scale deterministic trends within domain boundaries, and (5) predicting with a trend model. The aim of this dissertation is the development and presentation of this support system for managing these consequences a decision of stationarity has on the workflow of a geostatistical project. The context, modeling approaches, and criteria for evaluating the reasonableness of each step are identified in this chapter. Additional details on specialized subjects are given in subsequent chapters.

3.1 Framework of a Decision of Stationarity

Figures 3-1a to 3-1e illustrate the five geostatistical modeling steps proposed for making a reasonable decision of stationarity each with their own associated context, approaches to modeling, and reasonability criteria. In each figure, a flow chart is shown to the left and a schematic example is shown at the right. Each part of Figure 3-1 represents a geostatistical modeling step or phase that can potentially improve the reasonability of the decision of stationarity. A typical study will address these steps in the order (a-e) presented. The collective approach to all five of these steps encompasses a decision of stationarity.

The most important element of each geostatistical modeling phase is shown with the schematic example to the right of the flow chart. The setting is mining. There are four corehole traces (CH01 to CH04) of varying length below ground surface available in this 2D illustration; each corehole shows a petrophysical property profile to the right of its trace for an attribute of interest. No sample data are available above a certain elevation in overburden or below a certain elevation in bedrock. The decision of stationarity for this setting is described in the following sections.

3.1.1 Choosing Domain Types

The first modeling step for a decision of stationarity is choosing the number and type of domains. This is done to ensure the mathematical SRF assumptions within each domain type are as appropriate as possible. This choice is based on logical geological divisions. The approach to this aspect of the decision of stationarity should be hierarchical starting from the full accumulation limits to selecting increasingly smaller more geologically homogeneous domains. At each stage in such a hierarchy, the suitability of assumed SRF parameters and number of available data are balanced.

Accumulation limits are needed to identify regions where a numerical model is required. The choice in Figure 3-1a avoids modeling the attribute within overburden and bedrock material; these boundaries are marked on the corehole traces with level bars where data becomes unavailable. Assuming a single SRF applicable within the accumulation limits, however, may be inappropriate considering the heterogeneity suggested by the corehole profiles. Separate SRFs for the low and high attribute intervals may be more appropriate. These intervals are also separated with level bars and labeled non-net and net.

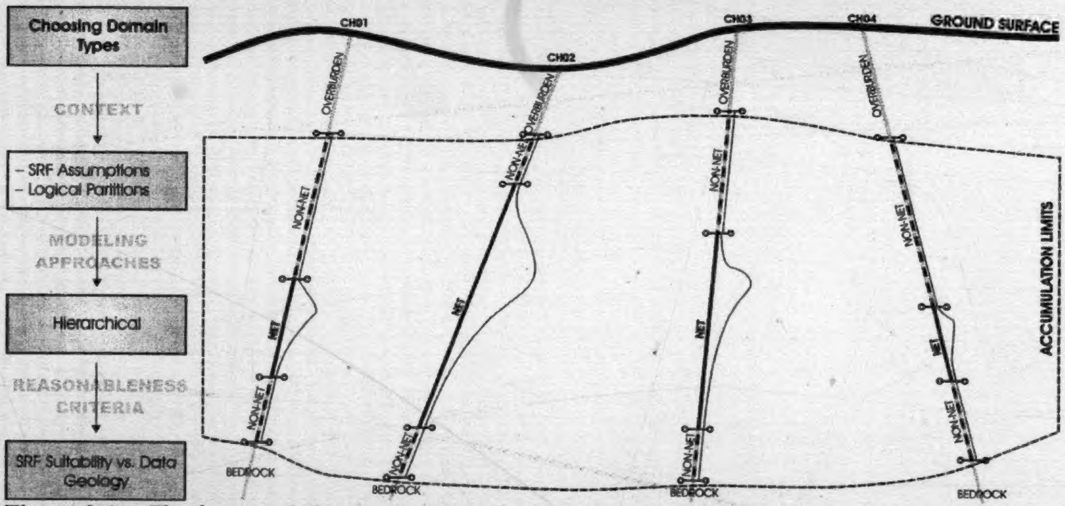
Choosing Domain Types
CONTEXT
- SRF Assumptions
- Logical Partitions
MODELING APPROACHES
Hierarchical
REASONABLENESS CRITERIA
SRF Suitability vs. Data Geology
CH01
CH02
CH03
CH04
GROUND SURFACE
OVERBURDEN
NON-NET
NET
BEDROCK
ACCUMULATION LIMITS

Figure 3-1a: *The framework for the decision of stationarity:* the first of five steps during geostatistical modeling is choosing domain types. The context, modeling approaches, and reasonability criteria are listed to the left; net and non-net rocktypes are indicated for the 2D example to the right.

3.1.2 Boundary Modeling

Once domain types are chosen, a model of their 3D bounding surfaces is needed to identify the spatial jurisdiction of separate SRFs. There is unavoidable uncertainty in these boundaries. A range of boundary modeling approaches can be considered.

One possible boundary model separating non-net from net material is sketched in Figure 3-1b. The uncertainty in this boundary is shown between CH01 and CH02 with arrows of varying length; in general, the amount of uncertainty increases away from data where the arrows are longer. Portions of a Cartesian grid are shown illustrating that it is uncertain which SRF the grid cells along the margins of the boundary model belong to. There is also uncertainty in the top and bottom accumulation limit surfaces between coreholes. In practice, several bounding surfaces would be considered inside the accumulation limits.

3.1.3 Nature of Boundaries

The geological boundaries separating predictions from significantly different SRF models can rarely be modeled by abrupt transitions. A model quantifying the influence of the predictions from surrounding SRFs may be required to create more geologically realistic transitions. A linear mixing model (LMM) parameterized by a contact analysis is one possible model available to quantify the influence of sample data and subsequent predicted values across geological boundaries; alternatively, a global or local linear model of coregionalization (LMC) can be used [49].

Two linear mixing models (LMMs) are shown between the CHO2 and CH03 coreholes in Figure 3-1c. For a particular grid cell a distance d_{NET} inside net material or $d_{\mathrm{NON\text{-}NET}}$ inside non-net material, the LMMs provide the weight to predictions from both a non-net SRF $w_{\mathrm{NON\text{-}NET}}$ and a net SRF w_{NET} at that same grid cell location. The LMM parameters may vary throughout the accumulation; the mixing model shown at the higher elevation will produce smoother transitions than the lower elevation mixing model.

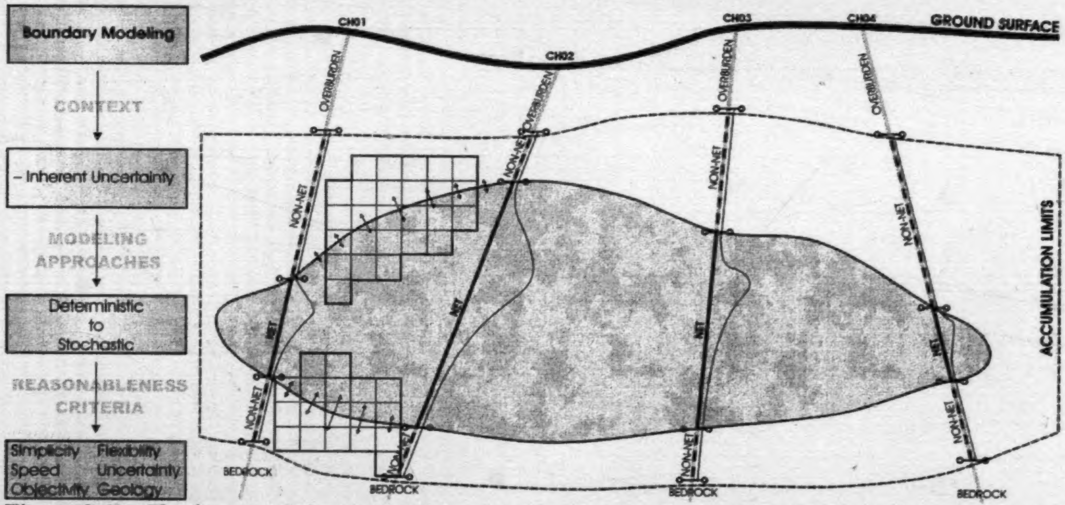
Boundary Modeling
CONTEXT
- Inherent Uncertainty
MODELING APPROACHES
Deterministic to Stochastic
REASONABLENESS CRITERIA
Simplicity Flexibility
Speed Uncertainty
Objectivity Geology
CH01
CH02
CH03
CH04
GROUND SURFACE
OVERBURDEN
NON-NET
NET
ACCUMULATION LIMITS
BEDROCK

Figure 3-1b: *The framework for the decision of stationarity:* the second of five steps during geostatistical modeling is modeling domain boundaries. The context, modeling approaches, and reasonability criteria are listed to the left; a boundary model and its uncertainty are indicated for the 2D example to the right.

3.1.4 Trend Modeling

There are two reasons for trend modeling: first, because geostatistical prediction requires a locally varying mean or trend model (often the trend model is ignored by adopting a constant first order stationary mean); and second, because it is usually possible to detect large-scale deterministic trends within geological domains where separate SRFs were previously deemed suitable. A trend model should always be built and reproduced in any legitimate numerical model. Trends are built manually or automatically and should represent large-scale deterministic geological interpretations.

Notice in Figure 3-1d the rapid increase and slow decrease of the petrophysical property value with increasing depth in net. This general relationship is proportionally contracted or expanded near the thinner ends and the thicker middle, respectively. In practice, this observed trend would be confirmed with deterministic geological interpretation. Two manually built vertical trend models are shown between CH03 and CH04 for two strings of unsampled grid cells. These smoothly varying local expectations should be reproduced in the final numerical model of predictions.

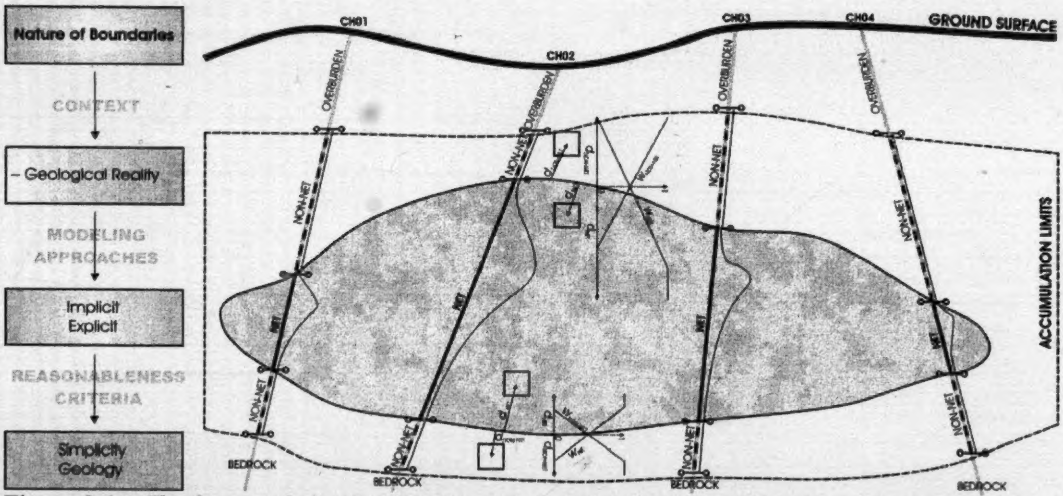
Nature of Boundaries
CONTEXT
- Geological Reality
MODELING APPROACHES
Implicit
Explicit
REASONABLENESS CRITERIA
Simplicity
Geology
CH01
CH02
CH03
CH04
GROUND SURFACE
OVERBURDEN
NON-NET
NET
BEDROCK
ACCUMULATION LIMITS

Figure 3-1c: *The framework for the decision of stationarity:* the third of five steps during geostatistical modeling is quantifying and modeling the transitional nature of the attribute over boundaries. The context, modeling approaches, and reasonability criteria are listed to the left; two LMMs are shown to the right.

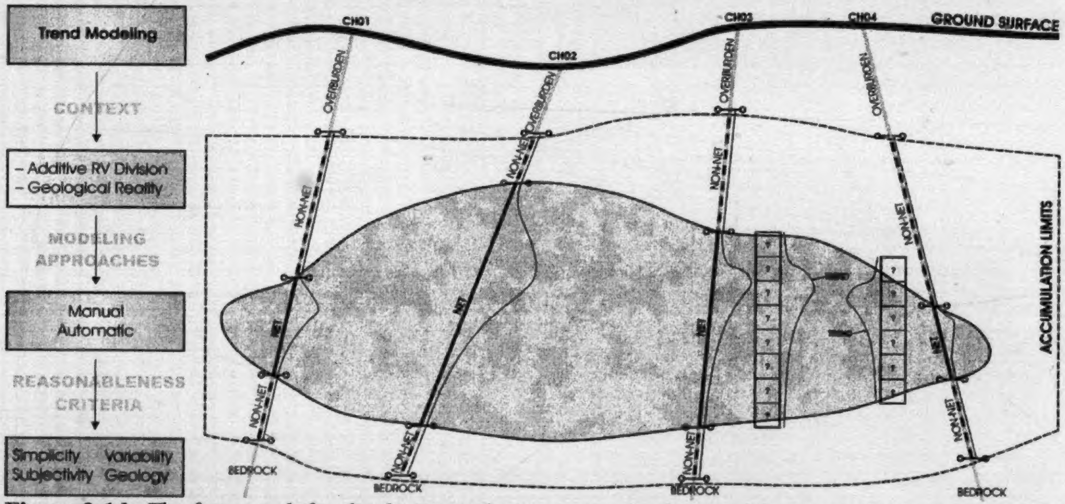
Trend Modeling
CONTEXT
- Additive RV Division
- Geological Reality
MODELING APPROACHES
Manual
Automatic
REASONABLENESS CRITERIA
Simplicity
Variability
Subjectivity
Geology
CH01
CH02
CH03
CH04
GROUND SURFACE
OVERBURDEN
NON-NET
NET
BEDROCK
ACCUMULATION LIMITS

Figure 3-1d: *The framework for the decision of stationarity:* the fourth of five steps during geostatistical modeling is trend modeling. The context, modeling approaches, and reasonability criteria are listed to the left; a trend model for two vertical strings of grid cells is shown to the right.

3.1.5 Prediction with a Trend Model

Classic geostatistical prediction does not guarantee the trend will be reproduced; in general, the discrepancy between predicted values and a trend model will increase away from the sample data. In these settings, it may be necessary to directly integrate the trend within a modified geostatistical algorithm to reproduce key large-scale geological features explicitly.

Figure 3-1e shows predicted petrophysical property profiles along the strings of unknown grid cells. The results fluctuate about the trend as they should. In practice, this is achieved implicitly with conventional geostatistical methods applied with a sufficient number of conditioning data or explicitly integrating the trend into the prediction method.

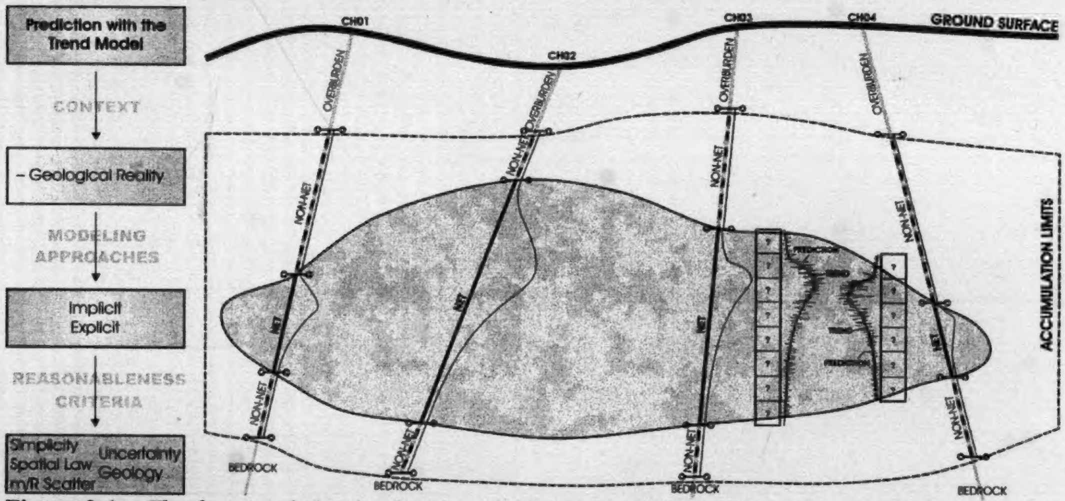
Prediction with the Trend Model
CONTEXT
- Geological Reality
MODELING APPROACHES
Implicit
Explicit
REASONABLENESS CRITERIA
Simplicity
Spatial Law
m/R Scatter
Uncertainty
Geology
CH01
CH02
CH03
CH04
GROUND SURFACE
OVERBURDEN
NON-NET
NET
BEDROCK
PREDICTION
TREND
ACCUMULATION LIMITS

Figure 3-1e: *The framework for the decision of stationarity:* the last of five steps during geostatistical modeling is predicting with a trend model. The context, modeling approaches, and reasonability criteria are listed to the left; a predicted profile for the two vertical strings of grid cells is shown to the right.

3.2 Choosing Domain Types

Choosing the number and type of geological domains for applying separate SRFs is the first step in making the decision of stationarity. This decision is needed to ensure the resulting numerical models are consistent with the geology.

3.2.1 Context

The context and motivation for choosing domain types is derived from both a theoretical and geological perspective.

Theoretical Context

Consider the domain $\mathbf{D}$. A SRF representation of the petrophysical property Z within $\mathbf{D}$ is a RF made up of the set of RVs $\{Z(\mathbf{u})$ for all $\mathbf{u}$ in $\mathbf{D}\}$ such that each RV $Z(\mathbf{u})$ has the same first order expected value m and each RV pair approximately separated by $\mathbf{h}$ $(Z(\mathbf{u}), Z(\mathbf{u} + \mathbf{h}))$ has the same second order covariance $C_Z(\mathbf{h})$ despite the location $\mathbf{u}$ within $\mathbf{D}$. This is a *decision* of stationarity since different choices of domain types results in different mathematical assumptions of homogeneity. For example, by replacing the full domain $\mathbf{D}$ with a set of N mutually exclusive sub-domains $\{\mathbf{D} = \mathbf{D}_1, \mathbf{D}_2, \ldots, \mathbf{D}_N\}$, the assumption of stationarity is transferred from the single SRF within $\mathbf{D}$ to the new set of N SRFs enclosed within the N corresponding sub-domains $\mathbf{D}_1, \mathbf{D}_2, \ldots, \mathbf{D}_N$.

Geological Context

Choosing domain types is necessary for most geological settings. Implementing different SRFs within domains chosen according to prevailing rocktypes and/or formation histories will often accomplish a reasonable level of homogeneity for the SRF assumptions. This is the geological context for boundary modeling. Two examples are presented to illustrate the choice of domain types. The first is a vein-type deposit encountered in the mining industry. The second is a clastic sedimentary sequence encountered in the petroleum industry. The formation history, mineralogy, and logical divisions for distinct SRFs are addressed in both settings.

Figure 3-2 shows a portion of a hydrothermal gold-quartz vein mineral deposit. There is a pen in the photograph for scale. The vein is formed from gold and quartz minerals being soluble and mixing in solution under the application of immense heat and pressure [9]. A gold-quartz ore precipitates out of solution accommodating space formed by the release of heat and pressure; mechanisms for the application and release of heat and pressure are usually intrusive, collisional, or shear [9]. The vein depicted in Figure 3-2 was formed along a shearing dextral fault zone.

Figure 3-2 also shows the mineralogy typical of gold-quartz veins. The ore material is a quartz mixture. The example shows an arsenopyrite-quartz composition (top right). A variety of host rocks are possible; however, mafic to ultramafic igneous material is most common [9]. The example shows a basalt host rock (bottom right).

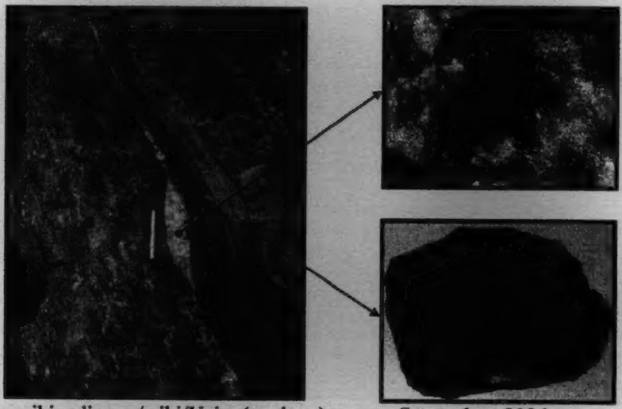

Source: Internet, http://en.wikipedia.org/wiki/Vein_(geology), access September, 2006

Figure 3-2: A photograph of a gold-quartz vein (left) showing arsenopyrite quartz ore (top right) and basalt waste (bottom right) rock samples. A pen is shown for scale on the left. The photographs on the right measure 1cm (top) and 10cm (bottom) a side.

Gold grades behave significantly different within quartz ore versus mafic waste material. The gold grades are higher and more variable within the ore vein. The assumptions of stationarity would be quite poor if a single SRF is used to model gold grade within both ore and waste since the mean m and covariance $C_Z(\mathbf{h})$ are significantly different within ore and waste. The numerical model will be more consistent with the geology when separate SRFs are used.

Figure 3-3 shows an outcrop of a shore face sand-shale sequence typically exploited in the subsurface for petroleum reserves. The exact scale is unknown, but the width of the photograph represents some order of kilometers. Deposition of sand and shale facies is controlled by relative sea level change. During transgressions, sea level lowers relative to the shore line and river delta sand spreads out over the shore; during regressions, sea level elevates relative to the shore line and marine shale migrates over the shore [10]. Common drivers of relative sea level change are tectonics and environment. A petroleum reservoir forms when oil migrates into and is trapped within the sequence.

Figure 3-3 also shows samples of sand and shale facies from the outcrop photo. The high energy river sands are coarse grained matrices of high porosity sandstone while the low energy marine shales are fine grained matrices of low porosity siltstone.

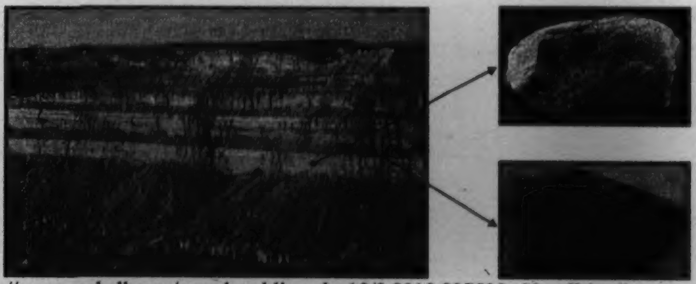

Source: Internet, http://wps.prenhall.com/esm_hamblin_eds_10/0,8010,837539-,00.utf8.html, access September, 2006

Figure 3-3: A photograph of a layered sand-shale clastic sedimentary sequence (left) and typical net sand (top right) and non-net shale (bottom right) facies samples. The scale on the left is on the order of a few kilometers. The photographs on the right each measure 15 x 30cm.

Sand facies will store recoverable hydrocarbons while shale facies act as barriers to flow. Petrophysical properties such as porosity, permeability, and oil saturation are very different within sand and shale. And since the mean m and covariance $C_Z(\mathbf{h})$ will also be significantly different, the numerical model will be more consistent with the geology when separate SRFs are used.

3.2.2 Modeling Approaches

There is essentially one modeling approach for choosing domain types. Choosing domain types should be done in a geometrically nested or hierarchical manner starting from the global mineral or reservoir accumulation domain to selecting increasingly smaller more geologically homogeneous domains.

Figure 3-4 illustrates the hierarchical approach to choosing the number and type of domains within a typical shore face reservoir. The first stage in the hierarchy is the option of applying a single SRF to the full hydrocarbon accumulation limits. Often, however, the assumption of stationarity in this case is inadequate to represent geological heterogeneity over multiple distinct geological compartments. Like the mining and petroleum examples presented earlier (Figures 3-2 and 3-3), the assumption of stationarity may improve when additional SRFs are applied within smaller more geologically homogeneous regions. And so moving down the example hierarchy in Figure 3-4, separate SRFs are considered within increasingly smaller domain sizes. In many settings, the identification of net versus non-net domains may drastically improve the assumption of stationarity. If this choice is still inadequate, structural layering may be identified within the net and non-net volumes. Figure 3-4 demonstrates five HST (high-stand systems tract) and one TST (transgressive systems tract) within net geology; and two LST (low-stand systems tract) and two FSST (falling stage systems tract) layers are shown within non-net geology [10].

If this level of detail is still inadequate for a reasonable assumption of stationarity, facies types can be considered within each layer. Figure 3-4 identifies four possible facies types: sand, breccia, inclined heterolithic strata (IHS), and shale.

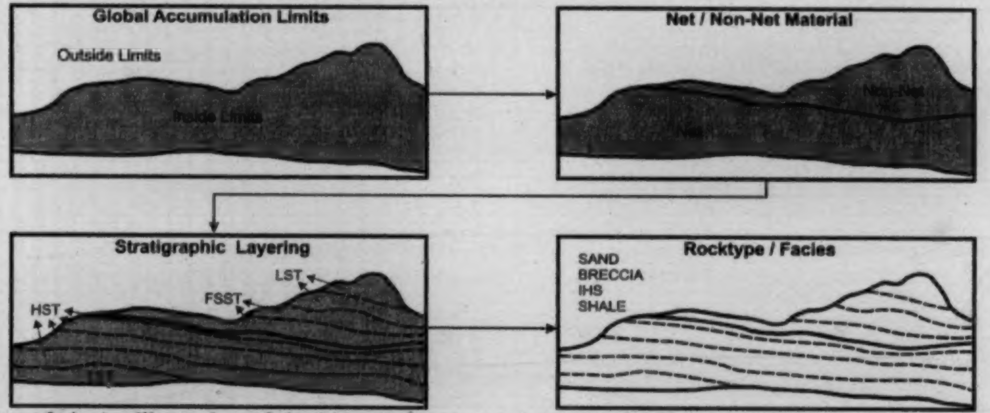

Figure 3-4: An illustration of the hierarchical approach to choosing the number and type of geological domains for a typical shore face reservoir. The scale is similar to that in the photograph of Figure 3-4.

3.2.3 Reasonableness

Choosing domain types for the application of separate SRFs is the first and likely most important out of five steps for making a decision of stationarity. There are significant practical challenges to overcome for making a reasonable choice.

Inference Challenges

At any level in the hierarchy of Figure 3-4, the stationary first order expected value m and stationary second order covariance $C_Z(\mathbf{h})$ parameters of the enclosed SRF are inferred from the available geological information. For reliable inference, a sufficient number of data are required. Limited data is a common problem even within the entire accumulation limits. The consequence of increased geological consistency with the stationary first and second order moments is a reduction in conditioning sample data. Choosing an additional domain type must always balance the degree of increased geological consistency with the number of data available to infer the enclosed SRF parameters.

Considering the extremes is instructive. The most geologically homogenous domain type would centre on a single sample datum; however, such a solitary sample is inadequate for calculating a reliable m parameter and impossible for calculating the $C_Z(\mathbf{h})$ parameters. In contrast, by pooling all possible sample data together to calculate m and $C_Z(\mathbf{h})$, there is a significant risk of masking important heterogeneous features that could otherwise be modeled more suitably with multiple SRFs each with different m and $C_Z(\mathbf{h})$ parameters.

Reasonability Criteria

The reasonability of choosing a particular set of domains each with a separate SRF is evaluated on the basis of an optimal balance between the level of geological consistency with an assumption of a SRF and the amount of available sample data to infer the SRF parameters. This balance is always subjective; a choice of domain types, therefore, can not be proven wrong, but can be argued unreasonable on this basis.

3.3 Boundary Modeling

A major model operation imposed on geostatistical modeling for a reasonable decision of stationarity is boundary modeling. Boundary models are needed to quantify the uncertainty in the spatial jurisdiction of SRFs throughout the numerical model. A more detailed treatment of this topic is given in Chapter 4.

3.3.1 Context

There is unavoidable uncertainty in the location of domain bounding surfaces where there is incomplete sample data and geological information. There is also then uncertainty in the assignment of grid cells to a particular SRF near geological boundaries. Quantifying this structural uncertainty with multiple possible boundary models is an essential aspect of making a reasonable decision of stationarity and a significant component of calculating geological uncertainty.

Figure 3-5 shows a schematic 2D example. Four corehole traces of varying length from ground surface are available. Net and non-net domain types are chosen for separate SRFs and shown as dark and shaded traces, respectively. The domain boundaries are known with zero uncertainty at corehole locations; however, between data, there is unavoidable uncertainty in the boundary location. This structural uncertainty is represented with six possible net/non-net boundary surfaces. The grid of prediction locations within known accumulation limits illustrates that grid cells near the net/non-net geological boundary will switch between being predicted with the net and non-net SRF models depending on the particular boundary realization.

Similar scenarios are constructed for the mining and petroleum examples presented in Figures 3-2 and 3-3, respectively. True geological models are created in each setting using image analysis. The original photo and these true geological models are shown on the left and in the middle of Figures 3-6 and 3-7, respectively. Net ore vein and sand facies are black while non-net waste and shale facies are shaded gray. Two drillholes are extracted from the mining example and two wells are extracted from the petroleum example. There is an implicit assumption that the scale in Figure 3-6 is increased from Figure 3-2 to something appropriate for the application of a block model. The right of Figures 3-6 and 3-7 show the location and geology of these samples. In both settings, the conditioning sample data are located relatively far apart meaning there will likely be a significant level of structural uncertainty in the boundaries.

3.3.2 Modeling Approaches

There is a full continuum of modeling approaches available to build domain bounding surfaces ranging from entirely deterministic techniques to entirely stochastic techniques. Figure 3-8 shows a sketch of this continuum. Several categories of boundary modeling algorithms are shown. The general position of deterministic digitization (DD), volume function (VF), object-based (OB), surface-based (SB), and stochastic pixel-based (SPB) algorithms are all indicated. Depending on how the algorithm is parameterized and implemented, these methods can shift along the scale. Choosing a boundary modeling method from this continuum depends on the geometrical nature of the boundaries as well as the amount and type of conditioning data available.

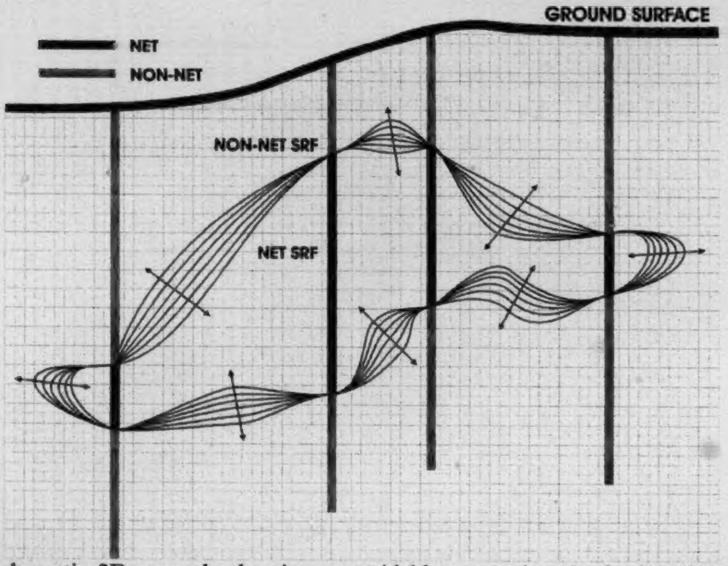
GROUND SURFACE
NET
NON-NET
NON-NET SRF
NET SRF

Figure 3-5: A schematic 2D example showing unavoidable uncertainty in the location of a net/non-net boundary between coreholes locations.

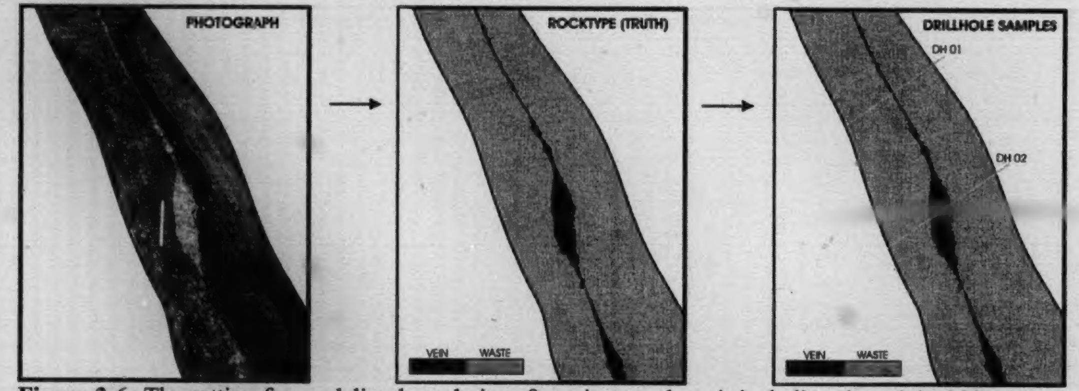
PHOTOGRAPH
ROCKTYPE (TRUTH)
DRILLHOLE SAMPLES
DH 01
DH 02
VEIN
WASTE
VEIN
WASTE

Figure 3-6: The setting for modeling boundaries of a vein-type deposit including the original photograph (left), the true vein/waste rocktype model after image analysis (middle), and two conditioning drillholes for subsequent modeling (right).

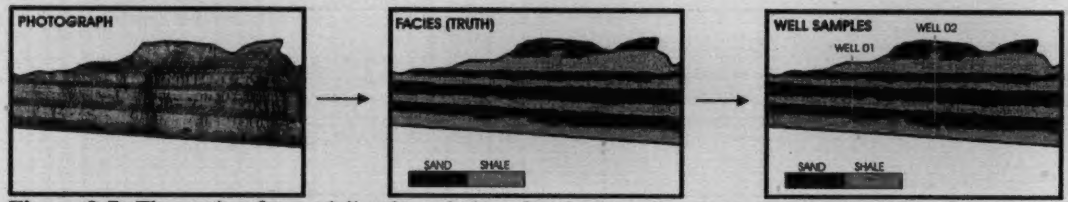
PHOTOGRAPH
FACIES (TRUTH)
SAND
SHALE
WELL SAMPLES
WELL 02
WELL 01
SAND
SHALE

Figure 3-7: The setting for modeling boundaries of a clastic sedimentary reservoir including the original photograph (left), the true sand/shale facies model after image analysis (middle), and two conditioning wells for subsequent modeling (right).

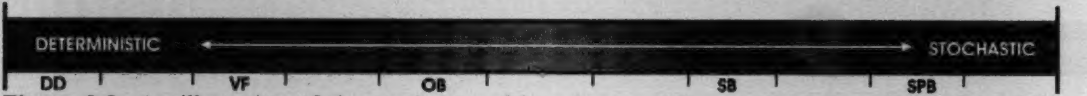
DETERMINISTIC
STOCHASTIC
DD
VF
OB
SB
SPB

Figure 3-8: An illustration of the continuum of boundary modeling approaches available from fully deterministic (left) to fully stochastic (right).

The drillhole and well data shown in Figures 3-6 and 3-7 are now used to demonstrate and compare the performance of different modeling methods. Figures 3-9 and 3-10 show DD (left), VF (middle) and SPB (right) boundary models built conditional to the two drillholes or two wells from each setting.

DD boundary models are time consuming and subjective exercises. The left of Figures 3-9 and 3-10 show digitized ore vein and sand facies boundaries (broken lines) for the mining and petroleum settings. The result is just one deterministic model. There is no objective measure of the inherent uncertainty in boundaries.

The top right of Figures 3-9 and 3-10 show an SIS realization of the geology from each setting. The construction of multiple realizations provides fast objective measures of uncertainty; however, the results may not be geologically realistic. Without a relatively large amount of conditioning data, large deviations from reality are possible. These uncertainties are theoretically correct, but geologically unrealistic. The SIS results in Figures 3-9 and 3-10 are clearly different from the true geology in each case. Cleaning algorithms [11] improve the image (bottom right of Figures 3-9 and 3-10), but do not fix the problem. There is a need to capture global uncertainty with realistic geology.

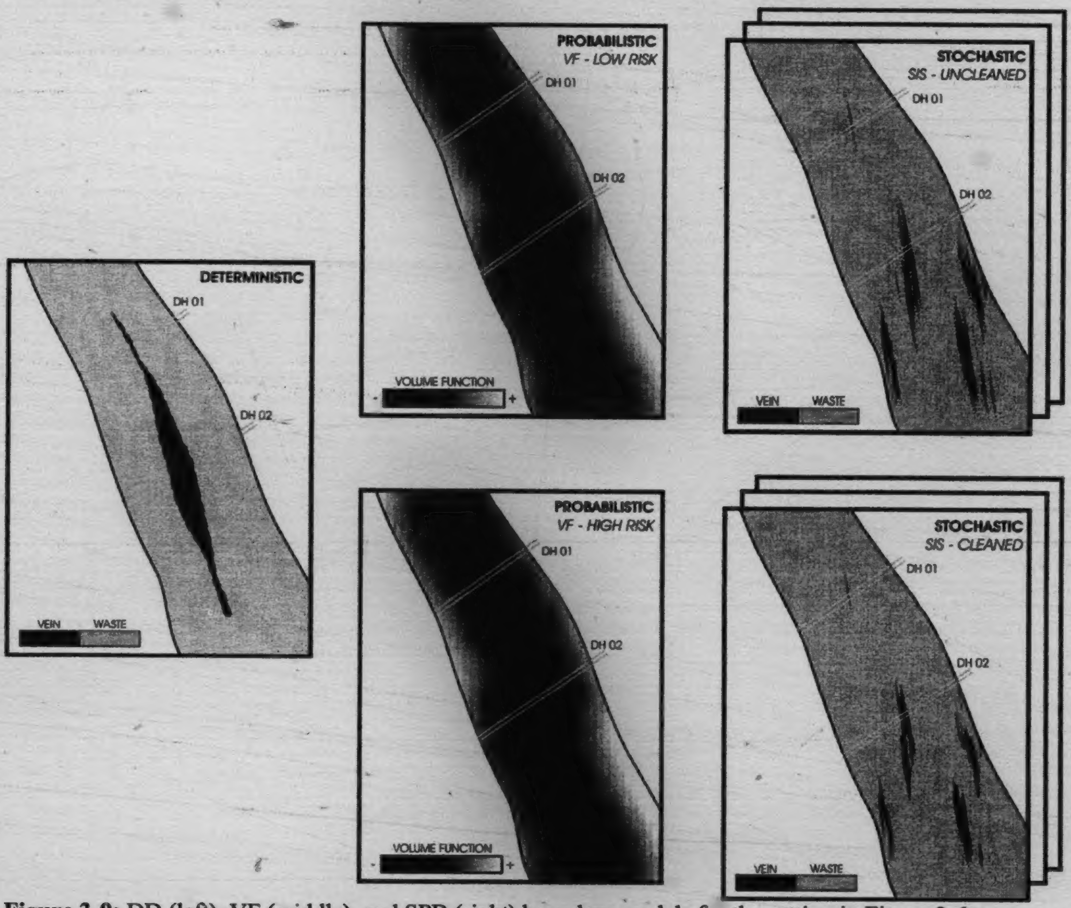
DETERMINISTIC
DH 01
DH 02
VEIN
WASTE
PROBABILISTIC
VF - LOW RISK
DH 01
DH 02
VOLUME FUNCTION
-
+
PROBABILISTIC
VF - HIGH RISK
DH 01
DH 02
VOLUME FUNCTION
-
+
STOCHASTIC
SIS - UNCLEANED
DH 01
DH 02
VEIN
WASTE
STOCHASTIC
SIS - CLEANED
DH 01
DH 02
VEIN
WASTE

Figure 3-9: DD (left), VF (middle), and SPB (right) boundary models for the setting in Figure 3-6.

Boundaries can also be defined with the relatively fast VF method. The middle of Figures 3-9 and 3-10 show a volume function in grayscale for the mining and petroleum settings. Darker shades represent distances farther inside the vein or sand facies. Different bounding surfaces can be extracted from different iso-values of the volume function. An expanded high risk (top) and contracted low risk (bottom) boundary separating vein from waste and sand from shale are shown. The iso-value where each boundary is extracted is represented with a vertical bar on the volume function scale. The VF method allows the fast construction of multiple boundaries with a measure of global uncertainty and realistic geological features.

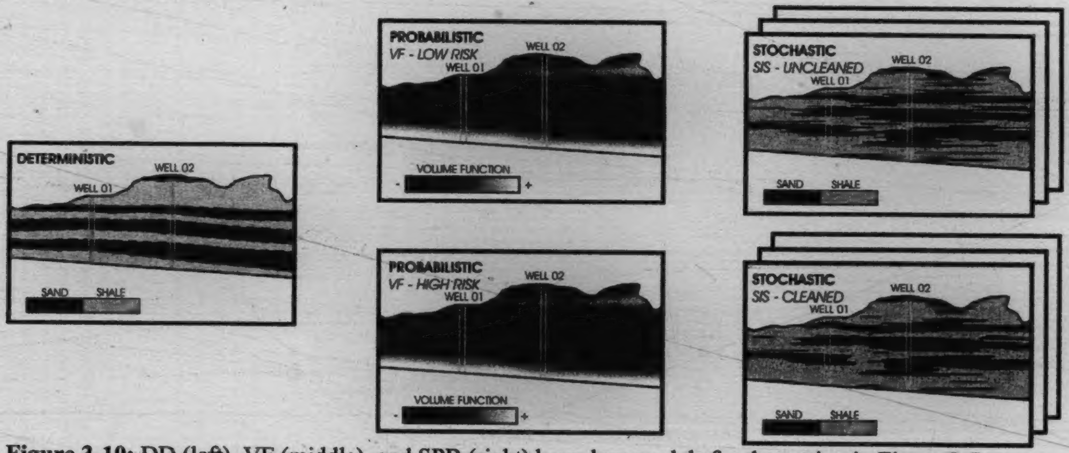
DETERMINISTIC
WELL 01
WELL 02
SAND
SHALE
PROBABILISTIC
VF - LOW RISK
WELL 01
WELL 02
VOLUME FUNCTION
-
+
PROBABILISTIC
VF - HIGH RISK
WELL 01
WELL 02
VOLUME FUNCTION
-
+
STOCHASTIC
SIS - UNCLEANED
WELL 01
WELL 02
SAND
SHALE
STOCHASTIC
SIS - CLEANED
WELL 01
WELL 02
SAND
SHALE

Figure 3-10: DD (left), VF (middle), and SPB (right) boundary models for the setting in Figure 3-7.

3.3.3 Reasonableness

Modeling uncertain domain boundaries that describe the spatial jurisdiction of separate SRFs throughout the numerical model is the second of five geostatistical modeling steps performed to making a decision of stationarity. There are some practical challenges to overcome for making a reasonable boundary modeling algorithm choice.

Inference Challenges

Six main challenges associated to choosing an appropriate boundary modeling algorithm are addressed in this dissertation:

1. *Simplicity*: The algorithm should be relatively straightforward to implement;
2. *Speed*: The algorithm should be capable of creating multiple possible boundary models in a reasonable amount of time;
3. *Objectivity*: The algorithm should avoid subjectivity in order to be repeatable;
4. *Data Integration*: The algorithm should be flexible and amenable to incorporate incremental geological information;
5. *Access to Uncertainty*: The algorithm should allow access to uncertainty; and
6. *Geologically Realistic*: The algorithm should be keyed to the geometrical nature of boundaries and create geologically realistic models.

The collective approach to these challenges is an important aspect of formulating and executing a credible decision of stationarity.

The most important challenges are the last two: access to global boundary uncertainty via multiple geologically realistic boundary model realizations. Neither fully deterministic nor fully stochastic methods are capable of overcoming both. DD methods sacrifice uncertainty quantification for realistic geology while SPB methods sacrifice realistic geology for uncertainty quantification. VF methods provide a potential alternative.

Reasonability Criteria

A reasonable boundary model and algorithm is evaluated on the basis of overcoming the six inference challenges listed above. As Figure 3-8 shows, there several approaches varying in their balance of determinism and stochasticity are available for addressing these challenges.

The reasonableness of different boundary models and boundary modeling methods will be evaluated with a yes/no type report card. An empty report card example is shown in Table 3-1. Both the description and evaluation of several specific boundary modeling methods will be given in Chapter 4. Emphasis is given to a new probabilistic approach using volume functions.

	Boundary Modeling: Evaluation Criteria					
Boundary Modeling Approach	Simplistic?	Fast?	Objective?	Data Integration?	Access to Uncertainty?	Geologically Realistic?
	•	•	•	•	•	•
	•	•	•	•	•	•
	•	•	•	•	•	•

Table 3-1: Empty report card for evaluating different boundary modeling algorithms.

3.4 Nature of Boundaries

Another model operation imposed on geostatistical modeling for a suitable decision of stationarity is recognizing and quantifying the nature of petrophysical properties across geological boundaries. A model describing these transitions is often needed to ensure the final numerical model contains geologically realistic petrophysical property transitions across boundaries. A more detailed treatment of this topic is given in Chapter 5.

3.4.1 Context

Conventional geostatistical prediction techniques populate petrophysical properties inside distinct geological domains enclosed by modeled boundaries. The predictions within each domain are derived from separate SRF models parameterized by the data available within the corresponding domain. The resulting numerical models built by pasting together these different predicted domains are not geologically realistic when smoother transitions are obvious from geological interpretations and/or sample data. The solution to this problem should not involve an amendment to the choice of separate domain type SRFs; this will damage the consistency of geological homogeneity with the assumptions of stationarity. A better solution is to quantify the influence of different SRFs near domain boundaries in order to reproduce geologically realistic transitions.

An example copper porphyry mining deposit is used to illustrate the need to quantify the transitional nature of geological boundaries. Copper porphyries usually initiate from a significant igneous granitic porphyry intrusion in a volcanically active region. Ascending hydrothermal hot water solutions circulate around the solidifying magmatic intrusion disseminating low grade primary copper sulphide mineralization. High grade secondary or supergene enriched copper oxide mineralization occurs when descending oxidized water leaches and reconcentrates copper minerals capping the primary zones along thin bands below the water table [9]. In general, copper grades increase from zero within the leached zone, continue to increase to a maximum and decrease within the secondary oxide zone, and then remain constantly low within the primary sulphide zone. However, the nature or spatial distribution of copper grades near the geological boundaries separating these distinct zones can be quite different.

Figure 3-11 shows representative copper grade profiles (in units of %Cu by weight) from two different copper porphyry deposits each with leached, oxide, and sulphide geological domain type intervals identified. The profile on the left indicates copper grades smoothly transition from leached to oxide and from oxide to sulphide zones; the nature of these boundaries are generally referred to as *soft*. The profile on the right indicates copper grades abruptly transition from leached to oxide and from oxide to sulphide zones; the nature of these types of boundaries are generally referred to as *hard*. The hard or soft nature of transitions across geological boundaries must be reproduced in any geologically realistic numerical model.

3.4.2 Modeling Approaches

The techniques for modeling the nature of boundaries can be classified into two general categories. The first category is referred to as implicit corresponding to the conventional method of pasting together domains predicted from separate SRFs and conditioning data sets. The resulting abrupt transitions across boundaries are realistic only when the nature of boundaries can be generalized as hard. For soft boundaries, however, a near-boundary model describing how separate SRF parameters interact is needed to build in realistic geological transitions explicitly.

The choice between implicit and explicit approaches to modeling transitions across a particular boundary is based on whether the boundary can be classified as hard or soft. The exact definition of hard and soft as well as a group of techniques collectively referred to as *contact analysis* used to quantify hard and soft natured boundaries are presented in Chapter 5.

An explicit approach to modeling soft boundary transitions and the implicit approach to modeling hard boundary transitions are both followed. Figures 3-12 and 3-13 show the copper grade profiles from Figure 3-11 positioned at the center of a small 2D portion of the full aerial accumulation, 275 x 120m for the soft boundary scenario (Figure 3-12) and 225 x 120m for the hard boundary scenario (Figure 3-13). A boundary model is shown with dark horizontal lines separating oxide from upper leached and lower sulphide ores. For both the explicit and implicit methods, three geostatistical realizations are simulated over the full 225 x 120m or 275 x 120m area assuming a single SRF for each of the three leached, oxide, and sulphide ores; each SRF is parameterized by separate first order mean and second order variogram/covariance moments inferred from the data exclusive to the corresponding domains. The predictions from separate SRFs are then merged with the boundary model to construct the full numerical model results in Figures 3-12 and 3-13. Explicit and implicit methods differ in the way separate SRF predictions are merged.

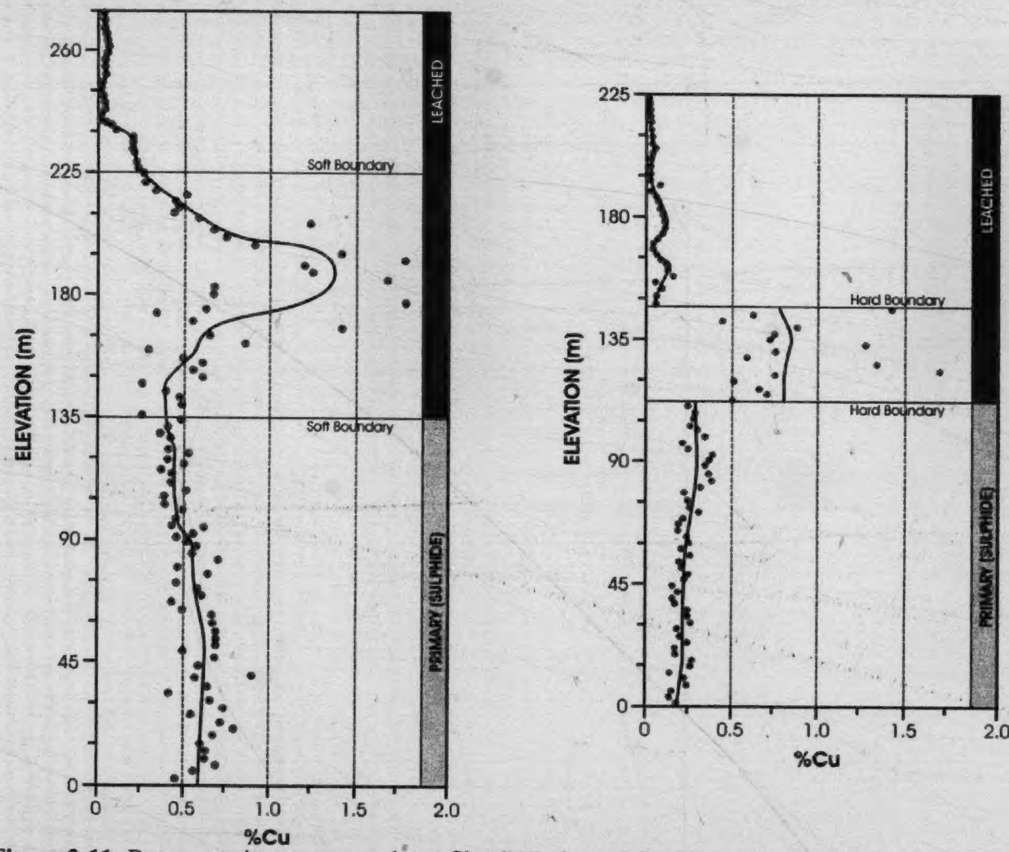

Figure 3-11: Representative copper grade profiles (%Cu by weight) illustrating soft (left) and hard (right) natured geological boundaries within two different copper porphyry deposits.

Figure 3-12 illustrates the explicit results. The two LMMs shown at the leached-oxide and sulphide-oxide soft boundaries are used to weight predictions from different SRFs. Consider, for example, the leached SRF. Zero weight is given to these predictions within the full 0 to 135m sulphide ore interval and the 135m to 205m portion of the oxide ore interval; at locations within oxide ore but within 20m of the leached-oxide boundary, the weight increases linearly from zero at 20m outside leached ore to one at 20m inside leached ore; the weight is then one for the remaining higher leached ore elevations. The resulting copper grade transitions are geologically consistent with soft boundaries.

The implicit results are shown in Figure 3-13. For predictions within a particular ore domain, the implicit approach corresponds to a particular LMM in which full weight is given to predictions coming from the corresponding enclosed SRF and no weight is given to predictions from surrounding SRFs. The resulting copper grade transitions are hard.

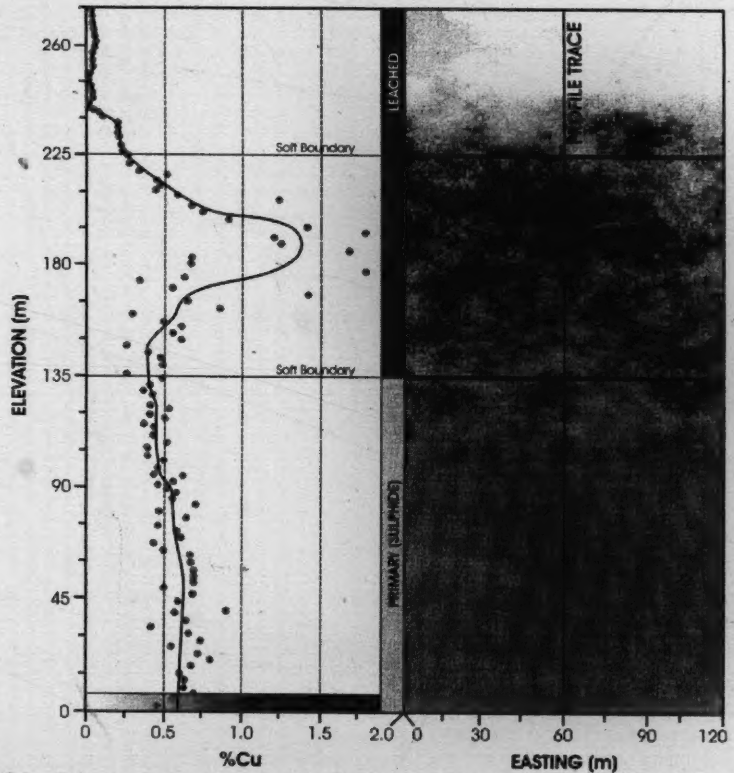

Figure 3-12: Soft boundary copper grade profile (left) and simulation model (right) using an explicit LMM approach. A separate LMM is used at each of the two soft boundaries.

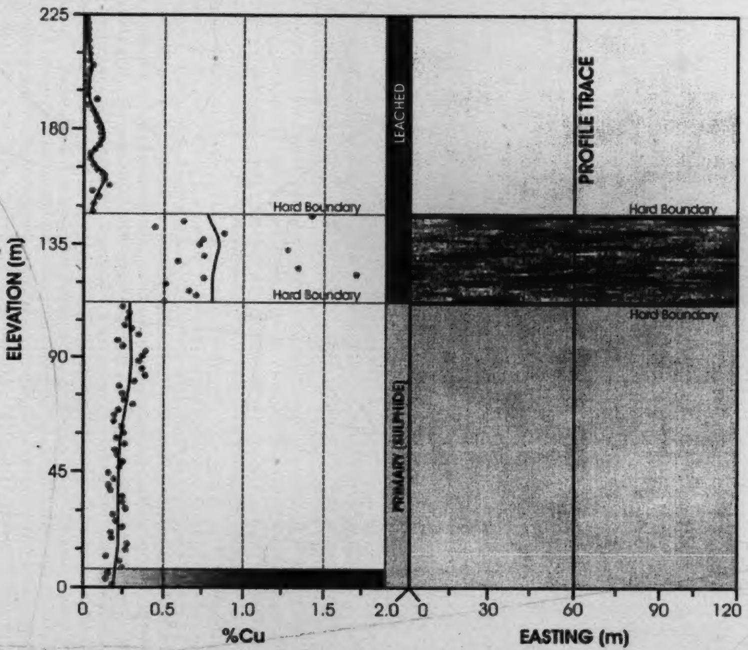

Figure 3-13: Hard boundary grade profile (left) and simulation model (right) using the implicit method.

3.4.3 Reasonableness

Decisions of stationarity are more reasonable when the character of petrophysical property transitions across geological boundaries is identified and reproduced accurately.

Inference Challenges

There is no direct control on the transition of petrophysical properties across the domain boundaries when choosing domain types or modeling the domain boundaries. Generating geologically realistic transitions with the most straightforward procedure possible can be challenging.

Reasonability Criteria

Credibility of the decision of stationarity depends on realistic depictions of petrophysical property transitions across domain boundaries. The best technique for identifying and reproducing the nature of boundaries is as geologically realistic and simple as possible. The implicit approach is the simplest, but appropriate only for hard boundaries. Explicit models are used for soft boundaries; alternative models such as the LMM, global LMC, or locally varying LMC are evaluated on the basis of simplicity and geological reality.

3.5 Trend Modeling

Another major model operation imposed on geostatistical modeling for a reasonable decision of stationarity is trend modeling. Trend models capture any unresolved large-scale variability that boundary modeling can not. A more detailed treatment of this topic is given in Chapter 6.

3.5.1 Context

There is definitely a geological context for the presence of large-scale deterministic trend models; however, there is also a theoretical one.

Theoretical Context

Geostatistical estimation is synonymous with kriging; and the foundation of more modern geostatistical simulation is kriging. Kriging is unquestionably an essential algorithm for standard geostatistical prediction. Derivation of the kriging equations requires a trend model. Recall in relation (2-34) the kriging estimator at an unknown $\mathbf{u}_0$ appears as the result of linear estimation of the residual value at the unsampled location $r^*(\mathbf{u}_0)$ from n surrounding residual data $r(\mathbf{u}_s)$. This interpretation is true for all varieties of kriging and requires additively decomposing $Z(\mathbf{u})$ as in relation (2-9). Therefore, a trend model $m(\mathbf{u})$ is needed at all sampled and unsampled locations within the domain to implement usual geostatistical estimation or simulation.

The mathematical first order assumption of a stationary mean assumes the trend model is a constant m value with no spatial variability. However, this assumption may not contain sufficient variability to reproduce large-scale deterministic geological variability in the final numerical model. In these cases, a locally varying mean or trend model must be incorporated into the prediction algorithm explicitly.

Geological Context

The additive decomposition of $Z(\mathbf{u})$ is convenient in that although it is required for kriging theoretically, it also has a rational geological interpretation. The trend is often referred to as the locally varying mean or the $m(\mathbf{u})$ component in (2-9) which can explain the deterministic nature of petrophysical properties due to clearly understood geological processes; the residual component $R(\mathbf{u})$ is then intended to explain the leftover chaotic nature of these processes. Although it is never fully correct and there may be more accurate approaches, geological phenomenon are assumed to conform to the additive division of smooth and erratic variability in (2-9) so that geostatistical prediction can be performed.

An example is presented to illustrate the geological context of a trend. Figure 3-14 shows a photograph of a corehole extracted from a 20m elevation interval within the Athabasca Oil Sands in Alberta, Canada. The darker shades indicate higher oil saturation within higher porosity sand facies; the lighter shades indicate lower oil saturation within lower porosity shale facies. The corresponding porosity profile is shown to the right of the core photo. A fining upward trend is clearly visible due to a transition of depositional environments from transgressive packages of fluvial to estuary sand facies dominating lower elevations to regressive packages of fine grained marine shale facies dominating higher elevations.

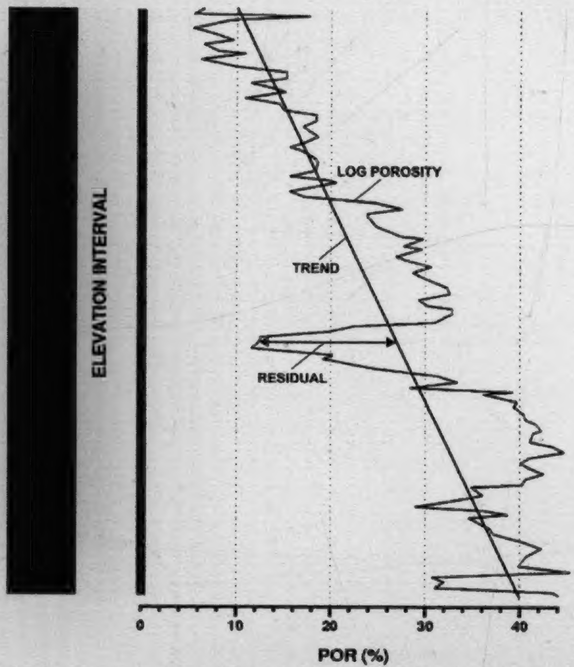

Figure 3-14: A corehole photograph from the Athabasca Oil Sands, Alberta, Canada (left) and related fining upward log porosity profile (right) with additive trend and residual components indicated.

The additive decomposition in (2-9) is also indicated in Figure 3-14. The trend $m(\mathbf{u})$ line represents a locally varying deterministic expectation in porosity; the leftover variability is represented by the stochastic residual $R(\mathbf{u})$.

3.5.2 Modeling Approaches

There are alternative algorithms available for building trend models. These alternatives are explored in this section with a continuation of the example shown in Figure 3-14.

The techniques for building trend models can be classified into two general categories. The first category is manual techniques including hand contouring and digitization. The second category is automatic techniques including moving window averages, inverse distance schemes, and kriging. The classic application of inverse distance and kriging for modeling the trend is very different than for classic estimation. Large search routines and smooth spatial correlation (low inverse distance powers and continuous long range variograms) must be used to ensure the trend does not represent too much variability and is consistent with geological interpretations.

Ten samples are extracted from the full porosity profile shown in Figure 3-14. Figure 3-15 shows the location of these samples (bullets) with manual (left) and automatic (right) trend models. No samples are available at elevations below the level indicated with the horizontal bar in order to represent regions of limited sampling typically encountered in practice. Nonetheless, the deterministic expectation of a fining upward porosity profile as shown in Figure 3-14 is still available and well understood from a reliable geological investigation of the area surrounding the corehole. The broken line in Figure 3-15 shows this trend; it is taken as a reference hereafter since it is interpreted from the entire profile of porosity values as well as reliable deterministic geological information.

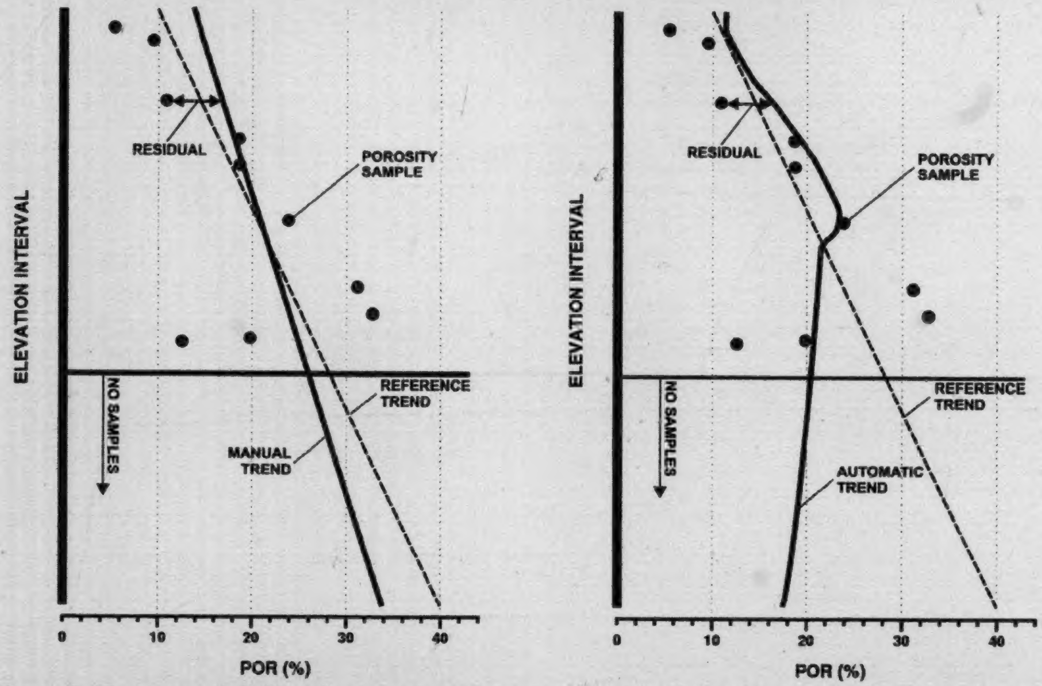

Figure 3-15: A manual (left) and automatic (right) trend model built from the ten available sample data (shaded bullets). The interpreted trend using all the available sample data and a high level geological understanding is represented by the broken line.

The manual trend model is easily adapted to the geological interpretation regardless of limited data. The manual trend also does not over-interpret the geological understanding by representing additional variability past what is deterministically discernable. However, special effort is required to adapt an automated method to the geological interpretation. For this example, simple kriging with a global search, 40% nugget effect, and long range variogram is used to ensure the trend model is as smooth as possible. Although smooth, the automated results are inconsistent with the reference trend. This contradiction is more pronounced at locations where no sample data are present. Actually, below the elevations where no sample data are available, the automatically built trend shows an opposite fining downward expectation. This is due to an increasing weight being assigned to the stationary expected vale. This is a common problem with automated methods. In general, automated methods are used only when the resulting trend models are consistent with basic geological interpretations.

It is the recommendation of this author to construct a valid trend model in all cases; even when the trend model will not be used explicitly for prediction. This is to ensure that large-scale deterministic geological features in the trend are reasonably captured in the final numerical model.

3.5.3 Reasonableness

Modeling trends improves the assumption of stationarity by handling any outstanding determinism not addressed by domain types and boundary models. However, there are some important inference challenges to overcome to generate an appropriate trend model.

Inference Challenges

Four main challenges face inference of a trend:

1. *Simplicity*: Choosing the parameters and implementing a trend modeling algorithm should be relatively straightforward;
2. *Subjectivity*: The trend modeling algorithm should emphasize subjective geological interpretations, but also be repeatable;
3. *Variability*: The trend model should not represent any more variability than what is not known with high certainty; and
4. *Geologically Realistic*: The trend model should portray key deterministic geological features and be consistent with the underlying genesis.

The collective approach to all these challenges is an important aspect of formulating and executing a decision of stationarity.

The most important challenges are the last two: ensuring the trend model is geologically realistic and does not represent too much variability. Manual trend modeling is well suited for this guideline; however, automated methods need to be tailored towards this.

Reasonability Criteria

Choosing a reasonable trend model and construction algorithm is evaluated on the basis of overcoming the four inference challenges listed above. The reasonability of different trend modeling methods is evaluated with a yes/no report card. An empty report card is shown in Table 3-2. Both the description and evaluation of several specific trend modeling methods will be given in Chapter 6.

	Trend Modeling: Evaluation Criteria			
Trend Modeling Approach	**Simplistic?**	**Subjective?**	**Low Variability?**	**Geologically Realistic?**
•	•	•	•	•
•	•	•	•	•
•	•	•	•	•

Table 3-2: Empty report card for evaluating different trend models and trend modeling algorithms.

3.6 Prediction with the Trend Model

The decision of stationarity must consider trends. The use of a trend model in prediction ensures the final numerical model contains important large-scale geological features. A more detailed treatment of this topic is given in Chapter 7.

3.6.1 Context

Regardless of how many SRFs and domains are chosen to model a regionalized variable, it is almost always possible to detect large-scale deterministic trends within each separate domain. Numerical models of geological heterogeneity must reflect these deterministic trends. The context and motivation for predicting with a trend model is ensuring trends are reproduced in the final numerical model.

3.6.2 Modeling Approaches

Methodologies used to account for the trend are classified as implicit or explicit. Implicit methods do not explicitly use a previously built trend model except for validating large-scale geological features in the numerical models built with conventional geostatistical methods. Explicit approaches are modified geostatistical algorithms to integrate and honor the trend by construction.

A trend model is always needed, but may or may not be used directly. The most common use of a trend model is verifying large-scale deterministic geological features are honored with standard prediction techniques; in this way, the trend is honored implicitly. When there is insufficient conditioning information, however, conventional methods must be adapted to incorporate the trend model exactly; here, the trend is honored explicitly. Therefore, whether it is used implicitly for checking or explicitly for prediction, a model of the trend is always needed to build geologically realistic numerical models.

The implicit and explicit approaches to geostatistical estimation with the trend model are implemented using the manual trend model from Figure 3-15. The implicit approach is illustrated in Figure 3-16. Simple kriging is used for estimation. A range of 40% of the elevation interval and 5% nugget effect are used. The resulting numerical model fails to reproduce both the reference and manual trend models. The discrepancies are spread throughout the entire elevation interval, but are increasingly severe where limited data are available. Below a certain elevation, for example, sample data are beyond the range of correlation and the SRF mean parameter of 18.35% porosity is exactly estimated.

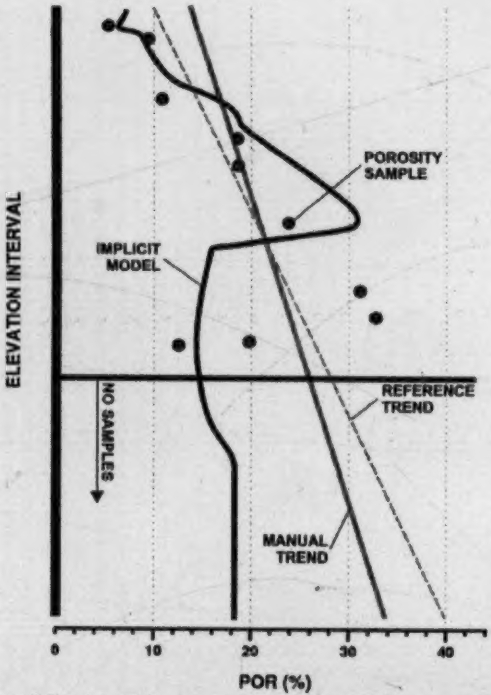

Figure 3-16: An illustration of the implicit approach to account for the trend in estimation. The kriging model (dark curve), manual trend (shaded solid line), and reference trend (dark broken line) are all shown.

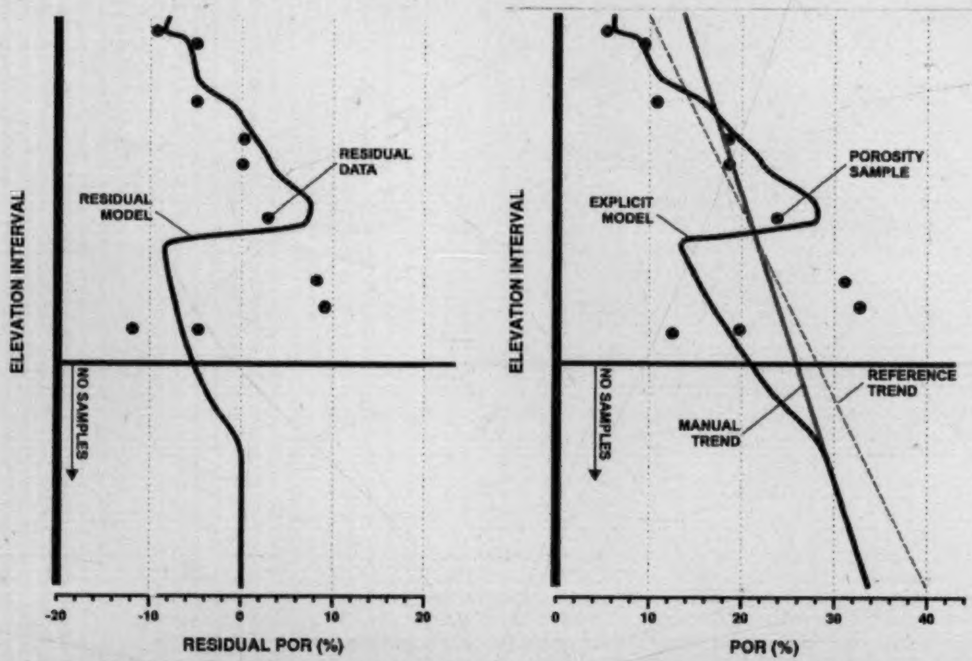

Figure 3-17: An illustration of the explicit approach to account for the trend in estimation. The residual data (shaded bullets) and kriged residual model are shown on the left. The final explicit model with the residuals added back to the manual trend (shaded solid line) is shown on the right.

An explicit approach is needed to capture a reasonable trend model in prediction models. Instead of kriging the original data, the residual data are kriged. The residual data and kriged residual model are shown in Figure 3-17 (left). The kriged residual model is then added to the manual trend model to generate the final explicit numerical model (right). Here, the trend is satisfactorily reproduced by construction.

3.6.3 Reasonableness

The fifth and last aspect of the decision of stationarity is predicting with the trend model. A number of challenges must be overcome.

Inference Challenges

Five key challenges facing inference with a trend are addressed in this dissertation:

1. *Simplicity*: The methodology used to incorporate the trend model into geostatistical estimation or simulation should be relatively straightforward;
2. *Spatial Law Inference*: Inference of the spatial law of the variable being predicted should be possible and straightforward;
3. *Accurate and Precise Uncertainty*: The resulting numerical models should represent accurate and precise local distributions of uncertainty [6];
4. *Reproduction of Bivariate Residual Distribution:* The bivariate distribution between the $R(\mathbf{u})$ RF and both the trend and original $Z(\mathbf{u})$ RF should be reproduced; and
5. *Geologically Realistic*: The resulting models should satisfactorily reproduce key deterministic geological features in the trend model.

The collective approach to all these challenges is an important aspect of formulating and executing a decision of stationarity.

The most important of these challenges is making certain the resulting numerical models reproduce the key large-scale geological features in the trend model. An explicit account for the trend is not needed when the assumption of a stationarity mean is enough to reproduce the trend implicitly; however, there are times when the trend model needs to be explicitly integrated into the prediction algorithm so that it is honored by construction.

Reasonability Criteria

Choosing a reasonable prediction algorithm is evaluated on the basis of overcoming the four inference challenges listed above. The reasonability of different algorithms to predict with the trend model is evaluated with a yes/no report card. An empty report card is shown in Table 3-3. Both the description and evaluation of several specific algorithms will be given in Chapter 7.

	Prediction with the Trend Model: Evaluation Criteria				
Prediction with the Trend Model	**Simplistic?**	**Spatial Law Inference?**	**Accurate/Precise Uncertainty?**	**Reproduction of Bivariate $R(\mathbf{u})$ Distributions**	**Geologically Realistic?**
[illegible]	•	•	•	•	•
[illegible]	•	•	•	•	•
[illegible]	•	•	•	•	•

Table 3-3: Empty report card for evaluating different approaches to accounting for the trend in prediction.

3.7 Remarks

A decision of stationarity involves five main modeling steps: (1) choosing domain types for separate SRFs, (2) modeling the domain boundaries, (3) quantifying the influence of SRFs across domain boundaries, (4) quantifying trends within the domains, and (5) predicting with the trends. The collective approach to all five steps encompasses the decision of stationarity.

Up until now, there was no structured approach available to make a reasonable decision of stationarity; this decision is often based solely on choosing domain types for separate SRFs. The comprehensive five step framework of geostatistical modeling phases, each with its own context, modeling approaches, and reasonability criteria, provide a source for making a suitable decision of stationarity. This is new to the practice of geostatistics.

Decisions of stationarity are routinely debated by practitioners on the basis of subjective geological conditions. The structure for decisions of stationarity presented in this chapter acknowledges this criterion by including realistic geological consistency as a minimum standard for reasonable modeling approaches, but also offers additional more objective criteria. Therefore, although the decision of stationarity can still never be tested or refuted in a theoretically precise manner, the decision can certainly be deemed unreasonable.

A separate decision of stationarity is made for each ReV of interest. The approach to the five consequences of a decision of stationarity identified in Figure 3-1 can be different for different ReVs. For example, within a layered reservoir, a single SRF may be suitable for modeling water saturation whereas porosity and permeability SRFs may be more suitable when applied on a by-layer or by-facies basis.

Stationarity is not a geological property; stationarity encompasses the first and second order mathematical properties of a RF needed to be a SRF. It is incorrect then to refer to a resource accumulation or geological compartment thereof as stationary. It is in fact the corresponding SRF and its first and second order moments that can be correctly referred to as stationary.

CHAPTER 4

BOUNDARY MODELING

A boundary model is needed when the full accumulation limits are divided into separate geological units consistent with SRFs. The utility of the boundary model is to identify the spatial jurisdiction of SRFs and the inherent uncertainty in the structural framework of the deposit or reservoir.

There is a variety of modeling approaches available to build bounding surfaces ranging from deterministic techniques to more probabilistic techniques. These techniques are reviewed and evaluated according to the criteria identified in Chapter 3. Choosing a boundary modeling method depends on the geometric character of the boundaries and the amount and type of available geological information. These dependencies are developed and discussed.

A volume function technique is developed, described, and implemented. This technique is linked to global uncertainty characterization.

4.1 Boundary Modeling Principles

The construction of a reasonable boundary model is an essential aspect of making the best possible decision of stationarity. Chapter 3 identified six main criteria used for evaluating the reasonableness of different boundary modeling approaches: (1) simplicity, (2) speed, (3) objectivity, (4) data integration ability, (5) access to uncertainty, and (6) geologically realistic. Before reviewing and evaluating alternative boundary modeling techniques, these evaluation criteria are briefly discussed.

The boundary modeling algorithm formulation, description, and implementation should be relatively straightforward. Too complex algorithms will be difficult to implement, explain, and justify in practical settings. More popular boundary modeling algorithms are generally more straightforward.

The algorithm should be capable of creating multiple realizations in a reasonable amount of time. Practically, it is generally inappropriate to spend more than one day generating a boundary model in the exploration phase of a natural resource venture. Algorithm speed should also be relatively independent from the geological complexity.

The boundary modeling algorithm should be repeatable by any professional geologist or engineer given the exact same input conditioning information.

Exploration drilling is often performed in campaigns. There is a need to quickly update the boundary model in the advent of new geological information. The boundary modeling algorithm should be readily amenable to incorporate incremental geological information.

An important criterion for boundary modeling methods is access to structural uncertainty. Boundary surface uncertainty can be a major source of exploration and production uncertainty needed to make informed planning decisions.

The uncertainty should be modeled by geologically realistic boundaries. Geologically realistic models are built from algorithms that are tailored to the geometrical nature of boundaries as well as the amount and type of conditioning data available.

4.2 Boundary Modeling Approaches

Deterministic digitization (DD), volume function (VF), object-based (OB), surface-based (SB), and stochastic pixel-based (SPB) algorithms were all indicated in Chapter 3. These boundary modeling techniques are now described and evaluated for reasonableness.

4.2.1 Deterministic Digitization (DD)

The traditional approach to modeling geological boundaries is through a 3D triangulation of polygons representing the solid body on a discrete series of offset cross sections. The cross sections are then joined by tie lines to guide the connectivity of a 3D triangulation of the solid boundary [13]. The procedure is referred to as an explicit model of the solid since the bounding surface is defined unequivocally by the 3D coordinates positioning the patchwork of triangles. The DD approach is implemented in most general mine planning packages (GMPs) such as GEMS [14] and VULCAN [15].

Reasonableness

The DD boundary modeling approach is simple to apply and is capable of generating realistic boundaries; however, there are a number of important limitations. These include high professional time, subjectivity, inflexibility, and inaccessible uncertainty. Detailed comments organized by reasonableness criteria follow:

1. *Simplicity*: DD techniques of digitizing offset polygons and tying them together by way of triangulation is simple, owing to the highly visual nature of this method;
2. *Speed*: Drawing 2D polygons and tie lines demands an often overwhelming amount of time in many practical geological settings;
3. *Objectivity*: The resulting boundaries are the result of a prolonged series of small subjective decisions specifying where the volumetric surface exists; although this may generate a geologically realistic model, a non-repeatable signature of the interpreter is inevitably imparted to the boundary surface;
4. *Data Integration*: It is difficult to update a DD boundary model with new corehole information – modifications are often undertaken in costly campaigns;

5. *Access to Uncertainty*: No direct measure of uncertainty is possible; only a rough measure is possible when there is enough professional time and resources to create multiple DD models;
6. *Geologically Realistic*: Since the interpreter has direct control on the digitization procedure, DD type boundaries are usually geologically realistic.

4.2.2 Volume Function (VF)

VF techniques represent boundary surfaces indirectly with a volume function model. *Leapfrog* is the only commercial implementation of the volume function method at the time of writing this dissertation [16, 17, 18]. This technique is reviewed here.

There are four major steps to the Leapfrog implementation of the VF approach: (1) data preparation, (2) radial basis function (RBF) interpolation, (3) geological interpretation, (4) morphological interpolation, and (5) morphologically constrained interpolation [17]. At least the first two phases are required. The result is a smooth volume function within which a constant valued surface representation of the desired boundary exists and can be extracted at any desired resolution [18].

Reasonableness

The Leapfrog approach is straightforward, fast, objective, flexible, and realistic; however, current applications do not allow direct access to uncertainty. Some additional comments:

1. *Simplicity*: Coding data to the volume function and subsequent smooth interpolation of these codes is straightforward;
2. *Speed*: Interpolation is fast on the order of hours using a VF approach;
3. *Objectivity*: The choice of interpolation method and parameters may be subjective, but the volume function will be identical for the same data and interpolation setup;
4. *Data Integration*: Additional conditioning data can be included easily;
5. *Access to Uncertainty*: Boundary uncertainty is only accessible subjectively through different morphological interpretations;
6. *Geologically Realistic*: Although there is more direct control with DD methods, realistic boundaries can still be generated in various settings.

The VF approach is simple, flexible, and can easily be fully automated to construct geologically realistic boundary models quickly and objectively. However, there is no direct access to global uncertainty.

4.2.3 Object-Based (OB)

DD and VF methods do not account for uncertainty in geological boundaries. Stochastic models are needed for this purpose. The first boundary modeling algorithm with stochastic functionality explored in this thesis is object-based approaches.

OB modeling algorithms are formulated for reservoirs of fluvial origin. Fluvial sediments are deposited along sinuous sand-filled channels. Plan and section view illustrations of some key architectural elements of a fluvial system are shown in [19].

In 1979, Bridge and Leeder [20] presented a process-based computer model to simulate multiple equally possible fluvial stratigraphic realizations. The program calculates a set of fluvial flood plain surface geometries based on various interdependent channel sand deposition processes. Stochasticity is introduced by randomizing some key geometric parameters. This original approach was the beginning of a series of process-based and OB modeling algorithm advance. The work of Haldorsen and others [21, 22] popularized the implementation to practical settings in the mid 1980s.

OB modeling currently refers to direct location of spatial geological bodies (geobodies) and is differentiated from process-based models referring to the placement of geobodies in space according to time-dependant processes [23]. The term OB, however, is often used interchangeably with process-based. Deutsch and Wang [24] created a fully OB algorithm involving a hierarchical progression of geometric coordinate transformations in 1996; a move towards process-based modeling was made in 2002 by Deutsch and Tran [25]; in 2004, Pyrcz and Deutsch [26] developed a process-based modeling algorithm using streamline events. Stochasticity is added to both process-based and OB models by randomizing geobody geometric parameters.

Conditioning hard and soft geological data is a common challenge facing OB models. Three possibilities exist: (1) constraining the evolution process and erodibility schedule [27], (2) kriging for conditioning [28], and (3) direct fitting of geometries to the data [29, 30]. Current OB technology is focused at conditioning of hard and soft geological data.

Reasonableness

OB methods are capable of generating realistic and probabilistic boundary realizations with relatively simple and fast algorithms; however, conditioning to well data remains a significant challenge. Detailed comments organized by reasonableness criteria follow:

1. *Simplicity*: The parameterization of governing fluvial geometries and processes can be made as straightforward or as complex as desired;
2. *Speed*: Object placement with multiple geometric parameter set realizations is relatively fast;
3. *Objectivity*: The choice of both object types and processes is subjective, but non-repeatable by different individuals;
4. *Data Integration*: Conditioning can be difficult in some settings in which case incorporating incremental hard and/or soft data would also be difficult;
5. *Access to Uncertainty*: Uncertainty is accessible by way of randomly drawing a set of geometric geobody parameters per object and per realization;
6. *Geologically Realistic*: The types of objects and processes chosen are aimed to be geologically realistic for the particular model setting.

4.2.4 Surface-Based (SB)

The second boundary modeling approach with stochastic functionality explored in this thesis is SB algorithms. These methods are relatively new, yet there are some well developed techniques available.

For several years, fluvial deposits have been the primary focus for petroleum research, development, and implementation of OB modeling. Lately, significant petroleum exploration energy is being focused on submarine turbidite systems [31]. There has been an effort to adapt fluvial OB methods to the submarine environment [32]; however, these variations do not mimic all turbidite processes. A new SB approach is proposed as a supplement for compensational stacking regimes in the more distal portion of turbidites. [33].

Large-scale stochastic surface modeling began in 1999 by Xie [34] based on a simulated annealing algorithm; this methodology was later refined into a streamline-based approach by Pyrcz in 2004 [35]; and then modified again by Zhang and Pyrcz in 2006 [36] to be capable of reproducing a hierarchy of stacked composite facies proportion trends. The large-scale algorithm was adapted to intermediate-scale SB model of the Cengio turbidite system and integrated into a geostatistical study in 2005 [33]. Stochasticity is added to these models by randomizing surface geometry parameters.

Small-scale stochastic surface modeling has also received some attention. SBED software [37], for example, has utilities for a wide variety of bedding and stacked bedding template patterns for smaller scale SB modeling.

Reasonableness

SB techniques can be applied in a simple, fast, objective, and flexible manner and are capable of assessing uncertainty with realistic boundary surface heterogeneity. Detailed comments organized by reasonableness criteria follow:

1. *Simplicity*: The parameterization of surface geometries and processes can be made as straightforward or as complex as desired;
2. *Speed*: Interpolation between data is fast;
3. *Objectivity*: Surface geometry can either be directly chosen and added as a constraint during interpolation or left unknown and objectively modeled;
4. *Data Integration*: The integration of a wide variety of soft and hard conditioning data into the algorithms is relatively straightforward;
5. *Access to Uncertainty*: Uncertainty is accessible by way of randomly drawing a set of geometric surface parameters per realization;
6. *Geologically Realistic*: When chosen, the geometry of surfaces are aimed to be geologically realistic for the particular model setting.

4.2.5 Stochastic Pixel-Based (SPB)

When clear geological objects or surface types and complimentary geological processes exist, OB and SB techniques are applied. However, lacking clear deterministic geological understanding, SPB methods are more appropriate.

The truncated Gaussian method was established in 1984 by Chiles [38] and Isaaks [39] and by Matheron in 1987 [40] to truncate a single Gaussian RF by experimentally determined facies proportions. Recognizing the facies associations and spatial correlation limitations of the truncated Gaussian method, Le Loch and Galli in 1996 formalized the truncated pluri-Gaussian method that uses multiple Gaussian RFs [41]. Sequential indicator simulation of indicator RFs, currently the most popular SPB method, was introduced in 1990 [42] and first implemented in 1993 by Journel and Gomez-Hernandez [43] on the Wilmington Clastic Sequence. Truncated Gaussian, truncated pluri-Gaussian, and sequential indicator simulation techniques are capable of constructing heterogeneity represented by only a two-point statistical semivariogram model. Multiple point statistics simulation, first proposed by Guardiano and Srivastiva [44] in 1993 and later developed by Strebelle and Journel [45] in 2000, is capable of reproducing multiple-point statistics from a training image.

Reasonableness

SPB techniques are simple, fast, repeatable, and flexible, but are generally unable to capture uncertainty with realistic geological heterogeneity. Some additional comments:

1. *Simplicity*: Histogram and spatial correlation inference are straightforward;
2. *Speed*: Interpolation and simulation is relatively fast;
3. *Objectivity*: The interpolation and simulation algorithms are repeatable;
4. *Data Integration*: The integration of a wide variety of soft and hard conditioning data into can be achieved easily;
5. *Access to Uncertainty*: Local uncertainty is characterized through the local conditional cumulative distribution functions (ccdfs) built with simple kriging;
6. *Geologically Realistic*: The results may not be geologically realistic in some settings due to the presence of isolated cells surrounded by a contrasting facies types.'

Many comments above do not apply to MPS. MPS techniques are more complex, slower, more subjective (due to the choice of training image), less flexible, and are capable of generating geologically realistic models.

4.2.6 Reasonableness Summary

The detailed comments made above are summarized into the report card in Table 4-1 organized by boundary modeling approach.

	Boundary Modeling: Evaluation Criteria					
Boundary Modeling Approach	**Simplistic?**	**Fast?**	**Objective?**	**Data Integration?**	**Access to Uncertainty?**	**Geologically Realistic?**
DD	yes	no	no	no	no	yes
VF	yes	yes	yes	yes	no	yes
OB	yes	yes	no	no	yes	yes
SB	yes	yes	yes	yes	yes	yes
SPB	yes	yes	yes	yes	yes	no

Table 4-1: Report card for evaluating the continuum of boundary modeling approaches in Figure 4-1.

For certain settings, OB and SB methods are capable of accessing geologically realistic uncertainty. But only SB approaches achieve this goal objectively and flexibly. DD and SPB approaches may not be easily modified to achieve this goal. The VF approach, however, can easily be customized to access uncertainty. This is the major focus of this chapter and one of the developments made in this dissertation.

Now the topic of choosing a particular boundary modeling approach is discussed. All the approaches can be parameterized straightforwardly. Relative to DD, all approaches are fast; but, out of these faster approaches, only OB and SB techniques are capable of quantifying structural uncertainty with geologically realistic realizations. Since the OB approach is subjective and inflexible and the SB approach is objective and flexible, the SB approach is logically the method of choice. However, depending on the geometrical nature of the boundaries and amount and type of available conditioning information, this is not necessarily the case.

4.3 Choosing a Boundary Modeling Technique

Reasonableness helps guide the decision as to which boundary modeling approach and technique is adopted for a particular setting. However, other than the six reasonableness criteria identified previously, two additional criteria are considered for this decision: (1) the boundary modeling approach chosen should be suitable for the geometrical nature of boundaries in the setting being considered, and (2) the amount and type of conditioning geological information available must be handled straightforwardly.

Consider a small example. An OB approach would be chosen over a SB approach in a fluvial setting with a well known channel sand complex dominating the reservoir. Yet, if numerous hard data are available and need to be honored, an OB method may not be appropriate. SB methods are also unsuitable. If uncertainty is required, a SPB approach may be applied. However, more realistic boundaries could be created with VF methods. Global uncertainty would be accessible with the work presented later in this chapter.

4.3.1 The Geometric Nature of Boundaries

The intention now is to present some different boundary types that the five boundary modeling approaches presented and described previously can be applied. Four general classifications are: (1) vein-type, (2) ellipsoidal, (3) process-based (fluvial/turbidite), and (4) layered. A schematic depiction of each of these geometries is shown in Figure 4-1.

The geometric nature of boundary surfaces is quite different in each of the geological settings depicted in Figure 4-1. And, certainly, no one boundary modeling approach is suitable for all possible geometrical varieties. The best boundary modeling approach is capable of generating boundary surfaces similar to the characteristic geometric features of the geological setting. Achieving this consistency depends on the modeling approach and on the amount and type of conditioning geological information available as well as professional judgment.

4.3.2 Conditioning Data

The geometric nature of boundaries and the amount of conditioning information are interdependent. The choice of a suitable boundary modeling approach, therefore, depends on the configuration and quality of conditioning information. The main concern is that geological complexity depends on sample data density. Less data imply less complex geometries. For example, when increasing conditioning data is available, the geometric complexity of the boundary will increase and DD techniques become too cumbersome to apply; VF, SB, or SPB are more appropriate approaches.

4.3.3 Geometric Capabilities and Required Geological Information

Both the ability of reproducing key geometric features from the geological setting and the dependability on the amount and type of conditioning geological information are now discussed for each of boundary modeling approaches separately.

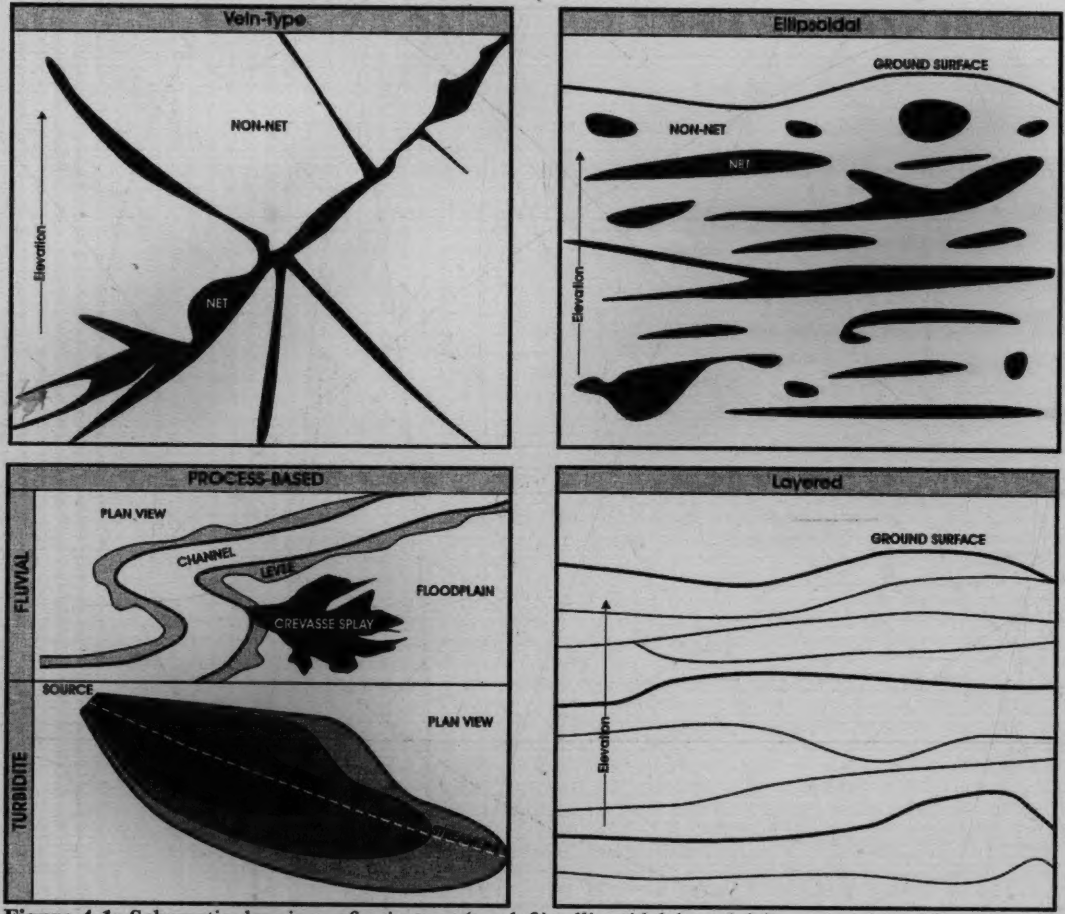
Vein-Type
NON-NET
NET
Elevation
Ellipsoidal
GROUND SURFACE
NON-NET
NET
Elevation
PROCESS-BASED
PLAN VIEW
CHANNEL
LEVEE
FLOODPLAIN
CREVASSE SPLAY
FLUVIAL
SOURCE
PLAN VIEW
TURBIDITE
Layered
GROUND SURFACE
Elevation

Figure 4-1: Schematic drawings of vein-type (top left), ellipsoidal (top right), process-based (bottom left) and layered (bottom right) boundary surface geometries.

Deterministic Digitization (DD)

The DD approach does not require large amounts of conditioning information to generate geometrically realistic boundary surfaces. In fact, digitizing boundaries becomes more difficult and time consuming as the amount of conditioning data increases. This is true for all varieties of geometries in Figure 4-1. An example is Figure 4-1 where boundary surfaces are easily drawn deterministically without any conditioning information.

Volume Function (VF)

With the exception of process-based geometries, the VF approach is capable of modeling any geometry in Figure 4-1; vein-type and ellipsoidal geometries are particularly well modeled. However, a relatively large amount of hard data control is required to condition the creation and interpolation of the volume function.

Object-Based (OB)

OB approaches are tailored to process-based geometrical boundaries and are generally inappropriate for modeling the other geometrical varieties in Figure 4-1. OB approaches do not require a large amount of hard conditioning data and often perform better with few hard data. Alternate techniques may be considered when hard data integration is a priority. The OB approach is more amenable to the integration of soft data.

Surface-Based (SB)

Layered boundary geometries are most reasonably modeled with SB approaches. The SB approach is also applicable for process-based boundary surface geometries, but currently only for turbidite processes in particular. Most of the conditioning geological information for layered geometries consists of structural rules; only a small amount of hard data is required.

Stochastic Pixel-Based (SPB)

The SPB approach is equally applicable to all varieties of boundary surface geometries in Figure 4-1. However, these techniques are best applied with a large amount of hard and soft conditioning geological information. Unrealistic boundary surface geometries can be generated in the presence of sparse data.

4.4 Volume Function Boundary Modeling with Global Uncertainty

VF boundary modeling was reviewed in the beginning of this chapter. Out of the six reasonability criteria used to evaluate boundary modeling approaches, only one was left unsatisfied: that of objectively capturing structural uncertainty with multiple possible geologically realistic boundary surfaces. This section describes the framework of the VF approach and then presents some simple modifications for quantifying global uncertainty.

4.4.1 The Volume Function Concept

The definition of a VF is attached to the notion of distance to an interface where the interface is defined as the surface separating two distinct domains within which different SRFs will subsequently be developed for geostatistical modeling. Distance is measured to the nearest interface. The bounding interface of interest is the surface corresponding to a particular iso-value of the VF.

Some Examples

Figure 4-2 shows four binary indicator models (left) and their corresponding VF (right) for four basic 2D geometries. The binary indicator models are analogous to a net (inside) / non-net (outside) rocktype model. From top to bottom in Figure 4-2, the boundary interface is a circle, square, plus (+) sign, and set of four small squares. The accumulation limits correspond to the same square outline in all four cases. The VF smoothly varies between increasingly negative values inside and further away from the boundary interface to increasingly positive values outside and further away from the boundary interface. The VF color scale ranges from black for highly negative values to white for highly positive values. Notice the boundary interfaces are where the VF value is zero.

VFs are used in practice to forecast the location of boundaries in between limited sample data. Figures 3-6 and 3-7 show a true binary geological model representative of a mining and petroleum setting using image analysis with separate digital photographs. A VF in each case was then constructed from two drillholes in the mining setting and two wells in the petroleum setting. Figure 4-3 shows the underlying geological model, the sample data locations, and the VF generated for both settings. The locations where the VF value is zero are predictions of the boundary interfaces.

VF Distance

A VF is essentially a *distance* function. Distance is measured to the nearest interface and increases with locations further away from an interface. Two important characteristics of this distance measure make its definition unique to VF applications. First, VF distance can be negative or positive depending on whether the location is inside or outside the solid; second, VF distance can be spatially correlated. Correlation of distance is a strange concept. These characteristics are now both addressed.

Although not necessary, a straightforward way of interpreting the boundary interface of interest is as the *zero-surface* of the VF, that is, the surface defined by all locations within the accumulation limits where the VF is valued at zero. This requires that the VF distance be either negative inside the boundary and positive outside the boundary or positive inside the boundary and negative outside the boundary. The former convention is taken in Figures 4-2 and 4-3 and in the remainder of this dissertation. Therefore, although the term *distance* is used, the sign is modified for VF distance.

Anisotropy introduces another complicating feature of VF distance. Realistic boundary geometries are not isotropic. The schematic boundaries in Figure 4-1, for example, all show different anisotropy. Since VFs contain anisotropic boundary surfaces of interest, VF distances must also be anisotropic. This can be taken into account by interpolating VF distance codes with anisotropic variogram models.

Coding Conditioning Data

An initial binary coding of the available sample data in terms of net and non-net geology is a prerequisite for constructing a VF. The VF distance of all the sample data must be calculated for subsequent interpolation. Figure 4-4 is a small example illustrating how samples are coded as VF distances for four vertical 1m composite coreholes. A binary net (1) / non-net (0) geological model is available at the sample locations. VF conditioning data for sample locations within net geology are set to the negative distance between the net sample location and the nearest non-net geological sample location; for sample locations within non-net geology, the VF conditioning data are set to the positive distance between the non-net sample location and the nearest net geological sample location. Each sample composite in Figure 4-4 is shaded with its corresponding VF value. A boundary is drawn with a broken line; it is known only at data locations.

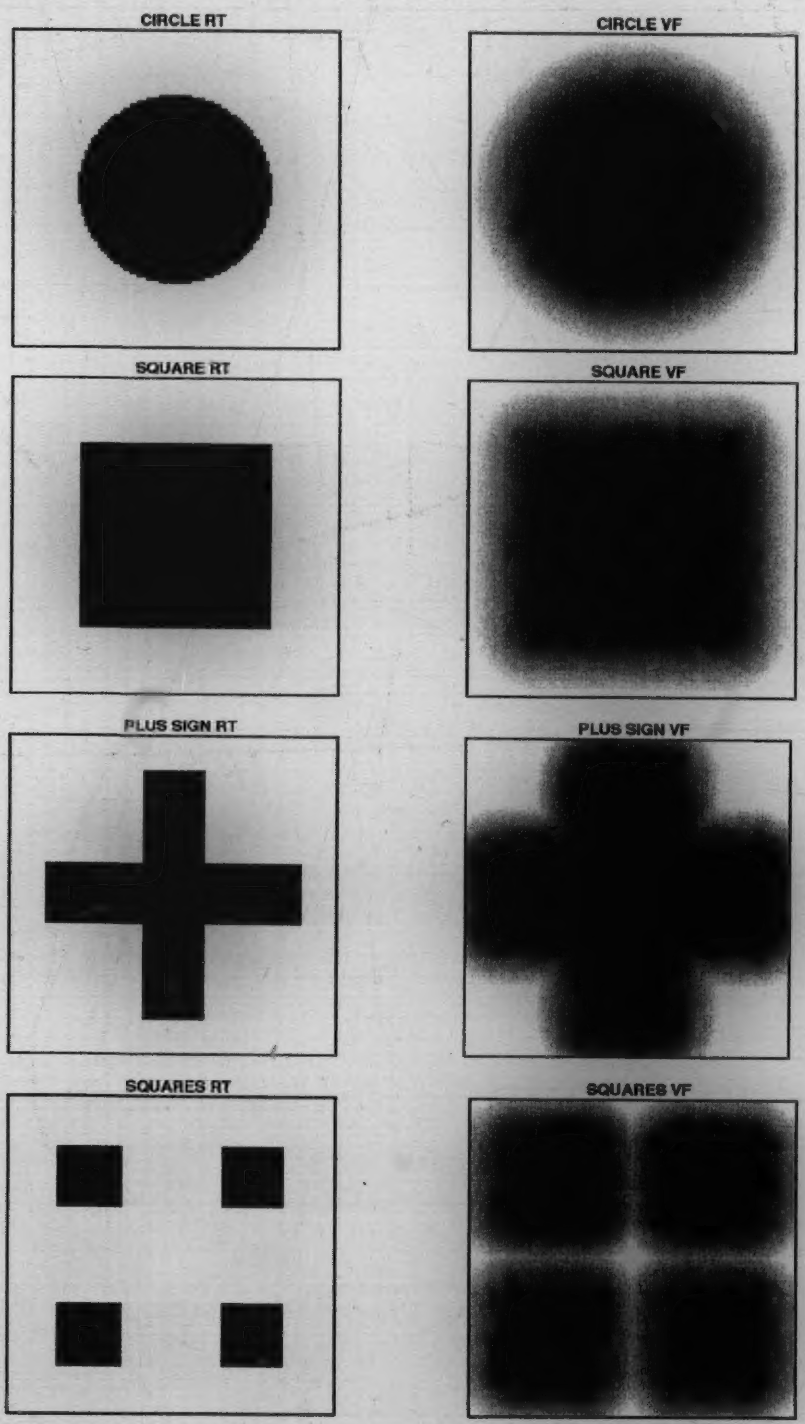
CIRCLE RT
CIRCLE VF
SQUARE RT
SQUARE VF
PLUS SIGN RT
PLUS SIGN VF
SQUARES RT
SQUARES VF

Figure 4-2: The rocktype model and corresponding volume function (VF) for some basic geometries.

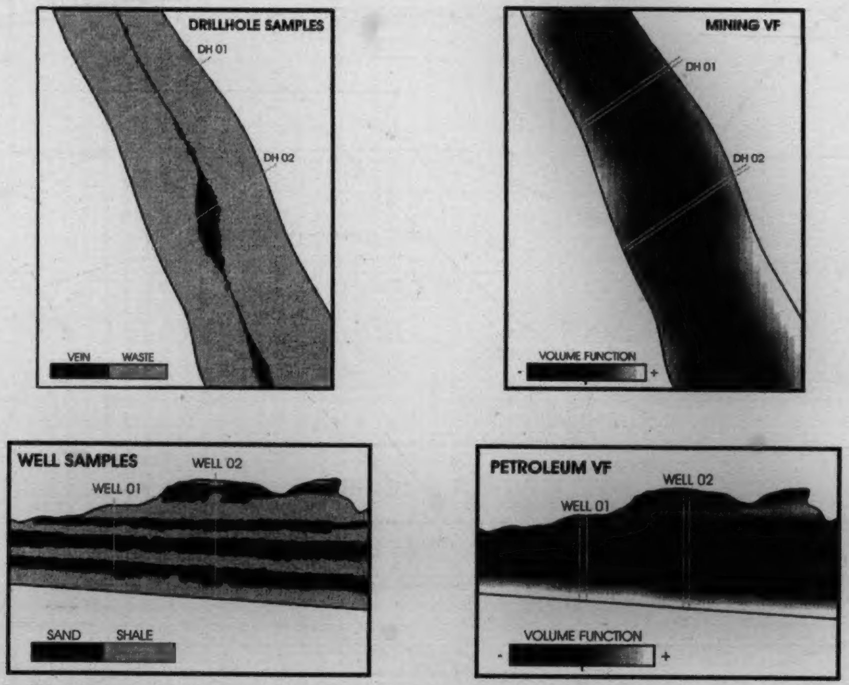
DRILLHOLE SAMPLES
DH 01
DH 02
VEIN
WASTE
MINING VF
DH 01
DH 02
VOLUME FUNCTION
-
+
WELL SAMPLES
WELL 01
WELL 02
SAND
SHALE
PETROLEUM VF
WELL 01
WELL 02
VOLUME FUNCTION
-
+

Figure 4-3: The true geological model, sample data locations, and VFs constructed using the sample data for a typical mining and petroleum setting.

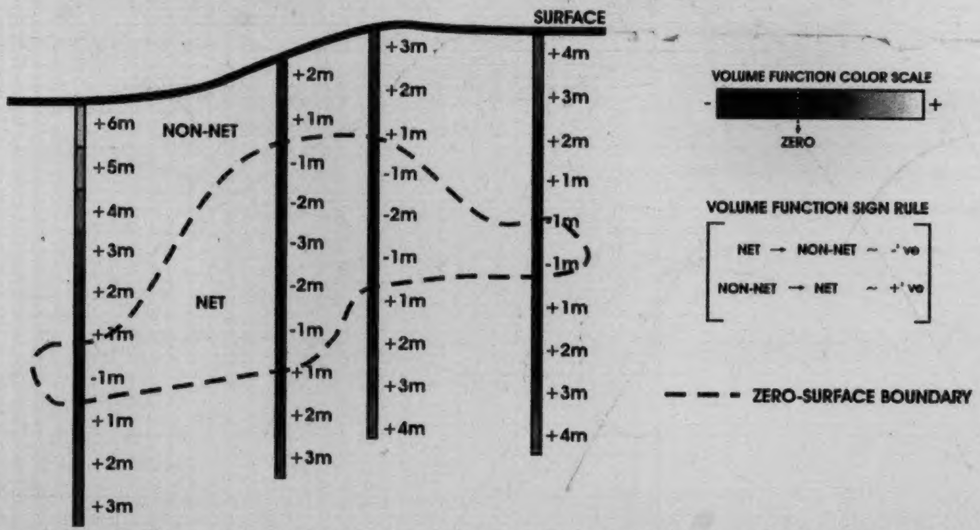
SURFACE
NON-NET
NET
+6m
+5m
+4m
+3m
+2m
+1m
-1m
+1m
+2m
+3m
+2m
+1m
-1m
-2m
-3m
-2m
-1m
+1m
+2m
+3m
+3m
+2m
+1m
-1m
-2m
-1m
+1m
+2m
+3m
+4m
+4m
+3m
+2m
+1m
-1m
-1m
+1m
+2m
+3m
+4m
VOLUME FUNCTION COLOR SCALE
-
+
ZERO
VOLUME FUNCTION SIGN RULE
NET → NON-NET ~ -' ve
NON-NET → NET ~ +' ve
ZERO-SURFACE BOUNDARY

Figure 4-4: A small example showing the VF distance codes in four vertical coreholes using net / non-net geological indicators and the sign rule indicated. A zero-surface boundary surface of interest is also shown.

VF Interpolation

The VF must be interpolated in order to define the boundary interface. Choosing an appropriate interpolation algorithm is crucial to the success of generating a reasonable boundary model. The algorithm used for interpolating VF codes must be capable of producing smoothly varying VFs. Geostatistical simulation is not recommended; short scale abrupt variations fluctuating between positive and negative VF values may generate unrealistic geological features in the boundary surface. Both kriging and inverse distance, however, are adequately flexible geostatistical estimation algorithms that can generate smooth VFs for realistic boundary surfaces. There is no possibility to predict a boundary where no intersecting corehole data exist. Therefore, as much data as possible should be used for interpolation.

The framework and derivation of kriging is addressed in Chapter 2. Like kriging, an inverse distance estimate at the unsampled location $\mathbf{u}_0$, is a weighted linear combination of n surrounding $z(\mathbf{u}_s)$ sample data:

$$z^{*}_{\mathrm{ID}}(\mathbf{u}_0)=\sum_{s=1}^{n}\lambda_{\mathrm{ID}}(\mathbf{u}_s)\cdot z(\mathbf{u}_s) \tag{4-1}$$

Unlike kriging, however, inverse distance weights $\lambda_{\mathrm{ID}}(\mathbf{u}_s)$ are not derived by minimizing the variance of error from estimating the true $z(\mathbf{u}_0)$ value with $z^{*}_{\mathrm{ID}}(\mathbf{u}_0)$. Inverse distance weights are calculated inversely proportional to the distance $d(\mathbf{u}_s)$ between the estimation location $\mathbf{u}_0$ and the $z(\mathbf{u}_s)$ sample data:

$$\lambda_{\mathrm{ID}}(\mathbf{u}_s)=\frac{\dfrac{1}{\left(d(\mathbf{u}_s)\right)^{\omega}+c}}{\displaystyle\sum_{s=1}^{n}\frac{1}{\left(d(\mathbf{u}_s)\right)^{\omega}+c}} \tag{4-2}$$

where ω is an inverse distance power and c is a constant. The inverse distance power ω controls the smoothness of the inverse distance estimates. Increasing ω generates more variable inverse distance estimates and will approach nearest neighbor estimates when ω nears infinity. Decreasing ω generates smoother inverse distance estimates and will approach arithmetic average estimates when ω nears zero. The constant c controls short-scale variability in the estimates. Increasing c has the same effect of increasing the nugget effect in the variogram model used for kriging.

Kriging and inverse distance algorithms are particularly suited to VF interpolation. Four essential features of a VF that both kriging and inverse distance are capable of producing are listed and described below:

1. *Exactitude*: VF conditioning data need to be honored exactly. Kriging possesses the property of exactitude. Inverse distance schemes do not; however, estimates can be set equal to conditioning data when $d(\mathbf{u}_s)$ is below a critically small distance.
2. *VF Variability*: A VF should show large-scale variability mimicking the continuous nature of geological boundaries. To avoid artificial short-scale variability, a zero nugget effect variogram model can be used for kriging and a constant c equal to zero can be used for inverse distance. To generate large-scale variability, variogram models with long ranges of correlation can be used for kriging and relatively small inverse distance powers ω (0.5 to 1.0) can be used for inverse distance. Moreover, it is very important to use large searches using all the data to ensure smooth kriging and inverse distance estimates.

3. *VF Anisotropy*: A VF should reproduce key anisotropy when the available sample and geological information suggests this. Kriging and inverse distance both account for anisotropy ratios through the scaling of $\mathbf{h}$ used to calculate the variogram value for kriging and the scaling of $d(\mathbf{u}_s)$ used in relation (4-2) for inverse distance.
4. *Uncertainty*: A VF can be tailored to a particular position of risk in known intersections using either kriging or inverse distance schemes. The techniques and implementation detail are reserved to a later section.

In general, a relatively large amount of VF conditioning data is needed to condition the construction of a VF containing geologically realistic boundary surfaces. This is because a VF is interpolated using two-point covariance weighted or two-point distance weighted functions incapable of producing curvilinear and undulating features unless there are ample conditioning data defining the geometry explicitly. That is, the kriging and inverse distance schemes will only reproduce geometries that are well delineated.

The continuous VF is represented discretely on a moderate resolution Cartesian grid. As the resolution of the volume function increases, the boundary interface of interest more closely honors sample VF data, is smoother, and possibly more realistic. Increased resolution, however, comes at the cost of computer resources and time.

VF Stationarity

A VF is not a stationary random function (SRF). A VF necessarily contradicts the level of homogeneity in relation (2-7) assumed of a typical first order stationary RF. Certainly, the expected VF value is not constant independent of location inside the accumulation limits. There must be significant populations of both positive and negative VF distance values in order to define and extract a boundary surface imbedded within the VF.

Figure 4-5 shows a histogram of the VF values for the simple circle geometry in Figure 4-2. In practice, the full VF distribution is not known, only a few samples are extracted. Since the circle position and geometry is known perfectly, the VF can be fully defined at any resolution in this case. Notice the marked density of negative values corresponding to locations inside the circle (net) and positive values corresponding to locations outside the circle (non-net).

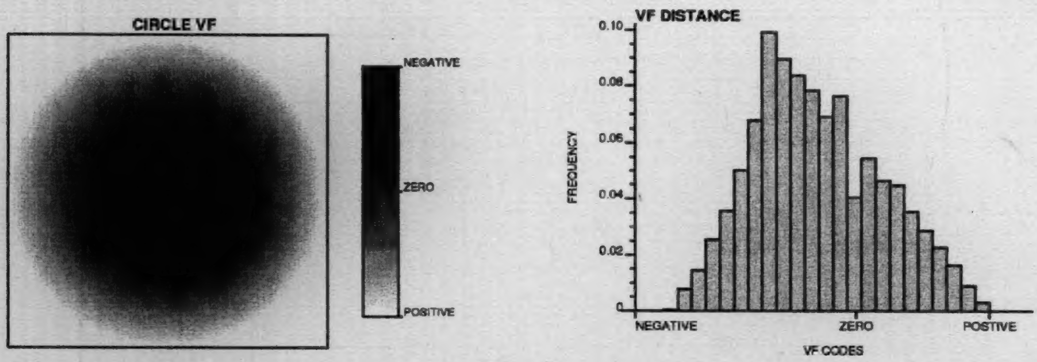

Figure 4-5: The VF for the circle geometry in Figure 4-2 shown in 2D and as a histogram.

Classic geostatistical prediction utilizes a stationary random function (SRF) to predict petrophysical properties within distinct domains that are geologically consistent with the assumptions of stationarity in relations (2-7) and (2-8). This is far from the case for VF techniques – the VF is not a SRF. Therefore, structural uncertainty assessed using a VF is not derived from traditional probabilistic measures of local and/or joint uncertainty like those based on estimation or kriging variance. Improvised procedures are needed.

VF Uncertainty

Since the VF is not a SRF and uncertainty cannot be assessed rigorously through a traditional probabilistic model, alternative less formal procedures are developed. These tools are not rigorously defined; the procedures investigated in this dissertation can be described as heuristic modifications to conventional approaches coupled with practical pre and post processing techniques.

The key to structural uncertainty quantification using VF techniques is the generation of a unique VF customized to a certain risk stance. Figure 4-6 is a modification of Figure 3-5 with the coreholes traces replaced with VF codes from Figure 4-4. The six boundary surfaces in Figure 4-6 are now interpreted as the zero-surface of six different interpolated VFs. The variation in these interfaces is a measure of structural boundary uncertainty. The conditioning VF data do not change. However, in between sample data, positive VF values are preferentially weighted in order to expand the interface towards a higher risk more optimistic structural interface or negative VF values are preferentially weighted in order to contract the interface towards a lower risk more conservative structural interface.

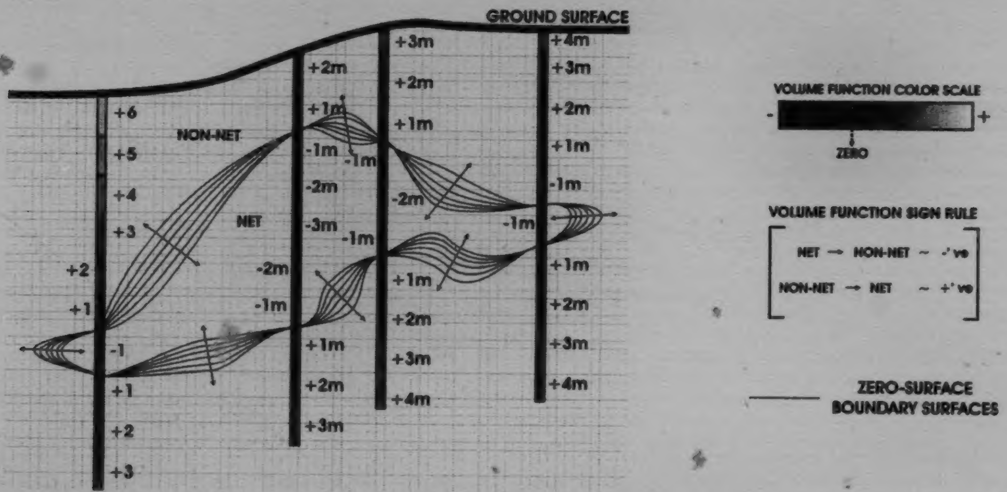

Figure 4-6: A schematic 2D example showing six risk based boundary models extracted from separate VFs that give weight to either positive or negative VF distance codes preferentially.

Two methods are developed in this dissertation to assign uncertainty in interpolated VF distances. The basis of the first is the spatial bootstrap to determine the uncertainty in the expected VF value. The basis of the second method is data conditioned inverse distance. Both methods produce uncertainty in the VF for quantification of structural uncertainty.

These methods are both described and implemented for the simple circle geometry shown previously.

The Place of VF Techniques

The most suitable utility of boundary models built from VF techniques is a preliminary volumetric uncertainty assessment during early exploration phases of a natural resources venture. Data must be easily accessible and inexpensive to have a sufficient amount in the exploration phase. Detailed local geological heterogeneity is not a high priority – a globally smooth geologically realistic boundary with an attached appraisal of volumetric uncertainty is the priority. In practice, a more probabilistic or stochastic boundary modeling approach may be implemented to quantify structural uncertainty on a localized scale and constrain the subsequent population of continuous petrophysical properties. The VF boundary can be used as an alternative model for validation.

There are exceptions. A VF boundary model may be used almost exclusively when volume is the primary variable influencing project economics. This may be the case for diamond deposits where the volume of diamond bearing kimberlite pipes is a key variable, the global uncertainty of which will directly translate to economic uncertainty. The interpolation and uncertainty of diamond grades may then be less important than structural uncertainty.

VF surfaces can be used in combination with different boundary modeling approaches. For example, net / non-net surface can be predicted with VF techniques, then a SB approach could be used to model system tract boundaries, and then an OB or SPB approach could be used to model lithofacies. Again, these methodology choices depend on the geometrical nature of the boundaries as well as the amount and type of data.

4.4.2 Bootstrap Technique for Quantifying Global Uncertainty

The first approach to quantifying global uncertainty with VF techniques is implementing a bootstrap of the expected VF value. Sample VF codes are interpolated with a smooth estimation algorithm with the intention to reproduce the mean VF parameter. Global uncertainty is accessed through (the mean) parameter uncertainty by interpolating a series of VFs, each with a different mean outcome.

A common challenge is encountered with this approach. The requirement for a smooth interpolation algorithm and several conditioning VF data undermines the capability of building significantly different VF distributions from which significantly different zero-surface boundaries can be extracted as bounding surfaces; post processing is then often required [illegible] enforce the interpolated VF distributions to honor specific mean VF values.

There are three steps to the overall spatial bootstrap technique towards quantifying global uncertainty: (1) pre processing with the spatial bootstrap, (2) interpolation with simple kriging, and (3) post processing with a histogram transformation. These steps are now described and demonstrated with an example.

Pre Processing: The Spatial Bootstrap

The bootstrap procedure is used as a pre processing step to a simple kriging interpolation setup. The mean VF distance is the parameter of interest. The uncertainty in the mean VF value is established with the bootstrap in order to parameterize the interpolation of different VF distributions from which different boundary surfaces can be extracted to represent global uncertainty.

The bootstrap is a resampling technique. We would resample VF distance codes with replacement to construct multiple realizations of the mean assuming the sampled VF code locations were spatially independent. However, the VF distances are not independent. Depending on the governing geological formation processes, they have a particular correlation structure manifested by the geometry of the boundary surfaces. The *spatial* bootstrap technique [46] accounts for correlation with the specification of a variogram model. Sampling is not random. Correlated sampling is undertaken according to the variogram so that VF samples that are highly correlated have a higher probability to be drawn and included in the calculation of the mean statistic for any particular bootstrap realization. The uncertainty predicted by the spatial bootstrap is always higher than that for the traditional bootstrap as long as there is some spatial correlation in the VF.

The circle example from Figures 4-2 and 4-5 is placed within accumulation limits 50m a side and used to demonstrate the spatial bootstrap technique as well as subsequent simple kriging and post processing steps. Figure 4-7 shows 25 sample locations drawn on a randomized 10 x 10m grid. These samples are superimposed on the true geological model (left) and used to calculate VF distance codes (right). Notice the VF sample codes do not directly sample the true underlying VF in Figures 4-2 and 4-5. However, the true circle geometry should reside within the smallest and largest possible zero-surface extractable from the subsequent VF distributions.

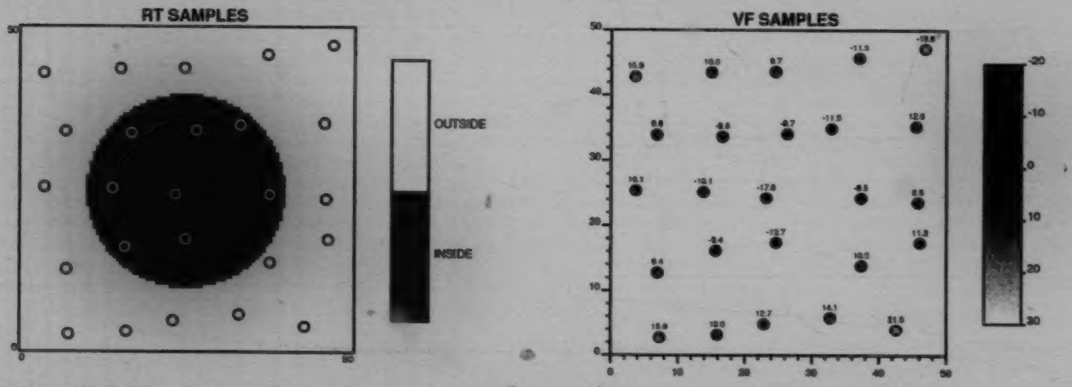

Figure 4-7: The 25 sample locations drawn on a randomized 10 x 10m grid used for the spatial bootstrap, simple kriging interpolation, and histogram post processing.

The traditional and spatial bootstrap are both implemented with the 25 VF sample data. A total of 10,000 mean VF realizations are generated. A Gaussian variogram model with no nugget and 30m isotropic range is used for the spatial bootstrap. The results are shown in Figure 4-8 in the form of cumulative distribution functions. The p10, p50, p90 VF quantiles are 2.0, 5.0, 7.8 using the traditional bootstrap and -1.1, 6.0, and 11.5 using the spatial bootstrap. The magnitude of difference between the VF mean p90 and p10 values is a quantitative measure of the expected VF value uncertainty and translates to structural uncertainty.

Interpolation: Simple Kriging

The histogram of 10,000 possible mean VF values in Figure 4-8 is the fundamental link to generating different boundary models with a spatial bootstrap approach. Consider building 10,000 different spatial VF distributions, each one exactly reproducing the conditioning VF data in Figure 4-7 but giving weight to just one of the 10,000 different mean VF values when predicting away from data. At a particular location in between conditioning data, therefore, the interpolated VF will increase when the mean VF value used for weighting increases; and since the boundary is always extracted at the zero-surface VF contour, higher VF values will effectively contract the boundary interface and enclosed volume. For example, high risk boundary surfaces can be generated by choosing lower VF quantiles as the expected VF value to weight for interpolated VF values.

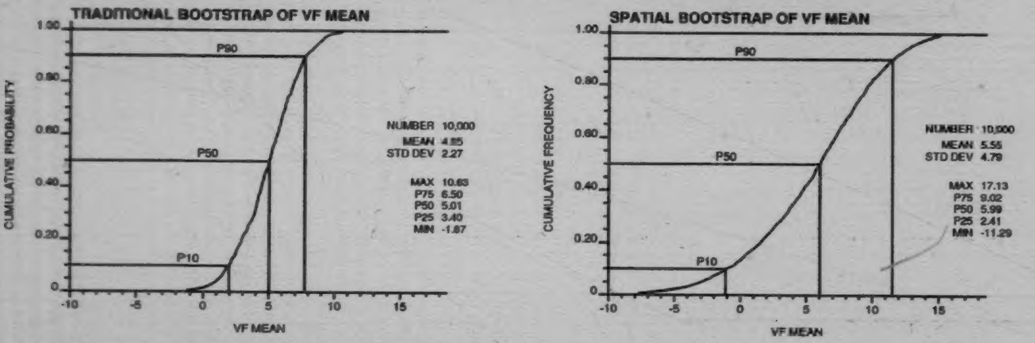

Figure 4-8: The 25 sample locations drawn on a randomized 10 x 10m grid used for the spatial bootstrap, simple kriging interpolation, and histogram post processing.

Simple kriging provides a convenient framework for weighting the mean while predicting unsampled locations. The simple kriging estimator in (2-37) is a function of the mean m. This mean m receives increasing weight further away from conditioning data. Although the VF mean is not stationary, m can be substituted for different mean VF values from the spatial bootstrap distribution in Figure 4-8. It is important to emphasize that there is a strong assumption of stationarity that is clearly violated. The mean m input for simple kriging VF interpolation is not stationary. And reference to kriging in this context should not be as a probabilistic tool. However, this procedure does allow the assignment of different boundary models based on different positions of risk.

Three simple kriging runs are performed for the circle geometry. The same conditioning data and the same Gaussian variogram model with zero nugget and 30m isotropic range is used for all three interpolated VF distributions. Global kriging, using all 25 conditioning data to estimate each location, is implemented in order to ensure the VF is smooth. The conventional stationary mean m is replaced by the p10 (-1.1), p50 (6.0), and p90 (11.5) expected VF values to parameterize the three simple kriging runs.

Figure 4-9 shows the resulting p10 and p90 simple kriging VF distribution as maps and histograms. The subsequent zero-surface boundary extracted from the p90 interpolated VF will be smaller than that from the p10 VF. This is because the probabilistic VF mean weighted for the p90 VF (+11.5) is higher than that for the p10 VF (-1.1). However, the difference between the p10 and p90 in Figure 4-9 is indiscernible; these VF distributions do not represent the mean VF parameter uncertainty calculated with the spatial bootstrap. The p10 and p90 VF maps are visually identical and their corresponding histograms show only a subtle difference of 0.147 in the expected VF value. Post processing is required to enforce the interpolated VF distributions honor specified probabilistic mean VF values.

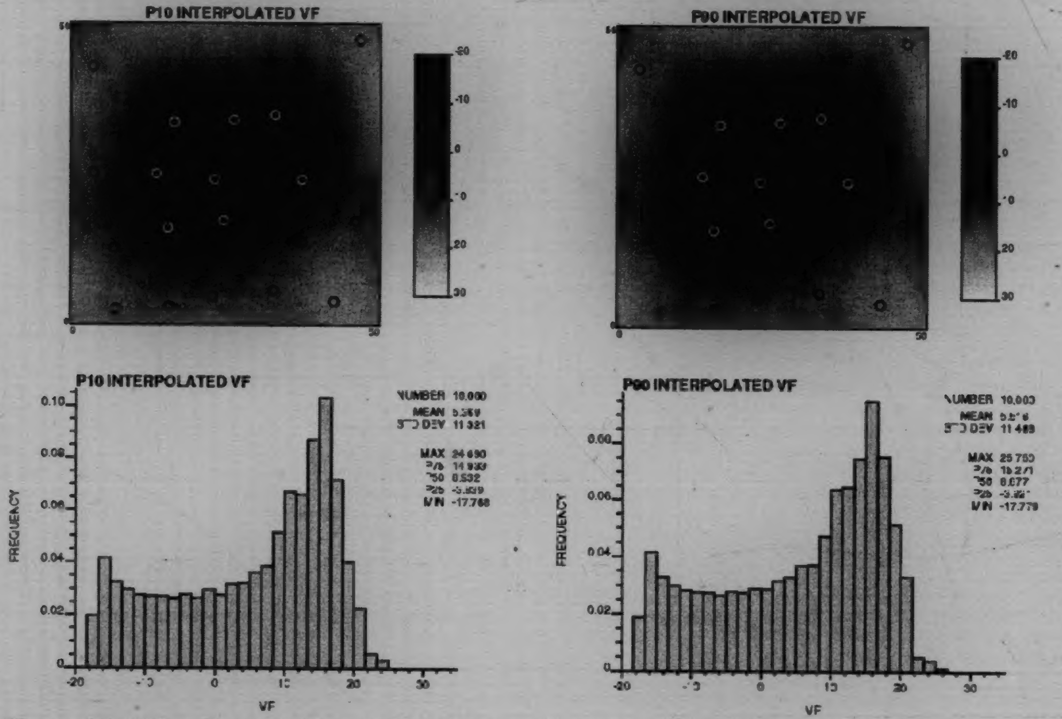

Figure 4-9: The p10 and (left) and p90 (right) simple kriging VF estimates shown as maps (top) and histograms (bottom).

Post Processing: Histogram Transformation

The requirement for a smooth interpolation algorithm retaining several conditioning VF data damages the ability to access boundary uncertainty with significantly different VF distributions. This is because simple kriging does give significant weight to the mean when there are many correlated surrounding data. This is the case in Figure 4-9 where a zero nugget long (30m) range Gaussian variogram model coupled with a global search routine is implemented. Although it necessitates a post processing step, the global search is needed to ensure smooth VF estimates.

In order to accurately represent structural uncertainty with boundaries derived from VF distributions, the corresponding VF distributions should honor the mean VF parameters specified from the spatial bootstrap. Therefore, the p10 and p90 interpolated VFs need to be changed towards honoring the input -1.1 and +11.5 expected VF values without changing the conditioning VF sample data or sacrificing smoothness.

In 1994, Journel and Xu [47] illustrate a continuous variable posterior transformation of an original distribution to a target distribution. The transformation method is a quantile transformation. The transformation is increasingly applied at locations further away from conditioning data. The intended application was matching the input possibly declustered distribution to a particular set of simulated realizations. Deutsch extended the algorithm capability to honor trends and probabilistic mean values from the spatial bootstrap [48]. This newest version of the transformation can be applied to the simple kriging VF distributions in Figure 4-14 to reproduce the target p10 and p90 VF mean values. The kriging variances are needed.

Figure 4-10 shows the transformed p10 and p90 VF results. Although the transformed expected VF values are still not exactly honored, they are much closer than in Figure 4-9. The transformed mean is 1.1 versus -1.1 for the p10 VF and 10.0 versus 11.5 for the p90 VF. These VFs better represent the prior mean VF values from the spatial bootstrap. Figure 4-11 shows the VF distributions within the -2.0 to 2.0 distance range for the p10 and within the -10.0 to 10.0 distance range for the p90.

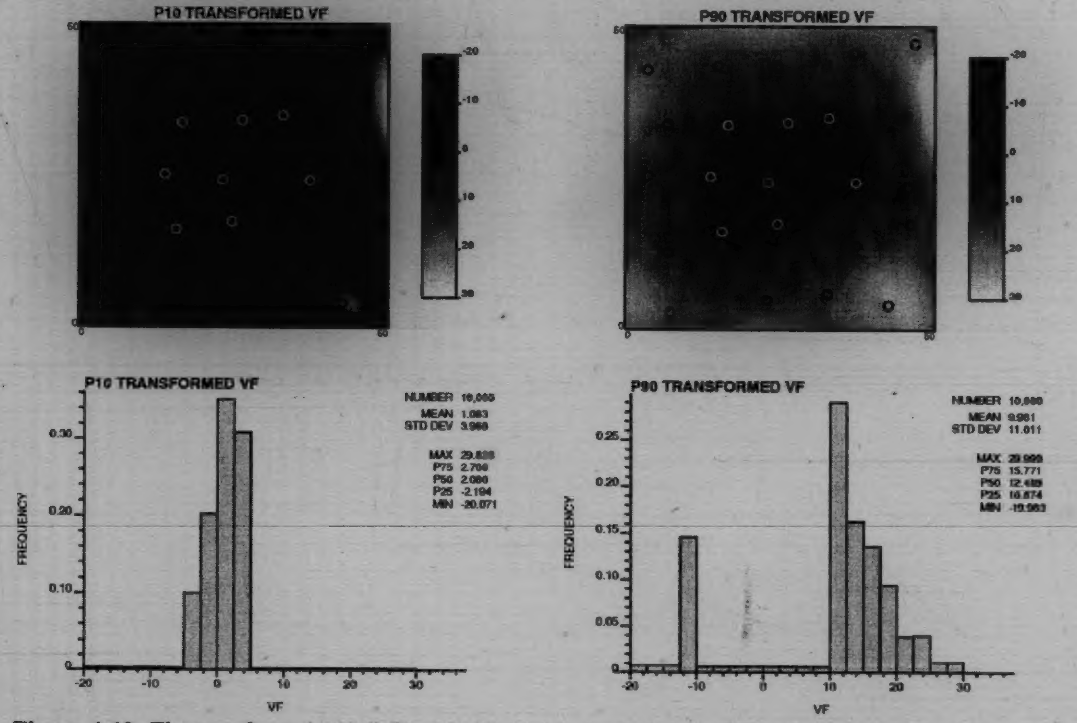

Figure 4-10: The transformed p10 (left) and p90 (right) simple kriging VF estimates shown as maps (top) and histograms (bottom).

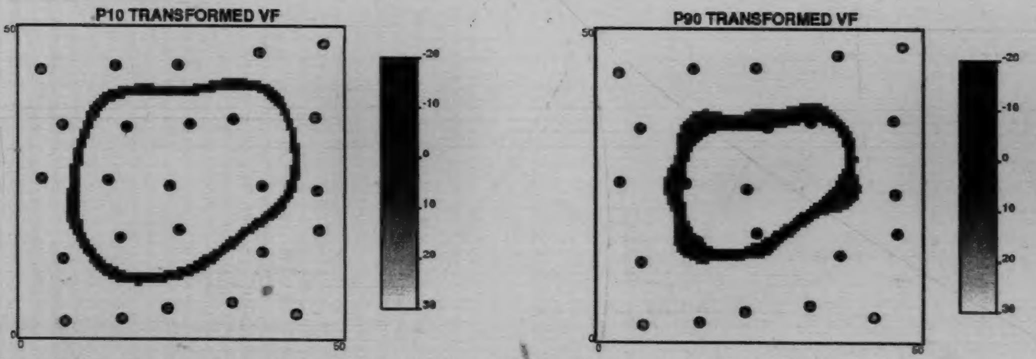

Figure 4-11: The transformed p10 (left) and p90 (right) VF rendered between VF values of -2.0 and 2.0 for the p10 and -10.0 and 10.0 for the p90.

4.4.3 Data Conditioning Techniques for Quantifying Global Uncertainty

The second approach to quantifying global uncertainty with VF techniques explored in this dissertation is applying data conditioning factors to VF predictions. The general idea of preferentially weighting negative or positive VF values to predict smooth p10 or p90 VF and imbedded optimistic or pessimistic boundary surfaces, respectively, is the same as for the spatial bootstrap technique. Here, however, global uncertainty is accessed via adjusting inverse distance weights with a factor that is calibrated to the VF conditioning data and the desired position of risk.

Data Conditioned Estimation

Kriging and inverse distance weights typically depend on the geometrical arrangement of data, but not the actual data values. The data-dependent weights are applied to the actual numerical values of the data to calculate the estimate as in (4-1) for inverse distance. The proposal is to alter the weights by a data conditioning factor in order assign uncertainty in the VF and extractable boundaries. Still, the kriging or inverse distance weights are calculated in the traditional manner; but they are now combined with the data values in the following manner:

$$z^*(\mathbf{u}_0)=\sum_{s=1}^{n} f^{DC}(\mathbf{u}_s)\cdot\lambda(\mathbf{u}_s)\cdot z(\mathbf{u}_s) \qquad (4\text{-}3)$$

where $z^*(\mathbf{u}_0)$ is the kriging or inverse distance estimate, $f^{DC}(\mathbf{u}_s)$ is the data conditioning factor, $\lambda(\mathbf{u}_s)$ are the kriging or inverse distance weights, and $z(\mathbf{u}_s)$ are the data values. The weights account for the geometrical configuration of the data while the $f^{DC}(\mathbf{u}_s)$ parameter accounts for the actual numerical values of the data. Classic kriging and inverse distance schemes correspond to a constant $f^{DC}(\mathbf{u}_s)$ value of 1.0 regardless of the data values.

The $f^{DC}(\mathbf{u}_s)$ data conditioning factor is the crucial element allowing structural uncertainty access in this approach. For example, to create a pessimistically small boundary surface, $f^{DC}(\mathbf{u}_s)$ can be set progressively lower than 1.0 as the $z(\mathbf{u}_s)$ VF data decrease in value from zero and be set progressively higher than 1.0 as the $z(\mathbf{u}_s)$ VF data increase in value from zero.

Data Conditioning Factor and Uncertainty Assignment

The assignment of $f^{DC}(\mathbf{u}_s)$ to the $z(\mathbf{u}_s)$ VF data corresponds to different positions of risk. Figure 4-12 shows a linear approach. The VF of zero and $f^{DC}(\mathbf{u}_s)$ of one are plotted with thin vertical and horizontal lines. The $z(\mathbf{u}_s)$ VF data are plotted on the abscissa axis ranging from a minimum to maximum conditioning VF sample value labeled $\mathrm{VF}_{\mathrm{MIN}}$ and $\mathrm{VF}_{\mathrm{MAX}}$, respectively. And the $f^{DC}(\mathbf{u}_s)$ factor is plotted on the ordinate axis ranging from the minimum to maximum VF data conditioning factor labeled f_{MIN} and f_{MAX}, respectively.

Optimistic and pessimistic boundaries can be generated with the linear parameterizations shown in Figure 4-12. The negative sloping line gives gradually higher weight to VF samples that are more negative and gradually lower weight to VF samples that are more positive producing a VF from which an optimistically large boundary surface can be extracted. The positive sloping line gives gradually lower weight to VF samples that are more negative and gradually higher weight to VF samples that are more positive producing a VF from which a pessimistically small boundary surface can be extracted. The zero slope flat line corresponds to traditional kriging or inverse distance schemes giving no influence to data values producing a VF from which an intermediate sized boundary surface can be extracted. All three linear parameterizations intersect at the $f^{DC}(\mathbf{u}_s)$ factor of one where the VF code is zero.

The linear calibration in Figure 4-12 is flexible. For symmetric optimistic and pessimistic boundaries, the absolute value slope is the same for both lines; also, for the same line, the slope is not allowed to be different within negative and positive VF values. However, the magnitude of uncertainty between optimistic and pessimistic boundaries can be changed by adjusting the slope through the f_{MIN} parameter. For example, the least extreme probabilistic boundaries would be achieved with lowest sloped lines built by the f_{MIN} parameter set slightly below one. Since the lines must cross the $f^{DC}(\mathbf{u}_s)$ factor equal to 1.0 line at the VF equal to zero line and have the same slope within negative and positive VF values, the f_{MAX} parameter can be calculated. More extreme boundaries are modeled with f_{MIN} closer but not lower than zero.

The $f^{DC}(\mathbf{u}_s)$ parameterization need not be linear. For example, if the upper 1.0 and lower zero limits on f_{MIN} do generate the desired level of uncertainty, the piecewise quadratic function in Figure 4-13 can be used to increase the uncertainty.

The $f^{DC}(\mathbf{u}_s)$ parameterizations in Figures 4-12 and 4-13 are very heuristic – virtually any amount of uncertainty can be tuned in with this method. In practice, the interpolated VF resulting from this process should be checked against the results of a spatial bootstrap. For example, f_{MIN} would be too low when the optimistic interpolated VF mean is lower than the minimum VF mean from a spatial bootstrap. Other geological validations can be performed depending on the setting.

Interpolation: Inverse Distance

Kriging is not recommended for data conditioned estimation of the VF for two reasons: The first is the elevated likelihood of calculating negative kriging weights due to the presence of corehole strings and the requirement for a continuous variogram model coupled with an extensive search routine. Negative weights should not be used in relation (4-3) since they will contribute to reversing the intended assignment of uncertainty. The second reason is the string effect where disproportionately large amounts of weight are given to data at the extreme ends of a string of corehole data. Since it is the VF that is being predicted with an imbedded boundary surface, the string effect can have a large effect on the location of boundary interfaces near the extreme locations of corehole data.

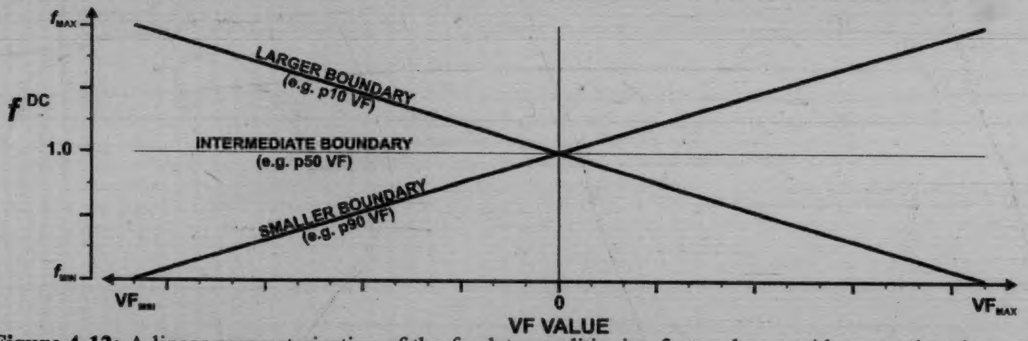

Figure 4-12: A linear parameterization of the f_{DC} data conditioning factor shown with a negative slope p10 VF, no slope p50 VF, and positive slope p90 VF calibration from which optimistically large, intermediate, and pessimistically small boundaries can be extracted, respectively.

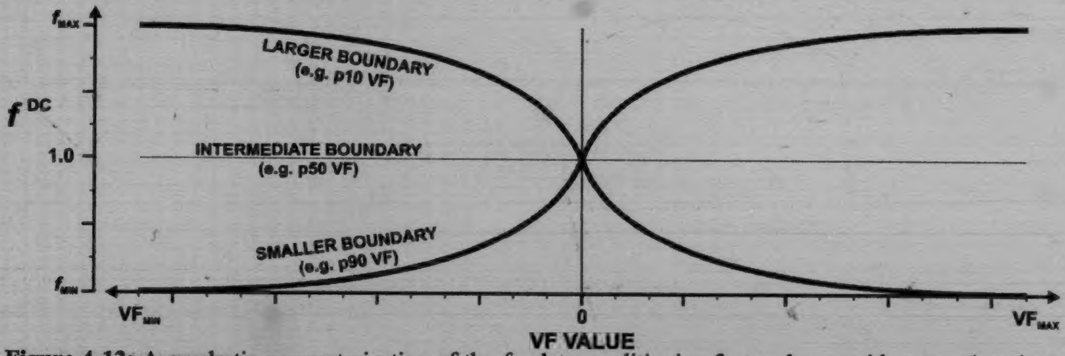

Figure 4-13: A quadratic parameterization of the f_{DC} data conditioning factor shown with a negative slope p10 VF, no slope p50 VF, and positive slope p90 VF calibration from which optimistically large, intermediate, and pessimistically small boundaries can be extracted, respectively.

Inverse distance avoids calculating negative weights and is not subject to the string effect. It is the recommended interpolation scheme to obtain the weights in relation (4-3). And, as previously mentioned, the inverse distance scheme can be parameterized with a small ω power near 0.5, zero c constant, and global search to ensure smooth VF distributions are generated.

Implementation: Circle Example

The data conditioned inverse distance approach is implemented for the circle example. A linear calibration of the f^{DC} factor is used with f_{MIN} equal to 0.75 in Figure 4-12 in order to generate a p10 and p90 VF. The inverse distance power ω and nugget constant are 1.5 and zero, respectively. Figure 4-14 shows the resulting p10 and p90 VF distributions as maps and histograms. Notice the data conditioned inverse distance estimated VF means are consistent with the kriged VF means in Figure 4-9 in that the expected p90 mean is slightly larger than the expected p10 mean. Figure 4-15 shows the VF distributions in the -1.0 to 1.0 distance range.

4.4.4 Boundary Surface Refinement and Extraction

The last step of the overall VF approach is to extract the boundary surface from the smooth spatial VF distributions. This step may involve refining the VF grid prior to extraction if additional geological detail is required.

Locally Varying Grid Refinement

The VF is interpolated at an intermediate resolution grid to avoid the increased computer resource demand associated with a kriging or inverse distance scheme with a large search routine at high resolutions. Additional VF resolution, especially in the area surrounding the zero-surface VF contour, may improve the geological realism of the extracted surface.

The locally varying grid refinement method is proposed as a compromise between computer resource demand and additional geological detail. The VF is downscaled within only those grid cells in the immediate area of the zero-surface VF contour. This allows the full VF grid to be interpolated first at a coarse resolution and then at finer resolution nearby the zero-surface VF contour in a practically reasonable amount of time without sacrificing geological detail.

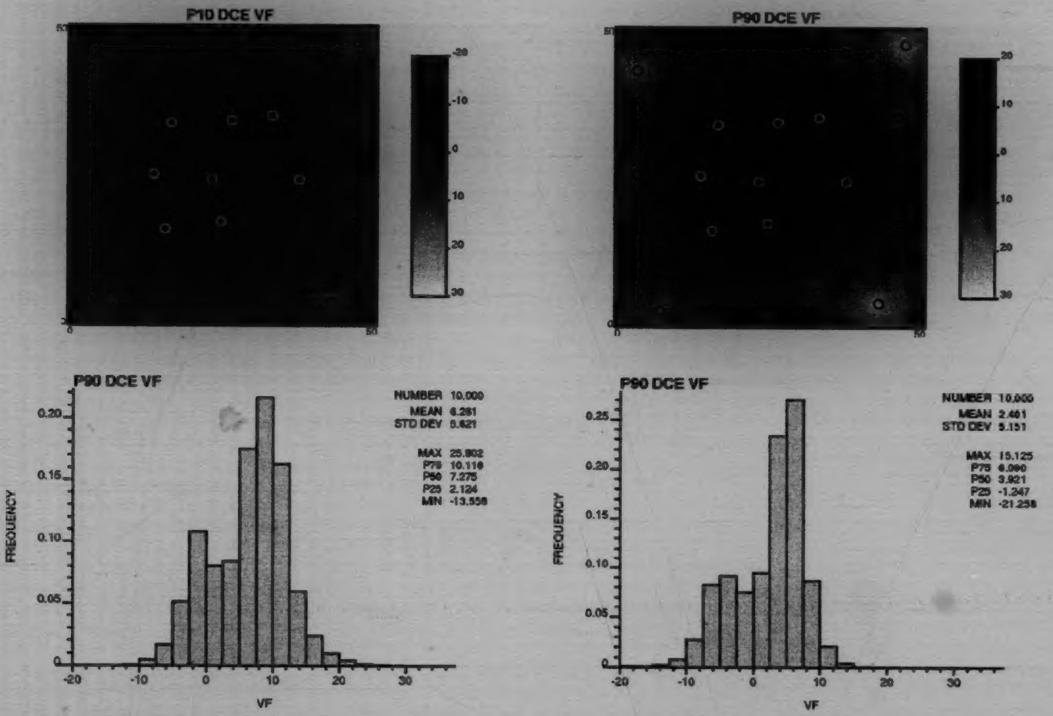

Figure 4-14: The data conditioned inverse distance p10 (left) and p90 (right) VF estimates shown as maps (top) and histograms (bottom).

Figure 4-16 demonstrates a locally varying grid refinement procedure in 2D. A schematic curvilinear boundary surface is drawn within a subset of a full VF grid. There are thirteen conditioning VF samples within this area, seven negative values (solid bullets) inside the boundary and six positive values (open bullets) outside the boundary. The sign of interpolated VF values on the grid is indicated. Within the 9 x 9 grid subset, a 3 x 3 grid cell template is centered on each of the 81 cells. Three such templates are shaded in Figure 4-16. The VF grid is then refined within grid cells that are connected diagonally (4 possibilities) or by face (4 possibilities) to the central cell in each template. For each of the three templates in Figure 4-16, connected cells are downscaled by a 3 x 3 refinement level. The downscaling approach is an inverse distance weighting scheme using all previously interpolated VF values and original conditioning VF values that are inside the template. Cells that are not connected are left at the coarse resolution.

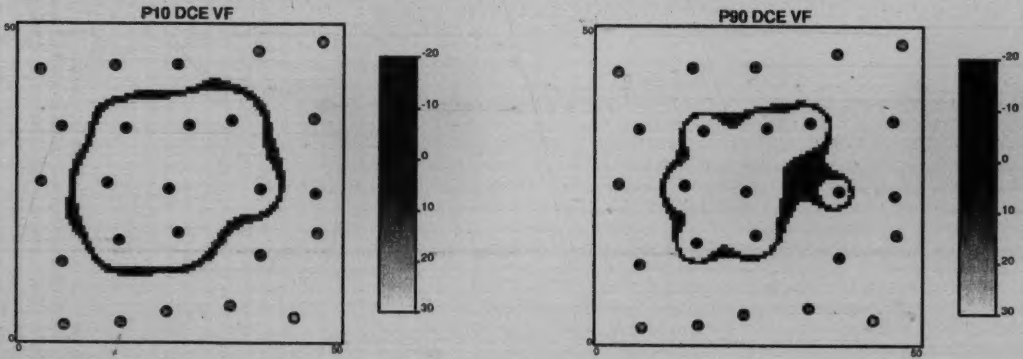

Figure 4-15: The data conditioned inverse distance p10 (left) and p90 (right) VF rendered between VF values of -1.0 and 1.0.

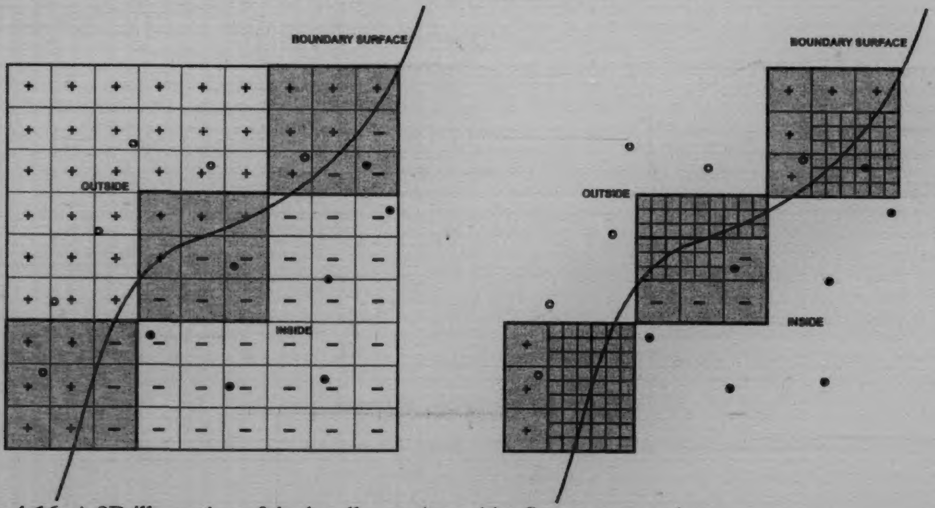

Figure 4-16: A 2D illustration of the locally varying grid refinement procedure.

In 3D, the process is the same. However, a 27 cell (3 x 3 x 3) template is superimposed on each of the interpolated volume function grid cell values. All 26 possible connections to the center (6 face, 12 edge, and 8 diagonal) are tested for candidate refinement sites.

The local boundary refinement procedure is applied to both the p10 and p90 VF boundary models in Figure 4-11. A 3 x 3 refinement level is used for downscaling with a 0.5 ω power and zero c inverse distance parameters. Figure 4-17 shows the locally refined VF distributions within the -2.0 to 2.0 distance range for the p10 and within the -10.0 to 10.0 distance range for the p90.

Extraction, Visualization, and Summary Calculations

Geologically realistic boundary surfaces are now extracted as the zero-surface from the VF distribution. The recommended approach for extraction in more complex geological settings is importing the refined VF into a commercial software package and triangulating the zero-surface. The boundary interface of interest can then be visualized from many perspectives in 3D. Simple volumetric summary calculations can also be performed.

For the circle example, the boundaries are extracted manually by hand. Figure 4-18 shows the optimistic and pessimistic zero-surface boundary surfaces drawn from Figure 4-17. The volumes assuming unit thickness are 802.5m^3 and 475.0m^3, respectively.

4.4.5 Implementation Issues

Two additional implementation details may occur in practice. The first is the choice of VF grid limits. The second is how VF techniques can be used for settings with more than two domain types within which separate SRFs will be used.

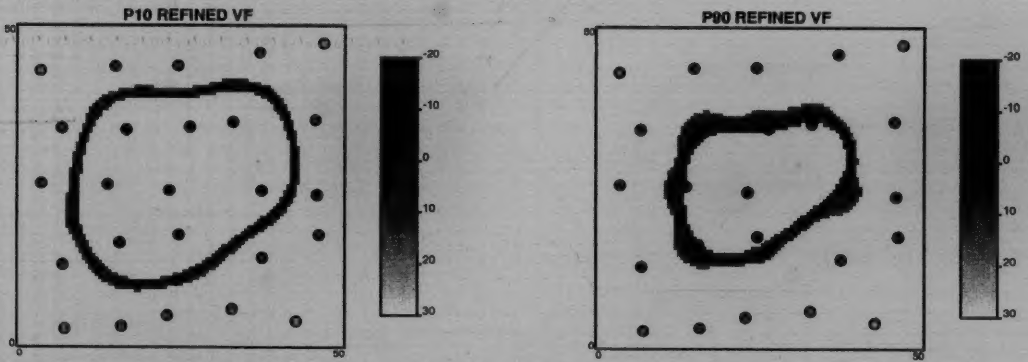

Figure 4-17: The refined p10 (left) and p90 (right) VF rendered between VF values of -10.0 and 10.0 for the p10 and -2.0 and 2.0 for the p90.

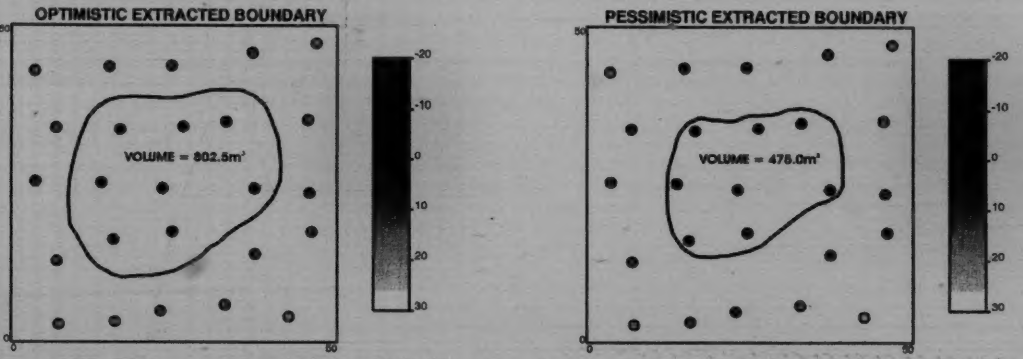

Figure 4-18: The extracted optimistic p10 (left) and pessimistic p90 (right) boundary surfaces.

VF Data Limits

VF grid extents are referred to as accumulation limits. In all previous examples, the VF distance codes are originally interpolated on a moderate resolution grid such as the one shown in Figure 4-6. The extent of this grid system and the data is important. The final VF limits can have a significant impact on the extracted boundary interface.

Regardless of what accumulation limits and data limits are used, the distribution of negative VF values remains constant. What changes is the distribution of positive VF values. This will have an effect on the geometry of extracted boundary models. In the spatial bootstrap, probabilistic VF values increase with larger data extents and result in larger volumetric boundaries. Furthermore, with increasingly positive VF distance codes, data conditioned estimation schemes increasingly transfer weight to positive VF values which also results in an ultimate increase in the ultimate boundary size.

In general, the VF grid system should be large enough to generate a mean VF value that is positive; a negative expected value means there are more VF distances inside than outside the boundary. In these situations, the grid system may be expanded. Exceptions to this generalization are when the boundary geometries are not required to close as is the case for layered geometries. Open boundary interfaces may be poor for visualization and may incorrectly suggest lower economic potential based on volumetric calculations in some settings.

Although the relationship of increasing boundary size with increasing data limits does exist, the effects are small with the relatively large amount of data used to condition the VF. The significance of this effect can be determined by comparing the change in volume due to different data extents versus the volumetric uncertainty.

Three or more Domain Types

VF techniques are applied with a binary geological model. The VF for multiple (greater than two) populations of negative and positive VF distance codes would be difficult to construct, understand, and use for global uncertainty.

An alternative is available when there are some well known geological rules that must be obeyed by the boundary surfaces. These rules are exploited in several stages to construct a binary geological model at each stage. For example, nesting and cutting rules based on geological age are often recognized in several settings. Reproduction of such fundamental rules may be an advantage over alternative boundary modeling approaches.

Figure 4-19 shows a schematic fluvial example with four diverse domain types identified by geometry: channel, lobe deposits, cutting, and flood plain. The boundaries in this setting can be modeled in four stages. Channel and lobe deposits may contain coarse and fine grained sand facies, respectively; cutting domains could host interbedded facies of sand and shale; and floodplain domains could represent mudstone. First, a VF would be constructed using channel and floodplain domains coded into net and non-net geology, respectively; the extracted interface would be the channel outline. To reproduce nesting of lobes within the channel, a second VF would be constructed using lobe and channel domain types coded as net and non-net, respectively; and finally, a third VF constructed by setting the cutting domain type to net and all the rest to non-net would be generated to represent the youngest cutting geological domain interfaces.

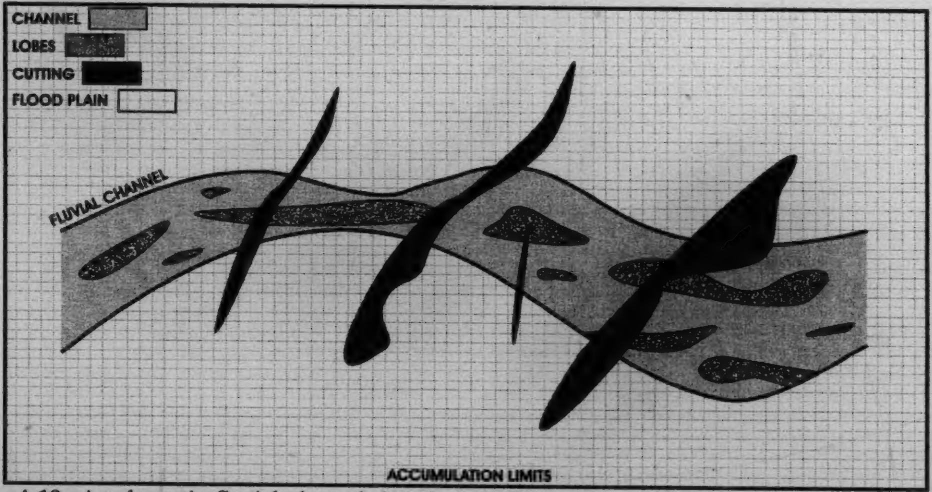

Figure 4-19: A schematic fluvial channel domain imbedded within a floodplain domain is shown with nested lobe and cutting domains used to illustrate a staged approach to modeling more than two domain types with VF techniques.

4.5 Application Example

Coal Bed Methane (CBM) is essentially natural gas produced from coal seams. CBM is gaining recognition within the oil and gas industry as an economically viable source of natural gas. Alberta, Canada has a promising CBM future with an estimated potential 500 trillion cubic feet (TCF) of reserves. EnCana is a leading CBM operator and producer in Canada focusing on shallow dry coal seams within the Horseshoe Canyon formation in south central Alberta. Figure 4-20 shows a regional map of EnCana land and the overall focus area for this application example.

Coalbed Methane
Focus Area
Suffield
Block
◄ BC
ALBERTA

Source: Internet, http://www.encana.com/flash/map, access February, 2007.

Figure 4-20: A regional map showing the overall CBM focus area from which the data for this example is made available.

VF Construction

From the focus area in Figure 4-20, an area of interest (AOI) is selected for investigation. All units are meters (m). An AOI spanning 9,000m in the easting direction by 7,000m in the northing direction is chosen to extract well data. Figure 4-21 shows the aerial location of 111 vertical wells available within the AOI, approximately five wells a section. A central 3,000 x 2,000m detailed focus area (DFA) padded by wells within the AOI perimeter is chosen for modeling, visualization, and post processing results. This model area is shaded in Figure 4-21.

The stratigraphic interval investigated within the DFA is taken between what are referred to as the Strathmore and Lower Bearspaw surfaces. The average thickness of this layer is 60m. Since significant structural deformation has occurred after the time of formation, a stratigraphic coordinate that is proportional to the top and bottom bounding surfaces is chosen and standardized to the 60m thickness for subsequent model construction. The back transform is available.

The stratigraphic top and bottom surfaces used for the back coordinate transformation are now modeled within the DFA using all 111 well picks. The mapping procedure is a global kriging using a variogram model with no nugget and long 1,500m isotropic range. Figure 4-22 shows the resulting top and bottom surfaces as histograms (left) and maps (right).

CBM is automatically detected in the 111 available wells with a high resolution (0.15m sample step) logging tool. A gamma ray cutoff is calculated and applied over the length of each well separately. The result is the appearance of several very thin coal beds. This presents some challenges. On average per well over the full accumulation interval, there are 21 coal seams each with an average thickness of just 0.7m. Gridding is an important issue. Balancing high computer resource demands with higher grid resolutions needed to accurately represent several thin coal beds must be a priority when deciding on any particular 3D modeling approach.

The VF approach is implemented in this example to model the coal bed boundaries. This approach is especially suitable in this setting for several reasons: forecasting methane gas reserves and subsequent project economics is directly related to the volume contained within modeled coal bed boundaries, the geometrical nature of the coal beds within the AOI can be characterized as ellipsoidal to layered to which VF techniques are suitable, there is a relatively large amount of data, and the locally varying grid refinement earlier described could be implemented to mitigate high computer resource demands without sacrificing high resolution coal bed heterogeneity. The complexity offered by the quantity and thinness of coal beds make deterministic digitization (DD), object-based (OB), and stochastic pixel based (SPB) approaches unsuitable. A surface-based (SB) approach could, however, also be taken.

To gain an appreciation of high potential areas within the DFA and an initial idea of original gas in place (OGIP), a total coal thickness map is generated for the stratigraphic layer. For each of the 111 wells, coal bed thicknesses are accumulated into a single 2D total coal thickness value. These conditioning data are then mapped with global kriging using a variogram model with no nugget and long 1,500m isotropic range. Figure 4-23 shows the histogram (left) and map (right) of estimates with the calculated conditioning data. Using the 3,000 x 2,000m area, an average thickness of 3.80m from the histogram in Figure 4-23, and assuming a recovery factor of 50%, a rough OGIP estimate of 402.59 million cubic feet (MCF) is calculated.

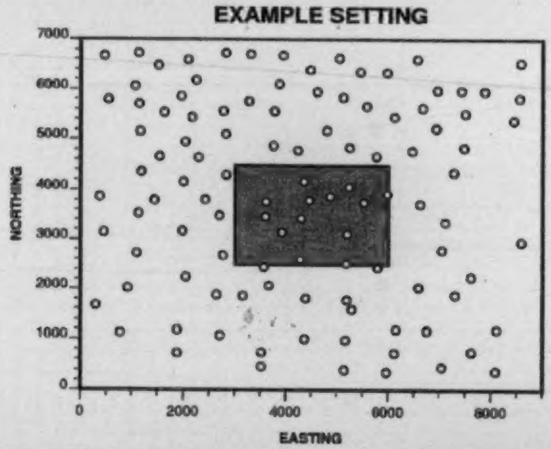
EXAMPLE SETTING
7000
6000
5000
4000
3000
2000
1000
0
NORTHING
0
2000
4000
6000
8000
EASTING

Figure 4-21: The application with 111 wells (open bullets) in the 9,000m (easting) by 7,000m (northing) area of interest (AOI) and a central 3,000m (easting) by 2,000m (northing) detailed focus area (DFA).

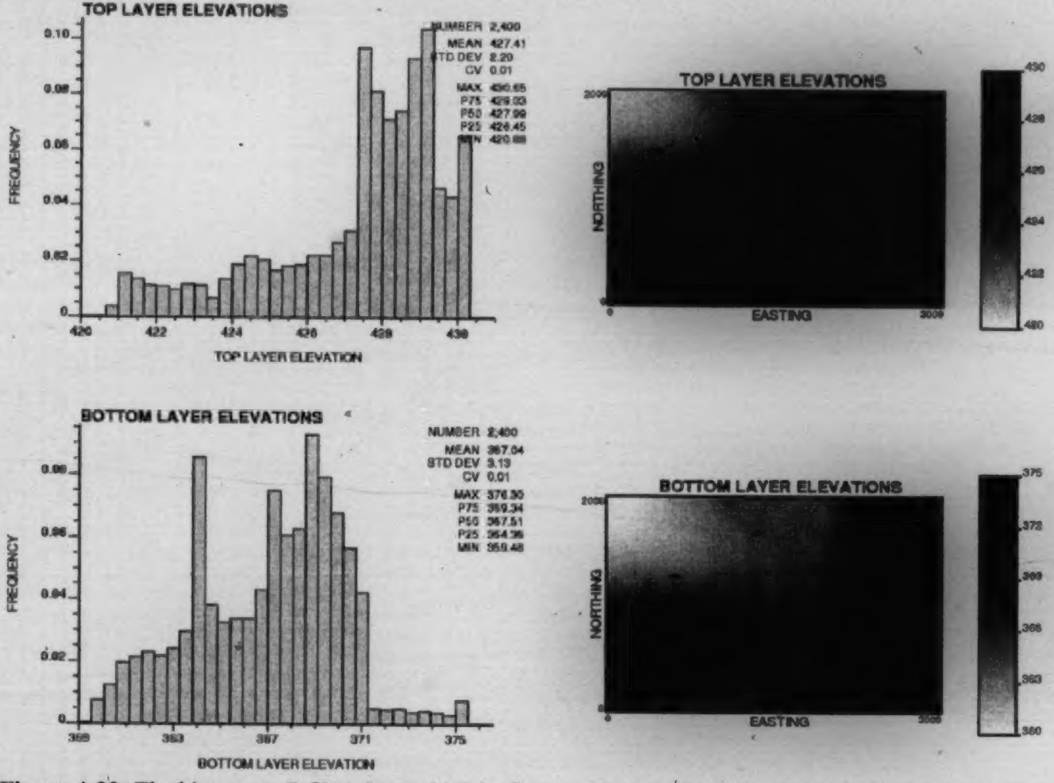

Figure 4-22: The histogram (left) and map (right) of top and bottom layer elevations within the DFA.

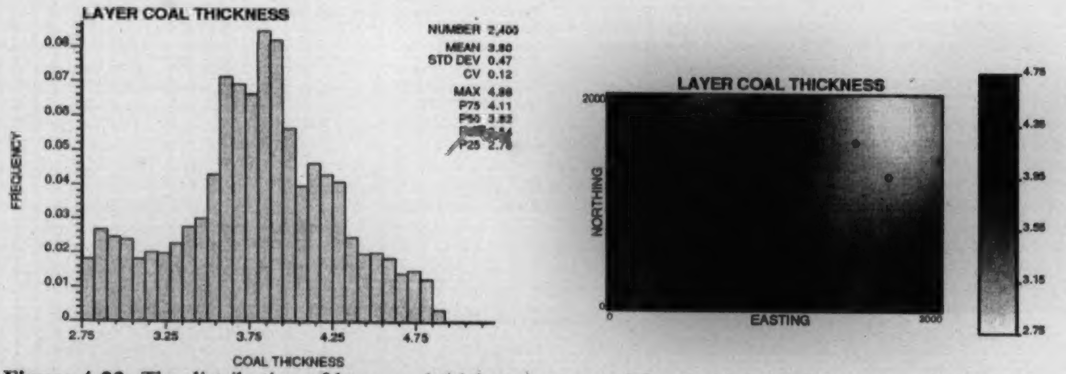

Figure 4-23: The distribution of layer coal thickness generated from a global kriging setup similar to that for trend modeling shown as a histogram (left) and map (right).

The VF distance codes are now calculated and investigated. There are a total of 47,541 sample data locations from the 111 wells within the AOI and layer of interest that need to be coded. Figure 4-24 illustrates the distribution of calculated VF codes. A small bin width is used to show the relatively small contribution of negative VF values, a signature of the laterally extensive and thin geometry of the coal seams. The accumulation limits could be reduced in order to reduce the dominance of positive values; however, in this setting, the accumulation limits are tied to the top and bottom layer surfaces which should not be modified. Moreover, reducing the positive VF value influence may undermine the high resolution log data and neglect to model the thin nature of the coal bed boundaries or even neglect to model boundaries that truly exist.

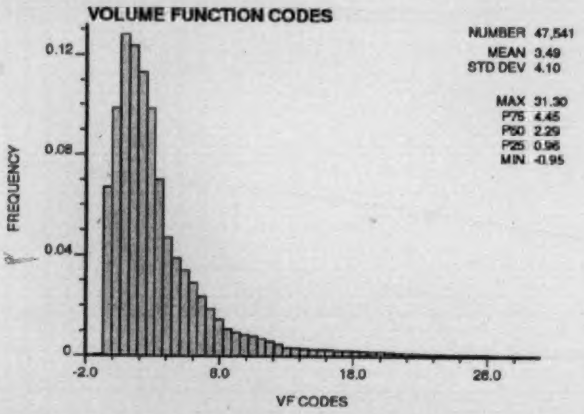

Figure 4-24: The distribution of 47,541 VF distance codes (left).

The VF distance codes are now interpolated to a grid within the 3,000 x 2,000m DFA. An initial grid of 60 x 40 x 120 cells (288,000 total) measuring 50 x 50 x 0.5m in the easting, northing, and elevation directions, respectively, is adopted. This initial grid is relatively coarse so that the computer resource demand is reasonable at this stage. This grid is later refined. The approach to interpolation is a data conditioned inverse distance scheme. A global search is utilized. A 300:1 horizontal to vertical anisotropy ratio is used with an inverse distance power of 1.5 and nugget constant of zero.

Parameterizing the f^{DC} data conditioning factor is a vital step to allow the assignment of structural uncertainty. Consider Figure 4-12 with VF_{MIN} and VF_{MAX} equal to -1.0 and 32.0, respectively. A series of six f_{MIN} parameters ranging from 0.85 to 0.90 increasing in increments of 0.01 are used for predicting 6 pairs of optimistic and pessimistic VFs.

Without the 50% recovery factor, an OGIP estimate of 805.20 MCF is calculated from Figure 4-23. OGIP can also be approximated from the VF distribution at the coarse grid resolution as the product of the full accumulation limits (3,000 x 2,000 x 60m) multiplied by the proportion of negative VF values interpolated. The p50 VF obtained with f_{MIN} set to 1.0 has an OGIP estimate of 728.97 which closely matches the 805.20 MCF estimate obtained from 2D coal thickness mapping. The pessimistic p90 and optimistic p10 interpolated VF distributions are taken to be the ones built with f_{MIN} set at 0.87; the OGIP estimates are 482.51 and 1087.56 MCF, respectively.

Figure 4-25 shows an *XZ* and *YZ* cross section through the p90 pessimistic, p50 medium, and p10 optimistic VF distributions. The vertical axis is exaggerated by a factor of 25. The location of each cross section is reported in the titles. The mean p90, p50, and p10 VF values are, 0.942, 0.753, and 0.566, respectively.

Boundary Model

On average, from the fine scale log data within the layer of interest, there are 6 to 7 coal seams with 0.70m thickness. The locally varying grid refinement procedure is implemented so that boundaries can be extracted from VFs at a high resolution. This procedure will also smooth the discontinuities created where well data is honored. The refinement is done in the proportional stratigraphic coordinate system. The original 50 x 50 x 0.5m grid cells located near a boundary where the VF switches sign are downscaled to a sub-grid of 5 x 5 x 5 cells each measuring 10 x 10 x 0.10m.

A facies model is then constructed by setting the fine scale VF values to CBM facies and positive VF values to an *outside* CBM facies. Figure 4-26 shows the facies models of the extracted p90, p50, and p10 coal seam boundaries at each of the cross sections in Figure 4-25.

Sequential Indicator Simulation Comparison

Sequential indicator simulation (SIS) is a popular technique used to model uncertainty. SIS is implemented within the proportional stratigraphic coordinate system to compare with the VF results. The experimental and model horizontal and vertical indicator variograms are shown in Figure 4-27. A total of 50 realizations are generated. The global proportion of the net coal indicator from log data is 0.0635.

The OGIP for each of the 50 realizations is calculated as the proportion of simulated net coal multiplied by the full layer volume (3,000 x 2,000 x 60m). The realizations are then ranked according to OGIP. The OGIP and realization numbers are 704.5 MCF and 27, 803.1 MCF and 24, and 944.5 MCF and 16, respectively. Figure 4-28 shows the SIS models at the same cross sections in Figure 4-25. Notice that although uncertainty is captured, the SIS boundaries are unrealistic compared to the VF boundaries.

4.6 Remarks

When two or more SRFs are employed to characterize the same petrophysical property within the full accumulation limits, there is unavoidable uncertainty in the assignment of grid cells to one SRF or another for subsequent prediction. A new boundary modeling technique using volume functions was developed, described, and implemented with real data. This method is aimed at quantifying global uncertainty with different geologically realistic boundaries. The decision to use this volume function methodology is made when data paucity is not an issue at the exploration phase of the project and the boundary geometry is not amenable to an OB or SB approach.

Uncertainty and probability can be defined in different ways. The classic interpretation of uncertainty is through probabilities which are actual proportions of favorable outcomes over a number of realizations. This analytical assessment is not always available, as is the case for boundary modeling with VF techniques. In these cases, a more subjective assessment is still available. Uncertainty can also be defined according to a combination of a degree of belief supported be expert knowledge.

The VF techniques presented in this chapter are referred to as probabilistic. Since p10 and p90 boundaries, for instance, do not represent actual proportions, the interpretation of these boundaries as probabilistic may be challenged. However, in light of the alternative definitions of uncertainty, more specifically its assessment through degree of belief and expert judgment, this is an accurate reference.

The volume function algorithm presented in this dissertation does not have to be applied to a binary categorical variable representing a geological model. It can also be applied to continuous variable models at several thresholds to generate grade shell boundaries. There are several other avenues for refining VF techniques. Interpolation with kriging in particular offers much flexibility. For example, other than specifying anisotropic boundaries through the variogram, more advanced shape parameters and controls exist. For instance, a deterministic interpretation of geological morphology could be integrated with prior volume function trend modeling.

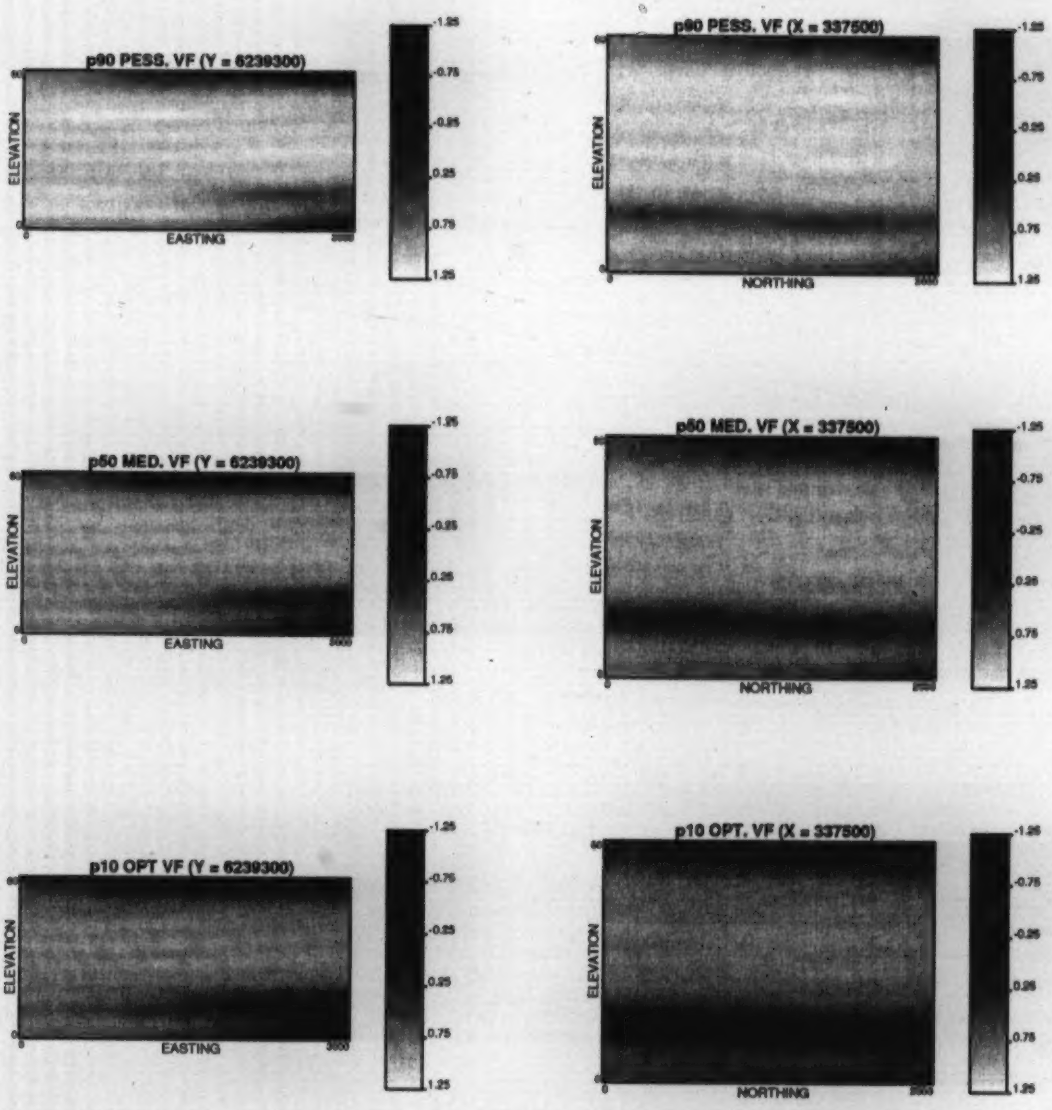

p90 PESS. VF (Y = 6239300)

p90 PESS. VF (X = 337500)

p50 MED. VF (Y = 6239300)

p50 MED. VF (X = 337500)

p10 OPT VF (Y = 6239300)

p10 OPT. VF (X = 337500)

Figure 4-25: Two elevation sections (*XZ* at *Y* = 6239300 on left; *YZ* at *X* = 337500) through the pessimistic p90 (top), p50 (middle), and optimistic (bottom) p10 coal seam VF.

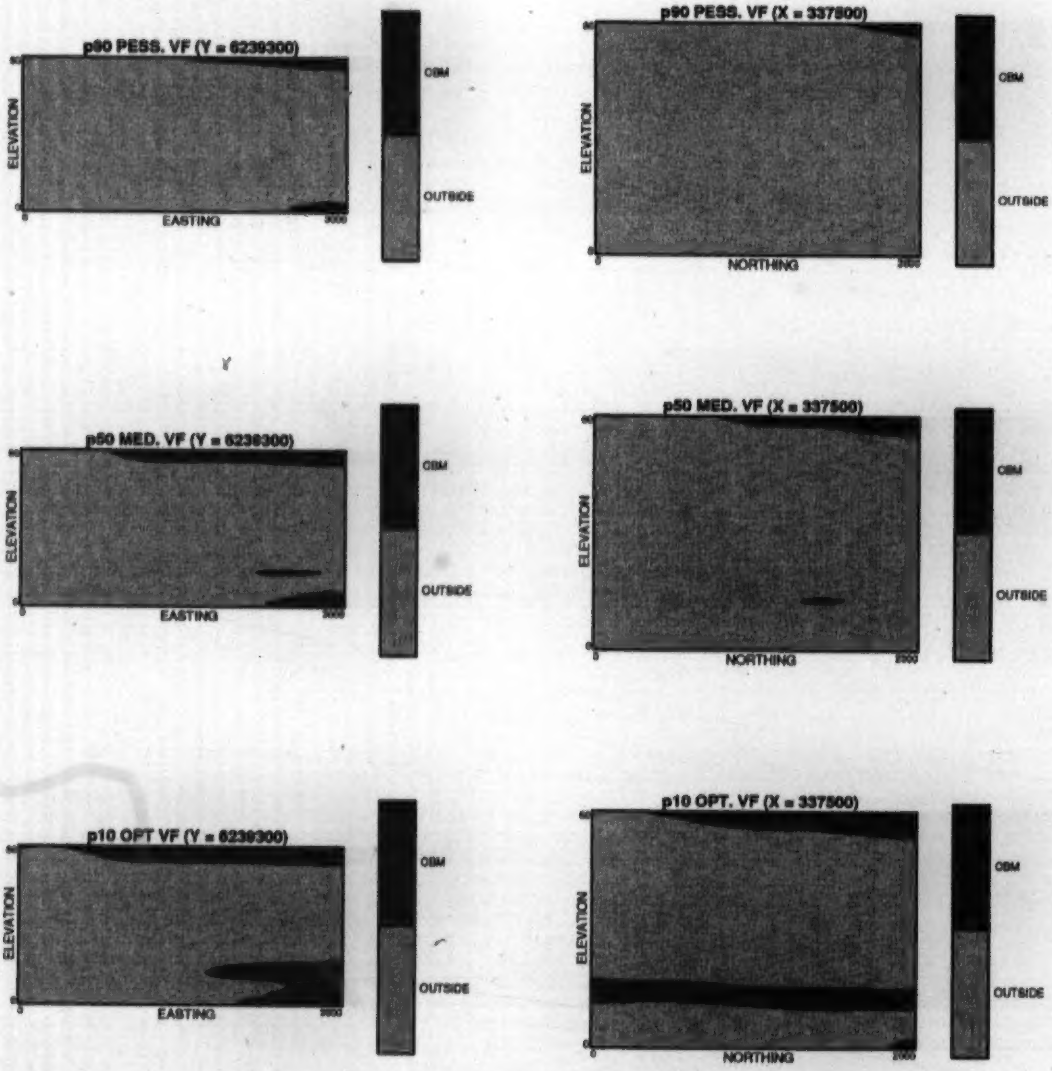

Figure 4-26: Two elevation sections (*XZ* at *Y* = 6239300 on left; *YZ* at *X* = 337500) through the pessimistic p90 (top), p50 (middle), and optimistic (bottom) p10 coal seam facies model built from the VF method.

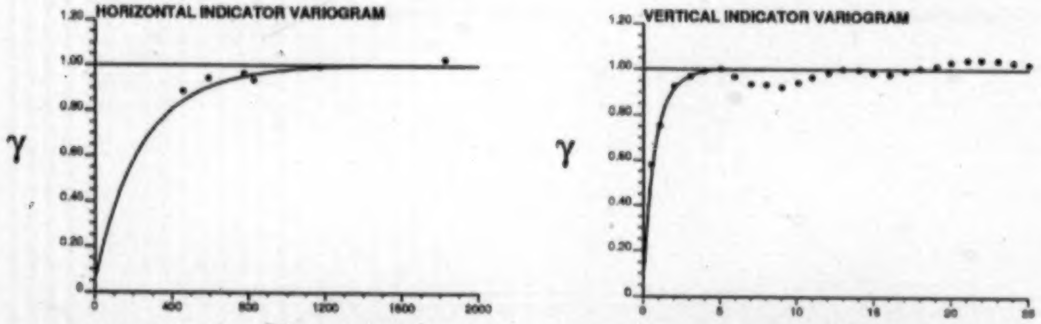

Figure 4-27: The experimental and model horizontal (left) and vertical (right) variograms for SIS.

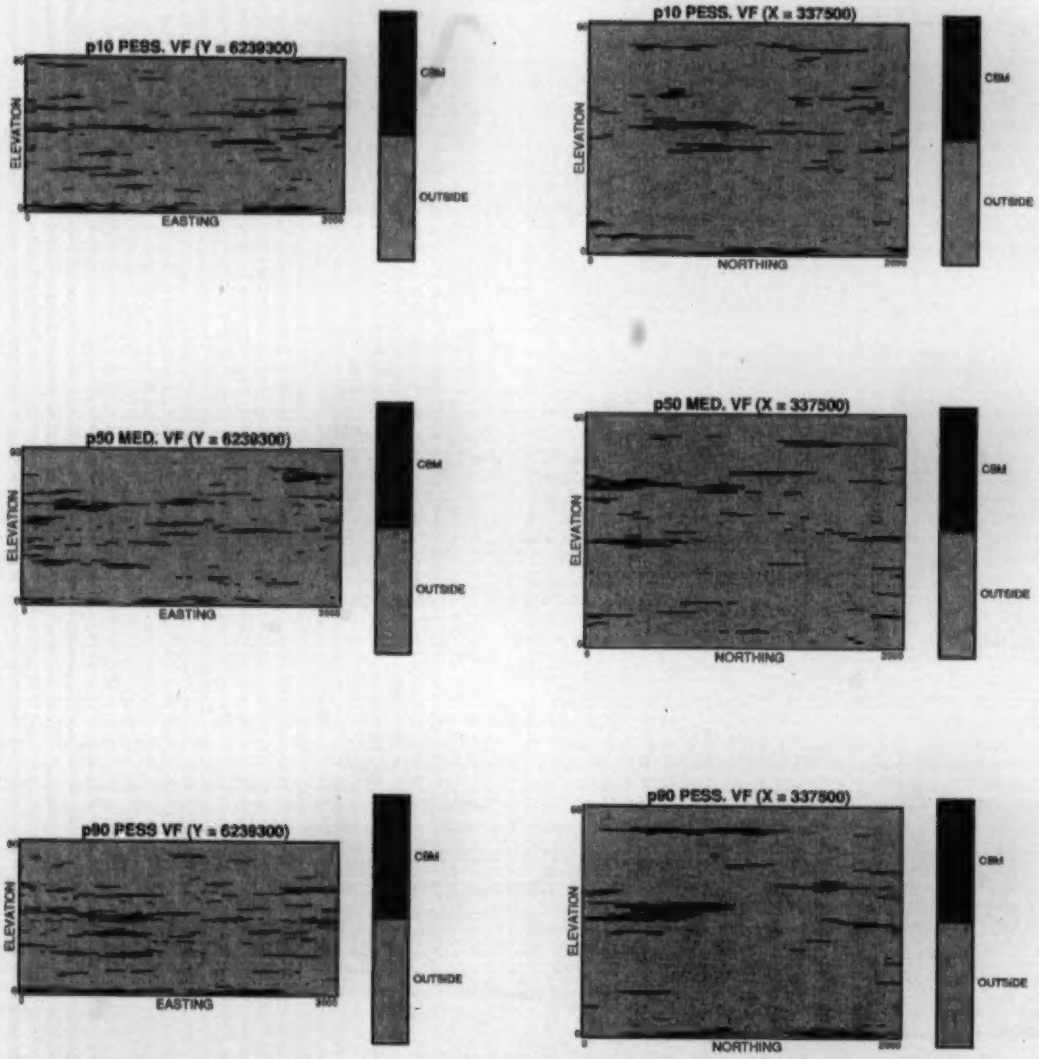

Figure 4-28: Two elevation sections (*XZ* at *Y* = 6239300 on left; *YZ* at *X* = 337500) through the pessimistic p10 (top), p50 (middle), and optimistic (bottom) p90 coal seam facies model built from the SIS method.

CHAPTER 5

NEAR BOUNDARY MODEL MIXING

Recognizing and quantifying the nature of petrophysical property transitions across geological boundaries is an important phase of natural resource characterization using geostatistics. The traditional geostatistical approach of independent SRF predictions in each geological domain may result in unrealistic models. When this more conventional approach is deemed unacceptable by geological interpretation and/or sample data, an alternative approach should be employed.

Domain boundaries are referred to as either *soft* or *hard*, referring to the nature of geological transitions across the boundary. A contact analysis can be undertaken to detect hard and soft boundary transitions as well as different types of soft boundary transitions. An expected value and covariance contact analysis is explained and demonstrated with a simple example. One well defined boundary model mixing approach using a global or local linear model of coregionalization (LMC) framework is briefly described and evaluated. The emphasis of this chapter then shifts to developing an alternative to the LMC framework. A new linear mixing model (LMM) approach to near boundary model mixing is presented with implementation details and an example.

5.1 Principles for Near Boundary Model Mixing

The construction of reasonable models in the presence of boundaries is a vital aspect of making the best possible decision of stationarity. In Chapter 3, two criteria to assess the reasonableness of different approaches to near boundary model mixing were identified: simplicity and geological realism.

5.2 Contact Analysis

To aid in choosing and parameterizing a near boundary mixing model, the geological nature of petrophysical property transitions across the boundary must be understood. This investigation is usually referred to as a contact analysis. The corehole data with rocktype or facies information are required for this analysis.

Four aspects of a contact analysis are addressed: (1) defining transitional behaviors that can occur near geological boundaries, (2) conducting a near boundary expected value study, (3) conducting a near boundary covariance study, and (4) choosing an approach to adopt for model mixing.

5.2.1 Boundary Transition Types

The general nature of petrophysical property transitions across boundaries is described as either soft or hard.

Soft boundaries show a gradational transition across and near boundaries. In Chapter 3, Figures 3-11 (left) and 3-12 show soft boundaries in a copper grade drillhole profile and then a conditioned 2D geostatistical model using near boundary model mixing.

Hard boundaries are described by abrupt changes across and near the boundary. Figures 3-11 (right) and 3-13 show hard boundaries in a copper grade drillhole profile and then a conditional 2D geostatistical model using independent SRFs within each rocktype.

5.2.2 Expected Value Contact Analysis

Soft boundaries show non-stationarity in the mean within a local boundary transition zone. A hard boundary does not show a transition zone; the mean is independent of distance to the boundary. The distinction between a soft and hard boundary can be made based on an expected value contact analysis alone.

Figure 5-1 illustrates a schematic 1D example of soft (left) and hard (right) boundaries separating two domains. Sample data values z are plotted against their distance inside either the left domain 1 d_{12} or right domain 2 d_{21} from the boundary. The expected values are represented with the solid lines. Notice the transition zone bound by broken vertical lines on the left. Although the size of transition zone varies, this zone will be present for soft boundaries. Both a smooth and abrupt non-stationarity is shown within the transition zone with dark and gray shade, respectively. The SRF to the left and right of the transition zone are denoted by $Z_1(\mathbf{u})$ and $Z_2(\mathbf{u})$. In contrast to soft boundaries, the $Z_1(\mathbf{u})$ and $Z_2(\mathbf{u})$ SRF expected values are applicable all the way through their respective domains up until the hard boundary. There is no transition zone present.

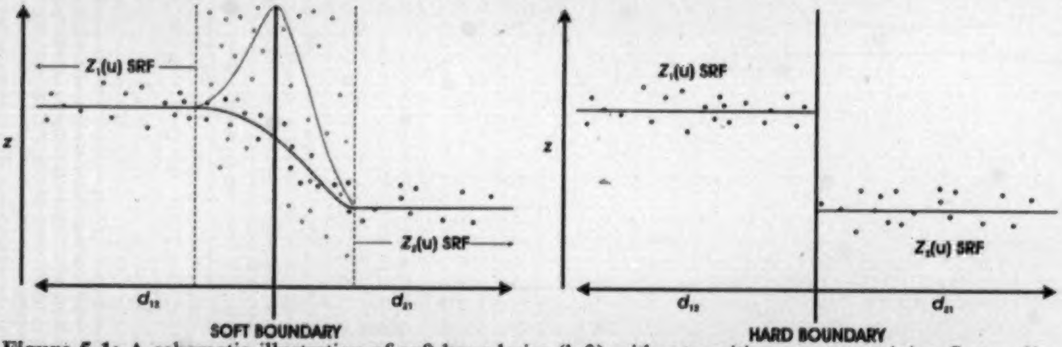

Figure 5-1: A schematic illustration of soft boundaries (left) with a transition zone containing first and/or second order non-stationarities and hard boundaries (right) without this transition zone.

A numerical example is now used to illustrate the expected value contact analysis. The example is derived from the reservoir quality example in Chapter 2. The coordinate axes are reversed, the quality sample values modified within a transition zone and taken to represent mineral quality, and a rocktype model is calculated. Figure 5-2 shows the 2D boundary/rocktype model (left) with the 310 mineral quality sample locations. Figure 5-2 (right) shows a posting of the 310 mineral quality sample grades. The dark rocktype is inside the boundary and generally hosts higher mineral potential while the shaded rocktype outside the boundary generally hosts lower mineral potential.

Figure 5-3 shows a histogram of all 310 samples (left), the 62 samples located inside the boundary (middle), and the 248 samples located outside the boundary (right). The choice to separate the accumulation limits and data into separate domain types is warranted by the presence of two distinct homogeneous distributions of mineral quality within the full distribution of 310 sample data. The domain type histograms are shown in Figure 5-3. The stationary means are 16.54 and 5.96 for rocktypes inside and outside the boundary, respectively.

To maintain the terminology and notation introduced in Figure 5-1, the inside boundary dark rocktype is domain 1 with the $Z_1(\mathbf{u})$ SRF and the outside boundary shaded rocktype is domain 2 with the $Z_2(\mathbf{u})$ SRF. A plot similar to that in Figure 5-1 is generated in Figure 5-4 (left) by plotting each mineral quality sample versus either the nearest distance from inside the boundary to the boundary interface d_{12} or the nearest distance from outside the boundary to the boundary interface d_{21}. The expected value is plotted as a line.

The boundary in Figure 5-4 shows a transition zone with locally varying mean. Choosing the extent of this transition zone is subjective; nonetheless, a 400 unit transition zone is assumed from $d_{12} = 100$ to $d_{21} = 300$ and indicated with broken vertical lines. Since the mean within the 100 unit transition zone from the boundary towards domain 1 is considerably different than the stationary $Z_1(\mathbf{u})$ mean and the mean within the 300 unit transition zone from the boundary towards domain 2 is considerably different than the stationary $Z_2(\mathbf{u})$ mean, the boundary is considered to be soft.

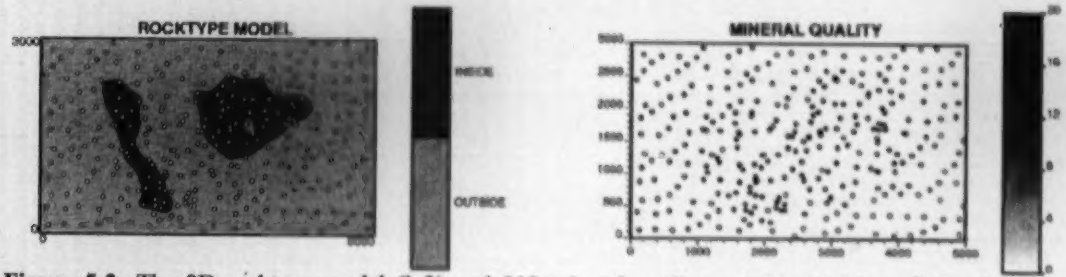

Figure 5-2: The 2D rocktype model (left) and 310 mineral quality samples (right) used for the near boundary mixing example.

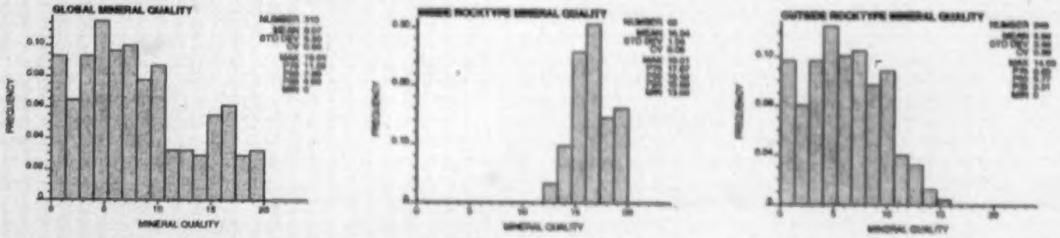

Figure 5-3: The histogram of all 310 samples (left), the 62 samples located inside the boundary (middle), and the 248 samples located outside the boundary (right).

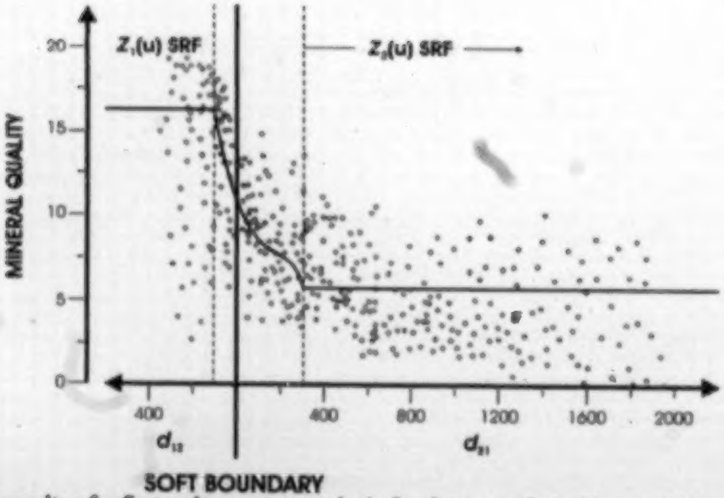

Figure 5-4: The results of a first order contact analysis for the example in Figures 5-2 and 5-3 illustrating that the expected value (solid line) within a transitional zone (broken vertical lines) is non-stationary for a soft boundary types.

5.2.3 Covariance Function Contact Analysis

A soft boundary shows a non-stationary mean within a transition zone near the boundary. A second order non-stationary covariance may or may not be present. This second phase of a contact analysis involves an investigation into the stationarity of the covariance within the transition zone. The result is a further classification of the soft boundary as either a soft boundary with a non-stationary covariance or not. The subsequent choice of a boundary model mixing approach depends on this classification.

The schematic soft boundary illustration in Figure 5-1 includes a smooth (dark line) and abrupt (shaded line) non-stationary mean within the transition zone. A non-stationary mean is a common underlying factor; however, the transition zone covariance of the domain 1 sample data from the abruptly varying case is significantly higher than that for the stationary $Z_1(\mathbf{u})$ covariance outside the transition zone (the variance of shaded points about the shaded line is larger than that for the dark points and line in domain 1). Similarly, the transitional zone covariance of the domain 2 sample data would be significantly higher than that for the stationary $Z_2(\mathbf{u})$ covariance outside the transition zone. Therefore, the type of boundary in the abruptly varying case is classified as a soft boundary with a non-stationary covariance. The boundary type for the smoothly varying case with dark would be a soft boundary without a non-stationary covariance.

The contact analysis for the simple 2D example in Figures 5-2 to 5-4 is continued with the covariance investigation. Figure 5-5 shows the calculated (points) and model (line) variogram function for both the domain 1 sample data (left) and the domain 2 sample data (right). The experimental transition zone domain sample data variograms are shown with shaded points whereas the full dataset variograms are shown with the dark points and modeled with the dark lines. Due to the extent of the transition in Figure 5-4, the transition zone variograms can only be calculated up to a maximum lag vector of 100 for domain 1 and 300 for domain 2; these variograms are not modeled. Notice the slight tendency of the domain 1 transition zone variogram points to decrease towards the domain 2 variogram and the domain 2 transition variogram points to increase towards the domain 1 variogram. Judging the significance of these departures is subjective; however, the non-stationarity of the covariance within the soft boundary transition zone in Figure 5-5 does seem slight. The boundary type for this example would then be classified as soft without a non-stationary covariance.

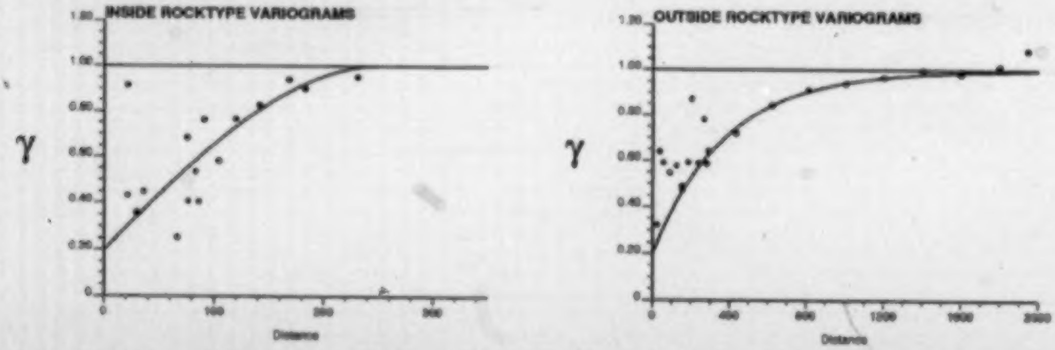

Figure 5-5: The calculated (points) and model (line) variogram for the domain 1 sample data (left) and domain 2 sample data (right). The transition zone sample data variograms are shown with shaded points and lines whereas the full dataset variograms are shown with the dark points and lines.

5.2.4 Independent versus Correlated SRFs

The decision whether or not to adopt a near boundary mixing model is made on the basis of the nature of boundary transitions. This decision can be based on the expected value contact analysis. In the case of a soft boundary, the choice of approach depends on the type of soft boundary as determined from the covariance contact analysis.

Correlated SRFs

A decision to adopt correlated SRFs is made when the nature of the geological boundary is soft. A characteristic feature common to all soft boundaries is non-stationarity in the transition zone surrounding the boundary. A non-stationarity may also be present in the covariance. Outside the transition zone, the SRF formalism is reasonable for prediction. Geologically realistic soft boundary transitions need to be generated with a model of the local non-stationary mean and possibly covariance.

Considering again the schematic in Figure 5-1, some mixture of the $Z_1(\mathbf{u})$ or $Z_2(\mathbf{u})$ SRFs must be considered within the transition zone. Neither $Z_1(\mathbf{u})$ nor $Z_2(\mathbf{u})$ is suitable for characterizing the gradational nature of petrophysical property transitions within the transition zone unless sufficient sample data are available. A model of the transitions may be required.

There are two techniques for near boundary model mixing. The first is the utilization of an LMC framework that can be parameterized to model both first and second order non-stationarity within a soft boundary transition zone [49]. LMC techniques are most suitable for soft boundaries with a non-stationary covariance such as the abrupt non-stationarity case (dark points and line) in Figure 5-1. The alternative linear mixing model

(LMM) approach proposed in this dissertation, is most suitable for modeling soft boundaries with a stationary covariance such as the smoothly varying case (lighter points and line) in Figure 5-1 and the example shown through Figures 5-2 to 5-5. These two models are described in the next two sections.

Independent SRFs

Independent SRFs are invoked for hard boundaries. Hard boundaries do not have a transition zone. The $Z_1(\mathbf{u})$ and $Z_2(\mathbf{u})$ SRF means are applicable all the way through their respective domains up until the hard boundary.

The SRF mean and covariance are defined from the sample data within each domain and used for prediction. The results are then merged together according to a rocktype model. Predictions in one SRF are not influenced by predictions from a different SRF.

5.3 The Linear Model of Coregionalization (LMC) Approach

Soft boundaries mean that both petrophysical property samples and model predictions influence both sides of the boundary within the transition zone. The SRFs surrounding the boundaries must somehow be correlated or mixed. The LMC approach explicitly defines the correlation between surrounding SRFs with a model of cross covariance.

The LMC technique was developed in 2004 by Larrondo [49]. Traditionally, the LMC models the direct and cross spatial law of different variables. Here, the same variable is used; it is the different rocktypes or facies surrounding the soft boundary that are used in the LMC. For example, the $Z_1(\mathbf{u})$ inside boundary SRF and the $Z_2(\mathbf{u})$ outside boundary SRF in Figures 5-1 through 5-5. Once parameterized, the LMC is used within a co-kriging or co-simulation prediction algorithm.

Larrondo also proposed and developed an LMC with non-stationary parameters inside the transition zone to handle soft boundaries with a non-stationary covariance such as the abrupt non-stationarity depicted in Figure 5-1 with a dark line. Implementation details and results are available in [49].

5.4 The Linear Mixing Model (LMM) Approach

The linear mixing model (LMM) is a special non-stationary RF model applied within the transition zone of a boundary classified as soft without a non-stationary covariance. The LMM amounts to specify the influence of surrounding SRFs with a linear weighting function. The form of the LMM RF is:

$$Z_{\text{LMM}}(\mathbf{u},\mathbf{d}) = \sum_{k=1}^{K} a_k(\mathbf{u},\mathbf{d}) \cdot Z_k(\mathbf{u},\mathbf{d}) \quad \forall \mathbf{u} \in \mathbf{D} \qquad (5\text{-}1)$$

where $Z_{\text{LMM}}(\mathbf{u};\mathbf{d})$ is the new non-stationary LMM RF model at the location $\mathbf{u}$ a distance $\mathbf{d}$ away from the soft boundary, $\mathbf{D}$ is the transition zone overlapping $k = 1,\ldots,$ K different surrounding rocktypes and corresponding $Z_k(\mathbf{u};\mathbf{d})$ SRFs, and $a_k(\mathbf{u};\mathbf{d})$ are the weights given to each $Z_k(\mathbf{u};\mathbf{d})$ SRF in the transition zone.

In practice, the $Z_{\text{LMM}}(\mathbf{u};\mathbf{d})$ RF is used for merging predictions together with the rocktype model. That is, original sample data are not mixed. Predictions from the $Z_k(\mathbf{u})$ SRFs are unchanged outside the transition zone. Inside the transition zone, the mixed predictions have the following form:

$$z^{*}_{\text{LMM}}\left(\mathbf{u},\mathbf{d}_{ij}\right)=\sum_{k=1}^{\text{K}} a_k\left(\mathbf{u},\mathbf{d}_{ij}\right)\cdot z^{*}_{k}\left(\mathbf{u},\mathbf{d}_{ij}\right) \quad \forall \mathbf{u}\in\mathbf{D}_{ij} \quad i=1,\ldots,\text{K}; j=1,\ldots,\text{K}\left(i\neq j\right) \tag{5-2}$$

where the $\mathbf{d}_{ij}$ notation is now used to indicate the portion of soft boundary transition zone being considered. For example, $\mathbf{d}_{12}$ are distances inside the domain 1 transition zone and $\mathbf{d}_{21}$ are distances inside the domain 2 transition zone in Figure 5-1.

The $a_k(\mathbf{u};\mathbf{d})$ weights identify the influence of the $Z_k(\mathbf{u};\mathbf{d})$ SRF predictions overlapping a soft boundary transition zone. The $a_k(\mathbf{u};\mathbf{d})$ weighting function is a linear function of the distance $\mathbf{d}$ from the soft boundary. The $a_k(\mathbf{u};\mathbf{d})$ weights for a particular distance $\mathbf{d}$ must sum to one:

$$\sum_{k=1}^{\text{K}} a_k\left(\mathbf{u};\mathbf{d}_{ij}\right)=1; \quad i=1,\ldots,\text{K}; j=1,\ldots,\text{K}\left(i\neq j\right) \tag{5-3}$$

Figure 5-6 shows two simple $a_k(\mathbf{u};\mathbf{d})$ weighting functions for a two domain setting. The weight profiles on the left were used earlier in Chapter 3 to merge simulated copper grade predictions from a primary copper sulphide SRF and from a secondary copper oxide SRF within a 100m transition zone, 50m into each domain from the soft boundary. The weight profiles on the right were then used to merge simulated copper grades from a leached SRF and the secondary copper oxide SRF within a 40m transition zone, 20m into each domain from this soft boundary. Figure 3-12 shows the final merged copper realization. Although the weight profiles in Figure 5-6 are symmetric about the boundary, they do not have to be. In practice, the weighting functions are determined with the expected value contact analysis results such as in Figure 5-4.

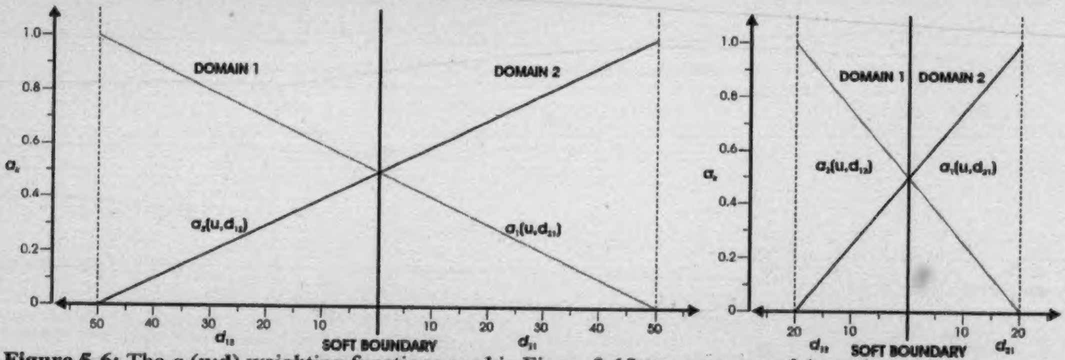

Figure 5-6: The $a_k(\mathbf{u};\mathbf{d})$ weighting functions used in Figure 3-12 to represent soft boundaries.

The $Z_{\text{LMM}}(\mathbf{u};\mathbf{d})$ RF is non-stationary in the first order expected value. This is necessary in order to accurately represent first order non-stationarities from the contact analysis. An assumption underlying the LMM technique, however, is the $Z_{\text{LMM}}(\mathbf{u};\mathbf{d})$ RF is stationary in the second order covariance, that is, the $Z_{\text{LMM}}(\mathbf{u};\mathbf{d})$ transition zone spatial laws are the same as the corresponding $Z_k(\mathbf{u})$ SRF covariance on either side of the boundary. There will always be some degree of second order covariance non-stationarity since the spatial correlation in the transition zone is a function of both the $Z_1(\mathbf{u})$ and $Z_2(\mathbf{u})$ covariance functions. However, it should be decidedly minor as in Figure 5-5 when implementing the LMM approach.

5.4.1 Application Example

The simple 2D example carried through this chapter in Figures 5-2 to 5-5 is also used to illustrate the application of the LMM. From the contact analysis results in Figures 5-4 and 5-5, the boundary is classified as soft without a non-stationary covariance; the LMM technique is appropriate.

Figure 5-2 shows the two domain rocktype model as well as the location and value of 310 mineral quality samples. The $Z_1(\mathbf{u})$ and $Z_2(\mathbf{u})$ SRF parameters were previously calculated. Figure 5-3 shows the stationary univariate distributions of mineral quality samples within both domains; the $Z_1(\mathbf{u})$ and $Z_2(\mathbf{u})$ SRF expected values are 16.54 and 5.96, respectively. Figure 5-5 then shows the second order stationary $Z_1(\mathbf{u})$ and $Z_2(\mathbf{u})$ SRF calculated (dark points) and variogram model (line). These isotropic 20% nugget variogram models are written analytically as:

$$\begin{aligned}\gamma_{Z_1}(\mathbf{h}) &= 0.20 + 0.80 \cdot Sph(\mathbf{h})_{\mathbf{a}=250\mathrm{m}} \\ \gamma_{Z_2}(\mathbf{h}) &= 0.20 + 0.80 \cdot Exp(\mathbf{h})_{\mathbf{a}=1150\mathrm{m}}\end{aligned} \qquad (5\text{-}4)$$

The first step is implementing prediction using each SRF parameterized by its histogram and covariance assuming the full accumulation limits for each SRF. The data is filtered by rocktype for each predicted model. Figure 5-7 shows the simulated $Z_1(\mathbf{u})$ predictions (left) and $Z_2(\mathbf{u})$ predictions (right). Notice the longer range and lower mineral quality of spatial correlation in the $Z_2(\mathbf{u})$ simulation results.

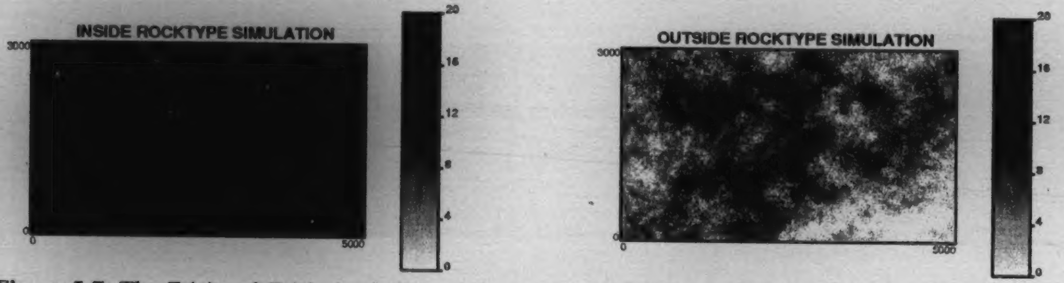

Figure 5-7: The $Z_1(\mathbf{u})$ and $Z_2(\mathbf{u})$ simulation results assuming the full accumulation limits are all the inside boundary rocktype (left) and all the outside boundary rocktype (right).

The next step is parameterizing the LMM with the $a_k(\mathbf{u};\mathbf{d})$ weighting function. The first phase expected value contact analysis results in Figure 5-4 are used to infer the $a_1(\mathbf{d}_{12})$ and $a_2(\mathbf{u};\mathbf{d}_{21})$ weight profiles in Figure 5-8 within the soft boundary transition zone. The profiles are not symmetric about the boundary line since the transition zone within domain 1 is smaller than that for domain 2.

The simulation results in Figure 5-7 are now merged using the $Z_{LMM}(\mathbf{u};\mathbf{d})$ RF within the transition zone. Figure 5-9 (left) shows the results. For comparison, the conventional merge without the transition zone $Z_{LMM}(\mathbf{u};\mathbf{d})$ is also shown (right). The near boundary LMM satisfactorily captures the transitional nature of the soft boundary described in the expected value contact analysis. It is a simple model and generates geologically realistic results. The conventional merge, however, does not capture geologically realistic soft boundary transitions as indicated in the contact analysis.

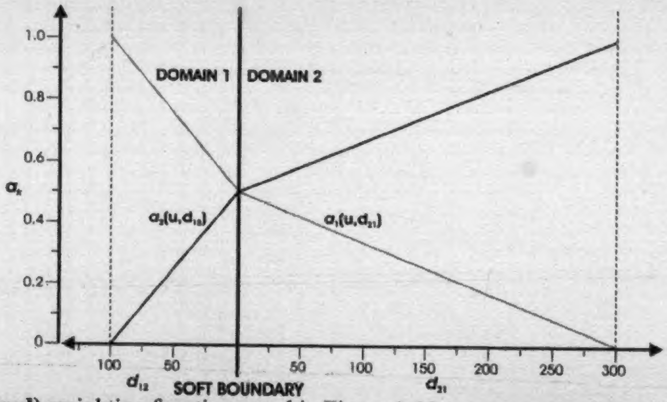

Figure 5-8: The $a_k(\mathbf{u};\mathbf{d})$ weighting functions used in Figure 3-12 to represent soft boundaries.

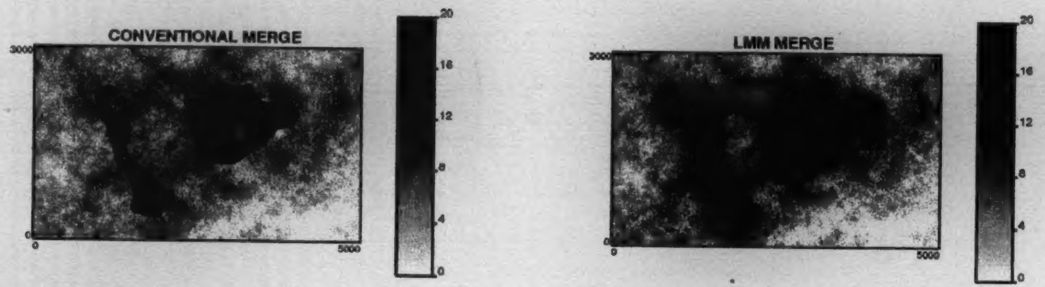

Figure 5-9: The conventional merge (left) and near boundary LMM mixing model merge (right) of the simulations in Figure 5-7.

5.5 Reasonableness

Reasonability is based on simplicity and the ability to capture geologically realistic boundary transitions. Independent SRFs are the simplest, but reasonable only for hard boundaries. Alternative models for transition zones such as the global LMC, LMC with locally varying mean and covariance parameters, or LMM are evaluated on the basis of simplicity and their suitability to the particular type of soft boundary transition determined from the contact analysis.

The global LMC technique will effectively capture soft boundary transitions such as the smoothly varying non-stationarity depicted in Figure 5-1 with a shaded line. However, the LMC is notoriously difficult to parameterize considering the number variograms that need to be calculated and modeled within constraints to ensure a licit LMC model. This level of complexity and effort is usually warranted only for soft boundaries with a non-stationary covariance. The LMC approach is overly complex for handling soft boundaries without a non-stationary covariance. The linear mixing model (LMM) is presented as a more straightforward option for handling this type of soft boundary.

5.6 Remarks

Near boundary model mixing can be important. Choosing separate and homogeneous domain types and modeling these domain boundaries will not account for the transitional nature of petrophysical properties across the boundaries. The only situation where this independent SRF approach is reasonable is when the domain boundaries can be classified as hard based on an expected value contact analysis.

There are two major categories of near boundary mixing models. The first is an LMC framework. This technique can be parameterized to account for a soft boundary with a non-stationary mean and covariance. The LMM technique proposed in this thesis is reasonable for a soft boundary without a non-stationary covariance.

CHAPTER 6

TREND MODELING

Generating numerical models with realistic geologic large-scale features is a critical aspect of natural resource characterization using geostatistics. A *trend* consists of deterministic variability. Modeling a trend should not incorporate any variability that is not deterministic and better suited for probabilistic modeling with geostatistics. The trend should be reproduced in prediction results; however, this does not mean the trend must always be used directly for prediction. Chapter 7 explains when and how the trend is used for prediction. This chapter is primarily concerned with creating reasonable trend models.

With many data the trend model is not important and deterministic knowledge is ensured through data conditioning. Data conditioning is based on the data values and improved knowledge of geological domains. The domains can be relatively small if there is enough data to parameterize the enclosed SRFs. Often, however, there are too few sample data to choose many domains and still reliably infer SRF parameters. In practice, domains are relatively large with a small amount of data. A deterministic interpretation of large-scale variability is important because it may not otherwise be captured by usual prediction with SRF parameters.

Trend modeling is unavoidably subjective and dependent on the interpreter. This has led to a variety of trend modeling techniques each with different implementation parameters. These methods could be categorized as either manual or automatic. Manual techniques are straightforward. Some different automatic techniques are reviewed with examples and implementation guidelines. They are then evaluated according to the reasonability criteria presented in Chapter 3. Automation can possibly undermine the required determinism of a trend model. Nonetheless, automated techniques can often be implemented to build a reasonable trend. Crucial implementation parameters pertaining to building reasonable models of the trend are explained.

Two probability combination schemes that can be used to construct 3D and 2D trend models from lower dimensional 2D and 1D trend models are presented.

6.1 Trend Modeling Principles

The construction of a reasonable trend model is an essential aspect of making the best possible decision of stationarity. Chapter 3 identifies four criteria used for evaluating the reasonableness of different trends: (1) simplicity, (2) subjectivity, (3) low variability, and (4) geological realism. These evaluation criteria are recalled.

The trend modeling algorithm formulation, description, and implementation should be relatively straightforward. Too complex algorithms with several sensitive parameters will be difficult to implement, explain, and justify in practical settings.

Although the trend is necessarily subjective, the trend should not be significantly different depending on the interpreter. This motivates careful parameterization choices in automated trend modeling.

Over-interpreting geological features incorporating too much deterministic information should be avoided. This is a common problem. The most important guideline for building reasonable trend models is avoiding the incorporation of spatial variability that cannot be accurately considered as deterministic and known. Such variability should be left to a SRF and modeled with conventional geostatistics. The resulting trend models that follow this guideline possess low variability. Highly variable trend models are only suitable when the geological formation is well known and fully supported by abundant hard sample data and soft secondary data sources.

The trend model should depict geologically realistic large-scale deterministic variability. Since the trend model should be honored in subsequent predictions, the final numerical model of any petrophysical property of interest should also be geologically realistic in that large-scale deterministic variability will be fairly represented together with stochastic variability representing the inherent uncertainty where the variability cannot be modeled deterministically.

6.2 Key Trend (Modeling) Concepts

Trends are subjective. It is for this reason that trends and modeling the trend is a notoriously elusive phase of the modeling process. Before modeling the trend, it is important to understand what constitutes a trend and what its role is in geostatistical modeling.

The *trend* is a deterministic gradually varying expectation in a variable over some domain of interest.

The term *trend* is used in many settings. For example, economists often use this term to describe an increase or decrease of a mineral or hydrocarbon commodity price over some time period. For geostatistical applications, the variable of interest is a petrophysical property and the domain of interest corresponds to the set of domain volumes identified by a previously built boundary model within which separate SRFs apply.

The trend describes variability that is known deterministically with certainty. Uncertain heterogeneity is then modeled with geostatistical techniques capable of quantifying the inevitable uncertainty.

The trend is denoted by $m(\mathbf{u})$ suggesting that the mean is a function of location $\mathbf{u}$ within the domain $\mathbf{D}$. Recall the definition of first order stationarity in relation (2-7) where $m(\mathbf{u})$

is set to a constant *m* value that is independent of location **u**. A trend is, therefore, a modification of first order stationarity. The presence of a trend does not necessarily imply that the second order covariance is location dependent; it may be possible to assume second order stationarity in the presence of a trend in the mean.

Purpose

The trend model has two purposes. The first includes visualizing deterministic variability and validating subsequent estimation and/or simulation models. Predicted models must honor the trend in expected value. The second purpose of a trend model is its explicit use for prediction. Here, the trend is directly included in prediction at unsampled locations. This is not always relevant and is used only when the trend cannot be satisfactorily reproduced with conventional geostatistical prediction techniques that do not explicitly use the trend. Different approaches to predicting with a trend are addressed in Chapter 7.

Significance

The significance of a trend model is established by whether or not it is reproduced by conventional geostatistical prediction results that do not explicitly account for the trend. As the inconsistency between these results and the trend increases, the significance of the trend increases. When significant, direct use of the trend should be implemented.

The trend is often more significant when data are sparse, but a relatively high level of deterministic understanding is also still available. The importance of the trend is highlighted in sparsely sampled areas where the deterministic nature of the trend is an important component of the variability. In densely sampled areas, the trend is less important.

Detection

The detection of significant trends is an important concept for subsequent prediction and validation. Although the trend is subjective with various deterministic information sources and interpretations, detection is often based on the sample data. Geological interpretation should form the primary basis for detection. Data should then support the interpretation.

The variogram inference phase of geostatistical modeling can also be used to support the presence of a trend. A trend is supported if the calculated variogram shows an increase above the sill variance for increasing lag vectors **h**. Anisotropy in the trend may be detected by noting this relationship in different directions.

Figure 6-1 shows a reproduction of the core photograph and derived porosity profile over a 20m elevation interval (see also Figure 3-14). Recall the geologically interpreted evidence for a trend: a fining upward tendency is present due to a transition of depositional environments from coarse grained fluvial to estuary sand facies dominating lower elevations to fine grained marine shale facies dominating higher elevations. The vertical variogram is calculated and shown to the right. The presence of this trend is supported with the systematically increasing variogram value above the sill for lags greater than roughly 10 units.

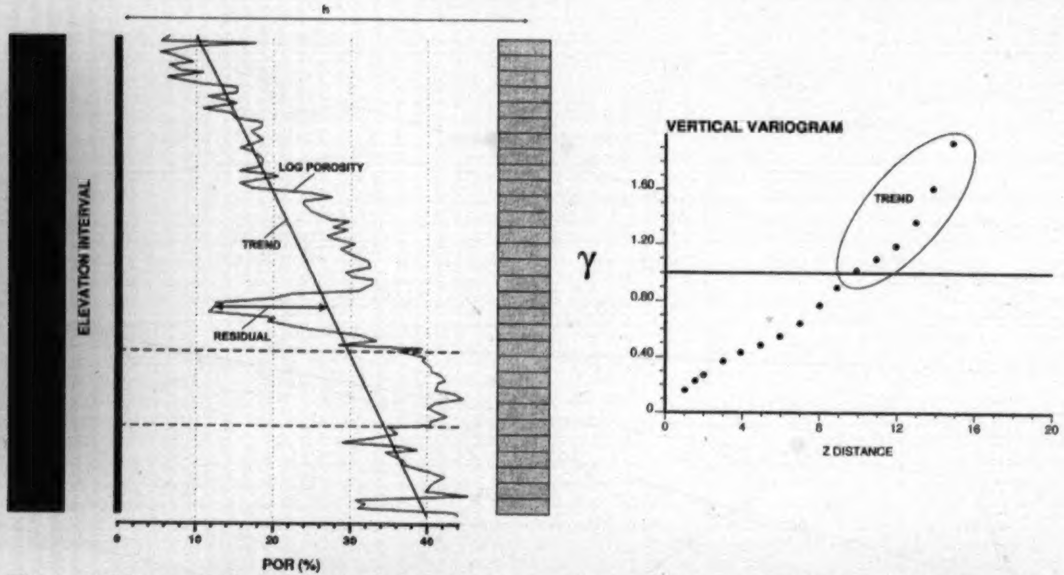

Figure 6-1: A corehole photograph from the Athabasca Oil Sands, Alberta, Canada (left) and related fining upward log porosity profile (right) with additive trend and residual components indicated. An unestimated vertical string of thirty grid cells is also shown at a lag vector **h** away from the porosity profile location.

Scale

Interpreting and modeling the trend is highly dependent on scale. For example, if the elevation interval is chosen too small, it is even possible to observe a coarsening upward trend in the porosity interval of Figure 6-1; conversely, the elevation interval enclosed by the broken horizontal lines suggests there is no trend at all. A deterministic understanding of the geology is required to support modeling a trend.

There is a reasonable scale for interpreting and modeling a trend. Previously constructed boundary models identify domain types within which separate SRFs can be applied. Each SRF assumes a constant mean and covariance throughout its corresponding domain. The trend model suggests that first order stationarity is inappropriate. In order to make this assessment fairly, the scale of the domain must be considered. It would be unfair, for example, to consider a trend at a much smaller scale.

Balancing Deterministic and Stochastic Variability

Most geostatistical prediction tools that employ kriging estimators requires the additive decomposition of the original $Z(\mathbf{u})$ RF into a locally varying mean or trend model RF component $m(\mathbf{u})$ and a stochastic residual RF component $R(\mathbf{u})$. This decomposition leads to a corresponding decomposition of the original $Z(\mathbf{u})$ RF variability:

$$\begin{aligned} C_Z(\mathbf{0}) &= C_m(\mathbf{0}) + C_R(\mathbf{0}) + 2\cdot C_{mR}(\mathbf{0}) \\ \sigma_Z^2 &= \sigma_m^2 + \sigma_R^2 + 2\cdot\sigma_{mR}^2 \end{aligned} \qquad (6\text{-}1)$$

where $C_Z(\mathbf{0})$ or σ_Z^2 is the $Z(\mathbf{u})$ variance, $C_m(\mathbf{0})$ or σ_m^2 is the $m(\mathbf{u})$ variance, $C_R(\mathbf{0})$ or σ_R^2 is the $R(\mathbf{u})$ variance, and $C_{mR}(\mathbf{0})$ or σ_{mR}^2 is the covariance between the $m(\mathbf{u})$ and $R(\mathbf{u})$ RFs.

Balancing deterministic and stochastic variability is the most important concept of trend modeling since it directly relates to the criteria for a reasonable trend model. In practice, due to the subjective nature of trends, it is quite challenging to separate variability that should be modeled deterministically with a trend model from variability that should be modeled stochastically with geostatistical techniques. However, relation (6-1) provides a mechanism to assign some quantitative guidelines to this balance.

The balance between deterministic and stochastic variability can be calculated from the ratio of σ_m^2 to σ_Z^2. For most practical settings, this ratio should be no greater than 0.50, that is, no more than 50% of the original $Z(\mathbf{u})$ RF variability should be modeled without uncertainty deterministically. Subjectivity is inescapable – the 50% guideline is still subjective. This guideline will change with the amount of hard and soft geological data.

The covariance term in relation (6-1), $C_{mR}(\mathbf{0})$ or σ_{mR}^2, is an important part of deciding on the approach to account for a trend. Some techniques are able to capture complex relationships between $m(\mathbf{u})$ and $R(\mathbf{u})$ with possibly high absolute $C_{mR}(\mathbf{0})$ or σ_{mR}^2 values; however, most prediction tools assume that $m(\mathbf{u})$ and $R(\mathbf{u})$ are independent. More detail is given in Chapter 7.

6.3 Trend Modeling Approaches

For most geological settings, the recommended procedure in this thesis is investigating and building a trend in 2D over the full aerial extent of the domain, doing the same for the 1D vertical extent of the domain, and then combining these lower dimensional trends into a 3D trend over the full domain.

There are several methods available for generating lower dimensional 2D and 1D aerial and vertical trends, each method with its own implementation details, advantages and disadvantages, as well as range of applicability. Five different trend modeling techniques are now presented: (1) hand mapping, (2) moving window averages, (3) global inverse distance, (4) global block kriging, and (5) kriging the trend.

These five trend modeling techniques can effectively capture any trend encountered in practice. The parameters may change depending on the geological setting and intended purpose of the numerical model.

The implementation of each automatic trend modeling technique is demonstrated with a common example that mimics geology found within the McMurray Formation located in northern Alberta, Canada. Trend modeling is performed for facies proportions. In this case, $m(\mathbf{u})$ is taken as $p_k(\mathbf{u})$, the locally varying probability of facies k. There is $k = 1,\ldots, 4$ facies: sand, breccia, interbedded sand/shale, and shale. The domain of the McMurray Formation example and 159 available corehole locations are shown in Figure 6-2. The domain is one township. The 36 sections are delineated with dark broken lines; half-section lines are shaded broken lines. The formation is about 100m thick. The trend may be significant near the outside of the lease where detailed sampling is not available.

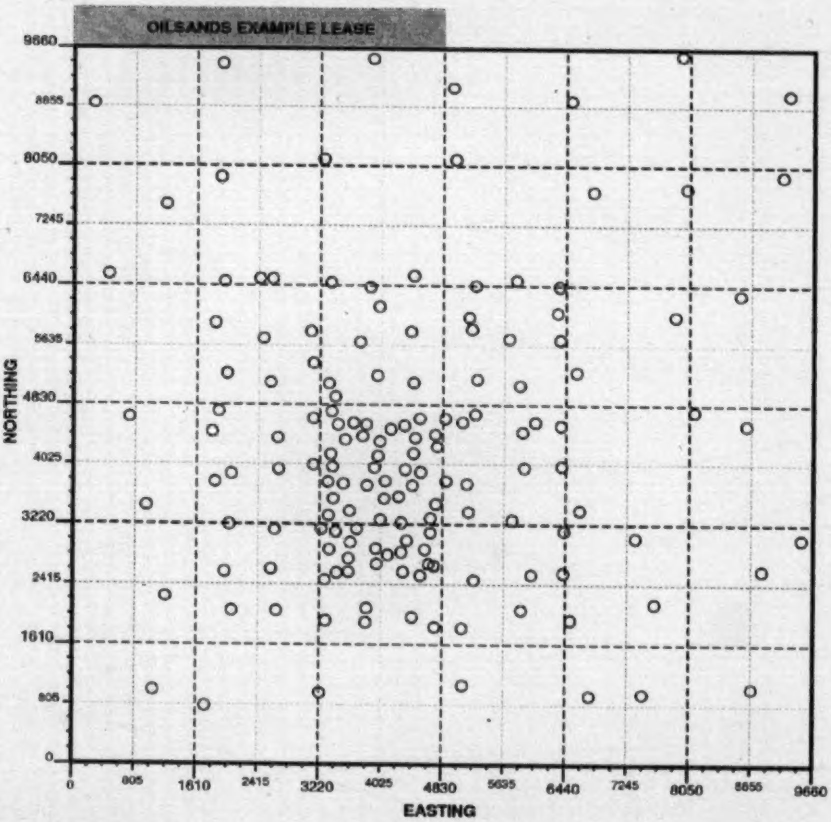

Figure 6-2: Township domain and 159 corehole locations used for describing trend modeling techniques presented in this chapter.

6.3.1 Hand Mapping

Hand mapping is the first of five techniques that can be implemented to generate 2D aerial or 1D vertical trend models. This is a manual trend modeling approach.

Description

The hand mapping process for trend modeling involves simply hand contouring large-scale deterministic features of the petrophysical property of interest. All the fundamental rules and guidelines for drawing contour maps apply. In general, a relatively large contour interval should be adopted in order to avoid incorporating too much geological heterogeneity. The contour map can be used for comparison to prediction results or and, when the trend is deemed significant, for direct integration into prediction algorithms.

Hand mapping forces the interpreter to make decisions about large-scale trends. In terms of the simplicity and subjectivity criteria cited previously, this approach is often the most reasonable. However, these methods are not repeatable and may be difficult to adjust when faced with new data. Moreover, if required, their digitization and incorporation into prediction algorithms may be time consuming and cumbersome.

Projects that require automation such as ones with abundant sample data within multiple large domain types should avoid hand mapping and contouring. An automatic trend modeling technique may be suitably parameterized and implemented.

6.3.2 Moving Window Average

Moving window averages of petrophysical properties are the first and simplest of the four automatic trend modeling techniques.

Description

Moving window averages are implemented by translating a specified 1D or 2D window over the domain and averaging data values. The window extents are centered on each grid cell location **u** to identify the sample locations that should receive influence. The windows overlap. Large windows result in more overlap and smoother trend models. This allows for the flexibility to generate low variability trends. A power law average could be applied for a permeability trend.

Moving window average techniques are simple and effective for trend modeling. Subjectivity, low variability, and geological realism criteria can all be satisfied by changing the size of window and amount of overlap. However, the trend is often calculated with equal weighted sample data regardless of where the samples are located within the windows. Direct control over spatial correlation is not possible.

It is recommended that the moving window average technique be applied to 1D trend modeling. Fitting the window averages is more straightforward in 1D. In 2D, the approach is similar to hand mapping techniques. There are more sophisticated techniques for 2D trend modeling capable of directly accounting for the spatial correlation and the configuration of the data.

Application

The moving window averages technique is used to generate a vertical trend model for all four facies types in the McMurray Formation example. There is a large amount of data; the 159 wells are logged at 0.50m intervals for a total of 31,800 sample locations. Therefore, a relatively small vertical window size of 4m can be used to calculate the moving window averages. Figure 6-3 shows the moving window averages at a 2m vertical grid cell resolution. At each 2m grid cell location, the facies averages or proportions are standardized so that they add to one.

The by-facies results in Figure 6-3 are smooth enough to interpret locally varying proportions, but not smooth enough for the final vertical trend model. These points are fit with lines and combined into a full by-facies trend model. This trend model, referred to as a vertical proportion curve, is shown in Figure 6-4. The most significant trend is in interbedded sand/shale facies where there is a strong tendency for low proportions deeper in the formation. The proportion of sand has a slight tendency to increase with depth, significant breccia proportions are found at elevations lower than 215m, and the proportion of shale is constantly low regardless of elevation.

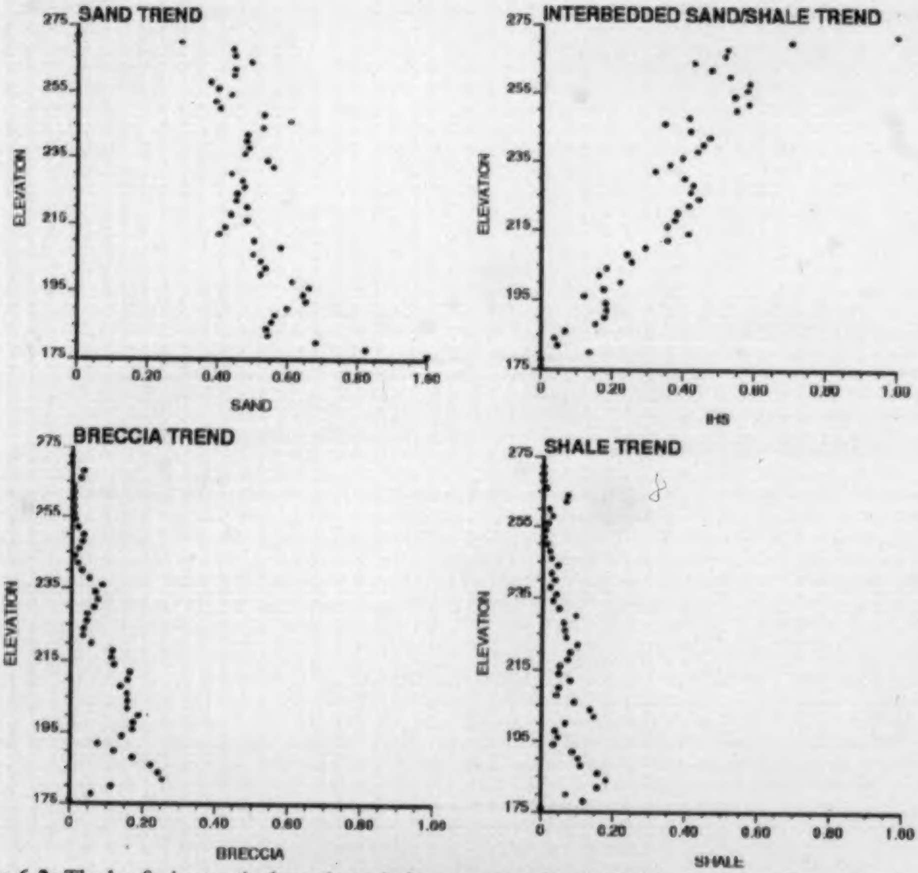

Figure 6-3: The by-facies vertical moving window averages for the McMurray Formation example.

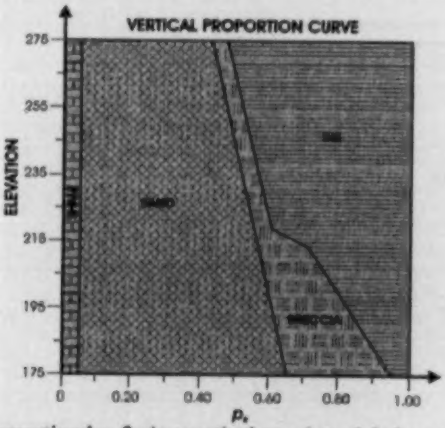

Figure 6-4: The McMurray Formation by-facies vertical trend model shown as a vertical proportion curve.

6.3.3 Inverse Distance

Inverse distance with a global search is the next automatic technique for modeling the trend presented in this dissertation. This estimation technique was discussed in Chapter 4 to interpolate volume function distance codes. The implementation here is similar.

Description

Recall the inverse distance estimator in relation (4-1) and relation (4-2) for the inverse distance weights in this estimator. Note that a global search and relatively low inverse distance power ω can be used to generate a smooth distribution of estimates. This inverse distance scheme was applied in Chapter 4 with VF distance codes; the implementation for constructing a trend model shares the common goal of generating a smooth spatial distribution of estimates. Anisotropy can be incorporated into the calculation of distances and weights.

There is, however, one essential difference between the implementation of global inverse distance in Chapter 4 versus the implementation here for trend modeling. This difference is exactitude. Exactitude is not a desired property for the trend. The next chapter shows that trend models that reproduce the original sample conditioning data exactly result in a fundamentally flawed $R(\mathbf{u})$ RF. The recommendation and implementation is using a non-zero nugget constant c.

Inverse distance is a straightforward tool for trend modeling. Flexibility can be achieved by adjusting the inverse distance power ω, the nugget constant c, and the anisotropy ratio. No additional post processing is required; the trend model is made up of the inverse distance estimates. One possible drawback may be that the variogram is not directly incorporated into the estimates; however, this is seldom a concern for trend modeling in many geological scenarios since the trend model should conservatively model spatial variability. Inverse distance is often applied in 2D to construct aerial trend models.

Application Example

The technique is now implemented to generate a horizontal trend model for all four facies types within the domain lease. The conditioning data used are the facies proportions for each of the 159 wells. At each well location, the facies proportions will add to one. The trend model is directly interpolated to a 60 x 60m aerial grid network within the township lease with a total of 25,921 grid cells (161 x 161). An inverse distance power of 1.5 is used with a global search.

Figure 6-5 shows the final trend model for each of the four facies types. The proportion of sand and interbedded sand/shale seems to have a tendency to decrease and increase, respectively, towards the center of the domain. Similar to the vertical trend, the breccia and shale facies proportions are low, constant, and independent of aerial location.

6.3.4 Global Block Ordinary Kriging

Block kriging with a global search is another automatic technique for modeling the trend. This estimation technique was presented in Chapter 4 to interpolate volume function distance codes. The implementation here is similar.

Description

Recall in relation (2-29) the general kriging estimator and the system of equations in (2-40) that minimize the error variance in (2-35). Recall also that a global search and relatively continuous variogram can be used to generate a smooth distribution of kriging estimates. Although in Chapter 4 this global kriging scheme is applied to VF distance codes, the implementation here for constructing a trend model shares the common goal of generating a smooth spatial distribution of estimates. Anisotropy is directly incorporated into the calculation of the weights through the variogram.

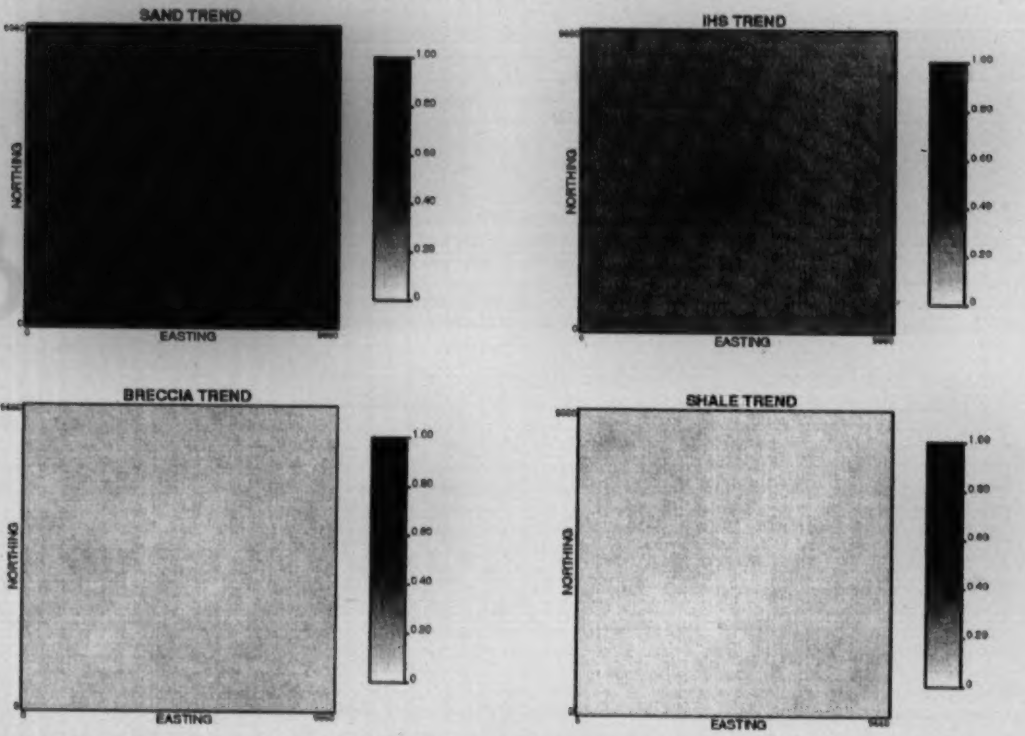

Figure 6-5: The McMurray Formation by-facies horizontal trend model calculated with inverse distance.

Like inverse distance for trend modeling, exactitude is not desired of the trend model. The recommendation here is to discretize each unknown grid cell and apply a block kriging scheme combined with a relatively significant nugget effect and global search.

Kriging is a well established technique for trend modeling. Flexibility can be achieved by adjusting the nugget effect, the block discretization level, and the anisotropy ratio in the variogram model. No additional post processing is required; the trend model is directly inferred with the estimates. This method is often applied in 2D to construct aerial trends.

Application Example

The technique is now implemented to generate a horizontal trend model for all four facies types within the domain lease. The conditioning data are the same facies proportions used in the previous section. The grid network is also the same. A spherical variogram model with a long 5,000m isotropic range and 30% nugget effect is used with a 6 x 6 discretization level. Figure 6-6 shows the trend model for each of the four facies types within the township domain. Although slightly different, the trend in Figure 6-6 is similar to the inverse distance results in Figure 6-5.

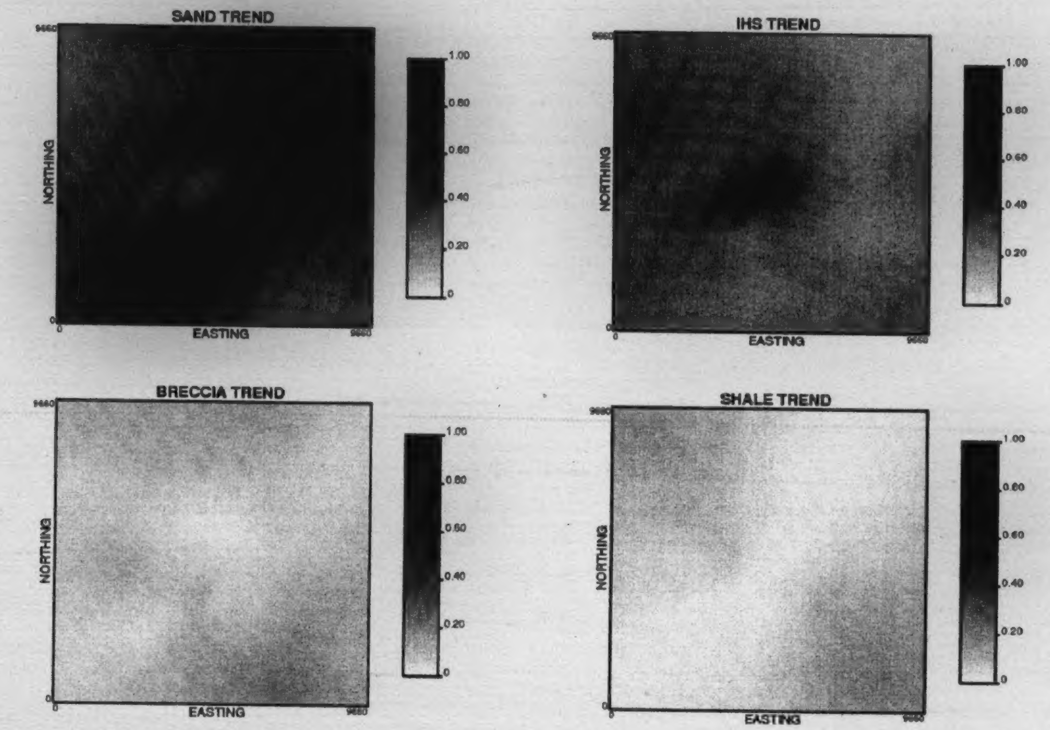

Figure 6-6: The McMurray Formation by-facies horizontal trend model calculated with global kriging.

6.3.5 Kriging the Trend (KT)

Kriging the trend (KT) is the next automatic technique for modeling the trend presented in this dissertation. It is the most complex technique.

Kriging with the Trend Description

The derivation of the system of equations for simple kriging is presented in Chapter 2. It was noted that there are several different variations of these simple kriging equations; KT is one variation where first order stationarity is no longer assumed and the mean function $m(\mathbf{u})$ is no longer set equal to m. Unbiasedness and minimum error variance must still be achieved; however, different constraints and procedures for minimization will be needed.

The current approach is assuming $m(\mathbf{u})$ is a smoothly varying deterministic function of the coordinates vector $\mathbf{u}$ whose unknown parameters are fit from the data within local search windows:

$$m(\mathbf{u}) = \sum_{v=0}^{V} a_v(\mathbf{u}) f_v(\mathbf{u}) \qquad (6\text{-}2)$$

The $f_v(\mathbf{u})$'s are known functions of the coordinate vectors over the domain **D**. The $a_v(\mathbf{u})$'s are estimated within local search windows centered on the unsampled locations. The actual $m(\mathbf{u})$ trend values are unknown since the $a_v(\mathbf{u})$'s are not estimated directly.

Ordinary kriging is a particular type of KT whereby convention $f_0(\mathbf{u}) = 1$ and $m(\mathbf{u}) = a_0(\mathbf{u})$. This corresponds to the case where $m(\mathbf{u})$ is re-estimated to a constant $a_0(\mathbf{u})$ value within local often overlapping search windows.

The shift parameter A in relation (2-33) then becomes:

$$\mathrm{A} = \sum_{v=0}^{V} a_v(\mathbf{u}_0) f_v(\mathbf{u}_0) - \sum_{s=1}^{n} \lambda_{\mathrm{KT}}(\mathbf{u}_s) \sum_{v=0}^{V} a_v(\mathbf{u}_s) f_v(\mathbf{u}_s) \tag{6-3}$$

And the kriging with the trend estimator $Z^*_{\mathrm{KT}}(\mathbf{u}_0)$ is then:

$$\begin{aligned} Z^*_{\mathrm{KT}}(\mathbf{u}_0) &= \sum_{v=0}^{V} a_v(\mathbf{u}_0) f_v(\mathbf{u}_0) - \sum_{s=1}^{n} \lambda_{\mathrm{KT}}(\mathbf{u}_s) \sum_{v=0}^{V} a_v(\mathbf{u}_s) f_v(\mathbf{u}_s) + \sum_{s=1}^{n} \lambda_{\mathrm{KT}}(\mathbf{u}_s) Z(\mathbf{u}_s) \\ &= \sum_{v=0}^{V} a_v(\mathbf{u}_0) f_v(\mathbf{u}_0) + \left(\sum_{s=1}^{n} \lambda_{\mathrm{KT}}(\mathbf{u}_s) \left[Z(\mathbf{u}_s) - \sum_{v=0}^{V} a_v(\mathbf{u}_s) f_v(\mathbf{u}_s) \right] \right) \end{aligned} \tag{6-4}$$

There are many ways to ensure the kriging with the trend estimator $Z^*_{\mathrm{UK}}(\mathbf{u}_0)$ is unbiased. The classic approach is to impose the following $V + 1$ constraint equations:

$$\sum_{s=1}^{n} \lambda_{\mathrm{KT}}(\mathbf{u}_s) f_v(\mathbf{u}_s) = f_v(\mathbf{u}_0) \quad v = 0, \ldots, V \tag{6-5}$$

where $f_v(\mathbf{u}_0)$ are the trend functions evaluated at the unsampled locations and $f_v(\mathbf{u}_s)$ the trend functions evaluated at the sampled locations. By considering these constraints, the resulting kriging with the trend estimator $Z^*_{\mathrm{UK}}(\mathbf{u}_0)$ is then unbiased:

$$\begin{aligned} \mathrm{E}\{E(\mathbf{u}_0)\} &= \mathrm{E}\{Z(\mathbf{u}_0)\} - \mathrm{E}\{Z^*_{\mathrm{UK}}(\mathbf{u}_0)\} \\ &= \sum_{v=0}^{V} a_v(\mathbf{u}_0) f_v(\mathbf{u}_0) - \sum_{v=0}^{V} a_v(\mathbf{u}_0) f_v(\mathbf{u}_0) - \left(\sum_{s=1}^{n} \lambda_{\mathrm{KT}}(\mathbf{u}_s) \left[Z(\mathbf{u}_s) - \sum_{v=0}^{V} a_v(\mathbf{u}_s) f_v(\mathbf{u}_s) \right] \right) \\ &= \sum_{s=1}^{n} \lambda_{\mathrm{KT}}(\mathbf{u}_s) \sum_{v=0}^{V} a_v(\mathbf{u}_s) f_v(\mathbf{u}_s) - \sum_{s=1}^{n} \lambda_{\mathrm{KT}}(\mathbf{u}_s) \sum_{v=0}^{V} a_v(\mathbf{u}_s) f_v(\mathbf{u}_s) \\ &= \sum_{v=0}^{V} a_v(\mathbf{u}_0) \left[f_v(\mathbf{u}_0) - f_v(\mathbf{u}_0) \right] = 0 \end{aligned} \tag{6-6}$$

KT can be considered as constrained kriging with $V + 1$ constraint equations in relation (6-5) that need to be imposed on the system in order to achieve unbiasedness in (6-6).

There remains to determine the kriging with the trend weights $\lambda_{\mathrm{KT}}(\mathbf{u}_s)$. These n weights are determined so that the error variance in relation (2-35) is a minimum. However, the minimization must be performed subject to the $V + 1$ constraint equations in (6-5). These constraints call for the definition of the following Lagrangian function $G(\mathbf{u}_0)$ that depends on the n weights in addition to the Lagrange parameter $\mu_v(\mathbf{u}_0)$:

$$G(\mathbf{u}_0) = \mathrm{VAR}\{E(\mathbf{u}_0)\} + 2\mu_v(\mathbf{u}_0) \left[\sum_{s=1}^{n} \lambda_{\mathrm{KT}}(\mathbf{u}_s) f_v(\mathbf{u}_s) - f_v(\mathbf{u}_0) \right] \quad v = 0, \ldots, V \tag{6-7}$$

The optimal weights $\lambda_{\mathrm{KT}}(\mathbf{u}_s)$ are obtained by setting to zero the n partial derivatives of the error variance in (2-35) with respect to $\lambda_{\mathrm{KT}}(\mathbf{u}_s)$ and the $(V + 1)$ partial derivatives of (6-5) with respect to $\mu_v(\mathbf{u}_0)$:

$$\frac{\partial\left(\mathrm{VAR}\left\{E(\mathbf{u}_0)\right\}\right)}{2\partial\left(\lambda_{\mathrm{KT}}(\mathbf{u}_s)\right)} = C_R(\mathbf{u}_0 - \mathbf{u}_s) - \sum_{s'=1}^{n} \lambda_{\mathrm{UK}}(\mathbf{u}_{s'}) C_R(\mathbf{u}_{s'} - \mathbf{u}_s)$$

$$- \sum_{v=0}^{V} \mu_v(\mathbf{u}_0) f_v(\mathbf{u}_s) = 0 \qquad (6\text{-}8)$$

$$\frac{\partial\left(G(\mathbf{u}_0)\right)}{2\partial\left(\mu_v(\mathbf{u}_0)\right)} = \sum_{s'=1}^{n} \lambda_{\mathrm{KT}}(\mathbf{u}_{s'}) f_v(\mathbf{u}_{s'}) - f_v(\mathbf{u}_0) = 0$$

This results in the following system of kriging with the trend equations:

$$\begin{aligned} &\sum_{s'=1}^{n} \lambda_{\mathrm{KT}}(\mathbf{u}_{s'}) C_R(\mathbf{u}_{s'} - \mathbf{u}_s) + \sum_{v=0}^{V} \mu_v(\mathbf{u}_0) f_v(\mathbf{u}_s) = C_R(\mathbf{u}_0 - \mathbf{u}_s) \quad s = 1,\ldots n \\ &\sum_{s'=1}^{n} \lambda_{\mathrm{KT}}(\mathbf{u}_{s'}) f_v(\mathbf{u}_s) = f_v(\mathbf{u}_0) \quad v = 0,\ldots,V \end{aligned} \qquad (6\text{-}9)$$

The key to estimating the trend $m(\mathbf{u})$ is simply setting all the right hand side $C_R(\mathbf{u}_0\text{-}\mathbf{u}_s)$ covariances to zero:

$$\begin{aligned} &\sum_{s'=1}^{n} \lambda_{\mathrm{KT}}(\mathbf{u}_{s'}) C_R(\mathbf{u}_{s'} - \mathbf{u}_s) + \sum_{v=0}^{V} \mu_v(\mathbf{u}_0) f_v(\mathbf{u}_s) = 0 \quad s = 1,\ldots n \\ &\sum_{s'=1}^{n} \lambda_{\mathrm{KT}}(\mathbf{u}_{s'}) f_v(\mathbf{u}_s) = f_v(\mathbf{u}_0) \quad v = 0,\ldots,V \end{aligned} \qquad (6\text{-}10)$$

There are $(n + V + 1)$ equations with n kriging with the trend weights $\lambda_{\mathrm{KT}}(\mathbf{u}_s)$ and $(V + 1)$ Lagrange parameters $\mu_v(\mathbf{u}_0)$ to be determined. The minimized kriging variance $\sigma^2_{\mathrm{KT}}(\mathbf{u}_0)$ is then:

$$\sigma^2_{\mathrm{UK}}(\mathbf{u}_0) = C_R(\mathbf{0}) - \sum_{s=1}^{n} \lambda_{\mathrm{KT}}(\mathbf{u}_s) C_R(\mathbf{u}_0 - \mathbf{u}_s) - \sum_{v=0}^{V} \mu_v(\mathbf{u}_0) \qquad (6\text{-}11)$$

Similar to inverse distance and conventional kriging schemes for predicting the trend, the implementation of KT should involve a global search. This is because the deterministic form of the trend should be decided on at the scale of the full domain and the KT trend is a least squares fit of this deterministic form from the available sample data.

The KT algorithm allows the incorporation of a variety of different types of deterministic trend information through the parameterization of a polynomial form for $m(\mathbf{u})$. However, this flexibility is traded for a number of implementation challenges. It is difficult to decide on the deterministic form of the trend. The number of data n must always be greater than the number of constraints V. And the sample data can not be perfectly aligned in a straight line perpendicular to the direction in which the mean is a function.

6.4 Combining Lower Order Trend Models

Recall an approach to three dimensional trend modeling is building separately a 2D aerial trend and 1D vertical trend then combining these lower dimensional trends into the full 3D trend model.

A variety of different combinatorial schemes exist. Probability combination procedures are addressed in this dissertation [50]. A relatively new probability scheme, an alternative to what is referred to as the full independence hypothesis, is proposed for building trend models [50]. Probability schemes have been applied in the past for categorical variable trends. An extension to continuous variable trends is made. These combination schemes are also applied with the lower dimensional 2D and 1D trends built for the McMurray Formation example in this chapter.

6.4.1 Theory

The following theoretical background for probability combination schemes is largely derived from the work of Journel in 2002 [50]. Consider the assessment of any unknown event A through its posterior probability P(A|B,C) given two conditioning events B and C. A, B, and C can be any events as long as the prior P(A) and pre-posterior P(A|B) and P(A|C) probabilities can be inferred. Figure 6-7 shows the application in this dissertation where P(A|B,C), P(A|B), and P(A|C) represent the full 3D, 2D horizontal, and 1D vertical trend models, respectively. The idea is to combine the lower dimensional horizontal and vertical trend, the pre-posterior P(A|B) and P(A|C) probabilities, into a full 3D trend, the P(A|B,C) posterior probability.

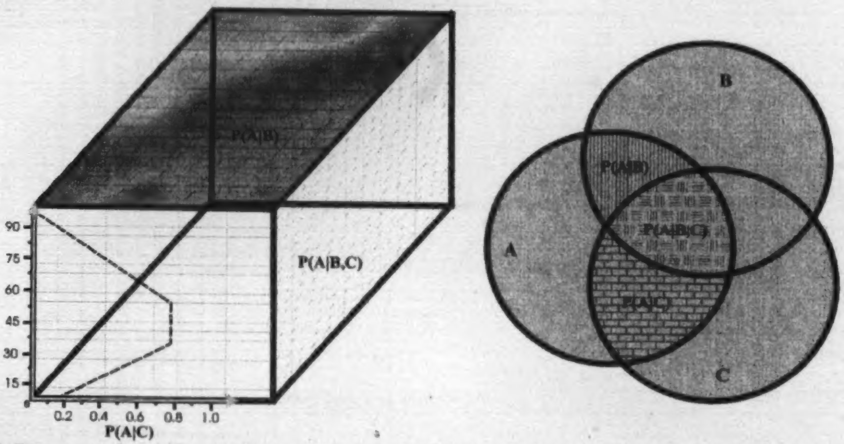

Figure 6-7: Pre-posterior A|B and A|C and posterior A|B,C probabilities represented on the left with events as the 2D horizontal, 1D vertical, and 3D trend model, respectively, and on the right with a Venn diagram.

There are two main approaches to assessing P(A|B,C). These are referred to as full independence and permanence of ratios. The difference between the two is the underlying assumptions about the dependence between events B and C. Full independence assumes events B and C are fully independent while the permanence of ratios assume events B and C are incrementally conditionally independent. Both techniques are now developed in all necessary detail.

Full Independence

The posterior P(A|B,C) probability is exactly:

$$P(A\mid B,C)=\frac{P(A,B,C)}{P(B,C)}=\frac{P(A)\cdot P(B\mid A)\cdot P(C\mid A,B)}{P(B,C)} \qquad (6\text{-}12)$$

The difficulty in solving for P(A|B,C) exactly is the dependence between events B and C in the P(C|A,B) and P(B,C) terms. The full independence approach to this challenge is to assume that events B and C are fully independent. This implies the following for the P(C|A,B) and P(B,C) terms:

$$\begin{aligned} P(C \mid A,B) &= P(C \mid A) \\ P(B,C) &= P(B) \cdot P(C) \end{aligned} \tag{6-13}$$

Relation (6-12) can then be simplified to:

$$P(A \mid B,C) = \frac{P(A) \cdot P(B \mid A) \cdot P(C \mid A)}{P(A) \cdot P(B)} \tag{6-14}$$

And then using Bayes inversion, the following is used to calculate P(A|B,C):

$$P(A \mid B,C) = \frac{P(A \mid B) \cdot P(A \mid C)}{P(A)} \tag{6-15}$$

Relation (6-15) is the full independence probability scheme for calculating P(A|B,C). This posterior probability is interpreted as a simple scaling of the P(A|B) probability with the P(A|B) probability and standardization by the prior P(A) probability. That is, the full 3D trend model is calculated from a scaling of the horizontal trend with the vertical trend standardized by the global mean.

The full independence scheme is simple; however, there is a fundamental problem with this procedure in practice. Notice that it is possible in (6-15) for extreme probabilities to exceed 1.0. For example, consider a 3D grid cell in Figure 6-7 where the aerial mean is P(A|B) = 0.89, the vertical mean is P(A|C) = 0.78, and the global mean is P(A) = 0.65. This results in an impossible trend value of P(A|B,C) = 1.07. The permanence of ratios version of P(A|B,C) is regarded as more robust since P(A|B,C) is guaranteed to be [0,1].

Permanence of Ratios

The derivation of the permanence of ratios approach starts by assuming that events B and C are conditionally independent. When B and C are independent conditional to the event A, the following is true:

$$P(B,C \mid A) = P(B \mid A) \cdot P(C \mid A) \tag{6-16}$$

Relation (6-12) can then be simplified to:

$$P(A \mid B,C) = \frac{P(A) \cdot P(B \mid A) \cdot P(C \mid A)}{P(B,C)} \tag{6-17}$$

Notice, however, this conditional independence assumption does not remove the difficult to evaluate P(B,C) term. Notice also that relation (6-17) does not ensure the following posterior probability closure:

$$\begin{aligned} &P(A \mid B,C)+P\left(A^{c} \mid B,C\right)=1 \\ &P(A)\cdot P(B \mid A)\cdot P(C \mid A)+P\left(A^{c}\right)\cdot P\left(B \mid A^{c}\right)\cdot P\left(C \mid A^{c}\right)=1 \end{aligned} \tag{6-18}$$

where the superscript c is used to denote *complement of.* The P(B,C) term is avoided by standardizing the P(A|B,C) to close within (6-18):

$$\begin{aligned} P(A \mid B,C) &= \frac{P(A)\cdot P(B \mid A)\cdot P(C \mid A)}{P(A)\cdot P(B \mid A)\cdot P(C \mid A)+P\left(A^{c}\right)\cdot P\left(B \mid A^{c}\right)\cdot P\left(C \mid A^{c}\right)} \\ &= \frac{\dfrac{P(A \mid B)\cdot P(A \mid C)}{P(A)}}{\dfrac{P(A \mid B)\cdot P(A \mid C)}{P(A)}+\dfrac{P\left(A^{c} \mid B\right)\cdot P\left(A^{c} \mid C\right)}{P\left(A^{c}\right)}} \end{aligned} \tag{6-19}$$

This posterior probability can be reshaped as follows:

$$P(A \mid B,C)=\frac{1}{1+x}=\frac{a}{a+bc}=\frac{x-b}{b}=\frac{c-a}{a} \tag{6-20}$$

where the a, b, c, and x terms are:

$$a=\frac{1-P(A)}{P(A)};\quad b=\frac{1-P(A \mid B)}{P(A \mid B)};\quad c=\frac{1-P(A \mid C)}{P(A \mid C)};\quad x=\frac{1-P(A \mid B,C)}{P(A \mid B,C)} \tag{6-21}$$

Relations (6-19) and (6-20) is the permanence of ratios scheme for calculating P(A|B,C). The notion of the permanence of ratios terminology can be found in relation (6-21) where the incremental contribution of event C over the contribution of event A to the P(A|B,C) posterior probability is the same regardless of event B. The interpretation is that events B and C are incrementally conditionally independent. This assumption is less severe that the full independence model.

The permanence of ratios scheme is slightly more complex than the full independence model; however, the P(A|B,C) posterior probabilities are guaranteed to lie within the interval [0,1]. Consider again the small example where P(A|B) = 0.75, P(A|C) = 0.78, and P(A) = 0.65. Relations (6-19) and (6-20) give P(A|B,C) = 0.85 versus the impossible P(A|B,C) value of 1.17 using full independence.

6.4.2 Categorical Variable Trends

The full independence and permanence of ratios probability combination schemes can be used to construct a full 3D trend model from lower dimensional 2D aerial and 1D vertical trends for categorical variables. The full independence (6-15) and permanence of ratios (6-19) probability combination schemes are written with the following substitutions:

$$
\begin{aligned}
&\mathrm{P}(\mathrm{A}\mid\mathrm{B},\mathrm{C}) = m_k(\mathbf{u}) = m_k(x,y,z) = p_k(\mathbf{u}) = p_k(x,y,z)\\
&\mathrm{P}(\mathrm{A}) = m_k = p_k\\
&\mathrm{P}(\mathrm{A}\mid\mathrm{B}) = m_k(x,y) = p_k(x,y)\\
&\mathrm{P}(\mathrm{A}\mid\mathrm{C}) = m_k(z) = p_k(z)
\end{aligned}
\tag{6-22}
$$

The lines in relation (6-22), from top to bottom, for facies k, correspond to the posterior 3D locally varying trend or proportion, prior global mean or proportion, pre-posterior 2D locally varying horizontal trend or proportion, and pre-posterior 1D vertical trend or proportion. With these substitutions, in terms of proportions, full independence becomes:

$$
p_k(\mathbf{u}) = \frac{p_k(x,y)\cdot p_k(z)}{p_k}
\tag{6-23}
$$

And the permanence of ratios relation becomes:

$$
p_k(\mathbf{u}) = \frac{\dfrac{(1-p_k)}{p_k}}{\dfrac{(1-p_k)}{p_k} + \left[\dfrac{(1-p_k(x,y))}{p_k(x,y)}\right]\cdot\left[\dfrac{(1-p_k(z))}{p_k(z)}\right]}
\tag{6-24}
$$

Application Example

The full independence and permanence of ratios schemes in relations (6-23) and (6-24) are now implemented on the McMurray Formation example. The by-facies vertical trend was created with a moving window average technique and is shown in Figure 6-4. The by-facies 2D trends are taken from the global block kriging models in Figure 6-6.

Figure 6-8 shows for the interbedded sand/shale facies some aerial cross sections through the full independence trend (left) and the permanence of ratios trend (right). The top cross sections are located at a high elevation of 270m where the trend suggests the facies proportion is higher; the bottom cross sections are located at a low elevation of 180m where the trend suggests the facies proportion is lower. Although the differences are slight due to the intermediate proportions, notice that the full independence trend seems to overemphasize low and high trend values while the permanence of ratios trend is less variable in the extremes.

6.5 Remarks

Regardless of domain size, the SRF formalism is incapable of accounting for smooth large-scale trends when there is inadequate amount of conditioning data. The trend is always constructed. It is used later for either validation or directly in prediction.

Trends are subjective. The criteria used to evaluate the reasonableness of the trend must then also be subjective. This has resulted in a wide variety of trend modeling practices. A collection of five trend modeling methods have been presented above. The essential underlying guideline is that the trend be smooth and not overly influenced by local data driven features.

A strong emphasis is made on parameterizing the last four automated trend modeling techniques so that a reasonably subjective and low variability trend model can still be constructed. For example, kriging parameters for building a trend model and for building local distributions of uncertainty are very different since exactitude is no longer a desired property and a smoothly varying representation of deterministic knowledge is a priority.

All categorical and continuous variable trend models can be represented as some combination of prior, pre-posterior, and posterior probabilities. For categorical variables, the trend is a proportion or probability model; for continuous variables, the inverse cdf is needed to convert real data to probabilities. The lower dimensional trends are then combined using a particular probability combination scheme to generate a full 3D model.

It is worth reemphasizing that although there are sound geological reasons to consider dissociating a smooth $m(\mathbf{u})$ and more random $R(\mathbf{u})$ component from $Z(\mathbf{u})$, the particular additive decomposition in (2-9) is arbitrary and not necessarily supported by any geological phenomenon.

The scale for interpreting and modeling the trend is important. There is a full continuum of scales, all of which a separate trend could be detected and modeled. This dissertation deals with a particular scale. Corehole samples are interpolated to a geo-cellular level. Trends are detected, interpreted, and modeled at this scale. This dissertation does not address trends that would exist at smaller and larger scales.

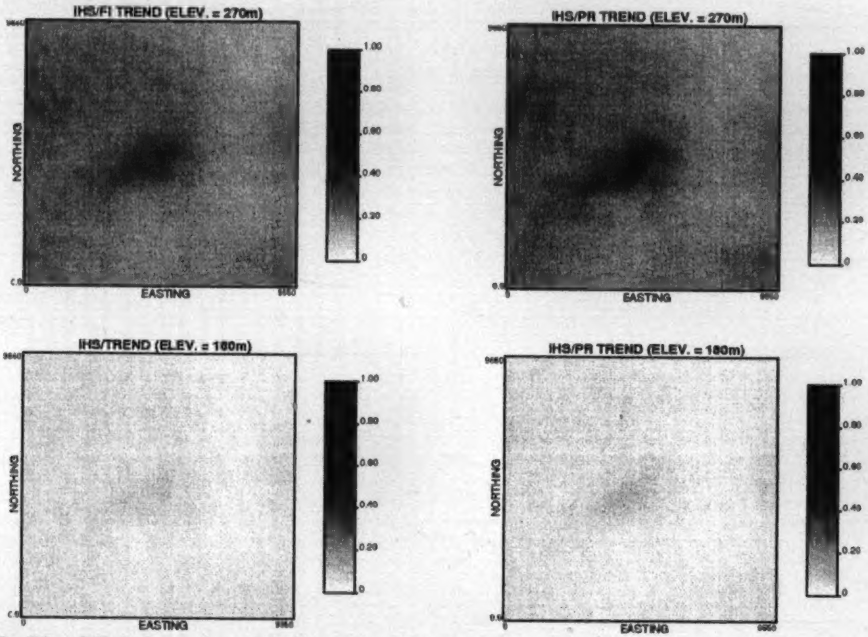
IHS/FI TREND (ELEV. = 270m)
IHS/PR TREND (ELEV. = 270m)
IHS/TREND (ELEV. = 180m)
IHS/PR TREND (ELEV. = 180m)
NORTHING
EASTING
0
1.00
0.80
0.60
0.40
0.20
0

Figure 6-8: The full independence (left) and permanence of ratios (right) interbedded sand/shale trend model at the higher 270m elevation (top) and lower 180m elevation (bottom).

CHAPTER 7

PREDICTION WITH A TREND

Predicting the spatial distribution of petrophysical properties is an essential aspect of natural resource characterization. Traditional geostatistical prediction without explicitly incorporating the trend does not guarantee reproduction of the trend. An *explicit* approach may be employed.

There is a variety of explicit approaches to perform estimation and simulation with a trend. These techniques are reviewed and evaluated according to the reasonability criteria identified in Chapter 3. In general, currently available explicit techniques are undermined by the same challenge of inferring the underlying spatial law of the decomposed residual RF $R(\mathbf{u})$ needed for prediction. This challenge is recognized, explained, and demonstrated with a 1D porosity profile example. Although subjective, a straightforward solution is proposed to infer this spatial law.

The emphasis of this chapter then shifts to developing, describing, and implementing a new explicit approach to estimation and simulation with the trend. The key feature of this method is the use of locally varying transformation tables for the transformation from original units to a Gaussian distribution.

7.1 Principles for Predicting with the Trend

The construction of reasonable petrophysical property models in the presence of the trend is an essential aspect of geostatistical modeling. Chapter 3 identified five criteria used for evaluating the reasonableness of prediction with the trend: (1) simplicity, (2) spatial law inference, (3) accurate and precise uncertainty, (4) reproduction of bivariate residual distributions, and (5) geologically realistic. These are briefly discussed.

The prediction algorithm formulation, description, and implementation should be straightforward. Too complex algorithms will be difficult to implement, modify, explain, and justify in practical settings. The most popular prediction algorithms incorporating the trend are also generally the simplest.

The spatial law of $R(\mathbf{u})$ is required for prediction with a trend. The usual assumption of stationarity for $Z(\mathbf{u})$ is transferred to the residual RF $R(\mathbf{u})$, but inference of the $R(\mathbf{u})$ spatial law is notoriously difficult since the $R(\mathbf{u})$ RF is not sampled in reality and its realizations are only a product of the artificial additive decomposition construct. Section

7.4 is devoted to understanding and solving the problem of inferring the underlying spatial law.

An important goal of geostatistical prediction is quantifying local and joint uncertainty. Uncertainty is model-dependent. Prediction algorithms incorporating the trend should generate more accurate and precise models of uncertainty compared to prediction without the trend. Accurate and precise uncertainty is defined by Deutsch [51] for both estimation and simulation. These criteria can also be used to evaluate the reasonableness of alternative trend models and trend modeling algorithms. Different trend models and prediction algorithms will result in different measures of uncertainty; therefore, the particular trend model and trend modeling algorithm that is associated with the lowest uncertainty and highest accuracy and precision would be deemed most reasonable.

The trend model value $m(\mathbf{u})$, original data value $z(\mathbf{u})$, and calculated residual value $r(\mathbf{u})$ are available at the sample data locations. The bivariate residual-mean *R-m* distribution built from all $(r(\mathbf{u}), m(\mathbf{u}))$ pairs and bivariate residual-variable *R-Z* distribution built from all $(r(\mathbf{u}), z(\mathbf{u}))$ pairs each reveal important relationships that should be reproduced by the predicted $r^*(\mathbf{u})$ and $z^*(\mathbf{u})$ values. Algorithms with direct control over replicating these features are more reasonable compared to ones that do not.

Petrophysical property uncertainty should be characterized by a framework of random fluctuations representing uncertainty combined with deterministic variability representing the trend.

7.2 Explicit Approaches to Estimation with the Trend

The goal of geostatistical estimation is to quantify local uncertainty. The pioneering work of Danie Krige [53] during the 1950s to correct conditional biases [52] was the seed for the popular group of estimation techniques collectively referred to as kriging. From the 1960s the utility of kriging has been for both large-scale trend modeling and calculating recoverable reserves for production planning. The trend modeling capability of kriging was dealt with in Chapter 6. The detail of recoverable reserves calculations is addressed in [8].

The techniques in this dissertation explicitly consider a trend model during quantification of local uncertainty. These techniques can also be referred to as non-stationary kriging implementations since the mean function $m(\mathbf{u})$ used is not a constant as in stationary or simple kriging. Three non-stationary kriging implementations now reviewed.

Kriging with a locally varying mean is the first technique. Recall the kriging estimator:

$$Z_K^*(\mathbf{u}_0) - m(\mathbf{u}_0) = \sum_{s=1}^{n} \lambda_K(\mathbf{u}_s)\left[Z(\mathbf{u}_s) - m(\mathbf{u}_s)\right] \qquad (7\text{-}1)$$

Instead of stationary simple kriging with stationary mean m inferred from $F(z)$, the mean $m(\mathbf{u})$ corresponds to a non-stationary trend [5].

Kriging with a trend (KT), originally known and developed as universal kriging (UK) by Matheron in 1969 [54], provides minimum error variance estimates of the original $Z(\mathbf{u})$ RF in the presence of a trend model $m(\mathbf{u})$. Given that $m(\mathbf{u})$ is a deterministic function of the coordinates vector $\mathbf{u}$, the trend is also estimated according to the same minimum error variance optimality criteria. Chapter 2 provides guidance on deriving the KT system of equations; and the recent reference [55] provides a more comprehensive derivation. The convenience of KT for simultaneously and optimally estimating both the $m(\mathbf{u})$ trend and the original RF $Z(\mathbf{u})$ is offset by a number of practical implementation issues. Among others, Armstrong in 1984 [56] highlights the most important one: that of inferring the underlying spatial law.

Kriging with an external drift variable is an extension of KT where the functional form of the $m(\mathbf{u})$ trend model is limited to $V = 1$ functionals: $f_0(\mathbf{u}) = 1$ and $f_1(\mathbf{u})$ set equal to a secondary (external) variable [5]. This was first implemented successfully with secondary seismic data by Marechal, 1984 [57].

For a set of K indicator RFs, two methods are available to account for the trend. The first is the same as the approach for kriging with a prior mean except the prior mean $m(\mathbf{u})$ are the locally varying proportions of the particular k indicator variable denoted $p(\mathbf{u}_k)$ [4]. The second approach is referred to as *soft* kriging. As long as soft data is available and is amenable to a Bayesian coding into prior $p(\mathbf{u}_k)$ mean values, the Markov-Bayes model [58, 59] can be applied to explicitly integrate the trend into the resulting model of predicted geological heterogeneity and local uncertainty [5].

7.2.1 Reasonableness Summary

The reasonableness evaluation results for all three non-stationary kriging approaches to explicitly estimating local uncertainty with the trend are the same. These techniques are simple and capable of generating accurate and precise models of local uncertainty with geologically realistic heterogeneity; however, inference of the underlying spatial law is not evident and there is no guarantee the estimated bivariate *R-m* and *R-Z* relationships are reproduced. Detailed comments organized into the five reasonableness criteria follow:

1. *Simplicity*: Other than the subjective choice of functional form for the $m(\mathbf{u})$ trend in the KT approach, the implementation of non-stationary kriging is straightforward;
2. *Spatial Law Inference*: Since kriging of the residual RF $R(\mathbf{u})$ is being conditioned by synthetic $r(\mathbf{u})$ data derived from a non-stationary mean function $m(\mathbf{u})$, the spatial law of $R(\mathbf{u})$ is not evident;
3. *Accurate and Precise Uncertainty*: Accurate and precise uncertainty can be assessed and optimized by modifying the $m(\mathbf{u})$ model and changing kriging parameters;
4. *Reproduction of Bivariate Residual Distribution:* There is no direct control on the reproduction of the original scatter of $(r(\mathbf{u}), m(\mathbf{u}))$ or $(r(\mathbf{u}), z(\mathbf{u}))$ data by the scatter of $(r^*(\mathbf{u}), m(\mathbf{u}))$ or $(r^*(\mathbf{u}), z^*(\mathbf{u}))$ estimates;
5. *Geologically Realistic*: Since predictions explicitly honor the previously constructed trend model, non-stationary kriging approaches are capable of creating geologically realistic models of heterogeneity and local uncertainty.

The three non-stationary kriging approaches reviewed are equivalent in terms of the four reasonability criteria identified. All are simple and able to produce geologically realistic models. None are capable of either inferring a reasonable spatial law or reproducing the bivariate *R*-*m* and *R*-*Z* relationships.

Another practically important drawback of all of these estimation methods is that they cannot be used in simulation when joint uncertainty is required. The covariance of the predicted models is incorrect. A non-traditional approach to simulation without simple kriging is required to reproduce the reference covariance. Alternative approaches are investigated next.

7.3 Explicit Approaches to Simulation with the Trend

The goal of geostatistical simulation is to quantify joint uncertainty, that is, geological uncertainty over multiple locations with multiple realizations. For production planning, alternative geostatistical realizations must be geologically realistic and, consequently, should reproduce significant large-scale variability modeled by a trend.

There are a variety of explicit approaches to ensure geostatistical simulation models are geologically realistic and consistent with the trend. Three approaches are now discussed.

7.3.1 Intrinsic Random Functions of Order *k* (IRF-*k*)

The challenges associated with (1) inferring the spatial law of the residual RF $R(\mathbf{u})$ for the non-stationary kriging approaches and (2) the inability to use non-stationary kriging in the traditional SGS algorithm motivated the consideration and use of intrinsic random functions of order *k* (IRF-*k*) [12]. IRF-*k* are interpreted as random functions with second-order stationary increments of order *k*. A generalized covariance $K(\mathbf{h})$ is defined as the correlation structure of its IRF-*k*. Conventional geostatistics corresponds to the zero-order ($k = 0$) increments $[Z(\mathbf{u}+\mathbf{h}) - Z(\mathbf{u})]$ to which the variogram is the function $K(\mathbf{h})$. However, IRF-*k* applications are restricted to isotropic $K(\mathbf{h})$ models [60].

In 1990, Dimitrakopoulos [61] developed a comprehensive step-by-step non-stationary simulation procedure using IRF-*k*. There are four main steps: (1) on-line unconditional simulation of a Wiener-Levy process for the IRF-*k* in $\boldsymbol{R}^1$, (2) use of the turning-bands method to map the $\boldsymbol{R}^1$ realizations into $\boldsymbol{R}^n$, (3) conditioning to available data with kriging, and (4) verification of covariance reproduction. Unlike with non-stationary kriging using the variogram, the use of generalized covariances from IRF-*k* yield theoretically correct results in a conditional simulation framework.

Unlike KT, prediction results using IRF-*k* would reproduce both the theoretically correct input spatial law of the GC $K(\mathbf{h})$ and key large-scale geological features of the trend. For example, $K(\mathbf{h})$ for an IRF of order one ($k = 1$) would be capable of filtering a linear trend from the spatial law $K(\mathbf{h})$ of the IRF-1. The use of IRF-*k*, however, can be relatively complex and the generalized covariances used are usually arbitrarily assumed to be of rather restrictive isotropic form [60].

Reasonableness

The advantage of the IRF-*k* approach is a consistent underlying spatial law. However, this comes at a significant cost:

1. *Simplicity*: The Wiener-Levy simulation for the IRF-*k* and turning-bands simulation are relatively difficult procedures to implement;
2. *Spatial Law Inference*: Inference of the generalized covariance for IRF-*k* through the Wiener-Levy process is possible;
3. *Accurate and Precise Uncertainty*: The accuracy and precision of uncertainty can be measured;
4. *Reproduction of Bivariate Residual Distribution:* There is no $R(\mathbf{u})$ – this criterion is not applicable for IRF-*k*;
5. *Geologically Realistic*: The resulting IRF-*k* simulation model is capable of creating geologically realistic models of heterogeneity and joint uncertainty consistent with key large-scale features of the trend.

7.3.2 Residual Simulation

The most common and most straightforward explicit approach to geostatistical simulation with the trend model is a traditional simulation of the assumed stationary residual RF $R(\mathbf{u})$ after the modeled trend $m(\mathbf{u})$ is subtracted from the original RF $Z(\mathbf{u})$ at the available data locations [62]. The simulated residuals are then simply added back to the $m(\mathbf{u})$ trend model. The example in Chapter 1 implements this approach.

Reasonableness

The classic residual simulation approach is straightforward and is capable of generating geologically realistic models of joint uncertainty consistent with key large-scale features of the trend; however, the underlying spatial law of the residuals can not be inferred from residual data and there is no guarantee that simulated residual-mean or residual-variable distributions will reproduce key features of the original data versions. Detailed comments organized by reasonableness criteria follow:

1. *Simplicity*: The residual simulation algorithm is straightforward;
2. *Spatial Law Inference*: Since kriging of the residual RF $R(\mathbf{u})$ is being conditioned by synthetic $r(\mathbf{u})$ data derived from a non-stationary mean function $m(\mathbf{u})$, the spatial law of $R(\mathbf{u})$ is not equivalent to that of $Z(\mathbf{u})$ and is difficult to infer;
3. *Accurate and Precise Uncertainty*: It is possible to modify the simulation setup or use alternative $m(\mathbf{u})$ mean models to improve the accuracy/precision of uncertainty;
4. *Reproduction of Bivariate Residual Distribution:* There is no direct control on the reproduction of residual-mean or residual-variable distributions;
5. *Geologically Realistic*: Since the simulated residuals are added back to the prior trend model $m(\mathbf{u})$, the residual simulation approach is capable of creating geologically realistic models of heterogeneity and joint uncertainty honoring trends.

7.3.3 Stepwise Conditional Transformation of Residuals

An important disadvantage of both the IRF-k and residual simulation approaches is the inability to control the bivariate residual-mean and residual-variable distributions. In each of these distributions, a characteristic feature can possibly be present. Leuangthong and Deutsch [63] illustrate how each of these two features is detected:

1. Applications of traditional geostatistical simulation tools to the $R(\mathbf{u})$ SRF imply $R(\mathbf{u})$ is homoscedastic meaning the variance of the $r(\mathbf{u})$ residuals is independent of the trend values $m(\mathbf{u})$. However, virtually all residual-mean scatters of $(r(\mathbf{u}), m(\mathbf{u}))$ pairs will reveal some heteroscedastic behavior.
2. The additive dissociation of $Z(\mathbf{u})$ imposes the constraint $R(\mathbf{u}) \geq m(\mathbf{u})$ for non-negative $Z(\mathbf{u})$ variables. Simulating the spatial distribution of residuals and adding the mean back does not ensure this constraint is satisfied.

These two problems of the residual simulation approach motivate a stepwise conditional transformation technique proposed in [63]. The key idea is a stepwise transformation of the residual data conditional to the trend. This transformation assumes the following form:

$$Y_R(\mathbf{u}) = G^{-1}\left[F_{R|m}\left(R(\mathbf{u}) \mid m(\mathbf{u})\right)\right] \qquad (7\text{-}2)$$

where $Y_R(\mathbf{u})$ is the Gaussian G transform of the residual random variable $R(\mathbf{u})$ conditional to local $m(\mathbf{u})$ windows. Similarly, the solution when the second of these problems persists is a stepwise transformation of the original variable conditional to the trend:

$$Y_Z(\mathbf{u}) = G^{-1}\left[F_{Z|m}\left(Z(\mathbf{u}) \mid m(\mathbf{u})\right)\right] \qquad (7\text{-}3)$$

Both transformations complement conventional practice. The same decomposition in relation (2-9) is used in that the trend $m(\mathbf{u})$ and residual $R(\mathbf{u})$ is modeled separately and recombined. The pre and post processing steps are implemented in order to preserve heteroscedastic and constraint features. All necessary implementation details as well as mining and petroleum examples are given in [63].

Reasonableness

The stepwise conditional transformation approach is straightforward, reproduces the bivariate residual distributions, and is capable of generating low, accurate, precise, and geologically realistic uncertainty [15]. However, the problem of inferring the underlying spatial law persists. Detailed comments organized by reasonableness criteria follow:

1. *Simplicity*: The conventional Gaussian transformation applied to classes of Z or R is easy to implement;
2. *Spatial Law Inference*: The spatial law of $Y_R(\mathbf{u})$ is not equivalent to that of $Z(\mathbf{u})$ and is not immediately evident;
3. *Accurate and Precise Uncertainty*: It is possible to modify or optimize the simulation parameters or stepwise conditional transformation parameters or adopt alternative $m(\mathbf{u})$ mean models to improve the accuracy and precision of uncertainty;

4. *Reproduction of Bivariate Residual Distribution:* The SCT procedure ensures the predicted scatter of residual-mean or residual-variable pairs reproduces the original versions through the stepwise conditional transformation;
5. *Geologically Realistic*: Since the residuals are forward and backtransformed according to the stepwise conditional transformation tables, the trend model $m(\mathbf{u})$ is honored and the realizations of uncertainty are the geologically realistic.

7.3.4 Indicator Simulation Approaches

One common simulation technique that could account for a trend model consists of using the Markov-Bayes model for soft kriging. The covariance, cross-covariance, and Bayes probability calibration are as defined in [5]. Full implementation is presented in [64].

7.3.5 Reasonableness Summary

The detailed reasonability comments made above are summarized into the report card in Table 7-1 organized by simulation approach.

	Simulation with the Trend Model: Evaluation Criteria				
Simulation with the Trend Model	**Simplistic?**	**Spatial Law Inference?**	**Accurate/Precise Uncertainty?**	**Reproduction of Bivariate *R*(u) Distributions**	**Geologically Realistic?**
IRF-k	no	yes	yes	no	yes
RS	yes	no	yes	no	yes
SCT	yes	no	yes	yes	yes

Table 7-1: Report card for evaluating different approaches to account for the trend in simulation.

All of the approaches for simulation of the trend are capable of producing geologically realistic models of accurate and precise uncertainty. The IRF-*k* approach also allows inference of the underlying spatial law; however, it is a complex method. The stepwise conditional transformation is simple and the only one capable of controlling bivariate residual distribution behavior. Residual simulation is the simplest method but does not allow control over the bivariate residual distributions.

Each of the approaches to simulation with the trend can also be applied to estimation. For example, instead of simulating the residual RF $R(\mathbf{u})$ before adding back the mean $m(\mathbf{u})$, kriging could be applied as is done in the example shown in Chapter 3. Deutsch, 2006 describes the stepwise conditional transformation in estimation mode [65].

7.4 Inference of the Underlying Spatial Law

With the exception of the IRF-*k* and $R|m$ stepwise conditional transform methodologies, the approaches for prediction with the trend employ the additive decomposition in (2-9) to which the underlying spatial law is that of the unknown, unsampled, synthetically determined, and assumed stationary residual RF $R(\mathbf{u})$. This spatial law is difficult to infer since the $R(\mathbf{u})$ RF and $r(\mathbf{u})$ data do not exist in reality. This fundamental challenge facing prediction with the trend is addressed with a detailed problem description, solution, and illustrative 1D example.

SK and associated first order stationarity may be adequate to reproduce the large-scale variability of a trend. In this case, the variogram of the residual RF $R(\mathbf{u})$ is close to the variogram of the original variable RF $Z(\mathbf{u})$:

$$\gamma_R(\mathbf{h}) = \frac{1}{2P(\mathbf{h})}\sum_{s=1}^{P(\mathbf{h})}\left(\left[z(\mathbf{u}_s) - m(\mathbf{u}_s)\right] - \left[z(\mathbf{u}_s+\mathbf{h}) - m(\mathbf{u}_s+\mathbf{h})\right]\right)^2 = \gamma_Z(\mathbf{h}) \qquad (7\text{-}4)$$

The derivation of relation (7-4) requires the additive decomposition in relation (2-9) and the first order assumption of stationarity in relation (2-7). The original variable variogram $\gamma_Z(\mathbf{h})$ filters a constant mean and is equivalent to the residual variable variogram $\gamma_R(\mathbf{h})$. SK for estimation and simulation, therefore, is correctly applied using the variogram of the original data $\gamma_Z(\mathbf{h})$.

Consider now an explicit approach to predicting with the trend where the assumption of first order stationarity is relaxed. Relation (7-4) no longer holds since the trend model $m(\mathbf{u})$ varies locally, that is, the original variable variogram $\gamma_Z(\mathbf{h})$ does not filter a non-constant mean. The residual variable variogram $\gamma_R(\mathbf{h})$ must somehow be inferred.

Components of the Residual Variogram

Despite the theoretical consistency of inferring and predicting with the generalized covariance, simpler approaches to prediction with the trend have prevailed. The spatial law of the residual RF $R(\mathbf{u})$ can not be easily calculated, however, a variety of ad-hoc practices have emerged. Before describing these options, it will be useful to understand what the components of the residual variogram $\gamma_R(\mathbf{h})$ and how they are related. The residual variogram can be decomposed as follows:

$$\gamma_R(\mathbf{h}) = \gamma_Z(\mathbf{h}) - \gamma_m(\mathbf{h}) - 2\gamma_{mR}(\mathbf{h}) \qquad (7\text{-}5)$$

where $\gamma_Z(\mathbf{h})$ is the original variable variogram calculated with relation (2-15) using $z(\mathbf{u})$ data approximately separated by $\mathbf{h}$, $\gamma_m(\mathbf{h})$ is the mean variable variogram calculated with relation (2-15) using $m(\mathbf{u})$ data approximately separated by $\mathbf{h}$, and $\gamma_{mR}(\mathbf{h})$ is the cross variogram between $m(\mathbf{u})$ and $R(\mathbf{u})$ calculated with:

$$\gamma_{mR}(\mathbf{h}) = \frac{1}{2P(\mathbf{h})}\sum_{s=1}^{P(\mathbf{h})}\left(\left[m(\mathbf{u}_s) - m(\mathbf{u}_s+\mathbf{h})\right]\left[R(\mathbf{u}_s) - R(\mathbf{u}_s+\mathbf{h})\right]\right) \qquad (7\text{-}6)$$

using collocated $r(\mathbf{u})$ and $m(\mathbf{u})$ data approximately separated by $\mathbf{h}$. The derivation of relation (7-5) requires only the additive decomposition in relation (2-9).

The sill of the cross variogram $\gamma_{mR}(\mathbf{h})$ is the correlation coefficient between all $r(\mathbf{u})$ and $m(\mathbf{u})$ data calculated with relation (2-20). This correlation coefficient is zero when the trend $m(\mathbf{u})$ is independent of the residual RF $R(\mathbf{u})$. The $\gamma_{mR}(\mathbf{h})$ cross variogram for most $\mathbf{h}$ could be assumed negligible in many cases; therefore:

$$\gamma_R(\mathbf{h}) \approx \gamma_Z(\mathbf{h}) - \gamma_m(\mathbf{h}) \qquad (7\text{-}7)$$

There is no guarantee that $m(\mathbf{u})$ and $R(\mathbf{u})$ are independent; however, the stepwise conditional transformation of the residual data $r(\mathbf{u})$ does ensure independence.

After adopting relation (7-7) and the attached assumption of independence between $m(\mathbf{u})$ and $R(\mathbf{u})$, some important observations and interpretations become available. Figure 7-1 shows a schematic illustration of an experimental (open circles) and model (line) original variable variogram $\gamma_Z(\mathbf{h})$. One possible $\gamma_m(\mathbf{h})$ mean variable variogram model (broken line) and $\gamma_R(\mathbf{h})$ residual variable variogram model (line) calculated with relation (7-7) is shown.

The $\gamma_m(\mathbf{h})$ variogram is zero when the trend model $m(\mathbf{u})$ is a constant equal to the first order stationary mean m, increases as more spatial variability is modeled within the trend $m(\mathbf{u})$, and approaches $\gamma_Z(\mathbf{h})$ when the mean model is highly variable and honors the $z(\mathbf{u})$ sample data. Considering now all trend models within this range, the shaded region between $\gamma_Z(\mathbf{h})$ and zero in Figure 7-1 represents where the residual variogram can theoretically exist according to relation (7-7). The upper and lower residual variogram $\gamma_R(\mathbf{h})$ limits are the $\gamma_Z(\mathbf{h})$ variogram and zero, respectively.

$$0 \le \gamma_R(\mathbf{h}) \le \gamma_Z(\mathbf{h}) \qquad (7\text{-}8)$$

Notice that $\gamma_Z(\mathbf{h})$ and $\gamma_R(\mathbf{h})$ are nearly equivalent for relatively small $\mathbf{h}$ where the mean is approximately constant. For these distances and directions $\mathbf{h}$ where $\gamma_Z(\mathbf{h})$ and $\gamma_R(\mathbf{h})$ are effectively equal, $\gamma_Z(\mathbf{h})$ acts as an effective filter of a relatively constant mean. As $\mathbf{h}$ increases, however, the $m(\mathbf{u})$ and $m(\mathbf{u} + \mathbf{h})$ values become significantly different and $\gamma_Z(\mathbf{h})$ is then no longer an effective filter. Intuitively, there is a critical $\mathbf{h}$ value where the approximation of $\gamma_R(\mathbf{h})$ with $\gamma_Z(\mathbf{h})$ breaks down.

Options for Calculating the R(u) Spatial Law

The problem of inferring the underlying spatial law of the $R(\mathbf{u})$ RF after decomposing the original $Z(\mathbf{u})$ RF according to relation (2-9) has been addressed by way of various informal inference options. Four options are generally available in practice: (1) calculate $\gamma_R(\mathbf{h})$ using $r(\mathbf{u})$ data, (2) approximate $\gamma_R(\mathbf{h})$ with $\gamma_Z(\mathbf{h})$ using $z(\mathbf{u})$ sample data, (3) calculate $\gamma_Z(\mathbf{h})$ at only $\mathbf{h}$ distances and directions where $\gamma_Z(\mathbf{h})$ can be anticipated to effectively filter a constant mean, or (4) use $\gamma_Z(\mathbf{h})$ to represent $\gamma_R(\mathbf{h})$ up to certain $\mathbf{h}$ lag vectors after which $\gamma_R(\mathbf{h})$ and $\gamma_Z(\mathbf{h})$ are significantly different, and then extrapolate from this $\mathbf{h}$ to an intermediate $\gamma_R(\mathbf{h})$ range between the $\gamma_Z(\mathbf{h})$ and $\gamma_m(\mathbf{h})$ ranges. Each of these options is now briefly described.

The most logical approach to inferring the underlying $R(\mathbf{u})$ spatial law is calculating $\gamma_R(\mathbf{h})$ using residual data approximately separated by $\mathbf{h}$, $(r(\mathbf{u}_s), r(\mathbf{u}_s + \mathbf{h}))$. This approach, however, usually results in a significant practical problem: the resulting $\gamma_R(\mathbf{h})$ variogram consistently predicts too much spatial variability. More specifically, $\gamma_R(\mathbf{h})$ often is greater than the original variable variogram $\gamma_Z(\mathbf{h})$, which contradicts the original variable variogram decomposition in relation (7-7) and the inequality in (7-8). Nevertheless, the $\gamma_R(\mathbf{h})$ variogram often appears as a nugget effect model.

The problem with calculating $\gamma_R(\mathbf{h})$ directly is related to the residual data, which are calculated using relation (2-9) as $r(\mathbf{u}) = z(\mathbf{u}) - m(\mathbf{u})$. These are not actually *data* since they exist only as artificial outcomes of the additive decomposition assumed in (2-9). The problem worsens when too much spatial variability is incorporated into the trend model $m(\mathbf{u})$. Understanding the origin of this problem is described in more detail and illustrated with an example below.

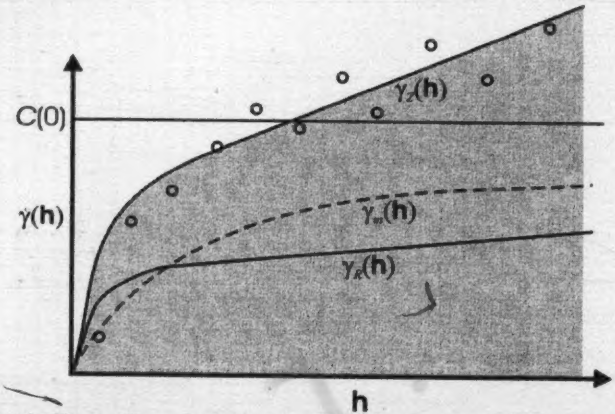

Figure 7-1: A schematic illustration of relation (7-7) with a trend model and associated $\gamma_m(\mathbf{h})$ variogram model. The residual variable variogram model $\gamma_R(\mathbf{h})$ calculated from an experimental and model original variable variogram $\gamma_R(\mathbf{h})$ and the mean variable variogram $\gamma_m(\mathbf{h})$ is shown. The shaded region represents the residual variogram $\gamma_R(\mathbf{h})$ range in the inequality in (7-8) when considering multiple trend models.

The appearance of too much spatial variability in $\gamma_R(\mathbf{h})$ is an infamous problem; yet it is not well documented. A common solution is to approximate $\gamma_R(\mathbf{h})$ with $\gamma_Z(\mathbf{h})$ calculated using the original sample data. However, as Figure 7-1 shows, this is effective only for **h** distances and directions where the trend $m(\mathbf{u})$ is roughly constant; beyond **h** lags where $m(\mathbf{u})$ and $m(\mathbf{u} + \mathbf{h})$ are significantly different, $\gamma_Z(\mathbf{h})$ will overestimate $\gamma_R(\mathbf{h})$. This approach can only be recommended within regions or directions where the trend is not strong and in settings where there are many conditioning data and the short range variogram is used almost exclusively for prediction. This approach is not recommended when there are limited conditioning data and overestimation of the long range variogram will have a high impact on prediction.

Another option is approximating $\gamma_R(\mathbf{h})$ with $\gamma_Z(\mathbf{h})$ for **h** within relatively homogeneous regions where the trend model is known to be relatively constant and can be effectively filtered with $\gamma_Z(\mathbf{h})$. Identifying areas where the trend is relatively constant is subjective and may be difficult to determine in some settings. This is the classic recommendation for practice [3].

The last option combines an approximation of $\gamma_R(\mathbf{h})$ with $\gamma_Z(\mathbf{h})$ for all **h** such that $m(\mathbf{u})$ is nearly equal to $m(\mathbf{u} + \mathbf{h})$ and an extrapolation of $\gamma_R(\mathbf{h})$ beyond this **h** lag to a $\gamma_R(\mathbf{h})$ range between $\gamma_Z(\mathbf{h})$ and $\gamma_m(\mathbf{h})$. This is currently the most reasonable approach even if it is subjective.

Inference of Residual Variogram

Although a sensible approximation of the underlying $R(\mathbf{u})$ spatial law can be made using one of the previously described options for inferring $\gamma_R(\mathbf{h})$, none of these draw on the $r(\mathbf{u})$

data directly or attempt to address why these data may appear significantly more random than they truly are. The reason why $r(\mathbf{u})$ data show too much variability is investigated.

Some attention is due to the significant inconsistency between the expected spatial law of the $R(\mathbf{u})$ RF and the inferred one using $r(\mathbf{u})$ data derived from relation (2-9). The residual RF $R(\mathbf{u})$ decomposed from the original RF $Z(\mathbf{u})$ does not exist in reality – there are no $r(\mathbf{u})$ sample data from the $R(\mathbf{u})$ RF as there are $z(\mathbf{u})$ samples from the $Z(\mathbf{u})$ RF. Both the $r(\mathbf{u})$ *data* and $\gamma_R(\mathbf{h})$ calculated using $r(\mathbf{u})$ data are reliant on the trend model $m(\mathbf{u})$. For example, if $m(\mathbf{u})$ is nearly a constant value m over all possible $\mathbf{u}$, $\gamma_R(\mathbf{h})$ is approximately equal to $\gamma_Z(\mathbf{h})$; as the trend increases in variability and approaches the $z(\mathbf{u})$ data at their locations, $\gamma_R(\mathbf{h})$ approaches a nugget effect model with low variance.

One solution is to assign the $z(\mathbf{u})$ sample data very little if any direct influence in building the trend. The trend model should incorporate no more variability than what a deterministic understanding of the geological processes suggests. When this guideline is followed, the $R(\mathbf{u})$ RF will exhibit the correct amount of spatial variability. Still, in practice this is difficult because the trend variability is revealed by through the $z(\mathbf{u})$ data.

If the $R(\mathbf{u})$ RF existed in reality, we could sample for $r(\mathbf{u})$ data and calculate $\gamma_R(\mathbf{h})$ with residual sample data $r(\mathbf{u})$. This calculated $\gamma_R(\mathbf{h})$ variogram would be correct in that it would satisfy (7-7), (7-8), and fall within the shaded region in Figure 7-1. However, since $R(\mathbf{u})$ does not exist in reality, focus must be given to correctly modeling the trend $m(\mathbf{u})$ as a strictly deterministic component of the overall $Z(\mathbf{u})$ variability in order to avoid artificially inflating the true randomness of the $R(\mathbf{u})$ spatial law.

7.4.2 Example

A porosity profile example is presented to illustrate the commonly encountered problem of overestimating the spatial variability of $R(\mathbf{u})$ when calculating $\gamma_R(\mathbf{h})$ directly with $r(\mathbf{u})$ data. Particular attention is given to the relationship between how much spatial variability is modeled in the trend $m(\mathbf{u})$ and the severity in which $\gamma_R(\mathbf{h})$ is overvalued. A practical solution to this problem is also demonstrated.

Setting

A synthetic porosity profile is generated by first simulating a correlated residual variable profile and adding it to a predetermined trend model according to the decomposition in (2-9). The resulting true porosity profile $Z(\mathbf{u})$ is analogous to the underlying true spatial distribution of the original variable value that is inaccessible in practice. Furthermore, the true $R(\mathbf{u})$ RF and associated spatial law are known in this example; these are inaccessible in practice. Since the true porosity profile is created with a known trend, this locally varying mean model can be viewed as the true or reference trend, still only known subjectively. Prior knowledge of the true $Z(\mathbf{u})$, $R(\mathbf{u})$, and $m(\mathbf{u})$ components and their corresponding variogram or spatial laws allows comparisons to be made with common experimental models inferred using limited samples from the $Z(\mathbf{u})$ RF in practice.

A stationary Gaussian residual porosity profile is simulated within a 20m elevation interval at 0.10m increments (200 points total) using a variogram model with an isotropic

10m range of correlation and zero nugget effect. The units of porosity are in fractions. The variance of $R(\mathbf{u})$ is standardized to 0.0025 by multiplying through by 0.05. Figure 7-2 shows the full $R(\mathbf{u})$ profile (top left) within the 20m elevation interval as well as the histogram of the true residual values (bottom left); the simulated residual porosity mean and variance are 0.00310 and 0.00130, respectively.

It is previously known that there is a clear fining upward trend in the porosity variable. The mean function is fully defined by a linear increase in porosity from 0.15 to 0.25 over the 20m elevation interval:

$$m(z_{\text{STRAT}}) = 0.15 + 0.10\left({z_{\text{STRAT}}}\big/_{20} \right) \qquad (7\text{-}9)$$

where $\mathbf{u}$ is replaced by z_{STRAT} which is the stratigraphic elevation coordinate incremented by 0.10m starting at zero and ending at 20m. Figure 7-2 (top right) shows this reference linear trend model $m(\mathbf{u})$. The true $Z(\mathbf{u})$ porosity profile is then calculated by adding $m(\mathbf{u})$ to $R(\mathbf{u})$ as in (2-9). Figure 7-2 also displays $Z(\mathbf{u})$ (top right) and its histogram (bottom right); the simulated porosity mean and variance are 0.20320 and 0.00108, respectively.

Figure 7-3 depicts the true or reference spatial laws for the $Z(\mathbf{u})$ and $R(\mathbf{u})$ RFs and the $m(\mathbf{u})$ trend component with normalized $\gamma_Z(\mathbf{h})$, $\gamma_R(\mathbf{h})$, and $\gamma_m(\mathbf{h})$ variograms, respectively. Notice the consistency with relation (7-7), the inequality in (7-8), and the shaded region for $\gamma_R(\mathbf{h})$ in Figure 7-1. The $\gamma_m(\mathbf{h})$ variogram is a smooth quadratic with more spatial correlation than both the $Z(\mathbf{u})$ and $R(\mathbf{u})$ RFs. The residual data $r(\mathbf{u})$ are more correlated than $z(\mathbf{u})$ values. Since the trend model is very smooth and nearly constant, the $\gamma_Z(\mathbf{h})$ and $\gamma_R(\mathbf{h})$ variograms are similar.

Trend Modeling and $\gamma_R(\mathbf{h})$

Fifty random z_{STRAT} locations are chosen to extract $z(\mathbf{u})$ samples from the reference $Z(\mathbf{u})$ profile. Four trend models are created using block ordinary kriging conditioned by the 50 sample data. These $m(\mathbf{u})$ trend models are built to increase in spatial variability by way of decreasing the nugget effect of the variogram model from 80% to 60% to 40% to 20%. The variogram and kriging setup are otherwise identical. The resulting trend models are shown together with the sample data in Figure 7-4.

Figure 7-5 shows the $r(\mathbf{u})$ residual data at the fifty random sample locations using the original $z(\mathbf{u})$ sample data and the four different $m(\mathbf{u})$ trend models previously constructed. Notice that as the nugget effect decreases and more variability is modeled by the trend, the $z(\mathbf{u})$ sample data are honored more closely and the $r(\mathbf{u})$ values appear more random. To confirm this observation, the residual variogram $\gamma_R(\mathbf{h})$ is calculated using each set of $r(\mathbf{u})$ data and compared to the true $\gamma_R(\mathbf{h})$ variogram and spatial law shown in Figure 7-3 and calculated from the simulated $R(\mathbf{u})$ profile in Figure 7-2. This residual variography comparison is shown in Figure 7-6. All four calculated $\gamma_R(\mathbf{h})$ variograms overestimate the true $\gamma_R(\mathbf{h})$ variogram model. The overestimation of the true $R(\mathbf{u})$ variability is more severe for $m(\mathbf{u})$ trends that are built to represent more spatial variability. The spatial law of $R(\mathbf{u})$, therefore, cannot be calculated correctly with the $\gamma_R(\mathbf{h})$ variogram measure using any of the previously constructed trend models and associated sets of $r(\mathbf{u})$ values.

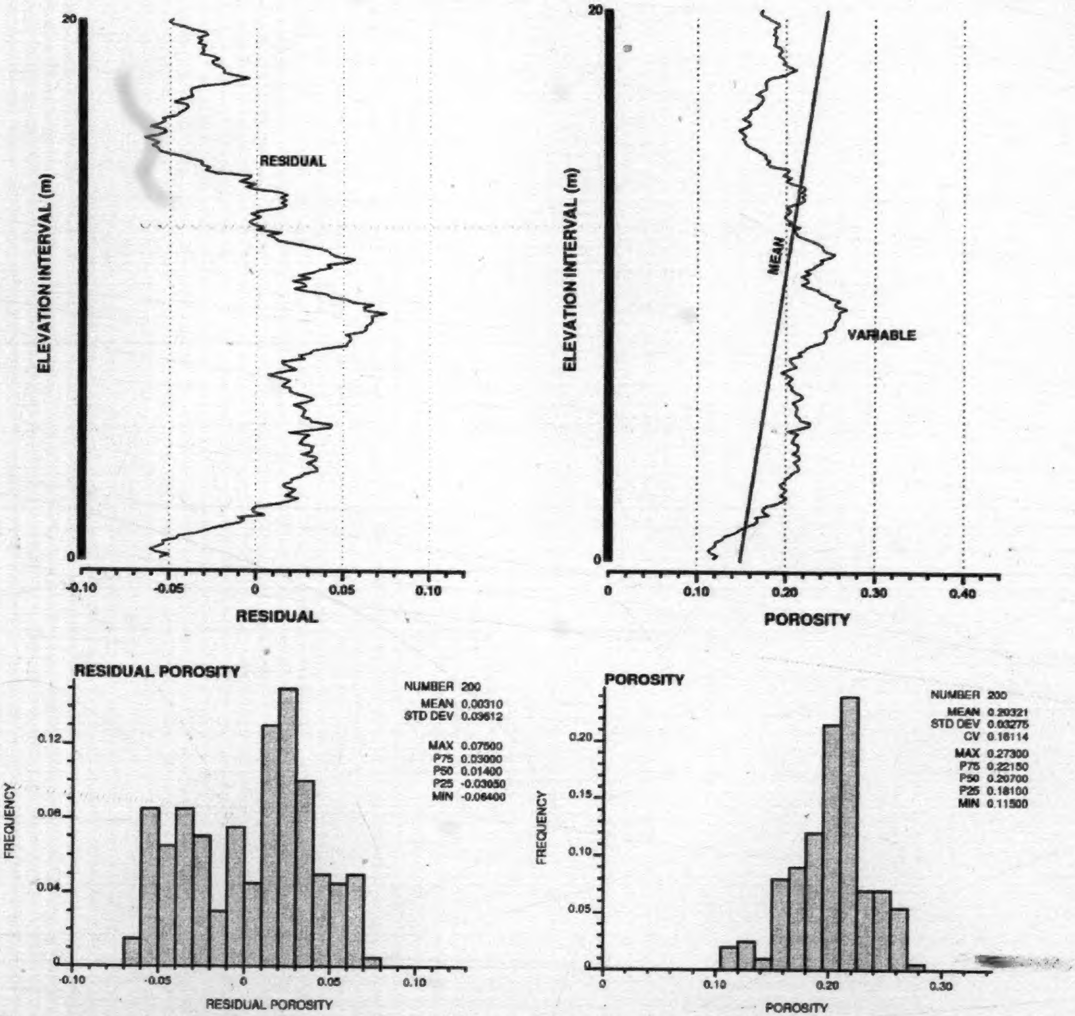

Figure 7-2: An illustration of the 1D porosity profile example setting including the reference residual $R(\mathbf{u})$ profile (top left) and histogram (bottom left), trend $m(\mathbf{u})$ (top right), and original variable $Z(\mathbf{u})$ profile (top right) and histogram (bottom right).

Figure 7-6 shows that too much variability is modeled by the block ordinary kriging trend modeling approach. The corresponding experimental residual variograms overestimate the true residual variogram and variability. Since the $r(\mathbf{u})$ values are an outcome of the construct in (2-9) rather than actual samples from $R(\mathbf{u})$, the spatial law of $R(\mathbf{u})$ inferred in practice relies greatly on the model of $m(\mathbf{u})$. Automatically built trends unfortunately incorporate too much variability by too closely honoring conditioning $z(\mathbf{u})$ sample data. The result is $r(\mathbf{u})$ values that appear more random than the true $R(\mathbf{u})$ spatial law as shown in Figure 7-6.

A reasonable trend model represents no more spatial variability than is available deterministically. Sample data should only be used as a rough guide. This criterion is often satisfied with the manual trend modeling technique that does not place undue influence on honoring the original $z(\mathbf{u})$ sample data.

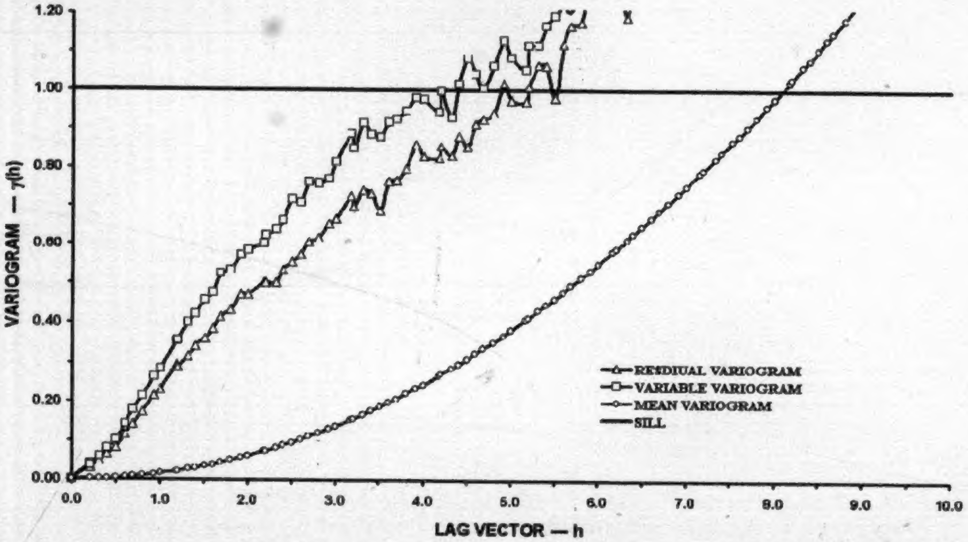

Figure 7-3: The true $R(\mathbf{u})$, $Z(\mathbf{u})$, and $m(\mathbf{u})$ spatial laws as $\gamma_R(\mathbf{h})$, $\gamma_Z(\mathbf{h})$, and $\gamma_m(\mathbf{h})$ variograms, respectively.

Given the fifty $z(\mathbf{u})$ sample data in the example, there is no deterministic geological evidence for a trend model or significant lack of data control in this setting. That is, the spacing between the fifty $z(\mathbf{u})$ sample data in Figure 7-4 is small enough to reproduce key large-scale variability. Therefore, the stationary mean porosity of 0.20320 is used with a conventional approach to prediction. The underlying spatial law of the residual $R(\mathbf{u})$ RF is then equivalent to the spatial law of the original variable $Z(\mathbf{u})$ RF. The comparison between this spatial law and the reference $R(\mathbf{u})$ spatial law is shown in Figure 7-7. The underlying spatial law and $\gamma_R(\mathbf{h})$ variogram can be accurately inferred when a reasonable trend model is built, that is, when the trend is built without direct conditioning to $z(\mathbf{u})$ sample data.

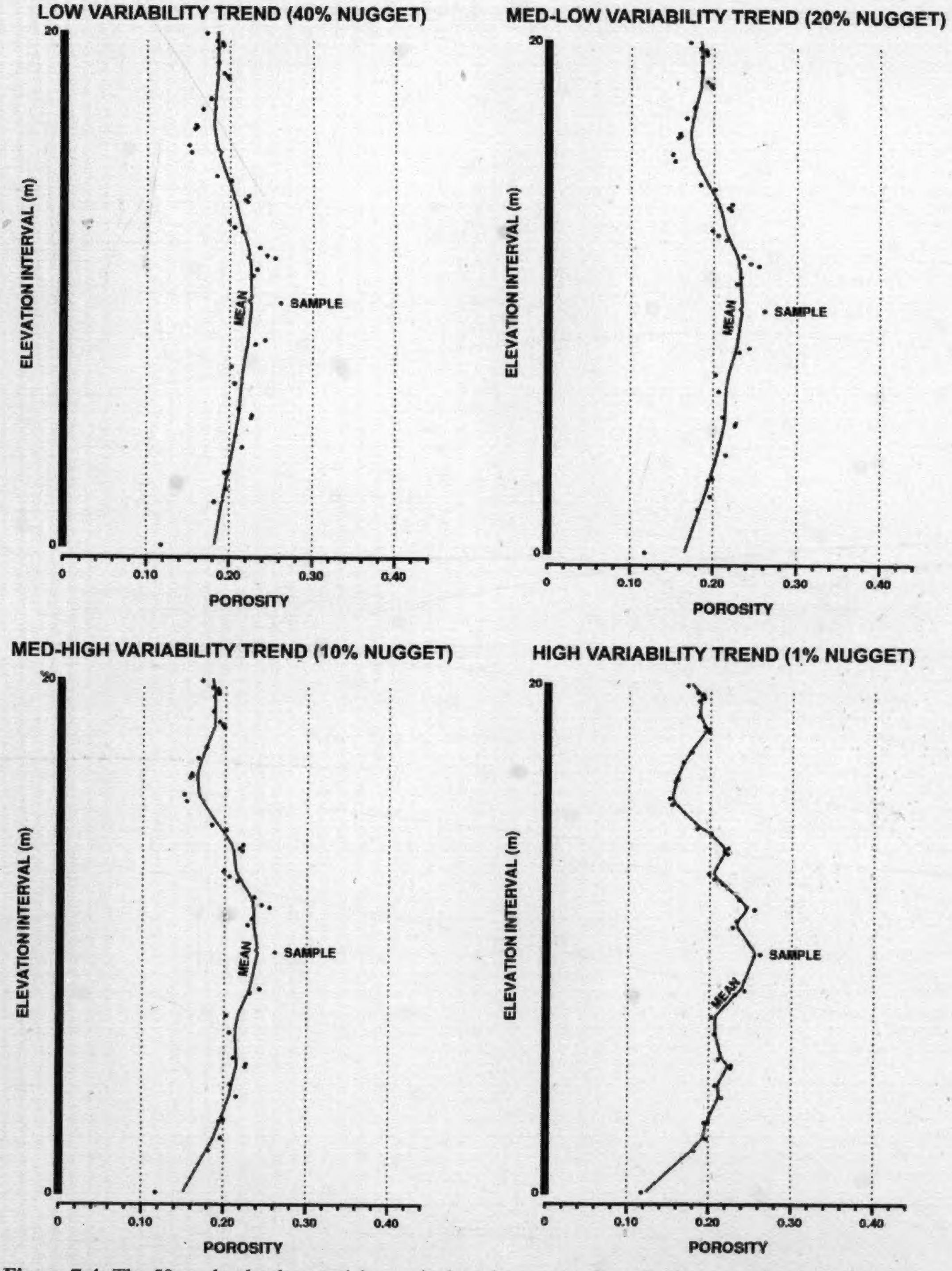

Figure 7-4: The 50 randomly chosen $z(\mathbf{u})$ sample data shown with four $m(\mathbf{u})$ trend models built to increase in spatial variability by decreasing the nugget effect in a block ordinary kriging scheme from 40% to 20% to 10% to 1%.

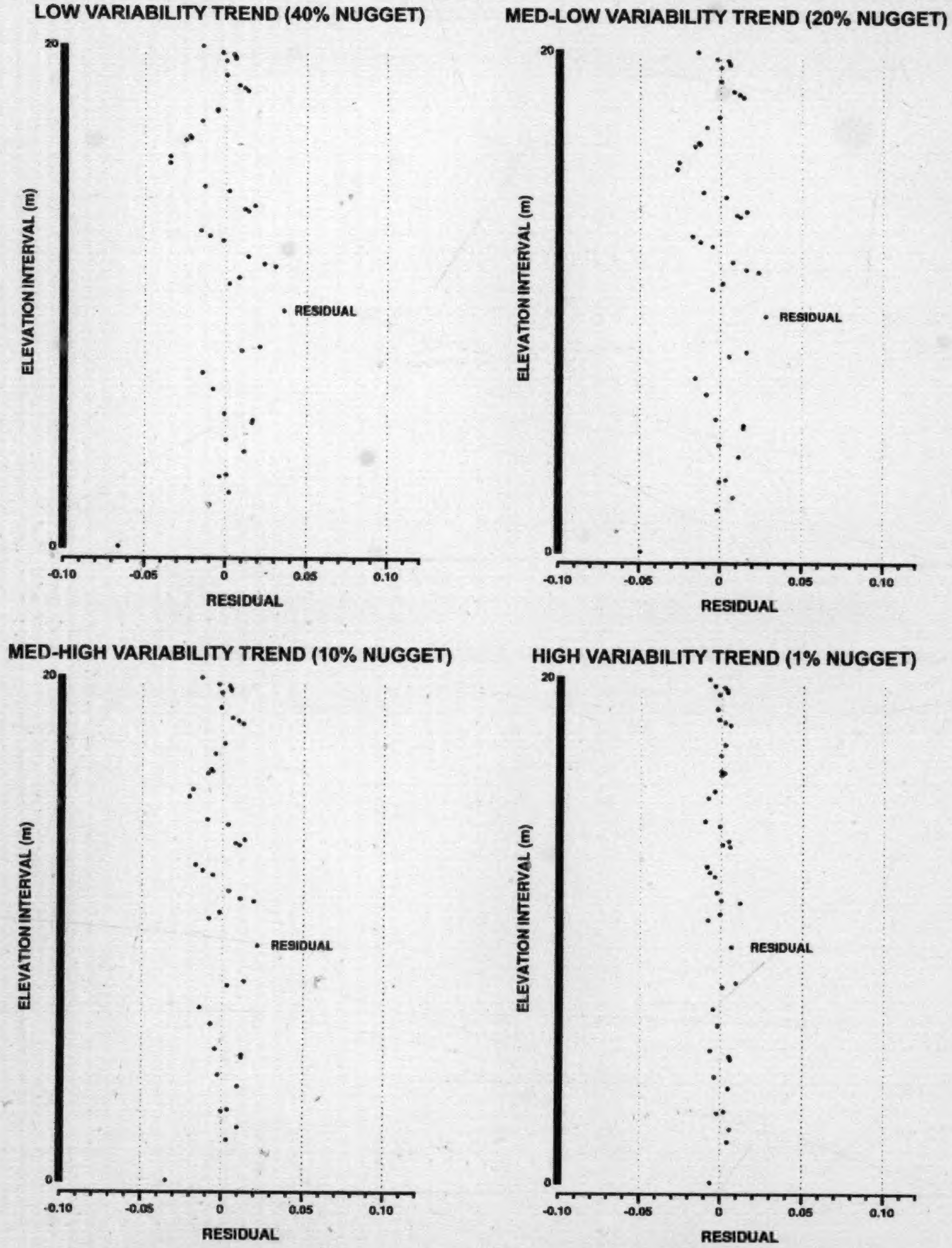

Figure 7-5: The $r(\mathbf{u})$ residual data at the 50 randomly chosen sample locations calculated with relation (2-9) using the sample $z(\mathbf{u})$ sample data and four $m(\mathbf{u})$ trend models shown in Figure 7-4.

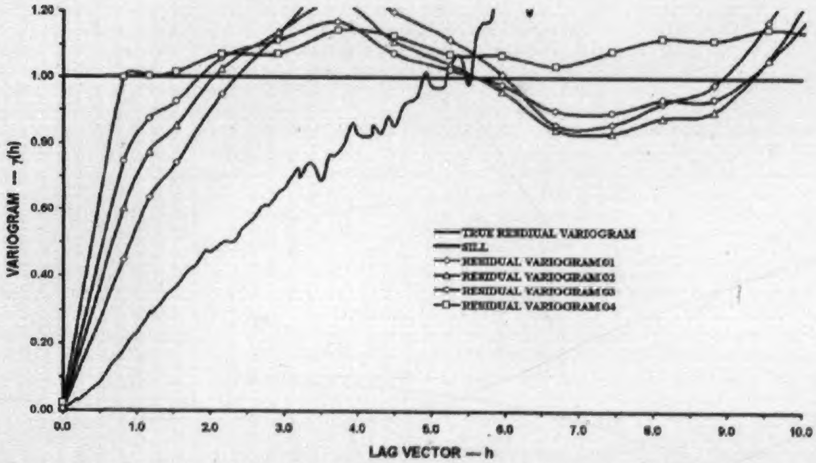

Figure 7-6: The true $\gamma_R(\mathbf{h})$ variogram and spatial law using simulated $r(\mathbf{u})$ residual data and the four $\gamma_R(\mathbf{h})$ variograms calculated using $r(\mathbf{u})$ residual data from the $z(\mathbf{u})$ sample data and four trend models shown in Figure 7-4.

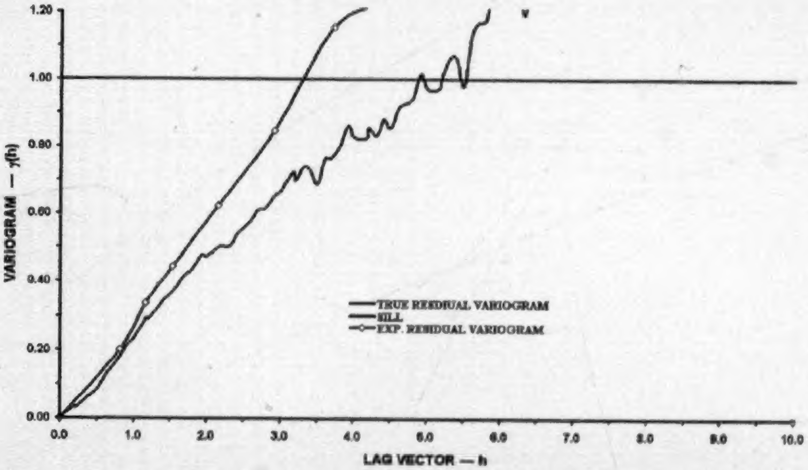

Figure 7-7: The true $\gamma_R(\mathbf{h})$ variogram and spatial law using simulated $r(\mathbf{u})$ residual data and experimental spatial law using a first order assumption of stationarity for an implicit trend model approach.

7.5 Simulation with the Trend via Locally Varying Transformations

A new approach to accounting for the trend within a geostatistical prediction framework is now presented. This method is based on a locally varying transformation (LVT) to account for non-stationarity. The trend is built into and honored through the LVT. The theoretical framework, inference of the LVT, inference of the spatial law, estimation and simulation procedures, and implementation details are presented.

7.5.1 Theoretical Framework

The LVT approach does not conform to traditional Gaussian theory underlying multi-Gaussian kriging and sequential Gaussian simulation approaches. Two unique theoretical aspects of the LVT approach differentiate it from traditional theory. The first aspect is the use of a transformation that is unique to each location in place of the common global transformation. The second aspect is the use of locally transformed conditioning data instead of globally transformed Gaussian values to infer the spatial law for subsequent prediction.

Locally Varying Transformation (LVT) Tables

Recall the first order assumption of stationarity in Chapter 2 and relation (2-7) where all prior $F_Z(\mathbf{u}; z)$ cdfs are equivalent to a single stationary univariate distribution $F_Z(z)$ at all locations $\mathbf{u}$ within a preset domain. The stationary $F_Z(z)$ distribution and associated first order moments are inferred with the cdf of all z sample data available within the domain where the SRF will be subsequently applied. The usual computation of the global $F_Z(z)$ cdf is performed using relation (2-10); however, the $F_Z(z)$ distribution and associated first order mean and variance moments may be adjusted with declustering weights as in (2-22) to (2-24) when preferential sampling is prevalent.

Traditionally, a single stationary transformation between original z sample data values and subsequently transformed Gaussian y values is defined using the single stationary $F_Z(z)$ distribution as follows:

$$y = G_Y^{-1}\left(F_Z(z)\right) \qquad \text{(7-10)}$$

Original z data is forward-transformed according to (7-10), predictions are performed using conditioning y values, and then the predicted y values are back-transformed into original z unit predictions with the reverse of (7-10):

$$z = F_Z^{-1}\left(G_Y(y)\right) \qquad \text{(7-11)}$$

Quantiles, not estimates, are back-transformed according to (7-11). Estimates are derived then by numerical integration. The forward and back transformation in (7-10) and (7-11) converts the original $Z(\mathbf{u})$ SRF to a standard normal Gaussian $Y(\mathbf{u})$ SRF for the purpose of prediction and then converts $Y(\mathbf{u})$ back to $Z(\mathbf{u})$ predictions for post processing and visualization. All that is needed to perform these transformations is an assumption of multi-Gaussianity and the representative stationary $F_Z(z)$ cdf.

The theoretical framework for the LVT technique is fundamentally different than the traditional theory underlying geostatistical prediction in that an assumption of first order stationarity is not employed. That is, the local $F_Z(\mathbf{u}; z)$ cdfs are not equivalent to a single stationary univariate distribution $F_Z(z)$ built from all z sample data available within a fixed domain $\mathbf{D}$:

$$F_{Z(\mathbf{u};z)}(z) \neq F_Z(z) \quad \forall \mathbf{u} \in \mathbf{D} \qquad \text{(7-12)}$$

The inequality in relation (7-12) is the foundation of the LVT approach and the following theoretical developments and prediction procedures.

The local $F_Z(\mathbf{u}; z)$ cdfs are calculated at each $\mathbf{u}$ location by applying locally varying weights $w^{LT}(\mathbf{u}; \mathbf{u}_s)$ to each available conditioning sample data:

$$F_{Z(\mathbf{u};z)}(z)=\frac{1}{\sum_{s=1}^{S} w^{\mathrm{LT}}(\mathbf{u};\mathbf{u}_s)}\sum_{s=1}^{S} w^{\mathrm{LT}}(\mathbf{u};\mathbf{u}_s)\cdot x(z(\mathbf{u}_s);z) \quad \forall z \tag{7-13}$$

where the notation $w^{\mathrm{LT}}(\mathbf{u};\ \mathbf{u}_s)$ indicates a location-dependent set of weights applied to the conditioning data available within the determined domain **D**. The indicator transform $x(z(\mathbf{u}_s);\ z)$ is:

$$x(z(\mathbf{u}_s);z)=\begin{cases}1, & \text{if } z(\mathbf{u}_s)\le z\\ 0, & \text{otherwise}\end{cases} \quad \forall z \tag{7-14}$$

The $w^{\mathrm{LT}}(\mathbf{u};\ \mathbf{u}_s)$ weights are not declustering weights that adjust $F_Z(z)$ to be representative of the domain **D** in the presence of biased sampling. The weights in relation (7-13) adjust the global $F_Z(z)$ distribution to be representative at that particular location **u**.

The $w^{\mathrm{LT}}(\mathbf{u};\ \mathbf{u}_s)$ weights are calculated with a smooth kriging or inverse distance scheme parameterized similar to that for building a smoothly varying trend model. A different set of weights and different local $F_Z(\mathbf{u};\ z)$ cdf are calculated at different **u** locations since the configuration of available sample data relative to the **u** location changes depending on **u**.

All univariate summary statistics addressed in Chapter 2 can be calculated to summarize each local $F_Z(\mathbf{u};\ z)$ distribution. The locally varying transformed mean $m(\mathbf{u})$ for each of the $F_Z(\mathbf{u};\ z)$ cdfs is calculated as:

$$m(\mathbf{u})=\frac{1}{\sum_{s=1}^{S} w^{\mathrm{LVT}}(\mathbf{u};\mathbf{u}_s)}\sum_{s=1}^{S} w^{\mathrm{LVT}}(\mathbf{u};\mathbf{u}_s)z(\mathbf{u}_s) \tag{7-15}$$

And the locally varying transformed variance $\sigma^2(\mathbf{u})$ for each of the $F_Z(\mathbf{u};\ z)$ cdfs is:

$$\sigma^2(\mathbf{u})=\frac{1}{\sum_{s=1}^{S} w^{\mathrm{LVT}}(\mathbf{u};\mathbf{u}_s)}\sum_{s=1}^{S} w^{\mathrm{LVT}}(\mathbf{u};\mathbf{u}_s)\left(z(\mathbf{u}_s)-m(\mathbf{u})\right)^2 \tag{7-16}$$

Prediction utilizing an underlying assumption of Gaussianity is still employed in the LVT approach. However, $Z(\mathbf{u})$ is no longer assumed a SRF. It is a RF without first order stationarity since there is no longer a single stationary $F_Z(z)$ distribution from which a global transformation from original $Z(\mathbf{u})$ space to a Gaussian SRF $Y(\mathbf{u})$ space for prediction as in relation (7-10) can be defined.

An intermediate RF $T(\mathbf{u})$ is used to convert from original $Z(\mathbf{u})$ space to a Gaussian SRF space. A locally varying transformation between original z sample data values and subsequently transformed t values is defined using the standard Gaussian distribution G_Y and the previously defined local $F_Z(\mathbf{u};\ z)$ cdfs as follows:

$$t=G_Y^{-1}\left(F_{Z(\mathbf{u};z)}(z)\right) \tag{7-17}$$

Since the z sample data are transformed to t from a set of different $F_Z(\mathbf{u};\ z)$ cdfs, the resulting global distribution of transformed t values denoted by $F_T(t)$ is Gaussian but not standard Gaussian with zero mean and unit variance. The expected value of the $T(\mathbf{u})$ RF is zero, and the variance will be less than unity for increased variability in the $w^{\mathrm{LT}}(\mathbf{u};\, \mathbf{u}_s)$ weights.

Unlike $Z(\mathbf{u})$, the $T(\mathbf{u})$ RF will be assumed to have stationary first order mean and second order covariance because the non-stationary trend model $m(\mathbf{u})$ is built into the locally varying transformation through the $F_Z(\mathbf{u};\, z)$ cdfs calculated from the $w^{\mathrm{LT}}(\mathbf{u};\, \mathbf{u}_s)$ weights. Traditional Gaussian estimation and simulation procedures can be performed using this non-standard Gaussian $T(\mathbf{u})$ SRF. Nonetheless, the $T(\mathbf{u})$ SRF is converted to a standard Gaussian SRF for prediction.

A transform of the t values to standard Gaussian y_{LT} values is defined using the stationary $F_T(t)$ distribution:

$$y_{\mathrm{LT}} = G_Y^{-1}\left(F_T(t)\right) \qquad (7\text{-}18)$$

Original z data is forward-transformed according to the locally varying transformation in relation (7-17), the transformed t values are forward-transformed according to (7-18), and predictions are made with conditioning y_{LT} values.

The predicted y_{LT} quantile values are then back-transformed to the intermediate $T(\mathbf{u})$ SRF space with the reverse of (7-18):

$$t = F_T^{-1}\left(G_Y\left(y_{\mathrm{LT}}\right)\right) \qquad (7\text{-}19)$$

And then the back-transformed t quantiles from (7-19) are back-transformed to original unit values using the reverse of (7-17):

$$z_{\mathrm{LT}} = F_{Z(\mathbf{u};z)}^{-1}\left(G_Y(t)\right) \qquad (7\text{-}20)$$

Estimates are derived by numerically integrating over a series of quantiles.

The stepwise forward transformation procedure converting from the non-standard Gaussian non-stationary RF $Z(\mathbf{u})$ to the intermediate non-standard Gaussian stationary RF $T(\mathbf{u})$ to the standard Gaussian stationary RF $Y_{\mathrm{LT}}(\mathbf{u})$ space can be summarized as:

$$\begin{aligned} t &= G_Y^{-1}\left(F_{Z(\mathbf{u};z)}(z)\right) \\ y_{\mathrm{LT}} &= G_Y^{-1}\left(F_T(t)\right) \end{aligned} \qquad (7\text{-}21)$$

Similarly, the stepwise backward transformation procedure converting from a standard Gaussian stationary Gaussian RF $Y_{\mathrm{LT}}(\mathbf{u})$ to the intermediate non-standard Gaussian stationary RF $T(\mathbf{u})$ to the original non-standard Gaussian non-stationary RF $Z(\mathbf{u})$ space can be summarized as:

$$\begin{aligned} t &= F_T^{-1}\left(G_Y\left(y_{\mathrm{LT}}\right)\right) \\ z_{\mathrm{LT}} &= F_{Z(\mathbf{u};z)}^{-1}\left(G_Y(t)\right) \end{aligned} \qquad (7\text{-}22)$$

Notice that even though both $Y_{\mathrm{LT}}(\mathbf{u})$ and $Y(\mathbf{u})$ are standard Gaussian SRFs, the $Y_{\mathrm{LT}}(\mathbf{u})$ SRF is different than its traditional analog $Y(\mathbf{u})$ due to the locally varying transformation.

The y conditioning data are calculated only once; they are the same regardless of the $\mathbf{u}$ location being estimated.

Notice that the local $F_Z(\mathbf{u}; z)$ cdfs need to be defined at all sample data and potential prediction locations $\mathbf{u}$. To implement the forward stepwise transformation in relation (7-21), $F_Z(\mathbf{u}; z)$ is only needed at the sample data locations $\mathbf{u}$. To visualize the trend model $m(\mathbf{u})$ and to implement the backward stepwise transformation in relation (7-22), $F_Z(\mathbf{u}; z)$ is needed at all prediction locations $\mathbf{u}$.

It is through the $w^{LT}(\mathbf{u}; \mathbf{u}_s)$ kriging or inverse distance weights and resulting local $F_Z(\mathbf{u}; z)$ cdfs that the non-stationary trend model $m(\mathbf{u})$ is built into prediction. The transformation procedure in relation (7-21) including the locally varying transformation in relation (7-18) removes the trend to create a standard normal Gaussian SRF where traditional geostatistical prediction can be performed. The back transformation in relation (7-22) preserves the trend model $m(\mathbf{u})$ or non-stationarity.

Consider a small example where a location $\mathbf{u}$ resides within a high potential area inside the domain $\mathbf{D}$. High valued sample data will receive higher $w^{LT}(\mathbf{u}; \mathbf{u}_s)$ weights, low sample data values will receive lower $w^{LT}(\mathbf{u}; \mathbf{u}_s)$ weights, and the local $F(\mathbf{u}; z)$ cdf will be lower for lower z values and higher for higher z values. The forward transformed y_{LT} conditioning values using relation (7-21) and the y_{LT} predictions will tend to be lower than forward transformed y conditioning values using relation (7-10) and y predictions. The back transformation using relation (7-22) to z_{LT} predictions will then tend to be higher than z predictions effectively accounting for the trend model $m(\mathbf{u})$ or locally varying mean in this high valued area.

The Underlying Spatial Law

The spatial law or SRF is defined by a multivariate Gaussian distribution and a covariance or variogram function. The original $Z(\mathbf{u})$ SRF is transformed to a standard normal Gaussian SRF $Y(\mathbf{u})$ for prediction in a multivariate Gaussian context. The Gaussian variogram $\gamma_Y(\mathbf{h})$ identifies the spatial law used for subsequent prediction. The $\gamma_Y(\mathbf{h})$ variogram in integral notation and incorporating the transform in (7-10) is:

$$\gamma_Y(\mathbf{h}) = \frac{1}{2}\int_{\mathbf{u}\in\mathbf{D}}\left[y(\mathbf{u}) - y(\mathbf{u}+\mathbf{h})\right]^2 d\mathbf{u} = \frac{1}{2}\int_{\mathbf{u}\in\mathbf{D}}\left[G_Y^{-1}\left(F_Z\left(z(\mathbf{u})\right)\right) - G_Y^{-1}\left(F_Z\left(z(\mathbf{u}+\mathbf{h})\right)\right)\right]^2 d\mathbf{u} \qquad (7\text{-}23)$$

where the integration volume $\mathbf{u}$ includes all possible $\mathbf{h}$ lag vector locations within the domain $\mathbf{D}$. The $\gamma_Y(\mathbf{h})$ variogram is required by theory. Relation (2-19) is then used to calculate the $C_Y(\mathbf{h})$ covariance needed for prediction.

The inference of $\gamma_Y(\mathbf{h})$ is straightforward. Replacing z with y in relation (2-15), $\gamma_Y(\mathbf{h})$ is inferred by calculating:

$$\gamma_Y(\mathbf{h}) = \frac{1}{2P(\mathbf{h})}\sum_{s=1}^{P(\mathbf{h})}\left(y(\mathbf{u}_s) - y(\mathbf{u}_s+\mathbf{h})\right)^2 \qquad (7\text{-}24)$$

$Y_{LT}(\mathbf{u})$ is a standard Gaussian SRF. The first order mean and variance moments are zero and one, respectively. The spatial law of the $Y_{LT}(\mathbf{u})$ SRF can be identified with the variogram $\gamma_{Y_{LT}}(\mathbf{h})$. In integral notation the $\gamma_{Y_{LT}}(\mathbf{h})$ variogram is written:

$$\gamma_{Y_{LT}}(\mathbf{h}) = \frac{1}{2}\int_{\mathbf{u}\in\mathbf{D}}\left[y_{LT}(\mathbf{u}) - y_{LT}(\mathbf{u}+\mathbf{h})\right]^2 d\mathbf{u} \qquad (7\text{-}25)$$

One approach to infer $\gamma_Y{}^{LT}(\mathbf{h})$ is with the direct calculation:

$$\gamma_{Y_{LT}}(\mathbf{h}) = \frac{1}{2P(\mathbf{h})}\sum_{s=1}^{P(\mathbf{h})}\left(y_{LT}(\mathbf{u}_s) - y_{LT}(\mathbf{u}_s+\mathbf{h})\right)^2 \qquad (7\text{-}26)$$

This approach results in the same problems as attempting to calculate the residual $\gamma_R(\mathbf{h})$ variogram directly with $r(\mathbf{u})$ data derived from relation (2-9) with a non-stationary mean previously. These problems were discussed earlier in this chapter.

A procedure for calculating and inferring the $\gamma_{Y_{LT}}(\mathbf{h})$ variogram is developed below. This offers a distinct advantage over other conventional methods for predicting with the trend.

7.5.2 LVT and $\gamma_{Y_{LT}}(\mathbf{h})$ Inference

There are two inference problems with the LVT approach. The first is inference of the locally varying $F(\mathbf{u}; z)$ cdfs with $w^{LT}(\mathbf{u}; \mathbf{u}_s)$ weighting. The second is that of inferring the $\gamma_{Y_{LT}}(\mathbf{h})$ variogram and spatial law.

Inference of Locally Varying Transformation Tables

The local non-stationary prior $F_Z(\mathbf{u}; z)$ cdf representative of the area surrounding the $\mathbf{u}$ location must be constructed. All available sample data $z(\mathbf{u}_s)$ within the predetermined domain $\mathbf{D}$ are used to construct each local $F_Z(\mathbf{u}; z)$ cdf. The weights $w^{LT}(\mathbf{u}; \mathbf{u}_s)$ assigned to the $z(\mathbf{u}_s)$ data at a particular $\mathbf{u}$ location are based on either global kriging or global inverse distance schemes presented earlier in Chapter 6 for modeling the trend. The spatial distribution of $w^{LT}(\mathbf{u}; \mathbf{u}_s)$ weights are used to generate a set of local $F_Z(\mathbf{u}_n; z)$ cdfs containing a first order mean moment $m(\mathbf{u})$ that varies smoothly through $\mathbf{D}$ representing a deterministic understanding of the trend or non-stationarity.

Figure 7-8 illustrates the LVT idea using a simple 2D schematic example with 10 $z(\mathbf{u}_s)$ sample data shaded lighter for lower values and darker for higher values. The example is conceptual. Two hand-drawn contour lines separate the domain $\mathbf{D}$ into high, medium, and low valued locations. The conventional approach to prediction, invoking the assumption of stationarity, assumes all local $F_Z(\mathbf{u}; z)$ cdfs are equivalent to the stationary $F_Z(z)$ cdf built from the 10 sample data weighted equally ($w(\mathbf{u}_s) = 1/S = 1/10$) or by weighted by declustering ($w(\mathbf{u}_s) = w^D(\mathbf{u}_s)$). This cdf is shown in Figure 7-8. The proposed LVT approach to prediction does not assume first order stationarity and instead calculates each local $F_Z(\mathbf{u}; z)$ cdf differently by weighting the 10 $z(\mathbf{u}_s)$ data. A low, medium, and high valued location $F_Z(\mathbf{u}; z)$ cdf is shown in Figure 7-8 with light, medium, and dark lines, respectively. When $\mathbf{u}$ is located within high valued zones, $F(\mathbf{u}; z)$ shifts to the right (high values) since lower valued and further away sample data receive lower $w^{LT}(\mathbf{u}; \mathbf{u}_s)$.

Recall an essential guideline to trend modeling is to avoid the tendency to model too much spatial variability. This principle is relevant here when calculating the $w^{\mathrm{LT}}(\mathbf{u};\,\mathbf{u}_s)$ weights to determine each $F_Z(\mathbf{u};\,z)$ cdf, since these locally varying cdfs have the trend $m(\mathbf{u})$ imbedded within them. For both the kriging and inverse distance schemes, a global search is used retaining all S sample data at each $\mathbf{u}$ location. A relatively low inverse distance power and significant nugget constant c are used for an inverse distance approach while a relatively high nugget and long range is combined with a block discretization for the kriging approach.

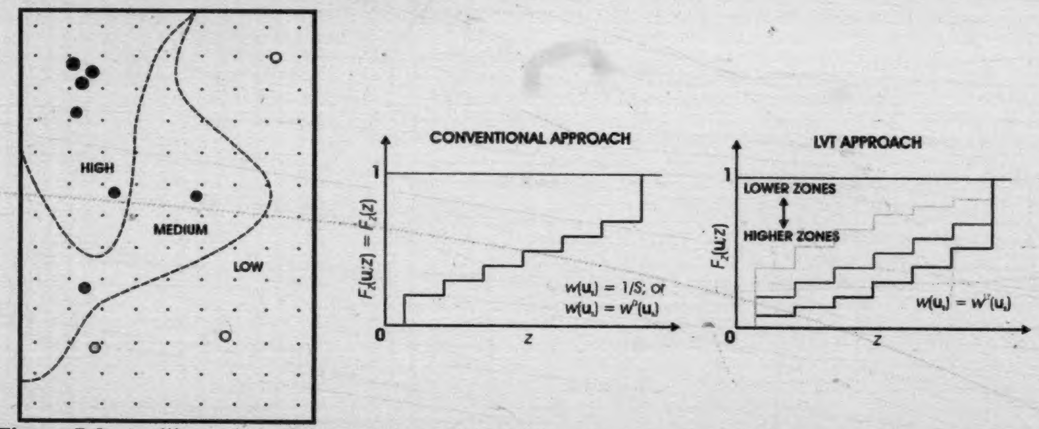
HIGH
MEDIUM
LOW
CONVENTIONAL APPROACH
1
0
$F_Z(\mathbf{u};z) = F_Z(z)$
z
$w(\mathbf{u}_i) = 1/S$; or
$w(\mathbf{u}_i) = w^{p}(\mathbf{u}_i)$
LVT APPROACH
1
0
LOWER ZONES
HIGHER ZONES
$F_Z(\mathbf{u};z)$
z
$w(\mathbf{u}_i) = w^{\mathrm{LT}}(\mathbf{u}_i)$

Figure 7-8: An illustration of the stationary cdf used for conventional prediction and a low, medium, and high case local $F_Z(\mathbf{u};z)$ cdf used for the proposed LVT prediction approach within a schematic 2D domain.

The spatial variability of the local $F_Z(\mathbf{u};\,z)$ cdfs and trend model $m(\mathbf{u})$ is sensitive to the inverse distance power and variogram parameters. Figure 7-9 (top) schematically shows these parameters for a low and high variability trend model. The resulting local $F_Z(\mathbf{u}_n;\,z)$ cdfs are also shown (bottom). For inverse distance powers near zero or kriging with high nugget effect variograms, the set of $w^{\mathrm{LT}}(\mathbf{u};\,\mathbf{u}_s)$ weights are nearly equal to $1/S$ at all $\mathbf{u}$ locations; the assumption of stationarity is strong, and the variation between $F_Z(\mathbf{u};z)$ cdfs is small. For increasing inverse distance powers and decreased nugget effect variograms, the set of $w^{\mathrm{LT}}(\mathbf{u};\,\mathbf{u}_s)$ weights increase from one $\mathbf{u}$ location to another, the assumption of stationarity is relaxed, and the variation between local $F_Z(\mathbf{u}_n;z)$ cdfs increases.

Calculating locally varying $F_Z(\mathbf{u};z)$ cdfs as described above will account for trends in the variable of interest. The $F_Z(\mathbf{u}$[illegible]$z)$ cdfs are implemented within prediction as locally varying transformation tables.

Inference of the Spatial Law

The variogram for the $Y_{\mathrm{LT}}(\mathbf{u})$ RF is not as straightforward as calculating $\gamma_{Y_{\mathrm{LT}}}(\mathbf{h})$ according to relation (7-25) using y_{LT} data. There are several qualitative solutions to approximate the spatial law of $R(\mathbf{u})$ and $Y_{\mathrm{LT}}(\mathbf{u})$; the one proposed earlier in this chapter was modeling no more spatial variability in $m(\mathbf{u})$ than is offered deterministically; however, there is no robust calculation of the residual variogram when predicting with a trend.

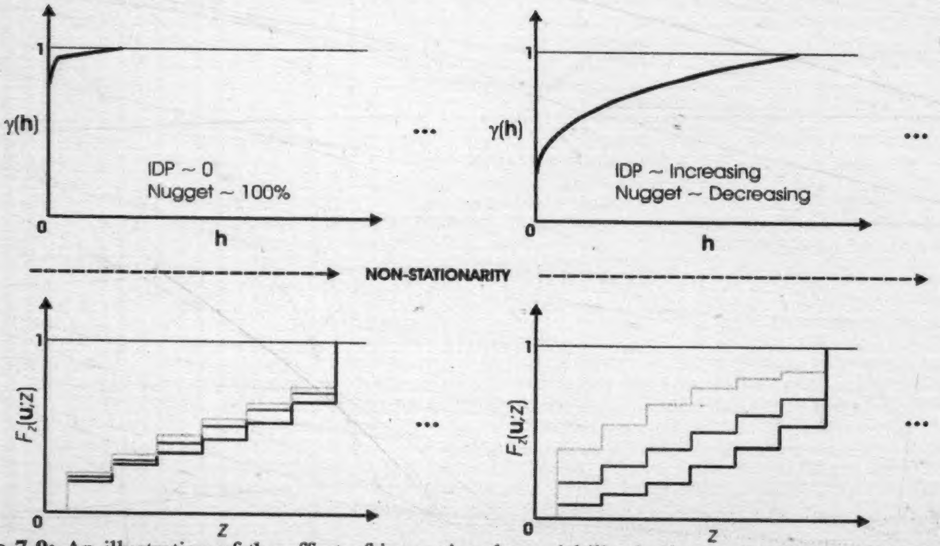

Figure 7-9: An illustration of the effect of increasing the variability in the trend with increasing inverse distance powers (IDP) or more continuous variograms has on the spatial variation of the local $F_Z(\mathbf{u}; z)$ cdfs.

An advantage of the LVT approach is that the variogram of the $Y_{LT}(\mathbf{u})$ RF can be calculated directly and quantitatively. Calculating the $\gamma_{Y_{LT}}(\mathbf{h})$ variogram is done with a mapping procedure starting from the $\gamma_Y(\mathbf{h})$ Gaussian variogram model and transforming through the locally varying $F_Z(\mathbf{u}; z)$ cdfs to the $\gamma_Y^{LT}(\mathbf{h})$ variogram model. There are two main steps required to map a γ_Y variogram value to its corresponding $\gamma_{Y_{LT}}$ variogram value for a given **h** lag vector.

The conventional Gaussian transformation in relation and associated Gaussian variogram model $\gamma_Y(\mathbf{h})$ is required. Figure 7-10 shows a calculated (open bullets) and modeled (line) $\gamma_Y(\mathbf{h})$ variogram.

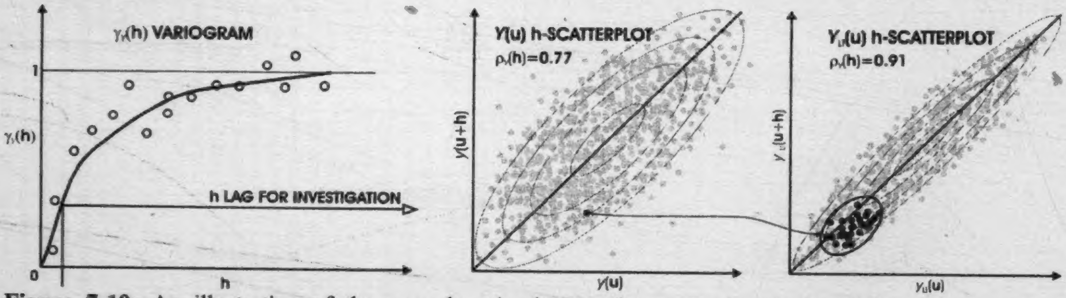

Figure 7-10: An illustration of the procedure implemented to map the single $\gamma_Y(\mathbf{h})$ variogram value indicated to its corresponding $\gamma_Y^{LT}(\mathbf{h})$ variogram value.

The next step entails constructing the **h**-scatterplot for the particular **h** lag of interest and sampling many *y* pairs. These pairs are denoted:

$$\left(y(\mathbf{u}), y(\mathbf{u}+\mathbf{h})\right)^l \quad l=1,\dots,L \tag{7-27}$$

where L is on the order of 1,000 to 10,000 pairs. In the space of $Y(\mathbf{u})$, the distribution of pairs in (7-27) is bivariate Gaussian and fully parameterized by the correlation $\rho_Y(\mathbf{h})$, which is calculated:

$$\rho_Y(\mathbf{h}) = 1 - \gamma_Y(\mathbf{h}) \qquad (7\text{-}28)$$

Relation (7-28) is derived from relation (2-19) with Z replaced with Y and $C(\mathbf{0})$ equal to one. An underlying assumption is that a reliable variogram model and correlation in (7-28) can be derived from the available y data.

The L sample pairs in (7-27) are then drawn from a bivariate Gaussian **h**-scatterplot with a Monte Carlo Simulation procedure. Two values, $d(\mathbf{u})$ and $y(\mathbf{u}+\mathbf{h})$ are drawn randomly from each marginal distribution; the correlation between $y(\mathbf{u})$ and $y(\mathbf{u}+\mathbf{h})$ is then imparted with the following equation:

$$y(\mathbf{u})^l = \rho_Y(\mathbf{h}) \cdot d(\mathbf{u})^l + \sqrt{\left(1-\rho_Y(\mathbf{h})^2\right)} \cdot y(\mathbf{u}+\mathbf{h})^l \quad l = 1,\ldots,L \qquad (7\text{-}29)$$

Relation (7-29) is equivalent to sequential Gaussian simulation with a single conditioning datum. Figure 7-10 shows an **h**-scatterplot of the L $y(\mathbf{u})$ and $y(\mathbf{u}+\mathbf{h})$ pairs for the **h** lag indicated on the $\gamma_Y(\mathbf{h})$ variogram plot.

The other main step is transforming these L pairs from the $Y(\mathbf{u})$ Gaussian SRF space to a new set of L pairs within the $Y_{\mathrm{LT}}(\mathbf{u})$ Gaussian SRF space where $\rho_{Y_{\mathrm{LT}}}(\mathbf{h})$ can be calculated directly. This new set of pairs is denoted:

$$\left(y_{\mathrm{LT}}(\mathbf{u}), y_{\mathrm{LT}}(\mathbf{u}+\mathbf{h})\right)^l \quad l = 1,\ldots,L \qquad (7\text{-}30)$$

There is, however, no single stationary $F_Z(z)$ cdf from which a unique transformation to $Y_{\mathrm{LT}}(\mathbf{u})$ can be made since, by definition of the local $F_Z(\mathbf{u}; z)$ cdfs, the transformation is locally varying. Therefore, a manageable number N of randomly chosen $\mathbf{u}_n$ head locations are used to identify N $\mathbf{u}$ and $\mathbf{u}+\mathbf{h}$ head-tail paired locations where the transformation from $y(\mathbf{u})$ to $y_{\mathrm{LT}}(\mathbf{u})$ and $y(\mathbf{u}+\mathbf{h})$ to $y_{\mathrm{LT}}(\mathbf{u}+\mathbf{h})$ is performed as:

$$\begin{aligned} z(\mathbf{u}_n) &= F_Z^{-1}\left(G_Y\left(y(\mathbf{u}_n)\right)\right) \\ t(\mathbf{u}_n) &= G_Y^{-1}\left(F_{Z(\mathbf{u};z)}\left(z(\mathbf{u}_n)\right)\right) \qquad n = 1,\ldots,N \\ y_{\mathrm{LT}}(\mathbf{u}_n) &= G_Y^{-1}\left(F_T\left(t(\mathbf{u}_n)\right)\right) \end{aligned} \qquad (7\text{-}31)$$

for all head locations and similarly for all $\mathbf{u}_n + \mathbf{h}$ tail locations (replace $\mathbf{u}_n$ with $\mathbf{u}_n + \mathbf{h}$). Relation (7-31) is a three stage stepwise transformation. The three transforms are: (1) from y values within $Y(\mathbf{u})$ space to z values within $Z(\mathbf{u})$ space, (2) from z values within $Z(\mathbf{u})$ space to t values within $T(\mathbf{u})$ space, and then (3) from t values within $T(\mathbf{u})$ space to y_{LT} values within $Y_{\mathrm{LT}}(\mathbf{u})$ space. The number of head-tail location pairs N is on the order of 10 to 100 depending on the size of domain.

The stepwise transformation in relation (7-31) is repeated for all L pairs to obtain a total of L x N $(y_{\mathrm{LT}}(\mathbf{u}), y_{\mathrm{LT}}(\mathbf{u}+\mathbf{h}))$ pairs. One $(y(\mathbf{u}), y(\mathbf{u}+\mathbf{h}))$ pair and the corresponding set of

N $(y_{LT}(\mathbf{u}), y_{LT}(\mathbf{u} + \mathbf{h}))$ pairs are shown in Figure 7-10. The full bivariate distribution of $(y_{LT}(\mathbf{u}), y_{LT}(\mathbf{u} + \mathbf{h}))$ pairs is then used to construct an **h**-scatterplot in bivariate Gaussian $Y_{LT}(\mathbf{u})$ SRF space from which the correlation $\rho_{Y_{LT}}(\mathbf{h})$ is calculated. Since the $Y_{LT}(\mathbf{u})$ SRF has unit variance, the $\gamma_{Y_{LT}}(\mathbf{h})$ variogram is calculated as:

$$\gamma_{Y_{LT}}(\mathbf{h}) = 1 - \rho_{Y}^{LT}(\mathbf{h}) \qquad (7\text{-}32)$$

This mapping procedure is then repeated for all **h** lags from the $\gamma_{Y_{LT}}(\mathbf{h})$ variogram model until the full $\gamma_{Y_{LT}}(\mathbf{h})$ variogram model is built. The mapped $\gamma_{Y_{LT}}(\mathbf{h})$ variogram is then used to interpolate conditioning y_{LT} values within $Y_{LT}(\mathbf{u})$ space.

7.5.3 Prediction

The traditional procedures for prediction must be modified in order to integrate the LVT approach. A step-by-step methodology is now presented for geostatistical estimation and simulation with the trend using the LVT approach.

Estimation: MG

Estimation is implemented within a multi-Gaussian framework. There are nine major steps to the methodology:

1. Collect all relevant hard $z(\mathbf{u}_s)$ sample data of the attribute of interest subsequently used for conditioning the estimation;
2. At each sample location **u**, perform global kriging or global inverse distance to determine the $w^{LT}(\mathbf{u}; \mathbf{u}_s)$ weights, calculate the local $F(\mathbf{u}; z)$ cdf using relation (7-13), and then transform the $z(\mathbf{u}_s)$ values to their corresponding $y_{LT}(\mathbf{u}_s)$ values using the stepwise forward transformation in relation (7-21);
3. Establish the local $F(\mathbf{u}; z)$ cdfs at all subsequent simulation locations **u** by applying global kriging or global inverse distance to determine the $w^{LT}(\mathbf{u}; \mathbf{u}_s)$ set of weights and calculating the local $F(\mathbf{u}; z)$ cdfs using relation (7-13);
4. Construct and display the trend model $m(\mathbf{u})$ at all subsequent estimation locations;
5. Determine the spatial law of $Y_{LT}(\mathbf{u})$ by transforming the original $z(\mathbf{u}_s)$ sample data to Gaussian $y(\mathbf{u}_s)$ data using (7-10), calculating the $\gamma_Y(\mathbf{h})$ variogram using relation (7-24), performing Monte Carlo Simulation from the $Y(\mathbf{u})$ space **h**-scatterplot with (7-29), transforming the $Y(\mathbf{u})$ space **h**-scatterplot to the $Y_{LT}(\mathbf{u})$ space **h**-scatterplot with (7-31), and calculating the resulting correlation $\rho_{Y_{LT}}(\mathbf{h})$ and $\gamma_{Y_{LT}}(\mathbf{h})$ variogram with (7-32) for all **h**;
6. Establish a regular path through the network of subsequent estimation locations **u**;
7. At an estimation location **u**, build the conditional cumulative distribution function (ccdf) with SK using the standard normal $y_{LT}(\mathbf{u}_s)$ conditioning data values and $\gamma_{Y_{LT}}(\mathbf{h})$ variogram established in steps 2 and 3. The resulting Gaussian ccdf is parameterized by the SK estimate $y_{LT}^*(\mathbf{u})$ and standard deviation $\sigma_{LT}^*(\mathbf{u})$;
8. Univariate summaries of the local ccdfs are calculated by back transforming a suitable number of quantiles:

$$z_{\mathrm{LT}}^{(j)}(\mathbf{u}) = F_{Z(\mathbf{u};z)}^{-1}\left(F_T\left(G_Y^{-1}\left(\sigma_{\mathrm{LT}}^{*}(\mathbf{u})\cdot\left(G_Y\left(p^{(j)}\right)\right) + y_{\mathrm{LT}}^{*}(\mathbf{u})\right)\right)\right) \quad j = 1,\ldots,J \tag{7-33}$$

where the p^j probabilities are evenly spaced between zero and one discretizing a standard Gaussian distribution. The resulting conditional distributions of $z_{\mathrm{LT}}^{(j)}(\mathbf{u})$ values can be used to calculate univariate summaries such as the mean and variance;

9. Proceed to the next estimation location **u** and loop over steps 7 and 8 until all estimation locations have been visited.

Simulation: SGS

Simulation is implemented within a sequential Gaussian simulation framework. There are twelve major steps to the methodology. The first five steps of the methodology are the same as the first five steps in the multi-Gaussian methodology above. There are seven additional steps:

6. Establish a random path through the network of subsequent simulation locations **u**;
7. At a simulation location **u**, build the conditional cumulative distribution function (ccdf) with SK using the standard Gaussian $y_{\mathrm{LT}}(\mathbf{u}_s)$ conditioning data values and $\gamma_{Y_{\mathrm{LT}}}(\mathbf{h})$ variogram established in steps 2 and 3. The resulting Gaussian ccdf is parameterized by the SK estimate $y_{\mathrm{LT}}^{*}(\mathbf{u})$ and standard deviation $\sigma_{\mathrm{LT}}^{*}(\mathbf{u})$;
8. Draw a simulated value $y_{\mathrm{LT}}^{(r)}(\mathbf{u})$ from the local ccdf;
9. Perform the stepwise backward transformation of $y_{\mathrm{LT}}^{(r)}(\mathbf{u})$ to $z_{\mathrm{LT}}^{(r)}(\mathbf{u})$ using (7-22);
10. Add the previously simulated $z_{\mathrm{LT}}^{(r)}(\mathbf{u})$ value to the pool of conditioning data;
11. Proceed to the next simulation location **u** according to the previously established random path established in step 6 and loop over steps 7 to 10 until all simulation locations have been visited;
12. Repeat steps 6 through 11 with a different random path and random number seed to construct $r = 1,.., R$ realizations.

7.6 Application Example

An example is presented to illustrate the LVT approach to simulation with the trend. The data used in this example are the same as in the introductory example in Chapter 1. The grades are from a vein-type gold deposit. There are 67 samples (g/t) located on a 2D easting-elevation section. Figure 7-11 shows the distribution of equally weighted gold data spatially in a location map (left) and statistically in a cdf (top right). Since clustered samples were taken from higher gold grade areas, polygonal declustering is performed to obtain a representative cdf (bottom right). Although this cdf is not used directly in the LVT approach, it will be referenced later for validation of the LVT simulation results. The representative gold grade distribution is positively skewed with a mean and variance of 0.86 and 1.32, respectively.

The location map in Figure 7-11 reveals a strong trend of decreasing gold concentration with depth that should be honored in simulation. Chapter 1 implemented the residual simulation approach reviewed earlier in this chapter. It was noted then, that since there is an inadequate amount of data for reproducing the trend automatically, the trend must be incorporated explicitly. The LVT simulation approach is now presented.

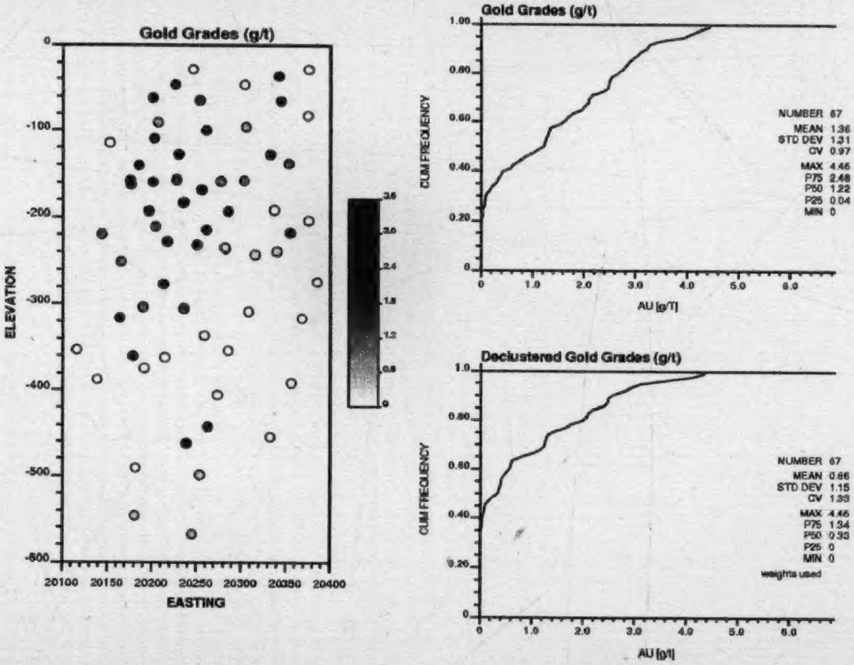

Figure 7-11: The distribution of original z sample data shown spatially in the location map (left) and as a cdf (top right) and the declustered distribution shown as a cdf (bottom right). The same grayscale is used throughout the remainder of the application example.

At each of the 67 sample data locations, global ordinary kriging is performed to determine the $F_Z(\mathbf{u}; z)$ cdf. A 3 x 3 discretization is combined with the 40% nugget variogram with 500m isotropic range. Figures 7-12 and 7-13 show the distributions of t and y_{LT} values, respectively, with a location map (left) and cdf (right). The standard normal cdf of transformed y values is also calculated and shown with both cdfs as a shaded line. Notice in Figure 7-12 that although both the $F_T(t)$ and $F_Y(y)$ cdfs are normal with a mean of zero, $F_T(t)$ is non-standard normal with a variance of 0.69. Both distributions in Figure 7-13 are standard normal.

To show the variation in the local $F_Z(\mathbf{u}; z)$ cdfs, a high valued and low valued location are considered for observation. Figure 7-14 shows the $F_Z(\mathbf{u}; z)$ and $w^{\text{LT}}(\mathbf{u}; \mathbf{u}_s)$ spatial distribution of weights for a low (left) and high (right) valued location. The exact sample locations are enclosed in a small square. The equally weighted $F_Z(z)$ cdf in Figure 7-11 is also shown here with a shaded line. Notice the increase of $F_Z(\mathbf{u}; z)$ in low valued areas and increase of $F_Z(\mathbf{u}; z)$ in high valued areas. The means $m(\mathbf{u})$ of the low and high valued $\mathbf{u}$ location $F_Z(\mathbf{u}; z)$ cdfs are 0.74 and 1.91, respectively.

Now the local $F_Z(\mathbf{u}; z)$ cdfs are calculated for each $\mathbf{u}$ location on a 150 x 300 grid of simulation locations. There are then a total of 45,000 $F_Z(\mathbf{u}; z)$ cdfs that are calculated.

The locally varying mean $m(\mathbf{u})$ or trend is extracted as the expected value of each of these local cdfs. Figure 7-15 shows the spatial distribution and cdf of the $m(\mathbf{u})$ trend values. Notice the smooth deterministic nature of the trend in the spatial distribution and low variance in the cdf. Also notice that the trend model lowers the equal weighted mean from 1.36 to 1.19 effectively accounting for the clustered high grade gold samples.

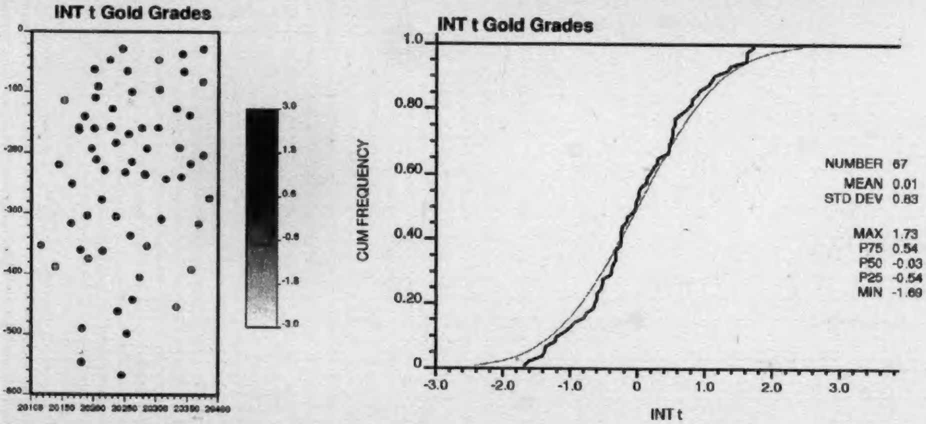

Figure 7-12: The location map (left) and cdf (right) of the 67 calculated t values. The distribution of y values is also shown with a shaded line for comparison.

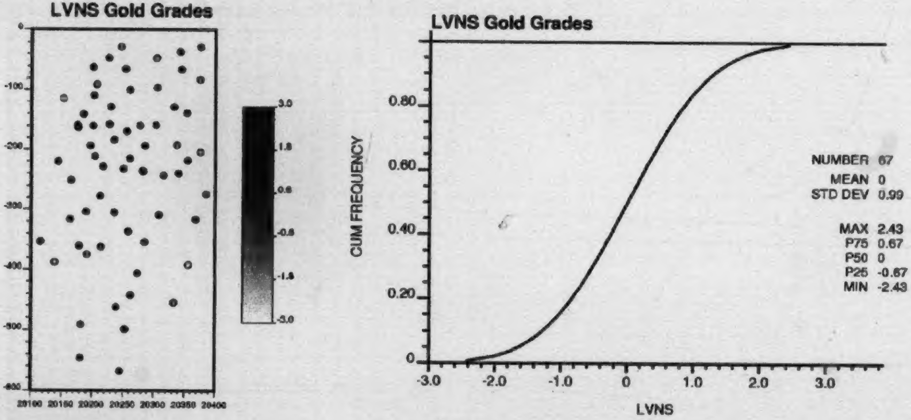

Figure 7-13: The location map (left) and cdf (right) of the 67 calculated y_{LT} values. The distribution of y values is essentially identical.

The variogram mapping procedure is now performed to convert the $\gamma_Y(\mathbf{h})$ variogram to the full $\gamma_Y^{LT}(\mathbf{h})$ variogram needed for the interpolation of y_{LT} data. A variography study was conducted on the normal score y values of the 67 original z gold sample data. The highest correlation and principle variogram direction is at 45° in the easting-elevation plane; the minor variogram direction is then at a 135° direction. Figure 7-15 shows the final calculated $\gamma_Y(\mathbf{h})$ variogram points and model line for both the 45° (dark) and 135° (shaded) direction. The analytical form of the $\gamma_Y(\mathbf{h})$ variogram model is:

$$\gamma_Y(\mathbf{h}) = 0.20 + 0.80 \cdot Sph(\mathbf{h})_{\substack{a_{45^\circ}=145\mathrm{m} \\ a_{135^\circ}=90\mathrm{m}}} \qquad (7\text{-}34)$$

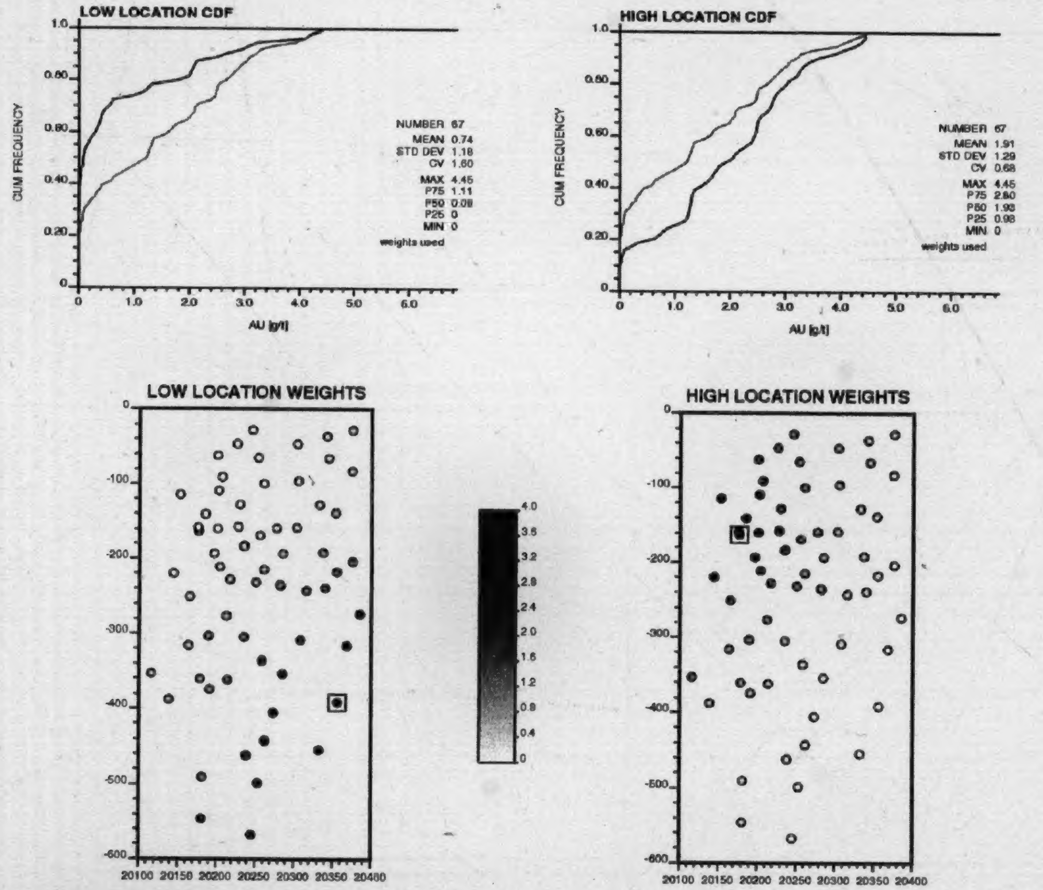

Figure 7-14: The local $F_Z(\mathbf{u}; z)$ cdf and spatial distribution of $w^{LT}(\mathbf{u}; \mathbf{u}_s)$ weights for the low valued **u** location (left) and high valued **u** location (right) indicated by the squares.

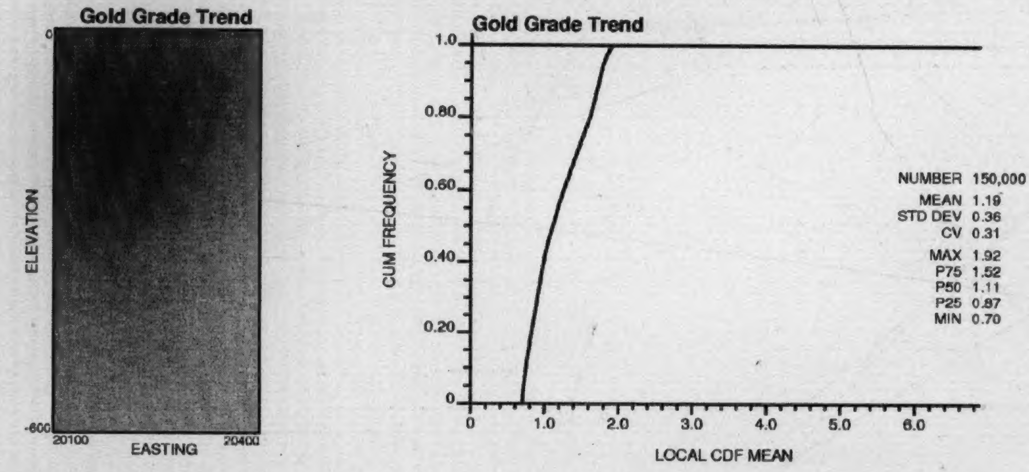

Figure 7-15: The trend $m(\mathbf{u})$ map (left) and cdf calculated from all 150,000 local $F_Z(\mathbf{u}; z)$ cdfs. The grayscale is the same as in Figure 7-11.

The variogram model in relation (7-34) is then mapped to the $\gamma_Y^{LT}(\mathbf{h})$ variogram model. The $\gamma_Y^{LT}(\mathbf{h})$ variogram model is shown in Figure 7-16 with the broken dark and shaded lines. Notice the spatial correlation of the y_{LT} values is much greater than that for the y values. The analytical form of the $\gamma_{Y_{LT}}(\mathbf{h})$ variogram model is:

$$\gamma_{Y_{LT}}(\mathbf{h}) = 0.10 + 0.69 \cdot Sph(\mathbf{h})_{\substack{a_{45^\circ}=140\text{m} \\ a_{135^\circ}=75\text{m}}} + 0.21 \cdot \mathbf{h}_{\substack{a_{45^\circ}=\infty \\ a_{135^\circ}=295\text{m}}} \qquad (7\text{-}35)$$

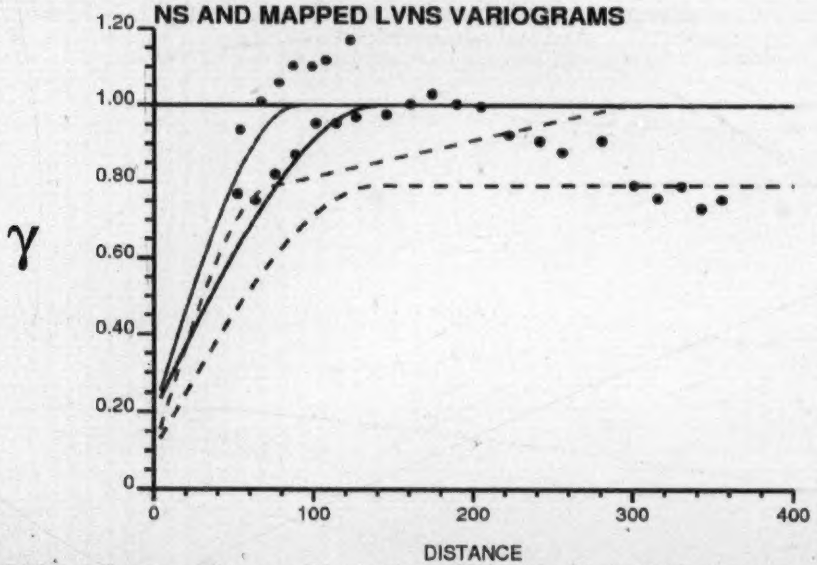

Figure 7-16: The y values normal score $\gamma_Y(\mathbf{h})$ experimental (points) and model (line) variogram shown with the mapped $\gamma_{Y_{LT}}(\mathbf{h})$ model (broken line) variogram. The principle 45° direction is shown in dark and the minor 135° direction is shaded.

All of the information required to perform simulation with the trend imbedded within locally varying $F_Z(\mathbf{u}; z)$ cdfs is ready. The z data have been collected and transformed to y_{LT} data with the 67 local $F_Z(\mathbf{u}; z)$ cdfs at sample $\mathbf{u}$ locations, the 150,000 simulation location $F_Z(\mathbf{u}; z)$ cdfs have been calculated, the trend $m(\mathbf{u})$ model has been extracted and visualized, and the $Y_{LT}(\mathbf{u})$ spatial law has been determined. The remaining seven steps in the SGS simulation procedure are now implemented for $R = 30$ realizations. The first four realizations are shown in Figure 7-17 spatially and in the form of a cdf. The declustered cdf and original cdf in Figure 7-11 are also shown with the shaded and broken lines, respectively, for comparison. The declustered distribution is honored via incorporating the trend through the locally varying transformation. The original cdf without declustering is not reproduced.

The LVT approach to simulation with the trend should honor the large-scale features of the trend. This check is performed by comparing the etype from the 30 realizations to the trend model in Figure 7-15. As Figure 7-18 illustrates, the large-scale features of the trend model are honored. The most important advantage of the LVT approach is the ability to reproduce key features in the trend with an underlying spatial law that can be calculated directly.

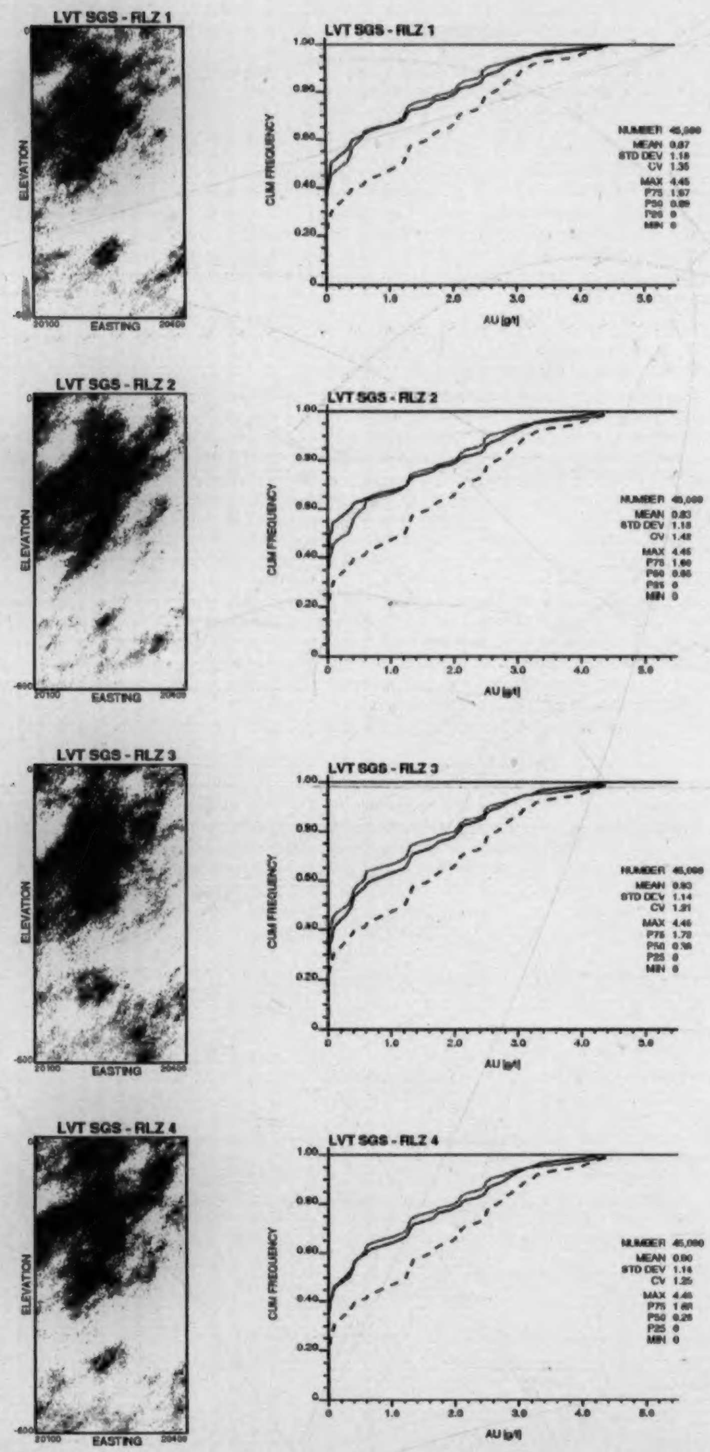

Figure 7-17: The first four LVT SGS simulated realization maps (left) and cdfs (right). The declustered distribution of *z* values is also shown with a shaded line for comparison. The grayscale is as in Figure 7-11.

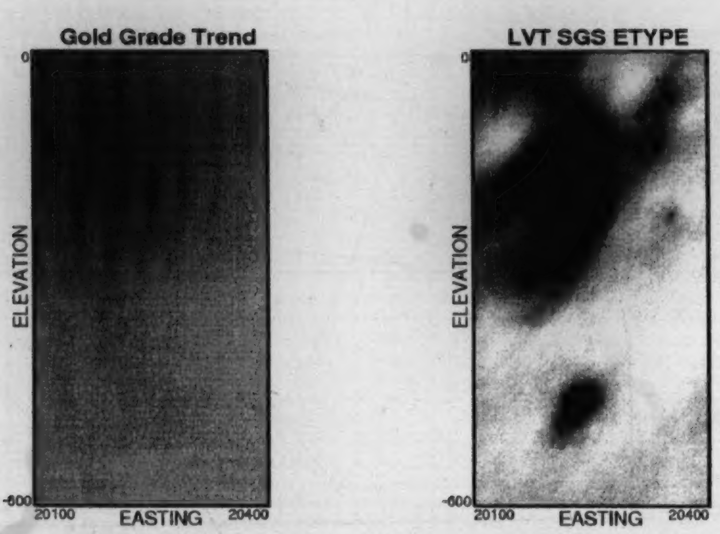

Figure 7-18: The comparison between the input $m(\mathbf{u})$ trend model imbedded within the local $F_Z(\mathbf{u}; z)$ cdfs and the etype from 30 SGS realizations using the LVT approach. The grayscale is as in Figure 7-11.

7.7 Remarks

Prediction with the trend can be an important aspect of improving predictions. Regardless of the chosen domain size, the SRF formalism may be incapable of accounting for large-scale continuity characteristic of the trend model when there is an inadequate amount of conditioning data.

There is a large variety of estimation and simulation techniques available to incorporate trends. Underlying these techniques, however, is an ambiguous definition of the variogram and spatial parameters needed. This problem can be addressed with techniques that combine separate RFs or by modeling the trend with no more variability than is offered deterministically. Still, there is no objective quantitative procedure for inferring the spatial law underlying prediction with the trend.

The motivation for the LVT approach to predicting with the trend was an alternative prediction technique for which the underlying variogram can be calculated directly. The fundamental basis of the LVT technique is the use of a locally varying transformation to and from standard normal space where conventional prediction can be performed. The local non-stationary cdfs used for the transformations effectively account for the trend and allow the correct spatial law to be calculated directly.

CHAPTER 8

CONCLUDING REMARKS

Geostatistical prediction is applied with a stationary random function (SRF). The mean and covariance parameters of this SRF are assumed independent of location. Stationarity is defined in this thesis as a decision involving five key phases of intervention from the practitioner: (1) choosing domain types, (2) boundary modeling, (3) determining the nature of transitions across boundaries, (4) trend modeling, and (5) predicting with a trend. This five step framework provides a support system for making a reasonable decision of stationarity.

Four new modeling techniques were proposed and prototyped within each of the last four chapters: (1) boundary modeling with volume functions, (2) near boundary model mixing with a linear mixing model, (3) probability combination schemes for building 3D trend models from lower dimensional trends, and (4) sequential Gaussian simulation with a locally varying transformation to account for the trend. Procedures and implementations are presented for each. These methodologies are not fully developed and require further testing and experimentation before mainstream use. Additional research and development is needed.

8.1 A Reasonable Decision of Stationarity

The key contribution of this research is offering guidelines and considerations to make a reasonable decision of stationarity. The reasonableness of a decision of stationarity can be evaluated on the basis of clearly defined criteria organized within each of the five phases.

Choosing Domain Types

The reasonability of choosing the number and type of domains for hosting separate SRFs is based on a subjective balance between the level of geologically homogeneity consistent with the mathematical first order expected value and second order covariance assumption of stationarity with the number of available data for inferring the SRF parameters.

Boundary Modeling

Reasonability criteria for boundary modeling techniques are summarized in Table 8-1. The acronyms are: (1) DD = deterministic digitization, (2) VF = volume functions, (3) OB = object based, (4) SB = surface based, and (5) SPB = stochastic pixel-based. The boundary modeling procedure using volume functions proposed at the end of Chapter 4 is not included in this table, but satisfies all five criteria.

Nature of Boundaries

The reasonability of a method used for quantifying and modeling the transitional nature of petrophysical properties near previously modeled geological boundaries is based on a subjective balance between simplicity and geological consistency of the resulting models with reality. The linear mixing model (LMM) proposed at the end of Chapter 5 satisfies this criteria for soft boundaries.

Trend Modeling

Reasonability for trend modeling techniques is evaluated with four criteria: (1) simplicity, (2) subjectivity, (3) low variability, and (4) geological reality. Five trend modeling methods were presented in Chapter 6: (1) hand mapping, (2) moving window averages, (3) global inverse distance, (4) global block ordinary kriging, and (5) kriging the trend. These five algorithms are all currently available. If they are properly implemented as explained in Chapter 6, all four reasonability criteria are satisfied. The probability combination procedures proposed at the end of Chapter 6 are reasonable when the results are geologically realistic and consistent with the lower dimensional models.

Prediction with the Trend

Reasonability criteria for techniques to estimate and simulate with the trend are reviewed in Tables 8-2 and 8-3, respectively. The acronyms are: KPM = kriging with a prior mean, KT = kriging with the trend, KED = kriging with an external drift, IRF-*k* = intrinsic random function of order *k*, RS = residual simulation, and SCT = stepwise conditional transformation. The locally varying transformation proposed at the end of Chapter 7 is not included in this table, but does satisfy all four criteria for estimation and simulation.

	Boundary Modeling: Evaluation Criteria					
Boundary Modeling Approach	**Simplistic?**	**Fast?**	**Objective?**	**Data Integration?**	**Access to Uncertainty?**	**Geologically Realistic?**
DD	yes	no	no	no	no	yes
VF	yes	yes	yes	yes	no	yes
OB	yes	yes	no	no	yes	yes
SB	yes	yes	yes	yes	yes	yes
SPB	yes	yes	yes	yes	yes	no

Table 8-1: Report card for evaluating boundary modeling approaches.

	Estimation with the Trend Model: Evaluation Criteria				
Estimation with the Trend Model	**Simplistic?**	**Spatial Law Inference?**	**Accurate/Precise Uncertainty?**	**Reproduction of Bivariate *R*(u) Distributions**	**Geologically Realistic?**
KPM	yes	no	yes	no	yes
KT	yes	no	yes	no	yes
KED	yes	no	yes	no	yes

Table 8-2: Report card for evaluating different approaches to account for the trend in estimation.

	Simulation with the Trend Model: Evaluation Criteria				
Simulation with the Trend Model	**Simplistic?**	**Spatial Law Inference?**	**Accurate/Precise Uncertainty?**	**Reproduction of Bivariate *R*(u) Distributions**	**Geologically Realistic?**
IRF-k	no	yes	yes	no	yes
RS	yes	no	yes	no	yes
SCT	yes	no	yes	yes	yes

Table 8-3: Report card for evaluating different approaches to account for the trend in simulation.

Making a decision of stationarity is inescapably subjective – it is impossible to defend a right or wrong decision. The evaluation criteria defined above are subjective. Without a full model of the physics underlying the regionalized variable, it is impossible to have objective criteria for the evaluation of a decision of stationarity. Nevertheless, the decision of stationarity can be deemed unreasonable based on judgment and experience.

Choosing an appropriate modeling approach within each of the five modeling phases is important to establish a reasonable overall decision of stationarity. The choices for one setting, however, may not be the best for a different setting.

Making a reasonable decision of stationarity is essential for building numerical models with realistic geological heterogeneity. The resulting models are better in the sense that they more closely reproduce the overall structural architecture, petrophysical property transitions across structural surfaces, and large-scale variability within structural surfaces. These improved models then lead to improved geological and production uncertainty characterization.

8.2 Practical Application

Practical application guidelines are crucial for proposed techniques or implementation parameters to be adopted for widespread use in the natural resources industry. For this reason, some practical application guidelines are now provided.

Many techniques were reviewed or developed within the five step framework of this thesis. There are many application guidelines for proper implementation. The following discussion is limited to the original methods proposed in this dissertation.

Boundary Modeling with Volume Functions

The volume function approach to quantifying structural uncertainty with probabilistic boundaries is normally chosen in the early exploration phase of a project if there is a relatively large number of conditioning data available. Two alternative volume function methods were proposed to generate probabilistic boundaries: the bootstrap combined with kriging, or data conditioned estimation combined with inverse distance.

The following issues may arise when adopting the bootstrap technique:

1. *Spatial Bootstrap*: The conventional random sample bootstrap cannot be used due to an underestimation of the VF mean uncertainty – correlated samples must be taken in a spatial bootstrap. Computer resource demand becomes intractable when more than approximately 5,000 sample data are used. Alternatives include using a subset of data representative of the full dataset or adjusting conventional bootstraps;

2. *Conditioning Data*: There must be a sufficient amount of data to fairly explore the space of structural uncertainty. There is no possibility to model boundaries where there are no intersection data. There must also not be too many data so as to make exploration obsolete;

3. *Simple Kriging*: Simple kriging must be used for interpolation due to the weighting of the mean away from data. Inverse distance should not be used with the bootstrap approach. A global search and continuous variogram should be used in order to ensure the VF results are smooth;
4. *Grid Resolution*: The grid resolution at the interpolation stage can be relatively coarse and then refined later around the vicinity of the boundary saving significant processing time. Grid refinement may also be needed when data is honored with a discontinuity at the sample locations;
5. *Histogram Transformation*: Since a large number of data should be available for the interpolation, the difference in location of the boundary and associated zero-surface VF contour is small and often undetectable between VFs interpolated with different probabilistic mean values in the simple kriging routine; a quantile transformation is often needed.

The following issues may arise when adopting the data conditioning technique:

1. *Interpolation*: Kriging should not be used for interpolation due to the combination of the data conditioning factor with extreme and negative weights that are subject to the string effect and/or screening. A relatively large search and low inverse distance power should be used to ensure the VF results are smooth.
2. *Grid Resolution*: The grid resolution at the interpolation stage can be relatively coarse and then refined later around the vicinity of the boundary saving significant processing time. Grid refinement may also be needed when data is honored with a discontinuity at the sample locations;
3. *Calibration*: The f_{MIN} value used for calibrating a linear f^{DC} data conditioning factor depends on the distribution of VF distance codes. When the separation between the magnitude of negative and positive VF codes is large, smaller f_{MIN} values down to zero can be used to identify probabilistic boundaries. As this magnitude separation decreases, probabilistic boundaries can be defined with f_{MIN} values nearer to one;
4. *Validation*: The p90/p50/p10 VFs interpolated with the f_{MIN} parameterization should be consistent with the spatial bootstrap. That is, the mean value from an interpolated probabilistic VF should be close to that probability on the distribution of uncertainty in the mean VF value.

Near Boundary Model Mixing

The linear mixing model (LMM) proposed at the end of Chapter 5 is chosen for soft boundaries without first order stationarity of the expected value, but with second order stationarity of the covariance.

The following issues may arise when adopting the linear mixing model technique:

1. *Hard Boundaries*: The choice to classify boundaries as hard and adopt independent SRFs is rare. There is almost always some degree of gradual transitional nature. The

choice of hard boundaries should be well known with sample data and a high degree of geological understanding;

2. *Covariance Function Contact Analysis*: The transition zone of many soft boundaries is considerably lower than the variogram range for RFs surrounding the boundary. The comparison between the inside and outside transition zone spatial correlation should be made within the lag vectors available within the transition zone;

Trend Modeling

All of the trend modeling techniques presented in Chapter 6 possess a common essential implementation principle, which is modeling no more spatial variability in the trend than what is previously known deterministically. The guidelines for applying any one of the five proposed techniques follow this principle. For example, kriging the trend with is done with a global search and continuous variogram models in order to ensure the trend model has low variability.

The full independence and permanence of ratios probability combinations proposed in Chapter 6 are used to build 3D trends from lower dimensional 2D horizontal and 1D vertical trends.

The following issues may arise when adopting a probability combination scheme:

1. *Full Independence*: The full independence probability combination scheme is a poor choice when there are extreme values in the trend. Extreme values in either the horizontal or vertical trend are over-exaggerated in the final 3D trend using this method;

2. *Continuous Variables*: Although some petrophysical properties such as porosity and water saturation exist in the interval [0,1], these should not be used within either the full independence or permanence of ratios probability combination scheme before transforming these values to probabilities through the inverse of their global cdfs;

Locally Varying Transformation

Geostatistical prediction with a locally varying transformation (LVT) accounts for a trend with a set of non-stationary univariate distributions and their associated locally varying transformations. The following issues may arise when implementing the locally varying transformation technique in practice:

1. *Declustering*: The LVT approach effectively declusters non-representative samples. Traditional polygonal or cell declustering techniques, therefore, declustering techniques do not need to be applied before or after application. The LVT realizations should compare well with declustered distributions;
2. *Simple Kriging*: Ideally, the local non-stationary ccdfs are conditioned by the entire set of sample data weights from a global kriging or inverse distance scheme similar to that used for constructing a trend model. This is because the LVT defined by the local ccdfs represents the trend and should share the deterministic smooth variability characteristics of the trend;

3. *Spatial Law*: The variogram mapping procedure followed to quantify the spatial law should be implemented with at least 1,000 sample pairs drawn from the bivariate Gaussian **h**-scatterplot and then for each of these sample pairs, at least 10 head-tail location pairs to transform through the LVT to the final locally varying bivariate **h**-scatterplot space;

8.3 Future Research

New techniques proposed in each of the last four modeling phases of the decision of stationarity are prototyped ideas. Numerous avenues of research and development can be followed from these prototyped ideas. Future research and development is also organized by phase of the decision of stationarity.

The Decision of Stationarity

Although different decisions could not be proven right or wrong, a case study that is amenable to different decisions of stationarity (different combinations of techniques from the five modeling phases) could be undertaken to further understand the significance different decisions of stationarity may have on project economics.

Boundary Modeling with Volume Functions

The following possible research venues for the volume function technique exist:

1. *Practical Implementation*: Implementation of the bootstrap and data conditioning technique to additional natural resource projects;
2. *Three or More Rocktypes/Facies*: The volume function implementations presented depend on a binary representation of the continuous data. However, it may be difficult or inaccurate to separate geological rocktype or continuous petrophysical property data into just two categories. The definition of a VF and probabilistic boundary modeling framework for three or more categories is an interesting avenue of research;
3. *Trend Modeling*: Incorporating trends into the interpolation of the VF may produce more geologically realistic boundaries. A KT formalism or prior trend model or prior secondary variable could be used to reproduce key structural controls;
4. *Expanding/Contracting Current Boundary Models*: Several natural resource projects already have a working geological boundary model usually built by deterministic digitization. Techniques to probabilistically inflate or contract a current boundary model could be developed;
5. *Single VF*: A single VF could also be used to extract probabilistic boundaries from. VF values above and less than zero would be used to extract probabilistic boundaries as iso-contours from a single interpolated VF. Conditioning exactly to data would be an important issue for this idea;
6. *VF Conditioning*: After calculating the VF distance codes and before interpolating them, the VF distance codes could be adjusted (increased or decreased) in absolute value to generate probabilistic boundaries.

Near Boundary Model Mixing with a Linear Mixing Model

Implementation of the linear mixing model and linear model of coregionalization to additional natural resource projects is needed for further comparison.

Trend Modeling

The following possible research venues for trend modeling exist:

1. *Practical Implementation*: Implementation of the trend modeling techniques and probability combination schemes to additional natural resource projects;
2. *Continuous Variables*: More testing of the probability combination schemes with continuous variables is needed to ensure that the combined probabilities derived from the inverse cdf do not result in artificial geological continuity;
3. *Random Function Decomposition*: Although there are sound geological reasons to consider dissociating a smooth $m(\mathbf{u})$ and more random $R(\mathbf{u})$ component from $Z(\mathbf{u})$, this particular additive decomposition technique is arbitrary and not necessarily supported by any geological phenomenon. Better approaches may exist, for example, $m(\mathbf{u})$ and $R(\mathbf{u})$ could be multiplicative. Alternative techniques such as these can and be should be investigated.
4. *Second Order Trends*: Second order non-stationarity in the variogram or covariance occur as frequently as first order non-stationarity in the mean, but were not directly addressed in this thesis. Prediction with locally varying variogram or covariance parameters is not new [6], but could be further explored to account for second order trends;

Locally Varying Transformation

The following possible research venues for prediction with the trend using locally varying transformation tables exist:

1. *Practical Implementation*: Implementation of the LVT technique coupled with alternative residual simulation and stepwise conditional transformation simulation to additional natural resource projects for further testing and comparison;
2. *Categorical Variables*: Accounting for the trend while estimating and predicting categorical variables is important. The locally varying cdfs and transformations can be built for categorical variables as well;
3. *Spatial Law*: The calculation procedure to obtain the underlying spatial law should be investigated further and validated analytically if possible;
4. *Sensitivities*: There are several parameters in the LVT procedure that are sensitive and affect the local cdfs and transformation tables. The most important ones that should be investigated include the inverse distance power and nugget effect used for assigning weights to the sample data;
5. *Computer Resources*: The global search used to calculate the weights can be time consuming in practice. CPU comparison between this and other techniques should be performed;

6. *Cross Validation*: Cross validation studies could be conducted for this method and alternative methods to evaluate the best approach for a particular setting.

8.4 Final Remark

Numerical modeling of regionalized variables in natural resource assessment requires the selection of a modeling approach and a decision of how to combine data for statistical analysis. The modeling approach and associated decisions can neither be refuted nor unequivocally accepted on the basis of the available data; we are necessarily predicting at locations where we have no data. People building numerical models must be sensitive to the consequences of their choices.

BIBLIOGRAPHY

[1] Ricardo, A. *Geostatistics for Engineers and Earth Scientists*. Springer, New York, 1999.

[2] Isaaks, E.H. and Srivastava, R.M. *An Introduction to Applied Geostatistics*. Oxford University Press, New York, 1989.

[3] Journel, A.G. and Huijbregts, Ch.J. *Mining Geostatistics*. The Blackburn Press, New Jersey, 1978.

[4] Goovaerts, P. *Geostatistics for Natural Resource Evaluation*. Oxford University Press, New York, 1997.

[5] Deutsch, C.V. and Journel, A.G. *GSLIB: Geostatistical Software Library: and User's Guide*, Oxford University Press, New York, 2nd Ed, 1998.

[6] Deutsch, C.V. *Geostatistical Reservoir Modeling*. Oxford University Press, New York, 2002.

[7] Chiles, J. and Delfiner, P. *Geostatistics: Modeling Spatial Uncertainty*. John Wiley & Sons, New York, 1999.

[8] David, M. *Geostatistical Ore Reserve Estimation*, Elsevier, Amsterdam, 1977.

[9] Guilbert, J.M. and Park, C.F. *The Geology of Ore Deposits*. W.H. Freeman and Company; 4th Edition, New York, 1985.

[10] Catuneanu, O. *Principles of Sequence Stratigraphy*. Elsevier Science, New York, 2006.

[11] Deutsch, C.V. *Cleaning Categorical Variable (Lithofacies) Realizations with Maximum A-Posteriori Selection*. Computers and Geosciences, 24 (6), 1998, pp. 551-562.

[12] Deutsch, C.V. *Direct Assessment of Local Accuracy and Precision*. Fifth International Geostatistics Conference: Wollongong 1996, Kluwer Academic Publishers, vol. 1, 1997.

[13] Houlding, S.W. *3D Geoscience Modeling: Computer Techniques for Geological Characterization*. Springer-Verlag, Berlin Heidelberg, 1994.

[14] Gemcom Software International Inc., Suite 1100 – 1066 West Hastings Street, Vancouver, British Columbia, V6E 3X1 Canada. *GEMS Suite of Software*. www.gemcomsoftware.com.

[15] Maptek Inc., Suite 900, 165 South Union Blvd., Denver, Colorado, 80228 USA. *Vulcan Software*. www.vulcan3d.com.

[16] Zaparo Ltd., 1060 Hay Street, Level 3, IBM Building, West Perth, Australia, WA 6005. *Leapfrog Software*. www.leapfrog3d.com.

[17] Cowan, E., Beatson, R., Fright, W., McLennan, T. and Mitchell, T. *Rapid Geological Modeling*. Presented at Applied Structural Geology for Mineral Exploration and Mining International Symposium, Kalgoorlie, Australia, 2002.

[18] Cowan, E., Beatson, R., Ross, H., Fright, W., McLennan, T., Evans, T., Carr, J., Lane, R., Bright, D., Gillman, A., Oshust, P., and Titley, M. *Practical Implicit Geological Modeling*. The Australian Institute of Mining and Metallurgy Publication Series, no. 8, 2003.

[19] Pyrcz, M. and Deutsch, C.V. *ALLUVSIM: A Program for Streamline-Based Stochastic Modeling of Fluvial Depositional Systems*. Center for Computational Geostatistics (CCG), University of Alberta, Report Six, 2004.

[20] Bridge, J.S. and Leeder, M.R. *A Simulation Model of Alluvial Stratigraphy*. Sedimentology, vol. 26, no. 5, 1979.

[21] Haldorsen, H.H. and Chang, D.M. *Notes on Stochastic Shales: From Outcrop to Simulation Model*. Reservoir Characterization, Academic Press, London, 1986.

[22] Haldorsen, H.H. and Lake, L.W. *A New Approach to Shale Management in Field-Scale Models*. SPE Journal, April, 1984.

[23] Cojan, I., Fouche, O., Lopez, S. and Rivoirard, J. *Process-Based Reservoir Modeling in the Example of the Meandering Channel*. Seventh International Geostatistics Conference: Banff 2004, Springer, vol. 2, 2005.

[24] Deutsch, C.V. and Wang, L. *Hierarchical Object-Based Stochastic Modeling of Fluvial Reservoirs*. Mathematical Geology, vol. 28, no. 7, 1996.

[25] Deutsch, C.V. and Tran, T.T. *FLUVSIM: A Program for Object-Based Stochastic Modeling of Fluvial Depositional Systems*. Computers and Geosciences, vol. 28, 2002.

[26] Pyrcz, M. and Deutsch, C.V. *Conditioning Event-Based Fluvial Models*. Seventh International Geostatistics Conference: Banff 2004, Springer, vol. 1, 2005.

[27] Lopez, S., Galli, A. and Cojan, I. *Fluvial Meandering Channelized Reservoirs: A Stochastic and Process-Based Approach*, Annual Conference of the International Association of Mathematical Geologists (IAMG), Cancun, 2001.

[28] Ren, W., Cunha, L. and Deutsch, C.V. *Preservation of Multiple-Point Structure when Conditioning by Kriging*. Seventh International Geostatistics Conference: Banff 2004, Springer, vol. 2, 2005.

[29] Shmaryan, L.E. and Deutsch, C.V. *Object-Based Modeling of Fluvial / Deepwater Reservoirs with Fast Data Conditioning: Methodology and Case Studies*. SPE Annual Technical Conference and Exhibition, Houston, Paper 56821, 1999.

[30] Viseur, S., Shtuka, A. and Mallet, J.L. *New Fast, Stochastic, Boolean Simulation of Fluvial Deposits*. SPE Annual Technical Conference and Exhibition, New Orleans, Paper 49281, 1998.

[31] Stow, D.A.V. and Mayall, M. *Deepwater Sedimentary Systems: New Models for the 21st Century*. Marine and Petroleum Geology, vol. 17, 2000.

[32] Deutsch, C.V. and Tran, T.T. *Simulation of Deepwater Lobe Geometries with Object-Based Modeling:* `LOBESIM`, Center for Computational Geostatistics (CCG), University of Alberta, Report One, 1999.

[33] Pyrcz, M., Catuneanu, O. and Deutsch, C.V. *Stochastic Surface-Based Modeling of Turbidite Lobes*. AAPG Bulletin, vol. 89, no. 2, 2005.

[34] Xie, Y. Deutsch, C.V. and Cullick, A.S. *A Short Note on Surface-Based Modeling for Integration of Stratigraphic Data in Geostatistical Reservoir Models*: Center for Computational Geostatistics (CCG), University of Albert, Report One, 1999.

[35] Pyrcz, M., and Deutsch, C.V. `SURFSIM`: *A Program for Stochastic Surface-Based Simulation for Strataform Sediments*: Center for Computational Geostatistics (CCG), University of Albert, Report Six, 2004.

[36] Zhang, X. and Pyrcz, M. *Advances in Stochastic Surface Modeling: Conditioning, Facies, and Non-Stationarity*. Center for Computational Geostatistics (CCG), University of Albert, Report Eight, 2006.

[37] Geomodeling Technology Corporation, 1100 665 – 8 ST SW, Calgary, Alberta, Canada, T2P 3K7. *SBED*. www.geomodeling.com/sbed_a.htm.

[38] Chiles, J.P. *Simulation of a Nickel Deposit: Problems Encountered and Practical Solutions*. Geostatistics for Natural Resources Characterization, vol. 2, Reidel Publishing Company, Netherlands, 1984.

[39] Isaaks, E.H. *Indicator Simulation: Application to the Simulation of a High Grade Uranium Mineralization*. Geostatistics for Natural Resources Characterization, vol. 2, Reidel Publishing Company, Netherlands, 1984.

[40] Matheron, G., Beucher, C, Fouquet and Galli, A. *Conditional Simulation of Fluvio-Deltaic Reservoirs*. SPE Annual Technical Conference and Exhibition, Dallas, Paper 16753, 1987.

[41] Le Loch, G. and Galli, A. *Truncated PluriGaussian Method: Theoretical and Practical Points of View*. Fifth International Geostatistics Conference: Wollongong 1996, Kluwer Academic Publishers, vol. 1, 1997.

[42] Alabert, F. and Massonnat, G.J. *Heterogeneity in a Complex Turbiditic Reservoir: Stochastic Modeling of Facies and Petrophysical Variability*. SPE Annual Technical Conference and Exhibition, New Orleans, Paper 20604, 1990.

[43] Journel, A.G. and Gomez-Hernandez, J.J. *Stochastic Imaging of the Wilmington Clastic Sequence*. SPE Formation Evaluation, 1993.

[44] Guardiano, F.B. and Srivastava, R.M. *Multivariate Geostatistics: Beyond Bivariate Moments*. Fourth International Geostatistics Conference: Troia 1992, Soares, A. (Ed), vol. 1, 1993.

[45] Strebelle, S.B. and Journel, A.G. *Sequential Simulation Drawing Structures From Training Images*. Sixth International Geostatistics Conference: Cape Town 2000, Kluwer Academic Publishers, vol. 1, 2000.

[46] Deutsch, C.V. *A Statistical Resampling Program for Correlated Data: Spatial Bootstrap*. Center for Computational Geostatistics (CCG), University of Alberta, Report Six, 2004.

[47] Journel, A.G. and Xu, W. 1994, *Posterior Identification of Histograms Conditional to Local Data*, Mathematical Geology, vol. 22, no. 8, 1994..

[48] Deutsch, C.V. *A New trans Program for Histogram and Trend Reproduction*. Center for Computational Geostatistics (CCG), University of Alberta, Report Six, 2004.

[49] Larrondo, P. and Deutsch, C.V. *Accounting for Geological Boundaries in Geostatistical Modeling*. Seventh International Geostatistics Conference: Banff 2004, Springer, vol. 1, 2005.

[50] Journel, A.G. *Combining Knowledge from Diverse Sources: An Alternative to Traditional Data Independence Hypotheses*. Mathematical Geology, vol. 34, no. 5, 2002.

[51] Deutsch, C.V. *Direct Assessment of Local Accuracy and Precision*. Fifth International Geostatistics Conference: Wollongong 1996, Kluwer Academic Publishers, vol. 1, 1997.

[52] McLennan, J.A. and Deutsch, C.V. *Conditional Non-Bias of Geostatistical Simulation for Prediction of Recoverable Reserves*. Canadian Institute of Mining and Metallurgy (CIM) Bulletin, vol. 97, no. 1080, 2004.

[53] Krige, D.G. *A Statistical Approach to some Mine Valuations and Allied Problems at the Witwatersrand*. Master's Thesis, University of Witwatersrand, South Africa, 1951.

[54] Matheron, G. *Le Krigeage Universel: Fascicule 1*. Cahiers du CMM, 1969.

[55] McLennan, J.A., Leuangthong, O. and Deutsch, C.V. *A Closer Look at the Kriging Equations*. Center for Computational Geostatistics (CCG), University of Alberta, Report Eight, 2006.

[56] Armstrong, M. *Problems with Universal Kriging*. Mathematical Geology, vol.16, no. 1, 1984.

[57] Marechal, A. *Kriging Seismic Data in Presence of Faults*. Geostatistics for Natural Resources Characterization, vol. 2, Reidel Publishing Company, Netherlands, 1984.

[58] Alabert, F. *Stochastic Imaging of Spatial Distributions Using Hard and Soft Information*. Master's Thesis, Stanford University, California, 1987.

[59] Journel, A.G. *Constrained Interpolation and Qualitative Information*. Mathematical Geology, vol. 18, no. 3, 1986.

[60] Journel, A.G. *Fundamentals of Geostatistics in Five Lessons*. American Geophysical Union, 1989.

[61] Dimitrakopoulos, R. *Conditional Simulation of Intrinsic Random Functions of Order k*. Mathematical Geology, vol. 22, no. 3, 1990.

[62] Deutsch, C.V. *Geostatistical Reservoir Modeling*. Oxford University Press, New York, 2002.

[63] Leuangthong, O. and Deutsch, C.V. *Transformation of Residuals to Avoid Artifacts in Geostatistical Modeling with a Trend*. Mathematical Geology, vol. 36, no. 3, 2004.

[64] Zhu, H. and Journel, A.G. *Formatting and Integrating Soft Data: Stochastic Imaging via the Markov-Bayes Algorithm*. Fourth International Geostatistics Conference: Troia 1992, Soares, A. (Ed), vol. 1, 1993.

[65] Deutsch, C.V. *Stepwise Conditional Transformation in Estimation Mode*. Center for Computational Geostatistics (CCG), University of Alberta, Report Eight, 2006.